

**Intravascular Ultrasound : Forward-Viewing  
Pulse-Echo and Doppler Imaging**

**Loukianos Gatzoulis**

Degree of Doctor of Philosophy

University of Edinburgh

2000



## **DECLARATION**

I hereby declare that the work contained in this thesis is my own and that the thesis has been composed by myself.

Loukianos Gatzoulis



*To my parents Giorgos and Athina*

*To my wife Kathleen*

*To my grandfather Hristos*

## ACKNOWLEDGEMENTS

Upon completion of this work, I would like to express my gratitude to those who have helped me throughout these years.

To Professor Norman McDicken and Dr Steve Pye, my supervisors, for all their continuous support, advice, guidance and encouragement throughout this work. I will always be indebted to you.

To Dr Harry Brash, my mentor, for his unconditional support whenever I needed it.

To Tom Anderson, for his suggestions and design ideas for the scan head of the scaled-up catheter. And of course, for all his help with electronics and his answer to all sorts of (strange) queries.

To Rab O'Donnell, for all his hard work in manufacturing the scanning rig and the catheters.

To John Campbell, for manufacturing the final versions of the electronic circuits and the PCBs.

To Dr Robin Watson, for his help and endless patience during the *in-vitro* work with the vessels in the lab 'upstairs'.

To Dr Calum McLean for his help in the implementation of the 'snake' algorithm and his expertise in computing.

To Dr Kumar Ramnarine for providing the BMF and his expertise in flow phantom design.

To Dr Lee Jordan, for carrying out the histological analysis of the vessels.

To Mr Scott Inglis for his assistance with photography.

To Dr Pete Hoskins for his feedback on the Doppler study.

To Dr Neil Uren and Dr David Newby, for their clinical expertise and assistance with interventional cardiology.

To Dr Tim Spencer and Dr Alcimar Soares, for their advice and endless discussions during the 'early days'.

To Dr Vasilis Sboros, a close friend next to me in the lab, day in day out.

To other members of staff at the Department of Medical Physics for their unconditional support. In particular, Irene Craig, Catrióna Morrison, Gillian Rae, Bill Ellis, Ian Peaston, Bill Wight, Dr Alistair Millar and Dr Carmel Moran, always there to help me one way or another.

To the European Commission for their financial support.

Last, but not the least, to my wife Kathleen, for her continuous love and support throughout this time.

# TABLE OF CONTENTS

<b>Acknowledgements .....</b>	<b>iii</b>
<b>Table of Contents.....</b>	<b>iv</b>
<b>Abbreviations.....</b>	<b>x</b>
<b>Abstract .....</b>	<b>xi</b>
 <b>Chapter 1 - Introduction.....</b>	 <b>1</b>
1.1 Introduction.....	1
1.2 Vascular disease.....	2
1.2.1 Arterial anatomy .....	2
1.2.2 Atherosclerosis .....	3
1.2.3 Diagnosis of atherosclerosis .....	4
1.2.3.1 Angiography .....	4
1.2.3.2 Angioscopy.....	5
1.2.3.3 Intravascular ultrasound .....	5
1.2.4 Treatment of atherosclerosis.....	7
1.2.4.1 Bypass graft.....	7
1.2.4.2 Balloon angioplasty.....	7
1.2.4.3 Stent.....	8
1.2.4.4 Atherectomy .....	9
1.2.4.5 Laser ablation .....	10
1.2.4.6 Spark erosion.....	10
1.2.4.7 Pharmaceutical therapies .....	11
1.3 Diagnostic ultrasound imaging .....	11
1.3.1 Ultrasound wave and echo signal .....	12
1.3.2 Imaging modes .....	13
1.3.3 Ultrasound transducer probes.....	14
1.3.3.1 Single element transducers .....	14
1.3.3.2 Linear and curvilinear arrays.....	15
1.3.3.3 Phased arrays.....	15
1.3.3.4 Annular arrays .....	15
1.3.4 Image quality .....	16
1.3.5 Real-time imaging .....	18
1.3.6 Doppler ultrasound and colour flow imaging.....	18

1.4 Intravascular ultrasound.....	19
1.4.1 Intravascular scanning techniques .....	20
1.4.1.1 Rotating transducer.....	21
1.4.1.2 Rotating mirror .....	22
1.4.1.3 Circular phased array.....	22
1.4.2 Advantages and disadvantages of catheter configurations .....	22
1.4.3 Catheter handling.....	27
1.4.4 Clinical applications of intravascular ultrasound .....	28
1.4.4.1 Visualisation of vessel wall layers .....	29
1.4.4.2 Imaging and characterisation of atherosclerotic plaque .....	30
1.4.4.3 Diagnostic value of intravascular ultrasound .....	32
1.4.4.4 Three dimensional intravascular ultrasound.....	34
1.4.4.5 Guidance of interventional procedures.....	35
1.4.5 The need for forward-viewing intravascular ultrasound .....	37
1.5 Aim of the thesis.....	38
1.6 Layout of the thesis.....	39

## **Chapter 2 - Development of the scanning and data acquisition system ....42**

2.1 Introduction.....	42
2.2 Common acquisition methods for 3D ultrasound .....	43
2.3 Scanning patterns for 3D forward-viewing IVUS .....	46
2.3.1 Conical scan.....	46
2.3.2 Spiral scan .....	47
2.3.3 Rotational scan .....	48
2.3.4 Fan scan .....	49
2.3.5 Compound scan .....	49
2.4 Scanning system .....	50
2.5 Data acquisition system .....	58
2.5.1 Transducer .....	58
2.5.2 Ultrasound scanner .....	60
2.5.3 Volume acquisition.....	61
2.5.4 Signal processing for image generation .....	62
2.6 Tissue mimicking material vessel phantoms .....	64
2.6.1 Tissue mimicking material .....	64
2.6.2 Specifications for the vessel phantoms.....	65
2.6.3 Preparation of the vessel phantoms .....	66

## **Chapter 3 - Evaluation of the experimental system ..... 71**

3.1 Introduction.....	71
3.2 Linearity of the RF amplifier in the ultrasound scanner.....	71
3.3 Frame image production and display.....	76
3.4 Geometrical accuracy of the scanning system.....	78
3.4.1 Accuracy of the transducer sweep motions.....	78
3.4.2 Accuracy of the transducer rotation.....	80
3.5 Display of frames acquired with the various scanning patterns.....	81
3.5.1 Frames acquired with the Conical scan.....	82
3.5.2 Frames acquired with the Spiral scan.....	83
3.5.3 Frames acquired with the Rotational scan.....	84
3.5.4 Frames acquired with the Fan scan.....	85
3.6 System limitations.....	86
3.6.1 Non-real-time operation.....	86
3.6.2 Field of view.....	87
3.7 Summary.....	88

## **Chapter 4 - Image quality of three dimensional forward-viewing IVUS data sets ..... 89**

4.1 Introduction.....	89
4.2 Three dimensional image reconstruction.....	89
4.2.1 Three dimensional reconstruction of the Conical and Spiral scans.....	90
4.2.2 Three dimensional reconstruction of the Rotational and Fan scans.....	90
4.2.3 Three dimensional reconstruction of the Compound scan.....	92
4.2.4 Interpolation.....	92
4.3 Image display.....	93
4.3.1 Volume visualisation.....	93
4.3.2 Display of two dimensional slices.....	94
4.3.3 Lumen cast display.....	94
4.4 Conditions for assessment of image quality.....	95
4.5 Image quality of data sets acquired with the various scanning patterns.....	96
4.5.1 'Single hump' eccentric stenosis.....	96
4.5.2 Symmetrical stenosis.....	102
4.5.3 'Double hump' eccentric stenosis and 'hard' plaque material.....	105
4.5.4 Eccentric and angulated positions of the catheter in the lumen.....	107
4.5.5 Effects of sparse data sets.....	113
4.6 Discussion.....	119
4.6.1 Image quality of the Compound scan.....	119
4.6.2 Image quality of the Conical scan.....	119
4.6.3 Image quality of the Spiral, Rotational and Fan scans.....	121

4.6.4 Potential for real-time imaging.....	123
4.6.5 Scanning with non-central and non-coaxial catheter positions .....	124
4.7 Conclusion .....	126

## **Chapter 5 - Quantitative accuracy of three dimensional forward-viewing IVUS data sets.....127**

5.1 Introduction.....	127
5.2 Image segmentation in side-viewing IVUS .....	128
5.3 Considerations for image segmentation in forward-viewing IVUS .....	129
5.3.1 Edge detection .....	130
5.3.2 'Snake' dynamic contour model.....	132
5.4 Quantitative measurements and analysis .....	133
5.4.1 Lumen area and volume measurement .....	133
5.4.2 Statistical analysis .....	134
5.5 Results.....	135
5.5.1 Segmented images and lumen cast display .....	135
5.5.2 Accuracy of lumen area measurements .....	138
5.6 Discussion and Conclusion.....	149

## **Chapter 6 - A three dimensional forward-viewing IVUS imaging system.....151**

6.1 Introduction.....	151
6.2 Clinical utility of the various scanning patterns .....	152
6.3 Manufacturing issues for forward-viewing IVUS catheters .....	153
6.4 Choice of scanning pattern for forward-viewing IVUS.....	156
6.5 Design of a three dimensional forward-viewing IVUS imaging system .....	157
6.5.1 The intravascular ultrasound scanner .....	157
6.5.2 Design of the forward-viewing IVUS catheter.....	159
6.5.2.1 Transducer design considerations.....	159
6.5.2.2 Catheter body design considerations .....	160
6.5.3 Data acquisition and image reconstruction.....	163
6.6 Resolution of the forward-viewing IVUS system.....	164
6.7 Geometrical accuracy of the forward-viewing IVUS system .....	167
6.7.1 Accuracy of the transducer sweep motion.....	167
6.7.2 Accuracy of the catheter rotation.....	168
6.8 System limitations .....	169
6.8.1 Non-real-time operation .....	169
6.8.2 Field of view.....	170

6.9 Summary.....	170
<b>Chapter 7 - Forward-viewing IVUS imaging of arteries <i>in vitro</i> .....</b>	<b>171</b>
7.1 Introduction.....	171
7.2 <i>In vitro</i> imaging protocol .....	171
7.2.1 Side-viewing IVUS imaging .....	172
7.2.2 Forward-viewing IVUS imaging.....	173
7.2.3 Histological analysis.....	175
7.3 Imaging results.....	175
7.4 Dimensional quantification.....	187
7.5 Discussion.....	188
7.6 Conclusion .....	194
<b>Chapter 8 - Doppler colour flow imaging and flow quantification with forward-viewing IVUS .....</b>	<b>196</b>
8.1 Introduction.....	196
8.2 IVUS techniques for functional assessment of stenosed vessels .....	197
8.2.1 Estimation of blood velocity and flow using Doppler wires.....	197
8.2.2 Limitations of measuring blood velocity and flow with Doppler wires..	199
8.2.3 Decorrelation based estimation of blood velocity and flow .....	201
8.3 A forward-viewing IVUS system for flow imaging and quantification .....	203
8.3.1 Blood mimicking fluid .....	203
8.3.2 Flow phantom.....	204
8.3.3 Data acquisition system.....	207
8.3.4 Blood velocity estimation and display .....	208
8.3.5 Flow quantification.....	210
8.4 Results.....	210
8.4.1 Measurement range .....	210
8.4.2 Parabolic flow.....	212
8.4.2.1 Flow disturbance caused by the catheter .....	212
8.4.2.2 Detection of parabolic flow with the forward-viewing IVUS system..	215
8.4.3 Symmetrical stenosis .....	218
8.4.4 Eccentric stenosis .....	227
8.5 Discussion and Conclusion.....	231

<b>Chapter 9 - Conclusions and further development .....</b>	<b>234</b>
9.1 Introduction.....	234
9.2 Conclusions from the study with the scaled-up system .....	235
9.3 Conclusions from the study with the small catheter .....	237
9.4 Future developments.....	239
 <b>References .....</b>	 <b>241</b>
 <b>Appendix : List of Publications .....</b>	 <b>267</b>



## ABBREVIATIONS

<b>1D</b>	-	One Dimensional
<b>2D</b>	-	Two Dimensional
<b>3D</b>	-	Three Dimensional
<b>APV</b>	-	Average Peak Velocity
<b>BMF</b>	-	Blood Mimicking Fluid
<b>CD-ROM</b>	-	Compact Disc Read Only Memory
<b>CSA</b>	-	Cross-Sectional Area
<b>DGC</b>	-	Depth Gain Compensation
<b>DSP</b>	-	Digital Signal Processor
<b>ECG</b>	-	ElectroCardioGram
<b>FFT</b>	-	Fast Fourier Transform
<b>IVUS</b>	-	IntraVascular UltraSound
<b>LoG</b>	-	Laplacian of Gaussian operator
<b>PC</b>	-	Personal Computer
<b>PCB</b>	-	Printed Circuit Board
<b>PRF</b>	-	Pulse Repetition Frequency
<b>PTFE</b>	-	PolyTetraFluoroEthylene
<b>PVDF</b>	-	PolyVinylDiFluoride
<b>PZT</b>	-	Lead Zirconate Titanate
<b>RF</b>	-	RadioFrequency
<b>SNR</b>		Signal to Noise Ratio
<b>TGC</b>	-	Time Gain Compensation
<b>TMM</b>	-	Tissue Mimicking Material

## ABSTRACT

Intravascular ultrasound imaging has developed rapidly in the last ten years and has become recognised as a high quality tool in imaging arterial disease. However, conventional intravascular ultrasound catheters are side-viewing devices, acquiring images at the site of the transducer. A limitation of this design is the inability to image severely stenosed or completely occluded vessels, where there is insufficient lumen space to advance the catheter to the site of interest.

This limitation could be overcome with the use of a forward-viewing intravascular ultrasound device. Such a device would emit the ultrasound beam in a forward direction ahead of the catheter tip, providing information about the morphology and the extent of stenoses without the need to insert the catheter into the diseased sites. This thesis investigates optimal scanning techniques for forward-viewing intravascular ultrasound imaging.

Scaled-up artery models, made of tissue mimicking material, were used in the first part of this work in order to study the scanning techniques without the need for miniaturisation. A versatile scaled-up scanning system was constructed, and five different pulse-echo scanning patterns were implemented and evaluated. A scanning technique referred to as the *rotational scan* emerged as the most suitable.

Based on this outcome, a small forward-viewing catheter was manufactured for imaging human vessels *in vitro*. Operating at 30 MHz, it was integrated with an intravascular ultrasound scanner and a radiofrequency data acquisition system. Two and three dimensional data sets were successfully acquired and assessed for a number of carotid and femoral arteries *in vitro*. The reconstructed images demonstrated the ability of this forward-viewing system, based on the rotational scan, to visualise healthy lumens, bifurcations, thickened atherosclerotic walls and, most importantly, very severe vessel occlusions.

At a further stage, the catheter was used for Doppler studies in tissue mimicking flow phantoms simulating cases of healthy and stenosed vessels, in an attempt to overcome sample volume location uncertainties associated with current Doppler wire techniques. The new intravascular Doppler technique was proven capable of providing velocity profiles, colour flow images and flow quantification.

The results show that the rotational scan is a very promising technique for implementing a forward-viewing intravascular ultrasound imaging system suitable for anatomical and functional assessment of stenosed vessels and for guidance of both interventional and pharmaceutical therapies. The results of this thesis will provide the basis for future manufacturing research and development in this field.

# CHAPTER 1

## INTRODUCTION

### 1.1 Introduction

Ultrasound imaging techniques have been widely used in diagnostic medicine over the recent decades. Interaction of ultrasound with human tissue gives rise to information related to the acoustic properties of tissue, enabling the production of images which allow the study of size and nature of tissue structures. The comparative safety of ultrasonic radiation, as opposed to other imaging techniques such as X-ray, computed tomography, magnetic resonance and isotope imaging, has boosted the use of ultrasound in several medical disciplines covering a variety of fields from gynaecology and obstetrics to paediatrics, ophthalmology and cardiology.

The majority of medical ultrasound applications are extracorporeal and transcutaneous. Nevertheless, human anatomy and in particular bones, ribs and air filled organs limit the penetration of ultrasound, hindering its application in some specific cases. These limitations have led to the development of invasive ultrasound probes for specialised use. Typical examples are the transesophageal probe for imaging the heart, the transvaginal and transrectal probes and the most recent intravascular catheters for imaging vascular disease.

Coronary artery disease is one of the leading causes of death in the industrialised western world. Since the end of 1980s, intravascular ultrasound (IVUS) probes have been developed for the investigation of coronary and peripheral arterial disease. This new imaging modality has proven a useful tool for providing valuable information about the pathology and distribution of vascular lesions, and also for guiding and assessing interventional treatment.

The scope of this chapter is to provide an introduction to vascular disease and the physics of medical ultrasound, followed by an update on the current state-of-the-art of intravascular ultrasound technology and its clinical applications. The chapter also tackles problems related to intravascular ultrasound imaging and addresses the need for forward-viewing IVUS imaging.

## **1.2 Vascular disease**

### **1.2.1 Arterial anatomy**

From a histological perspective, an artery consists of five distinct concentric layers. From inner to outer, these are: intima, internal elastic lamina, media, external elastic lamina and adventitia (Figure 1.1).

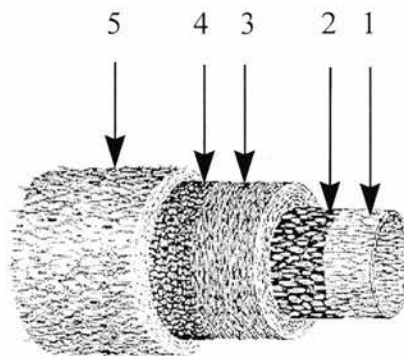


*Figure 1.1 : The five layers of a normal human artery. (1) Intima, (2) internal elastic lamina, (3) media, (4) external elastic lamina, and (5) adventitia (from ten Hoff 1993).*

The innermost layer, the intima, is a thin layer of endothelial cells which forms a biocompatible interface with blood (ten Hoff 1993). The internal and external elastic laminae are thin membranes which enclose the middle layer, the

media. According to the composition of the media two types of arteries exist in the human body: muscular and elastic. In muscular arteries such as coronaries and iliofemoral, the media consists mainly of tightly packed smooth muscle cells with a low concentration of collagen and elastin fibres dispersed in between. On the other hand, the media in elastic arteries such as aortas and pulmonary arteries, is composed of densely packed, concentrically arranged layers of elastin fibres amidst smooth muscle cells (Gussenhoven et al. 1989a; Lockwood et al. 1992). The outer layer of the arterial wall, the adventitia, consists mostly of dense collagen and elastin and forms the interface to the tissue surrounding the artery.

### **1.2.2 Atherosclerosis**

Atherosclerosis is the main cause of occlusive or stenotic lesions in blood vessels. When developed in coronary arteries it can lead to loss of vital blood supply to the myocardium, increasing the possibility of a myocardial infarction.

Atherosclerosis is primarily an intimal disease which secondarily affects the internal elastic lamina and the media of the artery. Plaque development can be caused by pathologic mechanisms as well as vessel wall injury (Cavaye and White 1993). Intimal cell proliferation along with lipid and cholesterol accumulation result in thickening of the intima and formation of plaque. As the intimal plaque thickens, the media may become thinner and the internal elastic lamina may be disrupted. In the first stages of plaque formation, the arterial wall becomes thicker as the plaque increases in size, and the whole artery is distended so that the original lumen size is maintained. This is known as 'arterial wall remodelling' and as a result of it, lumen stenosis may be delayed even if the plaque occupies a large portion, up to 40%, of the area enclosed by the internal elastic lamina (Glagov et al. 1987). When the plaque accumulates at much larger amounts, lumen reduction occurs and the artery becomes stenosed.

The composition of the atherosclerotic plaque varies considerably. Sometimes the lesion is composed mostly of fibro-fatty lipid pools, some other times

it is dominated by fibrous tissue, while there are also cases of calcium presence in the plaque (Gown et al. 1986; Hangartner et al. 1986). The extent of plaque formation is also variable and unpredictable, in both axial and radial directions, although intimal thickening and atherosclerosis develop largely in regions of relatively low wall shear stress and disturbed streamline flow, e.g. bifurcations (Glagov et al. 1988; Zarins et al. 1983). In many cases the plaque is formed eccentrically in the artery (Hangartner et al. 1986) causing the residual lumen to be placed 'off centre' with respect to the arterial wall.

In diseased arteries separation of the media can occur, known as 'arterial dissection'. A channel is formed in the vessel wall between the intimal plaque and the adventitia, providing a false lumen for blood flow. This dissection may finally break through the intimal layer, creating a flap and allowing the blood flow to rejoin the true vessel lumen, or break through the adventitia wall or even proceed along branch vessels causing ischemia to distal organs (Cavaye and White 1993).

### **1.2.3 Diagnosis of atherosclerosis**

A number of imaging techniques exist for assessing vascular disease *in vivo*. These include angiography, angioscopy, computed tomography, magnetic resonance imaging, epicardial ultrasonography and recently, intravascular ultrasound. While every individual technique has its own advantages, angiography and angioscopy along with intravascular ultrasound are the most widely used.

#### **1.2.3.1 Angiography**

Angiography is the most commonly used method clinically for diagnosis of vascular disease. It is an X-ray imaging technique which provides a 2D projection of the vessel lumen silhouette after injection of a contrast agent (radiopaque dye) into the vessel through a catheter. Stenoses are identified as reductions of the lumen diameter with respect to the lumen diameter of a nearby vessel segment which is

assumed to be normal. Angiography can be quite efficient in depicting the lumen shape and accurate in measuring luminal dimensions when the lumen cross-sectional area is circular, as in the case of normal or mildly diseased arteries. However, its use is limited in cases of eccentric stenoses, since the projected image depends hugely on the direction of the X-ray beams with respect to the stenosis. Even if biplane angiography is used, the projected images are not guaranteed to truly reflect the 3D geometry of the vessel lumen. This limitation often leads to underestimation of the severity of vascular disease (Isner et al. 1981; Nissen et al. 1993). Furthermore, an angiogram does not provide any information about the vessel wall morphology or the tissue types that compose the plaque, knowledge of which can be useful in clinical decision making.

#### **1.2.3.2 Angioscopy**

Angioscopy is an invasive fibre optic imaging technique developed in an attempt to visualise the composition of atherosclerotic plaque. It can yield reliable information about surface features of the vessel lumen and plaque not obtainable by angiography (Sherman et al. 1986; Siegel et al. 1990; Siegel et al. 1991). This technique is not suitable though in defining the underlying vessel wall morphology and cannot be used for quantitative measurements of lumen or plaque size. Furthermore, it requires a blood-free environment in order to visualise any luminal surfaces. This necessitates continuous flushing with a clear fluid during imaging, making it a difficult technique to perform especially in coronary arteries (Siegel et al. 1990).

#### **1.2.3.3 Intravascular ultrasound**

Intravascular ultrasound (IVUS) is a recently developed catheter based imaging technique for the assessment of vascular disease. It provides high resolution



2D cross-sectional images of the vessel wall and plaque, which carry information not obtainable by angiography and angioscopy (Figure 1.2).

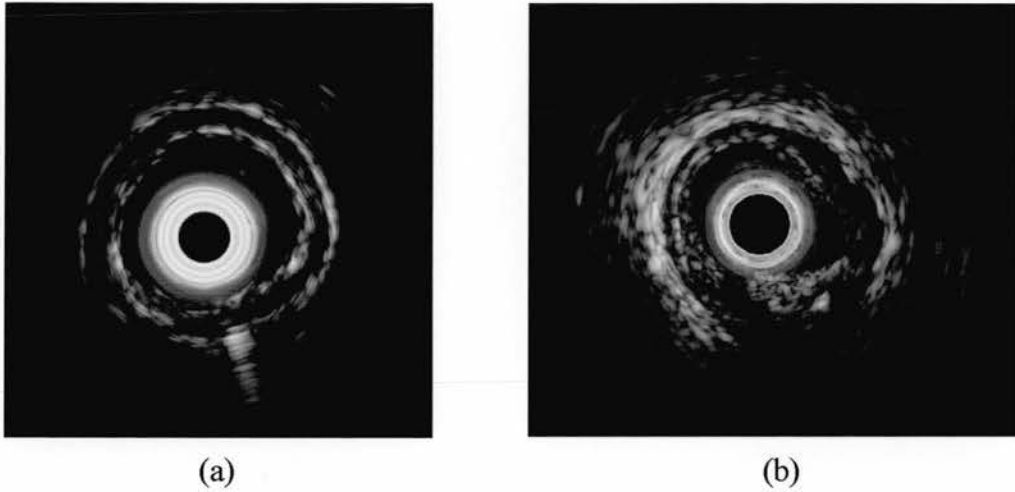


*Figure 1.2 : (a) IVUS image of a relatively healthy coronary artery. The catheter is displayed in as a black disc surrounded by a bright 'halo'. The vessel wall has a three-ring appearance (inner echogenic ring, middle echolucent ring, outer echogenic ring), indicative of the intima, media and adventitia respectively. (b) IVUS image of a diseased coronary artery with fibrous plaque formed round the whole vessel circumference.*

IVUS is unique in imaging the vessel wall morphology lying under the surface of the vessel lumen, and in providing valuable information about the histologic composition of the plaque (Di Mario et al. 1992; Gussenhoven et al. 1989a and 1989b; Nishimura et al. 1990; Potkin et al. 1990; Tobis et al. 1991). Moreover, IVUS imaging is an accurate tool for highly reproducible measurements of lumen area size (Li et al. 1994; Moriuchi et al. 1990; Nissen et al. 1990; Potkin et al. 1990).



#### **1.2.4 Treatment of atherosclerosis**

Treatment of stenosed or occluded arteries is based on surgical, interventional or pharmaceutical therapies. Interventional therapies can be divided into two categories: (a) techniques which enlarge the lumen area without removing the plaque, and these include balloon angioplasty and stenting, and (b) methods which physically remove the plaque, and these are the directional and rotational atherectomy, laser ablation and spark erosion.

##### **1.2.4.1 Bypass graft**

Bypass graft operation is a surgical method where a shunt is placed over the diseased lesion in order to direct the blood flow into a distal normal part of the vessel. The shunt is preferably a part of another vessel from the patient's body (Russo et al. 1986; Singh et al. 1983; Tyras et al. 1980) or alternatively an artificial vessel made of biocompatible material (Ascer et al. 1985; Veith et al. 1986). This method was the first one to be introduced for treatment of atherosclerosis and is still being used as the ultimate solution.

##### **1.2.4.2 Balloon angioplasty**

In the late 1970s, catheter-based interventional methods became popular for treatment of atherosclerosis. In particular, dilation of a balloon located at the tip of a catheter inserted in the stenosed vessel site, has been extensively used to increase the lumen area by compressing the plaque and stretching the vessel wall (Grüntzig et al. 1979) as seen in Figure 1.3.

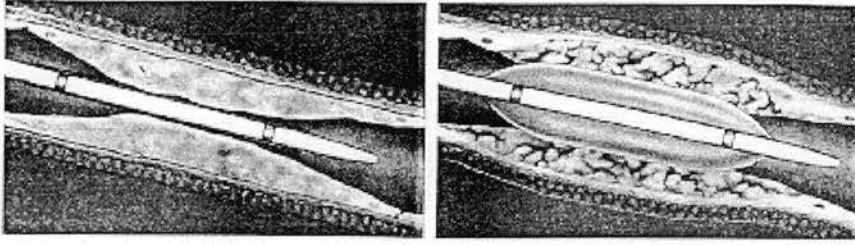


*Figure 1.3 : Balloon angioplasty of a stenosed vessel. Left panel shows a deflated balloon and the right one shows a dilated balloon compressing the plaque and stretching the vessel wall (from ten Hoff 1993).*

The primary success rate of this balloon angioplasty method is high, over 90%, however there are limitations which are inherent to its operational principle. The plaque material is practically incompressible, consequently the stretching of the vessel often leads to plaque rupture and creation of flaps in the lumen (Castaneda-Zuniga et al. 1980). There is practically no removal of the accumulated plaque and this causes gradual restenosis within a period of time as short as six months after angioplasty, necessitating further treatment (Guiteras et al. 1987). Furthermore, this method can be applied only in cases where the lumen is large enough to allow insertion of the balloon bearing catheter. These problems have led to the development of alternative catheter based therapies.

#### **1.2.4.3 Stent**

One direct evolution of balloon angioplasty was to place a stainless steel mesh, known as stent (Figure 1.4) over the balloon. Dilation of the balloon deploys the stent which provides mechanical support for the lumen at the stenosed site, reducing restenosis rates and preventing sudden occlusions after angioplasty (Sigwart et al. 1987).

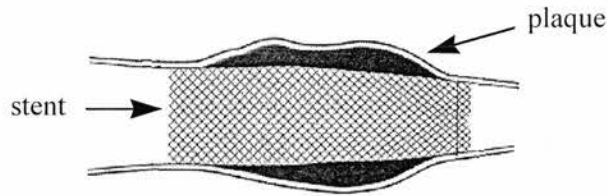


*Figure 1.4 : Stenting of a stenosed vessel with the use of a stainless steel mesh (from von Birgelen et al. 1996a).*

#### 1.2.4.4 Atherectomy

There are two different atherectomy techniques, namely the directional (Figure 1.5a) and the rotational (Figure 1.5b).

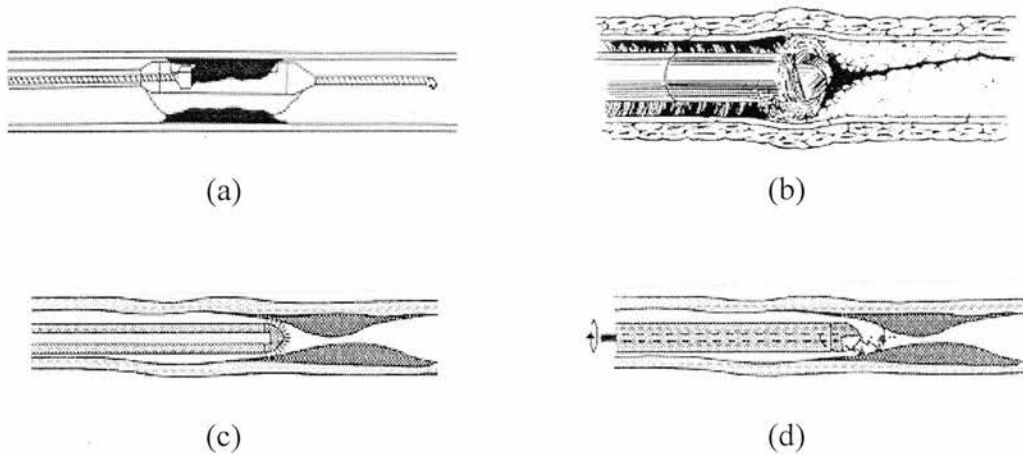


*Figure 1.5 : Recanalisation of stenosed vessels by removal of plaque material. (a) Directional atherectomy, (b) Rotational atherectomy, (c) Laser ablation, (d) Spark erosion (from Kensey et al. 1987, Simpson et al. 1988 and ten Hoff 1993).*

Directional atherectomy removes plaque by cutting it with a cutter located at one side of the catheter tip (Schwarten et al. 1988; Simpson et al. 1988). Removed pieces of plaque are trapped in a housing in the catheter. Following a successful procedure, the final lumen dimension is larger than the size of the catheter used.

There are three types of rotational atherectomy devices: the Kensey catheter (Kensey et al. 1987), the Rotarblator (Fourrier et al. 1989) and the transluminal extraction catheter (Stack et al. 1989). These devices operate in a forward fashion, using a fast rotating abrasive tip to cut the plaque and create a symmetrical tunnel ahead of the catheter. The obtained lumen size is equal to the diameter of the cutter. During the abrading procedure the Kensey and Rotarblator catheters generate debris, which is left to pass downstream. The particle sizes are however small, and are not expected to cause any significant embolisation to distal vessels. On the other hand, the transluminal extraction catheter uses suction to remove the cut plaque pieces from the vessel and direct them into a collection chamber outside the patient's body.

#### **1.2.4.5 Laser ablation**

This method is based on delivery of laser energy through optical fibres onto metal or sapphire contact probes incorporated at the tip of interventional catheters (Figure 1.5c). The probe is adherent to the plaque and dissipates the laser energy in form of heat, which causes evaporation of the obstructive tissue and creates 'new' lumen (Geschwind et al. 1987; Lammer and Karnel 1988).

#### **1.2.4.6 Spark erosion**

Spark erosion is similar in principle to laser ablation. Short electric sparks are applied from an electrode incorporated at the tip of a catheter adherent to the plaque (Figure 1.5d). The dissipated energy evaporates the plaque material generating new lumen space (Slager et al. 1985).

The angioplasty techniques which remove the atherosclerotic plaque are mostly applicable in severe lesions or total occlusions where the balloon catheters cannot be inserted. However, initial success is not always guaranteed, especially when large volumes of atheroma are present. Hence, balloon angioplasty is subsequently performed sometimes in an attempt to improve the results (Fourrier et

al. 1989; Sanborn et al. 1988; Schwarten et al. 1988). Moreover, without adequate guidance these methods are prone to non-selective cutting or evaporation of the plaque material which may lead to vessel wall perforation. This is probably one of the reasons why they are not used as frequently as the balloon and stent angioplasty.

#### **1.2.4.7 Pharmaceutical therapies**

Pharmaceutical therapies are used in lipid-rich plaques and thrombotic lesions. Most of the acute cardiac events are associated with rupture of 'unstable' lipid-rich atherosclerotic plaques in coronary arteries. A number of clinical trials have demonstrated the effect of lipid-lowering therapies on delaying atherosclerosis progression or even inducing regression (Brown et al. 1990; Herd et al. 1997; Jukema et al. 1995). It is suggested that lipid removal from lipid pools stabilises the plaque by changing the cellular composition to a fibro-calcified plaque with reduced risk of rupture. It is also believed that lipid-lowering therapies have a protective role on the prevention of new lesion development after recanalisation (Lansky et al. 1998). Rupture of an 'unstable' plaque is followed by haemorrhage and thrombus formation. The latter can lead to acute artery closure and myocardial infarction within a few hours or even minutes. Thrombolytic drugs are administered in such cases to treat the infarction and re-establish perfusion (Davies 1990; Gonzalez 1997; Stary et al. 1995).

### **1.3 Diagnostic ultrasound imaging**

Since the early days of its medical application (Donald et al. 1958; Donald and Brown 1961; Edler et al. 1961; Joyner et al. 1963; Tanaka et al. 1971), diagnostic ultrasound has developed and expanded rapidly, becoming one of the most widely used imaging modalities for medical diagnosis. The physics, technology and clinical applications of diagnostic ultrasound have been well documented in a

number of textbooks and review articles (Evans et al. 1989; McDicken 1991; Roelandt et al. 1993a; Wells 1977; Whittingham 1997; Whittingham 1999).

### 1.3.1 Ultrasound wave and echo signal

Ultrasound imaging is based on the transmission of sound energy in form of mechanical vibrations (waves) through matter. The waves are generated from excitations of a piezoelectric element (the *transducer*) by electrical pulses. The frequency of vibrations is very high, beyond the range detectable by the human ear, hence the name '*ultrasound*'. In ultrasound imaging, frequencies between 1 and 40 MHz are commonly used.

Diagnostic ultrasound is a pulse-echo technique. Ultrasound transducers are capable of both transmitting and receiving sound pulses. The waves transmitted into human tissue from the transducer are reflected and scattered by small particles and tissue boundaries where mismatches of acoustic impedance exist. Part of the reflected and scattered waves are picked up by the transducer and are converted to small electrical voltages, in the range of microvolts and millivolts, composing the radiofrequency (RF) echo signals (Figure 1.6).

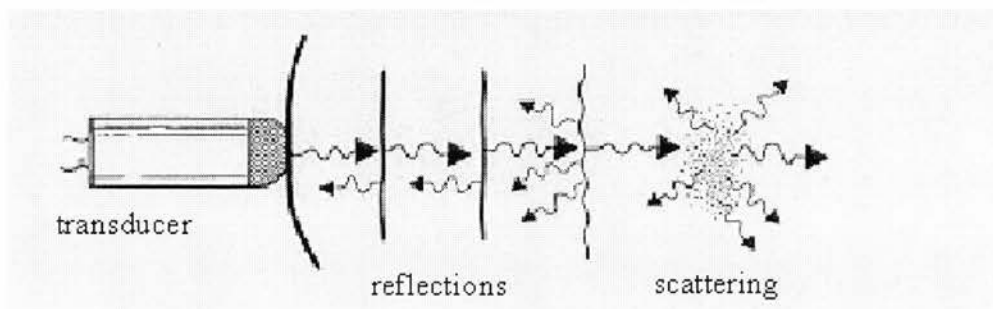


*Figure 1.6 : Generation of echoes at reflecting and scattering interfaces (from McDicken 1991).*

The electrical signals provided by the transducer need to be appropriately amplified and processed for display. The dynamic range of the RF echo signals can be very wide, even 100 dB, well beyond the display capabilities of TV monitors and the perception of human vision. Therefore, apart from amplification, there is a need to compress the dynamic range of the RF echo signal to a level appropriate for display on a monitor. Commercial scanners do this in two stages.

The first one is to apply variable gain amplification according to the distance of echoes from the transducer. Echoes arising from tissue interfaces away from the transducer are weaker than echoes from the proximity of the transducer, due to additional attenuation of ultrasound along the longer path. Consequently, echoes from structures away from the transducer are amplified more than those from the transducer proximity. This is known as Depth or Time Gain Compensation (DGC or TGC) and reduces the effect of attenuation of ultrasound and also the dynamic range of the echo signals, to a certain extent.

The second stage is a compression amplification usually of a logarithmic nature. Larger echoes are amplified less than weaker echoes in order to avoid saturation of the display.

Only the echo amplitudes are used for clinical diagnostic (B-mode) imaging, therefore the envelope of the amplified RF signals is 'detected'. The detected 'video' signals have a dynamic range of approximately 40 dB, suitable for display on a monitor.

### **1.3.2 Imaging modes**

The transmission speed of sound in soft tissue is known to within a few percent and this allows the pulse-echo technique to provide an estimate of distances between the transducer and tissue interfaces, by measuring the return time of flight of the pulses. The derived distances are used for image display purposes. There are three main imaging modes in diagnostic ultrasound and are described below.

- The **A-mode** is the simplest form of displaying ultrasound data. It is a plot of the echo signals along one beam as they arise from tissue interfaces, against time (depth) on an oscilloscope screen.
- In **B-mode** a two dimensional ultrasound image is generated by transmitting a number of beams at different directions on a scan plane. For each beam, the A-mode echo signals are displayed as spots on a related line of a display screen. The position of each spot on its related line corresponds to the distance between the transducer face and the tissue interface which produced the echo. The amplitude of the echo is converted to brightness, with high amplitude echoes displayed brightly and low amplitude echoes displayed dimly. In this way, a grey scale two dimensional image, is generated.
- In **M-mode** a single beam is plotted on the display screen in the form of bright spots, as in B-mode, on a moving time basis sweeping across the display. This mode is mostly used for tracking motion of cardiac structures.

### **1.3.3 Ultrasound transducer probes**

The transducer is a key component of an ultrasonic imaging system. Three basic types of transducer design are used: the single element, the linear array and the phased array transducers.

#### **1.3.3.1 Single element transducers**

This is the most basic transducer design. It is usually a cylindrical tube with a disc-shaped active element of either piezoceramic (lead zirconate titanate - PZT) or plastic (polyvinylidene fluoride - PVDF) material. This type of transducer emits one beam only in the direction ahead of it. In order to generate a two dimensional B-mode image it is mechanically moved (oscillated, rotated or reciprocated on a line) so that the beam is scanned across the desired area.



### **1.3.3.2 Linear and curvilinear arrays**

These transducers are composed of a number of small thin elements (crystals) placed side by side. Each element has its own circuitry as if it was an independent single element transducer. A small group of adjacent elements is activated at any time to form a beam. By moving the active group of elements from one end of the array to the other, the beam is advanced along the length of the array. In this way, a rectangular or sector field, for a linear or curvilinear array respectively, is scanned without moving the transducer. Using electronic beam forming techniques, the shape and the focus of the receive beam can be varied dynamically in the direction of the scan plane.

### **1.3.3.3 Phased arrays**

Phased array transducers are also composed of a number of small thin elements placed side by side. The beam is formed by exciting all elements together. The direction of the resultant beam is controlled by introducing slight time delays, i.e. phase differences, between the excitation of neighbouring elements. In this way, the beam is swept to scan a sector field without moving the transducer. As in linear arrays, the shape and the focus of the receive beam in the direction of the scan plane can be varied dynamically using electronic beam forming techniques.

### **1.3.3.4 Annular arrays**

Annular array transducers are disc-shaped, consisting of a small number (5 to 10) of concentric ring elements. This design is capable of achieving electronic focusing both in the direction of the scan plane, as well as in the out-of-plane (elevational) direction. Similar to the single element transducers, annular arrays are mechanically moved in order to generate a two dimensional B-mode image.

### 1.3.4 Image quality

The quality of ultrasound images is determined to a great extent by the characteristics of the transducer used and most importantly by its frequency and beam shape. This beam shape can be regarded as the combination of the transmit and receive field of the transducer and depends on the size, shape and frequency of the transducer and the presence of focusing on it. For a flat disc-shaped unfocused transducer operating in continuous wave mode, the beam shape consists of a gradually narrowing conical region known as the near field or Frensel zone, followed by another region known as far field or Fraunhofer zone, in which there is divergence (Figure 1.7). This model can be used as a rough guide for pulsed wave applications, too.

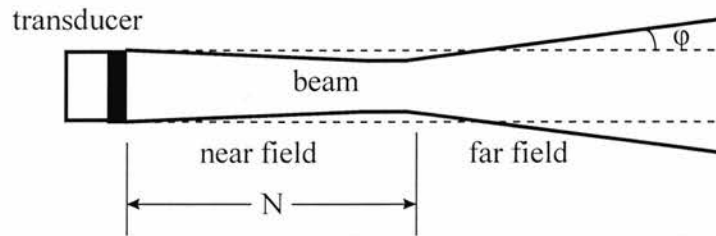


*Figure 1.7 : The ultrasonic field and the beam shape of a flat single element disc-shaped transducer.*

Transition from near to far field occurs at a distance  $N$  from the transducer face

$$N = \frac{D^2}{4\lambda} \quad (1.1)$$

where  $D$  is the transducer diameter and  $\lambda$  is the ultrasonic wavelength. The angle of divergence  $\phi$  in the far field is

$$\phi = \arcsin\left(\frac{1.22\lambda}{D}\right) \quad (1.2)$$

The detail visible in an ultrasound image depends on the *contrast* and *spatial* resolution of the system. The contrast resolution is the minimum detectable change of tissue reflectivity in an image. It is mostly defined by the conversion of the echo signals to grey levels and the image processing performed by the system. Noise in the image affects the contrast resolution, as does interference from echoes generated by closely spaced targets.

The spatial resolution is defined as the apparent size of a finite size point target. When imaging in three dimensional space, three resolution components exist: the axial resolution along the beam, and two lateral resolutions perpendicular to the beam. The axial resolution is determined by the length of the ultrasonic pulse, which is usually 2 or 3 wavelengths for most imaging systems. As the frequency increases the wavelength becomes shorter, thus the axial resolution improves. The lateral resolutions are determined by the beam width and vary with the distance from the transducer face. When the frequency is increased, a transducer of smaller diameter can be used to maintain the same near field length (useful imaging zone), according to equation 1.1. With the use of a smaller diameter transducer, the beam effectively becomes narrower and consequently the lateral resolutions improve.

Higher frequencies are clearly beneficial to the image quality. However, the attenuation of ultrasound in tissue is stronger, thus the penetration depth and the field of view are reduced. Therefore, the choice of a frequency for each individual application is a matter of compromising between resolution and penetration depth.

A way to narrow the beam and improve the lateral resolution in a region of the ultrasonic field without changing the frequency is to focus the beam either by attaching lenses on the front face of single element transducers, or by employing electronically controlled dynamic focusing on the reception zone in array transducers. Use of narrow beams also improves the contrast resolution since the echoes from structures outside the region of interest are reduced.

### 1.3.5 Real-time imaging

Early ultrasonic systems produced static images, which were prone to imaging artifacts caused by moving tissue and body organs during the imaging procedure. Real-time imaging was developed to eliminate this shortcoming and to permit visualisation of the motion of heart structures, to facilitate rapid searching for regions of interest through tissue and to enable three dimensional studies of organs. Since the speed of sound in tissue is very high, averaging  $1540 \text{ m s}^{-1}$ , echoes from each line are collected in a fraction of a millisecond. This means that the beam can be moved very quickly to the next location on the scan plane to collect the next echo signal and effectively complete the imaging of the desired area in a fraction of a second. The procedure can be repeated immediately resulting in an update of the displayed image which can track tissue motion. Modern scanners emit beams with a rate of 3 to 10 kHz and can even produce 100 or more B-mode images (frames) per second.

### 1.3.6 Doppler ultrasound and colour flow imaging

Ultrasound is also employed in detection of blood motion in human circulation, by making use of the Doppler effect. This effect is a change (shift) in the observed frequency of a wave as a result of the relative motion between the source and the observer. If an ultrasonic wave of frequency  $f_o$  is reflected by a target moving with speed  $v$ , then the Doppler shift  $f_D$  is approximately

$$f_D = f_o \frac{2v \cos \theta}{c} \quad (1.3)$$

where  $c$  is the speed of sound and  $\theta$  is the angle between the ultrasonic beam and the direction of the target's movement.

According to equation 1.3, the Doppler shift is proportional to the component of the target's velocity along the beam direction. Based on this property, Doppler ultrasound systems derive velocity estimations for a defined location (*sample volume*) of blood flow in arteries, simply by measuring the Doppler shift at that

location. By moving the sample volume on a 2D plane which intersects blood vessels, a velocity map is obtained for the flow in those vessels (*flow imaging*). This map is colour coded, with shades of red and blue representing flow towards and away from the transducer respectively. Colour flow imaging is essentially very similar to ultrasonic pulse-echo imaging, with the only difference being the use of the Doppler shift rather than the size of the reflected echo for producing the image.

The main techniques developed for colour flow imaging include the 1D autocorrelation algorithm (Kasai et al. 1985), the cross-correlation algorithm (Bonnefous and Pesque 1986; Bonnefous et al. 1986) and the 2D autocorrelation algorithm (Loupas et al. 1995a and 1995b). The 1D autocorrelation velocity estimator was the first one to be introduced and immediately gained wide acceptability, because of its simplicity for real-time implementation. The cross-correlation estimator is regarded as superior to the 1D autocorrelation, however it has not been widely adopted in commercial systems, probably due to the large amount of computing power required for real-time implementation. The 2D autocorrelation estimator has been shown to perform better than the other two methods, especially under noisy conditions. This advantage, in conjunction with the relatively simple real-time implementation, has recently led to use of the 2D autocorrelation estimator in commercial systems.

## **1.4 Intravascular ultrasound**

The need for intravascular ultrasound imaging was born out of the desire to image vessel structures which were originally inaccessible to ultrasound due to restrictions imposed by features of the human anatomy such as bones, ribs, lungs and deep tissue layers. Part of the driving force behind the development of intravascular ultrasound also arose from the appearance of interventional treatments for vascular disease, which require more detailed information than that provided by angiography.

The development of invasive catheter probes has allowed imaging of previously inaccessible structures from a very close distance, thus reducing penetration depth problems. This in turn allowed the use of higher frequency transducers with improved spatial resolution.

The first real-time catheter-tip scanning system was developed by Bom et al. (1972). It consisted of a 32-element circular array operating at 5.6 MHz, with the elements placed on the circumference of a 3 mm diameter catheter. This device was used to produce real-time images of cardiac chambers. Further reduction in catheter size and use of higher frequencies were employed in the development of intravascular probes.

#### **1.4.1 Intravascular scanning techniques**

The major approaches used in intravascular ultrasound imaging are based on principles described in the earlier days of diagnostic ultrasound (Bom et al. 1989). The current intravascular ultrasound systems provide a 360° cross-sectional image of the vessel by scanning the beam through a full circle around the catheter (Figure 1.8a). Three basic approaches are employed in achieving this:

- mechanical rotation of a single element ultrasound transducer,
- mechanical rotation of a mirror which deflects the ultrasound beam, and
- electronic switching of the elements of a circular phased array.

Systems based on these configurations are described below in more detail.

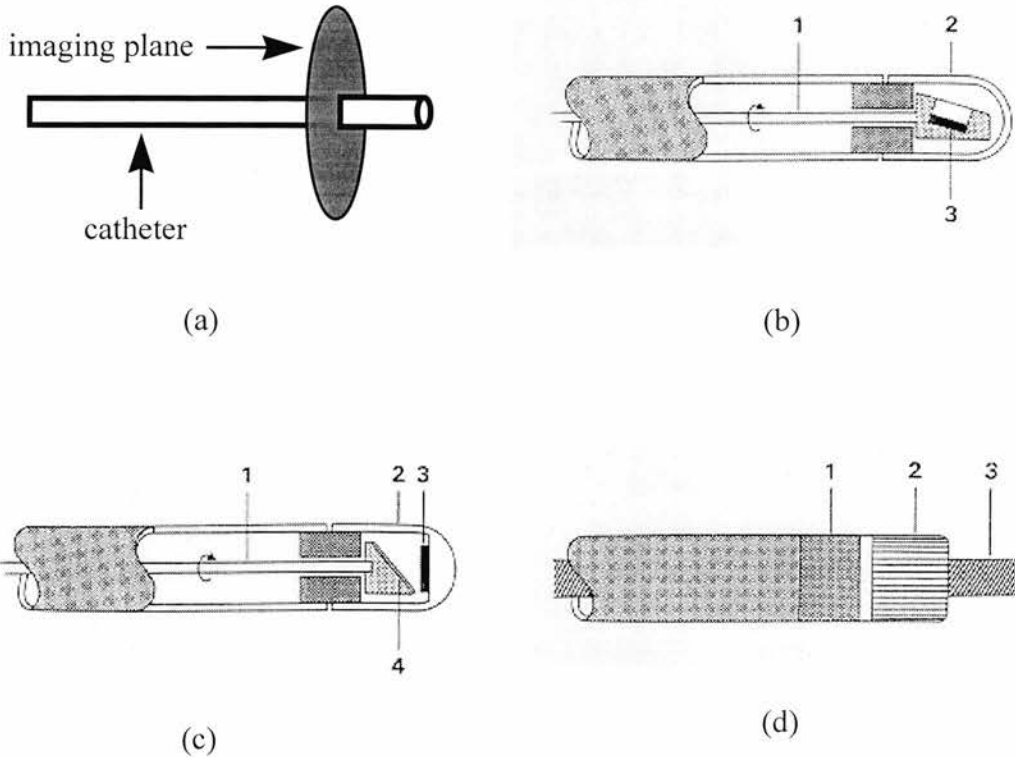


*Figure 1.8 : Schematic diagrams of: (a) the cross-sectional imaging plane of an intravascular catheter, (b) the rotating transducer catheter showing the flexible rotating shaft (1), sonolucent dome (2) and transducer (3), (c) the rotating mirror catheter showing the same components as in (a) together with the mirror (4), and (d) the circular phased array catheter showing the integrated circuits (1), array elements (2) and a guidewire (3) through the catheter lumen (from Bom et al. 1989).*

#### 1.4.1.1 Rotating transducer

A diagram of a mechanical catheter with a rotating single element transducer is shown in Figure 1.8b. The system consists of a transducer placed inside the catheter tip and enclosed by an acoustically transparent dome. The transducer is orientated at a slightly forward angle in order to avoid near field reverberations of the beam at the catheter surface. A flexible shaft, which contains the transducer wires,

runs along the catheter and rotates the transducer producing the cross-sectional image.

#### **1.4.1.2 Rotating mirror**

In this configuration (Figure 1.8c), the transducer is kept at a fixed position at the distal end of the catheter and emits the beam parallel to the long axis of the catheter. An angled mirror is placed opposite the transducer and deflects the beam at normal angles to the catheter axis. Similarly, the returned echo is deflected by the mirror back to the transducer. In order to scan the beam and generate the cross-sectional image, the mirror is rotated by a flexible shaft which runs along the catheter.

#### **1.4.1.3 Circular phased array**

A number of miniature transducers are placed around the surface of the catheter tip and the beam is swept around the array by electronically switching the array elements (Figure 1.8d). There is no need for rotating elements in this design. Integrated circuits are placed at the catheter tip to provide multiplexing of the transmission and reception functions for the array elements as well as interface to a single micro cable, eliminating the need for multiple wires running along the catheter.

### **1.4.2 Advantages and disadvantages of catheter configurations**

The majority of the catheters used in the early days of IVUS were based on the mechanically rotated element approach. A main reason was the manufacturing simplicity of mechanically rotated catheters at the small size needed for intracoronary use.



A high number of elements is required for the phased array catheter in order to achieve adequate sampling of the vessel cross-section. In addition to that, the inter-element space (the pitch) in an array should be less than half the wavelength in order to avoid image artifacts due to grating lobes. The small size of catheter requires that the array elements are very small. In the early days of IVUS it was not possible to cut piezoceramic material down to the required sizes, therefore PVDF films were used for manufacturing these arrays. Due to the low sensitivity of this material, the signal-to-noise ratio of the constructed catheters was low. Consequently, signal averaging was required to improve the image quality at the expense of reduced frame rate. The first array catheters incorporated 32 elements operating at 20 MHz (Hodgson et al. 1989; Nissen et al. 1990) providing compromised image quality. On the other hand, the mechanically rotated catheter utilised PZT transducers enjoying higher sensitivity and image quality.

Another disadvantage of the early phased array catheters was the so called 'ring-down' artifact. Generally speaking, the receiver circuit of the scanner is saturated by the high energy transmit pulse and takes some time until it recovers and is able to detect the echo signals. This results in a 'dead zone' in front of the transducer. The array elements are positioned on the circumference of the catheter, consequently an area around the catheter is not available for imaging. This effect was prominent in the first PVDF catheter arrays resulting in an 'acoustic' diameter larger than the physical diameter of the device. In the mechanically rotated catheters, the transducer lies inside the catheter and there is a short distance between the transducer face and the outer surface of the catheter, resulting in reduced ring-down artifact. In the rotating mirror design, in particular, this artifact is practically non-existing due to the additional path available between the transducer and the mirror. The rotating mirror catheters can effectively visualise vessel structures lying exactly next to them.

In the rotating mirror catheters, it is necessary for the electrical wire of the transducer to pass along the side of the imaging assembly. This wire is visualised and appears as an artifact in the cross-sectional image, occupying a part as large as 15°.

This artifact represents a significant problem when the device is used for 3D imaging and is perhaps the reason why this type of catheter has not become very popular.

It appears that, due to the previously mentioned 'wire' artifact of the rotating mirror design and the problems of the early phased arrays, catheters based on the mechanically rotated transducer design became the most widely used in practice. Their simple design has allowed production of relatively inexpensive disposable devices. The majority of catheters use 30 MHz PZT transducers with axial resolutions in the range of 75-80  $\mu\text{m}$  and lateral resolutions around 225-500  $\mu\text{m}$  (Foster et al. 1997; Hoskins and McDicken 1994; Li et al. 1994; Roelandt et al. 1993b), although other frequencies between 20 and 40 MHz are also used.

High resolution images at rates as high as 30 frames/sec are obtained by connecting the catheter to a driving unit attached to the scanner. The driving unit incorporates a motor which rotates the catheter at rates of 1000 rpm or so. It also includes slip-rings which connect the rotating electrical cable of the transducer to the static electronics of the scanner. The transducer cable runs along a flexible drive shaft which transfers the rotational force of the motor to the transducer at the catheter tip.

The construction of the flexible drive-shaft faces conflicting requirements. On one hand, high torsional rigidity is required to ensure high fidelity of rotation transmission to the transducer, while on the other hand, flexibility and low bending rigidity is necessary for negotiating tortuous paths in human vessels. The design of these drive-shafts consists typically of two layers of multi-strand stainless steel coils which are helically wound in opposite directions with respect to each other (ten Hoff 1993). This design has been successful to a certain extent, nevertheless non-uniform rotation artifacts are often seen in images acquired with mechanically rotated transducer catheters leading to erroneous measurements of plaque size (Di Mario et al. 1995a; Kimura et al. 1996; Roelandt et al. 1994a; ten Hoff 1989). A typical case of a non-uniform rotation artifact is shown in Figure 1.9 for a multi-wire test phantom. The same phantom is correctly visualised with a phased array catheter.

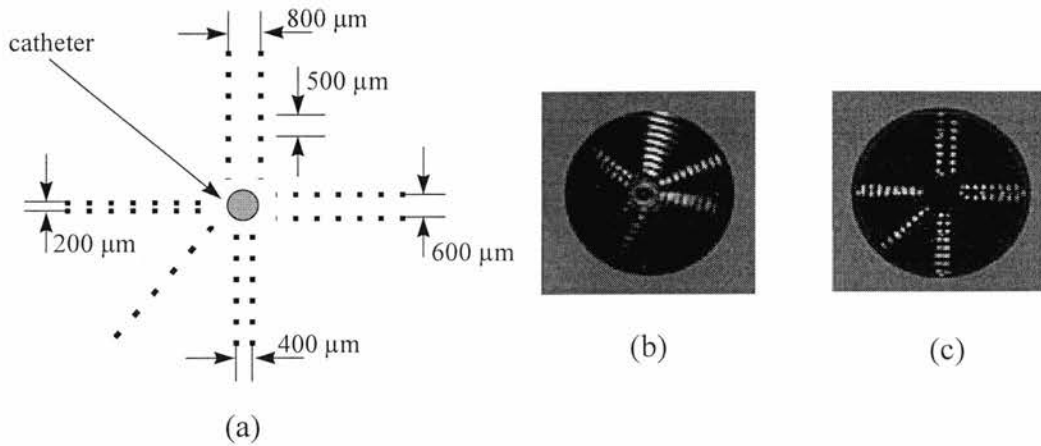


*Figure 1.9 : (a) Schematic diagram of a multi-wire test phantom. (b) Non-uniform rotation artifact seen in an image of this phantom acquired with a mechanically rotated catheter. (c) Artifact-free image acquired with a phased array catheter (from Eberle 1997 and O'Donnell et al. 1997a).*

As technology improved, dicing of ceramic PZT into smaller sizes has been achieved, allowing the introduction of a new generation of phased array catheters in recent years. Use of PZT transducer elements has significantly improved the sensitivity and the signal-to-noise-ratio of these devices, eliminating the previous need for signal averaging, thus increasing the frame rate. The latest array catheters incorporate 64 PZT elements operating at 20 MHz and use synthetic aperture imaging methods for reconstructing the cross-sectional images (Eberle 1997; O'Donnell et al. 1997a). The beam can be dynamically focused in both transmission and reception and the aperture size can be varied with depth. This results in an improved beam shape and lateral resolution compared to that of the mechanically driven catheters despite the lower frequency (Figure 1.10). Since the elements of phased array catheters are located on the circumference of the catheter, the available space inside the catheter tip has allowed the use of thicker transducer backing materials which improve the axial resolution and greatly reduce the 'ring-down' artifact.

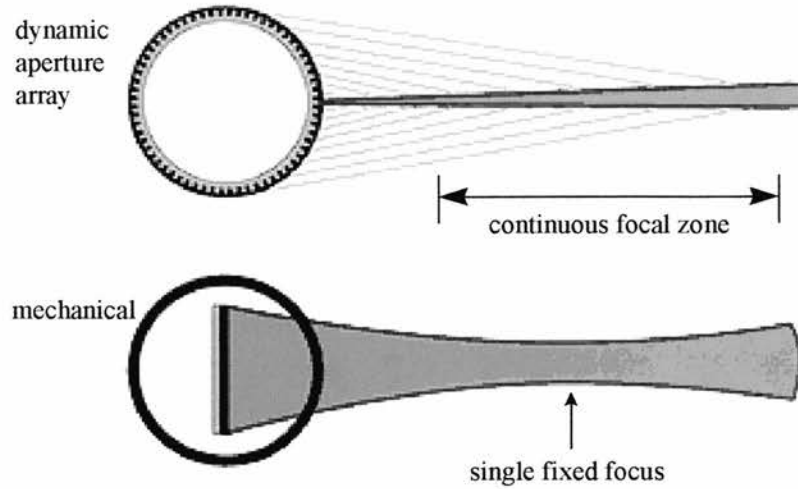


*Figure 1.10 : Resolution beam profiles of IVUS systems. Top panel: 20 MHz synthetic aperture array catheter. Bottom panel: 30 MHz mechanically driven catheter (extracted from the Internet site <http://www.endosonics.com>).*

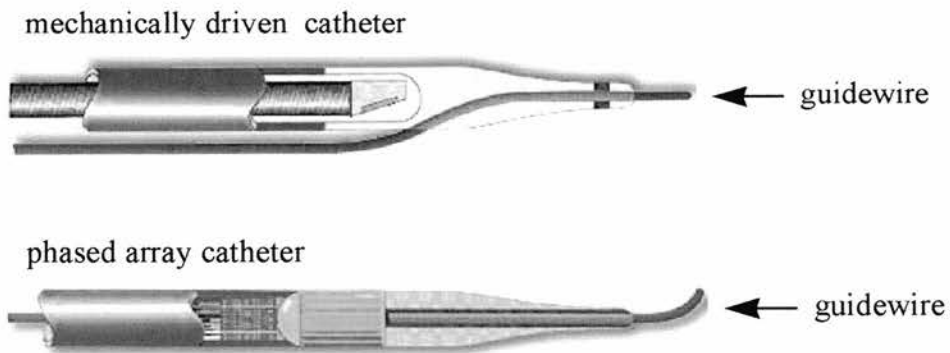


*Figure 1.11 : Combination of IVUS catheters and guidewires. Top panel: mechanically driven catheter with external guidewire. Bottom panel: phased array catheter with a guidewire passing through its lumen (extracted from the Internet site <http://www.endosonics.com>).*

During clinical use, IVUS catheters are inserted in the vessel lumen with the aid of a guidewire. In mechanically driven catheters the lumen is occupied by the flexible drive shaft, hence the guidewire is externally placed adjacent to the catheter (Figure 1.11). On the other hand, there is only one single micro-cable running along the lumen of the phased array catheters. This leaves available lumen space to accommodate the guidewire inside the catheter (Figure 1.11) and allows also the construction of a more flexible catheter.

The mechanically driven catheters seem to be reaching the limits of image quality they can provide and the scale at which they can be miniaturised. The latest developments on phased array catheters have resulted in image quality which matches that of the mechanical catheters, whilst the images are free of non-uniform rotation artifacts. Since only a number of miniature circuits and a single cable need to be accommodated in the lumen, there is also promise of further reduction of the catheter size while keeping the desired flexibility.

### **1.4.3 Catheter handling**

In the human body the vessels mostly affected by atherosclerosis are the iliofemoral and coronary arteries. The most common place to introduce a catheter into the vascular system in order to access these vessels, is the groin where a femoral artery runs close to the body surface. An 8 to 12 French<sup>1</sup> (Fr) diameter plastic sheath with thin wall is firstly placed into this artery. The proximal side of the sheath has a diaphragm valve which closes around any catheter inserted in the sheath, preventing blood loss. Once in the femoral artery, the catheter can then be advanced into the specific target region of the femoral or iliac artery. If coronary artery imaging is required, the catheter is advanced through the iliac artery into the abdominal aorta, then into the thoracic aorta, the aortic arch and aortic root, from where it can be inserted into the coronary arteries.

---

<sup>1</sup> The French is a unit used to describe catheter size. One French (1 Fr) corresponds to 1/3 mm.

Before the introduction of the IVUS catheter, a guidewire is inserted into the target region or even further than that. The guidewire is a very thin (0.35 to 0.45 mm diameter) and flexible wire which can be steered, from outside the body under angiographic view, through the vascular tree until it reaches the target region.

For patient safety reasons, no rotating parts are allowed to come in touch with the inner vessel wall surface. Due to this requirement, the mechanically driven catheters include the 'imaging core' (drive shaft plus transducer) enclosed in an 'ultrasonically transparent' plastic sheath. The imaging core can either be fixed in the sheath or moved inside the sheath telescopically. The distal tip of the sheath is constructed such that it can be hooked onto the guidewire and follow its path. In the case of telescopic imaging cores, the guidewire is withdrawn once the sheath is at the target region, and the imaging core is then advanced into the sheath to visualise the vessel. In order to enable the transmission of ultrasound, the catheter lumen is continuously irrigated with saline or water to ensure a bubble-free fluid medium within the imaging chamber.

The central lumen in the phased array catheters is practically free, hence these catheters can be advanced 'over-the-guidewire' and follow its track all the way to the target region. Since their design involves placement of the array elements on the outer circumference of the catheter, there is no need for saline flushing.

IVUS catheters are used in patients only once and are disposed of at the end of the examination. At the moment their cost is in the range of £220 per unit, which is considered relatively inexpensive.

#### **1.4.4 Clinical applications of intravascular ultrasound**

IVUS has had a great impact on interventional cardiology in a short time, having been used as a research tool and in a variety of clinical applications, both diagnostic and therapeutic. The most important factor which has led to the wide use of IVUS is its ability to discriminate plaque from normal vessel wall. This is based

on the fact that the different vessel wall layers and plaque components interact with ultrasound in different ways.

#### 1.4.4.1 Visualisation of vessel wall layers

In muscular arteries, IVUS is capable of discriminating the distinct vessel wall layers. The typical ultrasonic appearance of the wall of a muscular artery can be described as three-ringed, consisting of an inner echogenic, a middle echolucent and outer echogenic ring (Figure 1.12).

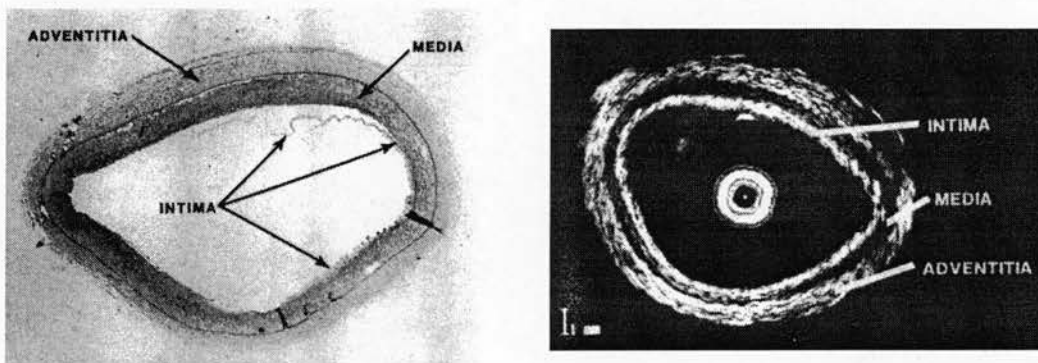


*Figure 1.12 : Cross-sections of a human muscular artery. The left panel shows the histologic image while the right panel is the corresponding intravascular ultrasound image, where a three-ringed appearance of the arterial wall is evident (from Tobis et al. 1991).*

Collagen and elastin found in arteries are known to result in high levels of scattering (Barzilai et al. 1987, Gussenhoven et al. 1989a). The fact that the media in muscular arteries consists mostly of smooth muscle cells with low concentration of collagen and elastin, results in an echolucent ultrasonic appearance. On the other hand, the dense concentration of collagen and elastin in the adventitia causes high scattering. The two elastic laminae constitute acoustic impedance mismatches with the media they enclose, thus strong echo reflections are produced at their borders with the media. These two reflections along with the echolucent media and the



scattering adventitia are responsible for the three-ringed appearance of the coronary arterial wall (Gussenhoven et al. 1989a; Lockwood et al. 1992). This is not seen in elastic arteries, where the media is highly echogenic because of its high concentration in elastin fibres (Figure 1.13).

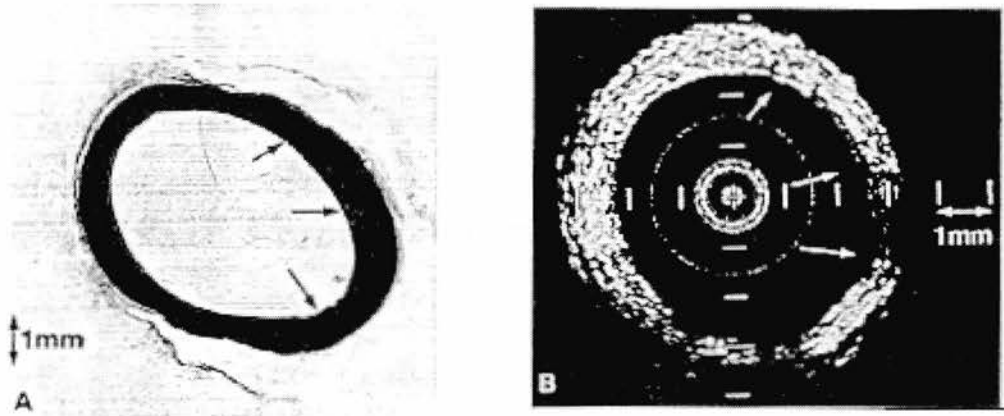


*Figure 1.13 : Cross-sections of a human elastic artery. The left panel shows the histologic image, while the right panel is the corresponding intravascular ultrasound image. The media of an elastic artery is as echogenic as the surrounding layers, hence there is no ringed appearance of the vessel wall in the ultrasound image (from Gussenhoven et al. 1989a).*

#### 1.4.4.2 Imaging and characterisation of atherosclerotic plaque

Most plaque is echogenic, thus it can be discriminated from blood and the muscular media (Yock et al. 1991). It is feasible to distinguish different plaque components using the information provided by IVUS. A typical example is shown in Figure 1.14. Local areas of different plaque types seen in the histologic section of an artery (left panel) can also be discriminated in the ultrasonic image (right panel). The part of the plaque which is mostly dense fibrotic tissue appears as bright echoes in the IVUS image (arrows 1). Lipid deposits appear as echolucent zones (arrows 2), while calcific deposits cause strong reflection and acoustic shadowing hindering



imaging beyond them (arrows 3). More sophisticated methods of spectral and textural analysis of the RF signal have also been developed, providing more confidence in characterising the basic plaque components (Linker et al. 1991; Nailon 1997; Spencer et al. 1997; Watson et al. 2000; Wilson et al. 1994).

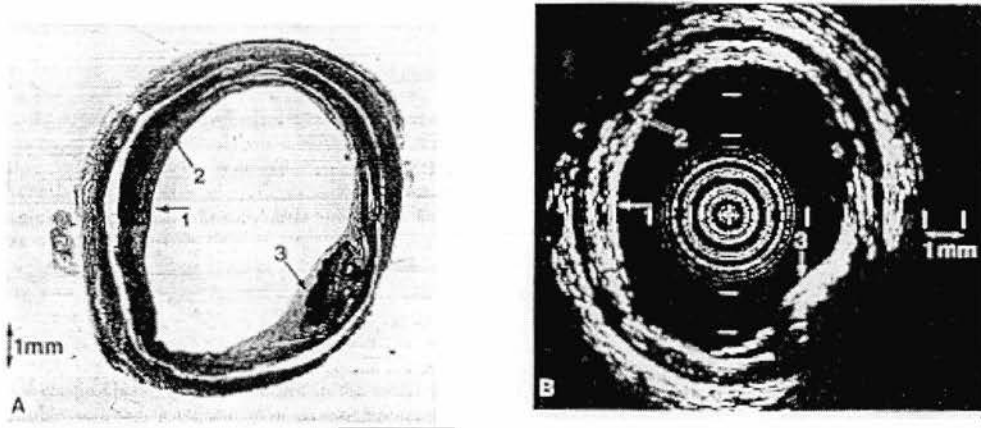


*Figure 1.14 : Distinction of plaque types by intravascular ultrasound in agreement with histology. (1) fibrous tissue, (2) lipid deposits, and (3) calcium deposits (from Gussenhoven et al. 1989a).*

A number of post-intervention studies with IVUS have provided assessment of the results achieved by the recanalisation therapies in correlation with certain plaque types (Kawata et al. 1997; Leon et al. 1993; Mintz et al. 1992; Nakamura et al. 1995). Clearly, knowledge of plaque composition and morphology can aid decision making on therapeutic strategies for atherosclerosis and potentially reduce the cost of treatment (Lee et al. 1995; Mintz et al. 1994a). In the case of plaques with superficially deposited calcium for example, rotational atherectomy is regarded as the most appropriate procedure.

#### 1.4.4.3 Diagnostic value of intravascular ultrasound

Due to its unique capability of imaging both the plaque and the vessel wall, IVUS offers increased diagnostic information compared to angiography and angioscopy. This is evident in the images of Figure 1.15, which were acquired by these different imaging techniques before and after interventional treatment. Angiography indicates an initially stenosed vessel (A), which appears normal after treatment (B). Angioscopy initially shows a mass in the vessel lumen (C), and following treatment it reveals an intimal tear (D) not seen by angiography. IVUS reveals a stenosed lumen before treatment (E) and an intimal tear as well as a separation of plaque down to the level of adventitia (F) (Siegel et al. 1990).

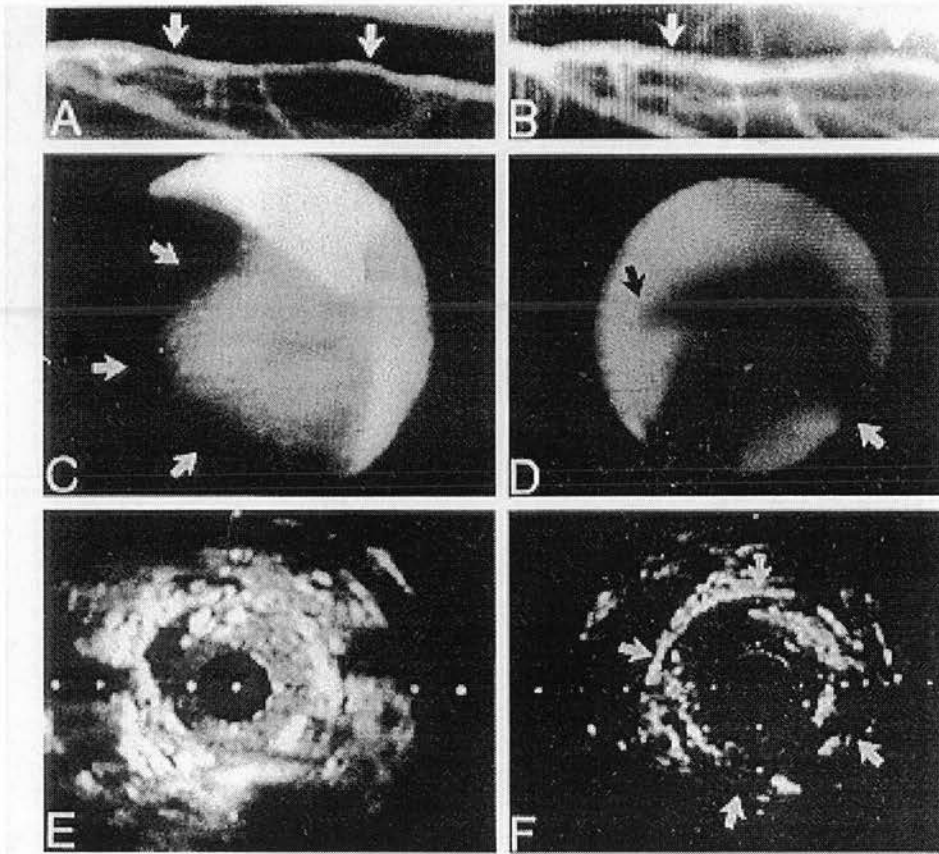


*Figure 1.15 : Images of a diseased vessel before (left column) and after (right column) interventional treatment. Images A and B are obtained by angiography, C and D by angioscopy, E and F by intravascular ultrasound (from Siegel et al. 1990).*

IVUS is now widely recognised as more reliable than angiography in assessing the extent of the vascular disease. Lesion information as provided by IVUS has led to recanalisation procedures despite angiographically 'normal' images (Mintz et al. 1994a). Moreover, several workers (Ge et al. 1994; St Goar et al. 1992; Tobis et al. 1991) have repeatedly shown the ability of IVUS to indicate residual plaque and dissections in vessels which appear angiographically 'normal' after treatment.

IVUS has also provided insights into the mechanisms of lumen gain following interventional treatment by balloon angioplasty (Losordo et al. 1992; Tenaglia et al. 1992; The et al. 1992), directional atherectomy (Baim et al. 1996; De Lezo et al. 1993; Nakamura et al. 1995; Tenaglia et al. 1992), rotational atherectomy (Kovach et al. 1993), laser ablation (Mintz et al. 1995) and stent implantation (Laskey et al. 1993). In addition, IVUS has enhanced the knowledge on mechanisms and predictors of restenosis (De Lezo et al. 1993; Di Mario et al. 1995b; Kimura and Nobuyoshi 1997; Mintz et al. 1994b; Painter et al. 1995; Post et al. 1997; Prati et al. 1999; Schwarzscher et al. 1997, Werner et al. 1999).

Recent research has engaged IVUS imaging in the assessment of local mechanical properties of the vessel wall and plaque. Information on the elasticity of the vessel and atherosclerotic plaque is derived by processing of IVUS images acquired at different levels of arterial pressure or intravascular pressure applied by a balloon (Céspedes et al. 1997; de Korte et al. 1997 and 1998; O'Donnell et al. 1997b). Identifying the mechanical properties of vessel wall and plaque can be of important diagnostic value, e.g. indication of risk areas for plaque rupture, and use in guiding interventional procedures.

Another diagnostic application of IVUS is related to functional assessment of vascular haemodynamics. Intravascular 'Doppler wires' incorporating a forward-looking transducer with a single beam 25°-30° wide, are used to measure the axial component of blood velocity based on the frequency shift of the echo signal (Doucette et al. 1992). Simultaneous use of a typical IVUS imaging catheter allows measurement of lumen cross-sectional area near the site of velocity measurement, thus providing an estimation of blood flow (Isner et al 1993; Sudhir et al. 1993). An

alternative approach is also used, based on the fact that the decorrelation rate of the RF echo signals is proportional to the velocity of red blood cells crossing the IVUS imaging plane. Thus, by using only a single imaging catheter and processing the RF signals, a cross-sectional image is acquired along with blood velocity information at the imaging site. A colour-code map of the blood velocities can be overlaid onto the grey scale image. By integrating the velocities over the entire cross-section, volume flow is obtained (Carlier et al. 1998; Crowe et al. 1996; Li et al. 1998).

#### **1.4.4.4 Three dimensional intravascular ultrasound**

Conventional two dimensional IVUS displays cross-sectional images of the vessel lumen, wall and plaque at the site of the transducer. Increased diagnostic information is obtained by moving the catheter tip and obtaining images at different sites along the vessel. This is done by initial advancement of the catheter to the most distal region of interest in the vessel, followed by withdrawal ('pull-back') of the catheter tip to more proximal sites. In this way, a set of images is acquired providing information for a segment of the vessel.

The catheter pull-back is performed either manually or under motorised control (Klein et al. 1992; Matar et al. 1994). During manual pull-back, the catheter is often connected to a displacement sensing device for accurate estimation of the catheter tip position (Gussenhoven et al. 1993b). The motorised pull-back is often ECG-gated in order to remove artifacts caused by motion of the catheter with respect to the vessel wall during the cardiac cycle (Bruining et al. 1996).

The acquired 2D images are firstly segmented in order to identify structures of interest and enable quantification analysis. Then, they are rendered for 3D reconstruction and visualisation. The resulting information is displayed in various ways, the most clinically useful of which is a *2D longitudinal image* showing the morphology and extent of atherosclerosis along the length of the vessel segment. Other display formats include *lumen cast* which provides a 3D view of luminal encroachments, and a *cylindrical display cut and open length-wise* which allows

direct view of the inner luminal surface (Roelandt et al. 1994a; von Birgelen et al. 1995).

Three dimensional IVUS has permitted an objective visualisation of the spatial distribution of atherosclerosis. The segmentation step of 3D IVUS has enabled measurements of lumen and plaque areas on the individual 2D images as well as estimation of the lumen and plaque volume along the vessel segment under examination (von Birgelen et al. 1996b and 1996c). Thanks to the above features, 3D IVUS is particularly suitable for serial studies, assessing the state of disease before and after interventional treatments. When performed at a pre-interventional stage, 3D IVUS facilitates the selection of appropriate type and size of interventional device (Prati et al. 1996; von Birgelen et al. 1996d), such as the diameter of a balloon or the length and diameter of a stent. Three dimensional IVUS is also particularly useful in guiding interventional procedures and assessing their outcome (Coy et al. 1992; Gil et al. 1996; Prati et al. 1996).

#### **1.4.4.5 Guidance of interventional procedures**

As mentioned previously IVUS is capable of guiding interventional treatment of atherosclerosis, enhancing the final outcome (Gil et al. 1996; Prati et al. 1996; Stone et al. 1997; White et al. 1992). However, the whole procedure has the disadvantage of requiring separate insertion of the imaging probe before and after each treatment with interventional devices, thus increasing the number of catheter exchanges. Moreover, arterial wall dissections and perforations have been observed due to the lack of adequate guidance, when recanalisation techniques based on plaque removal (atherectomy, laser ablation and spark erosion) are used in situations involving eccentric plaques and curved vessels.

The above reasons prompted research towards the design of combined imaging and therapeutic catheters, which would reduce the number of catheter exchanges and provide the necessary information about the localisation and geometry of the stenosis for guiding the recanalisation procedures. A number of devices have

been described in the literature, combining IVUS imaging with atherectomy (Fitzgerald et al. 1995), laser ablation (Aretz et al. 1989 and 1991) and spark erosion (Bom et al. 1988). However, for reasons relating to manufacturing complexity or cost they are not widely produced.

Currently, only a combined balloon imaging catheter is commercially available (Stone et al. 1996), where the balloon is at the tip of the catheter and the imaging part is located proximal to the balloon (Figure 1.16). Use of this type of catheter has improved the results of balloon angioplasty and stenting and appears more cost effective than the angiographic-guided interventions (Hodgson et al. 1996; Kawata et al. 1997; Mudra et al. 1994).

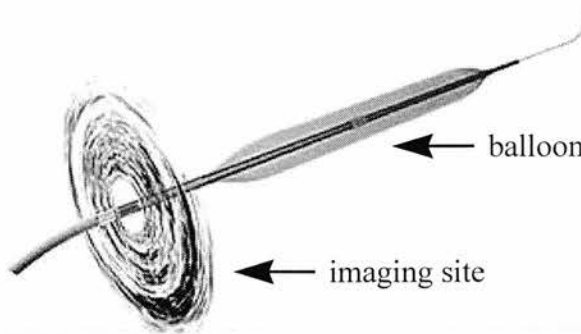


*Figure 1.16 : Combined IVUS imaging and balloon catheter (extracted from the Internet site <http://www.endosonics.com>).*

The use of combined catheters though, assumes that the size of the device to be used is chosen before intervention, based on angiographic rather than IVUS evidence. In addition to that, the imaging site is not always coincident with the treatment site. These limitations have initiated the development of the so called 'imaging guidewires'. These are imaging cores as small as the typical guidewires, with a miniature transducer at their tip. Such a wire would firstly provide pre-interventional imaging of the target lesion in order to determine the type and size of recanalisation device. Secondly, it would allow positioning of the therapy catheter in the stenosis as well as on-line guidance of the treatment procedure. Finally, after withdrawal of the therapy catheter, the wire would provide visual assessment of the



interventional outcome (ten Hoff et al. 1997). The first attempts with ‘imaging guidewires’ indicated adequate image quality and confirmed their clinical feasibility (Di Mario et al. 1997; Hiro et al. 1998). Further improvements are yet required in order to reach the levels of flexibility and steerability of the typical guidewires.

#### **1.4.5 The need for forward-viewing intravascular ultrasound**

Current commercial IVUS imaging systems are designed to image the vascular anatomy at the site of the transducer. The ultrasonic beam is emitted at approximately 80° to the vessel wall, hence the term ‘side-viewing systems’. Due to this design and principle of operation, atherosclerosis needs to be crossed by the side-viewing catheter in order to be imaged. What is more, the imaging site is about 8 mm away from the catheter tip. This limits the use of the side-viewing systems in the case of severely stenosed or totally occluded vessels. Due to lack of lumen space for advancing the catheter into the stenosed site, the side-viewing systems are unable to access the target region, thus they cannot provide any information about the structure which lies ahead of the catheter and blocks the artery. Furthermore, advancing the catheter towards a very stenosed lesion can restrict the blood flow even more and increase the ischemic risk for the myocardium or the end organ (McPherson and Kane 1997).

To overcome this limitation and obtain the desired information in such situations, a forward-viewing device is required. Such a device would direct the ultrasound beam in a forward fashion ahead of the catheter tip, providing information about the morphology and the extent of the stenosis, without the need to insert the catheter into the severely stenosed or occluded site. This possibility has been partly explored (Lee and Benkeser 1991) and some forward-viewing IVUS imaging attempts have been described (Back et al. 1994, Evans et al. 1994, Liang and Hu 1997a; Ng et al. 1994, Wiet et al 1994).

Ng et al. (1994) showed the potential of utilising 3D forward-viewing IVUS by rotating a sector acquisition plane. However, their work was limited to displaying

only a binary 3D volume, where the lumen was displayed in black and the vessel wall in white. Back et al. (1994) have presented the feasibility of nearly real-time 3D reconstruction of forward-viewing IVUS data by scanning the beam in a spiral forward-viewing fashion. A number of cross-sectional images could be displayed from an acquired conical volume, nevertheless the image quality did not match that of the side-viewing systems. The above attempts were also constrained by the catheters constructed. In the work of Back et al. (1994), the transducer was mounted on a stiff 7.5 Fr catheter, much larger than the side-viewing catheters (2.9 Fr). Thus, this device can be considered as suitable for in-vitro imaging only. In the work of Evans et al. (1994) and Ng et al. (1994) only manual rotation was available for the catheter which was also 4 mm in diameter, restricting its use to large peripheral arteries. Recently, a small sized catheter, 5 Fr diameter, has been constructed for intracoronary use (Liang and Hu, 1997a). This device scans a curved sector, which results in distortion of geometrical features. The use of this device in 3D acquisition and reconstruction has yet to be proven.

## **1.5 Aim of the thesis**

Imaging tubular structures from the inside, along the forward direction, is a new and largely unexplored field in ultrasound technology when referring to arterial dimensions. The previously mentioned efforts towards forward-viewing IVUS have shown, despite their limitations, the potential of this specific tool. To date no flexible forward-viewing catheter capable of 3D acquisition has been developed. Further improvements in design and performance are required in order to manufacture a cost-effective system which would provide good image quality and quantitative accuracy, thus becoming widely used in clinical practice. System cost and performance are directly related to the scanning and acquisition technique. There are many ways to scan ahead of the catheter tip and indeed, the previously mentioned works have used various methods. There has been no clear justification for the choice of the



acquisition formats, other than perhaps the relative manufacturing ability of the different groups.

The aim of this research is to investigate optimal scanning patterns, in order to assist the development of a future 3D forward-viewing IVUS system. A number of different scanning patterns are examined with the aid of a scaled-up scanning system and scaled-up vessel phantoms, so that the effort is concentrated on the development and assessment of the scanning patterns without being constrained by the small size of real life systems. The 3D data sets acquired with the different forward-viewing IVUS scanning patterns under investigation, are assessed with respect to their image quality and quantitative accuracy of luminal dimensions. The clinical utility and the manufacturing feasibility of a practical forward-viewing IVUS instrument are also taken into account in order to complete the framework of comparison among these scanning patterns.

Following on from that, the most promising scanning pattern according to all the above criteria, is implemented in a small catheter for imaging human arteries *in vitro*. This aims to assess the feasibility and suitability of the preferred scanning technique in imaging real arterial structures. At a further stage, the suitability of this technique for intravascular Doppler studies is also investigated, in an attempt to overcome sample volume location uncertainties associated with current Doppler wire techniques. It is hoped that this thesis will provide the basis for future manufacturing research and development in the field of forward-viewing intravascular ultrasound.

## **1.6 Layout of the thesis**

This thesis is organised into nine chapters. Chapter 1, the present chapter, has provided an introduction to vascular disease and intravascular ultrasound imaging. It has set out the problem of imaging severely stenosed vessels, the need for forward-viewing IVUS imaging and the motivation for the proposed investigations.

Chapter 2 describes the scanning patterns examined in this work for 3D forward-viewing IVUS imaging. The design and development of a mechanical scanning system for implementing these patterns is presented. The chapter also describes the development of an RF data acquisition system and of a software scheme for image production. Finally, Chapter 2 introduces the vessel phantoms used in conjunction with the scaled-up scanning system.

Chapter 3 evaluates various key components of the experimental system, including the fidelity of the RF amplifier in the ultrasound scanner, the suitability of the software procedure used for image production and the accuracy of the transducer motions provided by the scanning system. Initial frame images acquired with the various scanning patterns are presented and system limitations are discussed.

Chapter 4 deals with 3D image reconstruction and display issues regarding the scanning patterns under investigation. A number of images are presented from 3D data sets acquired with the different scanning patterns. These data sets provide the basis for assessing the image quality achieved by the various scanning patterns and allow comparative conclusions to be derived.

Chapter 5 investigates the accuracy of the examined forward-viewing IVUS scanning patterns when used for quantitative applications. At first, a review of image segmentation techniques used in IVUS is presented along with background theory of edge detection. The software scheme developed for lumen area measurements is described and results of the quantitative analysis are presented and statistically compared.

In Chapter 6 issues relating to clinical use and miniaturised construction are taken into account in order to complete the frame of comparison among the various scanning patterns and help identify the most promising one for practical clinical application. Following that, the design and development of a small scale system for 3D forward-viewing IVUS imaging of human arteries *in vitro* is described. The new system is based on a mechanical device implementing the scanning pattern regarded as the most suitable one, according to all the criteria set out.

Chapter 7 demonstrates the use of the small scale system in imaging human arteries *in vitro*. A number of forward-viewing IVUS images acquired from normal and diseased arteries are presented and correlated with histological analysis. The chapter assesses the suitability and utility of a forward-viewing IVUS system based on the preferred scanning pattern, in 3D imaging of real arterial structures.

Chapter 8 investigates the use of the above forward-viewing IVUS system in estimating and displaying blood velocity and flow. At first, the currently used intravascular techniques are presented along with their limitations. Subsequently, a new technique is described for blood flow estimation and colour flow imaging with the use of a forward-viewing IVUS system based on the preferred scanning pattern. Preliminary results are presented for flow through normal and stenosed vessel phantoms and the merits and limitations of this new method are discussed in view of its application in clinical practice.

Chapter 9 summarises the results and conclusions drawn from this research. Suggestions are also given to possible future work.

## **CHAPTER 2**

# **DEVELOPMENT OF THE SCANNING AND DATA ACQUISITION SYSTEM**

### **2.1 Introduction**

Conventional two dimensional ultrasound has developed into an important imaging modality in diagnosis and management of diseases. Nevertheless, despite the improvement over the years, 2D ultrasound still suffers from certain disadvantages. These are the variability of the examination and quantitative measurements which result from the difficulty of positioning the 2D imaging plane at a particular location between serial studies and also the inaccessibility of the optimum imaging plane due to patient's anatomy or orientation.

Three dimensional ultrasound is a relatively recent development aimed to overcome the limitations of 2D ultrasound. It reduces the variability of the conventional technique and enables more accurate diagnosis to be made by visualising the anatomy in three dimensions and allowing display of arbitrary planes not available by common 2D data acquisition. Volume acquisition is accomplished by acquiring a number of imaging planes at different locations and/or orientations.

This chapter describes the scanning patterns developed and examined in this study for 3D forward-viewing IVUS imaging. The design and development of a scaled-up mechanical scanning system for implementing these patterns is discussed. A description of the data acquisition and image production system is also provided. Finally, the current chapter introduces the vessel phantoms used in conjunction with the scaled-up scanning system.

## **2.2 Common acquisition methods for 3D ultrasound**

A variety of scanning techniques are commonly used for volume data acquisition with ultrasound. They are described in the review articles of Fenster and Downey (1996) and Nelson and Pretorius (1998) as:

- **Freehand Scan** : A series of B-mode images are acquired by placing the transducer probe in arbitrary orientations by hand (Figure 2.1). The exact location and angulation of the probe in space is tracked by position sensing systems which can be articulated arms, electromagnetic field transmitters/receivers, combinations of spark gaps and microphones, or combinations of video cameras and infrared light emitting diodes. The registration information provided by the position sensing systems is stored along with the ultrasound data and used for correct orientation of the imaging planes during the volume reconstruction procedure.

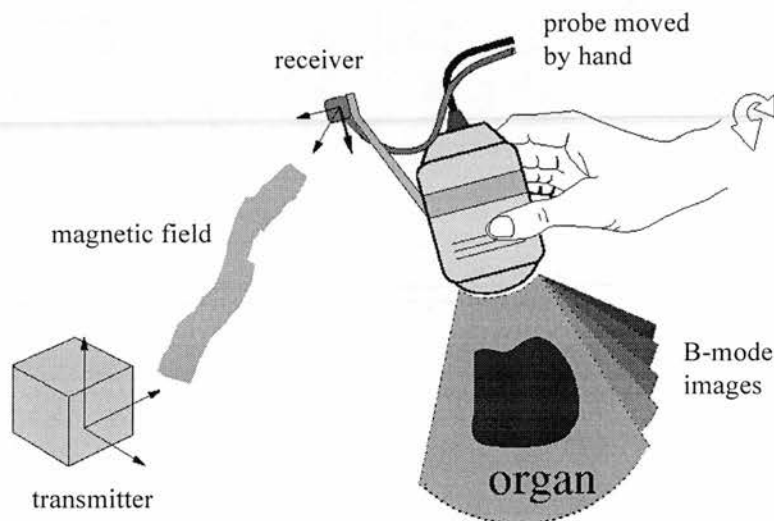


*Figure 2.1 : Freehand 3D scan utilising an electromagnetic position sensing system (from Rohling 1998).*

- **Linear Scan** : In this method the probe is attached to a motorised external assembly and moved in a linear fashion at a direction perpendicular to the imaging

plane. The acquired images are parallel to each other. The location of each imaging plane is derived from the motor positioning information. This is the acquisition method used in 3D side-viewing intravascular ultrasound, where the catheter is withdrawn within the vessel (Figure 2.2).

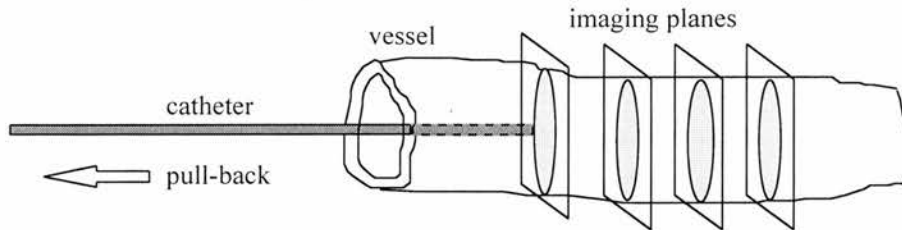


*Figure 2.2 : Linear ('pull-back') side-viewing intravascular ultrasound scan for volume acquisition.*

- **Rotational Scan :** A probe providing a sector image is rotated with the aid of a motorised external assembly. The axis of rotation is along the central axis of the probe. The acquired images compose a conical volume (Figure 2.3).
- **Fan Scan :** The imaging plane is swept around an axis at the face of the probe. The acquired images are arranged in a fan-like shape and compose a pyramidal volume (Figure 2.3).
- **Compound Scan :** This scanning method involves combinations of scanning techniques, such as freehand and sector scan (Figure 2.4) at different levels in order to scan the volume of interest. The main advantages are a more thorough scan of the tissue and organs and reduced noise in the image.

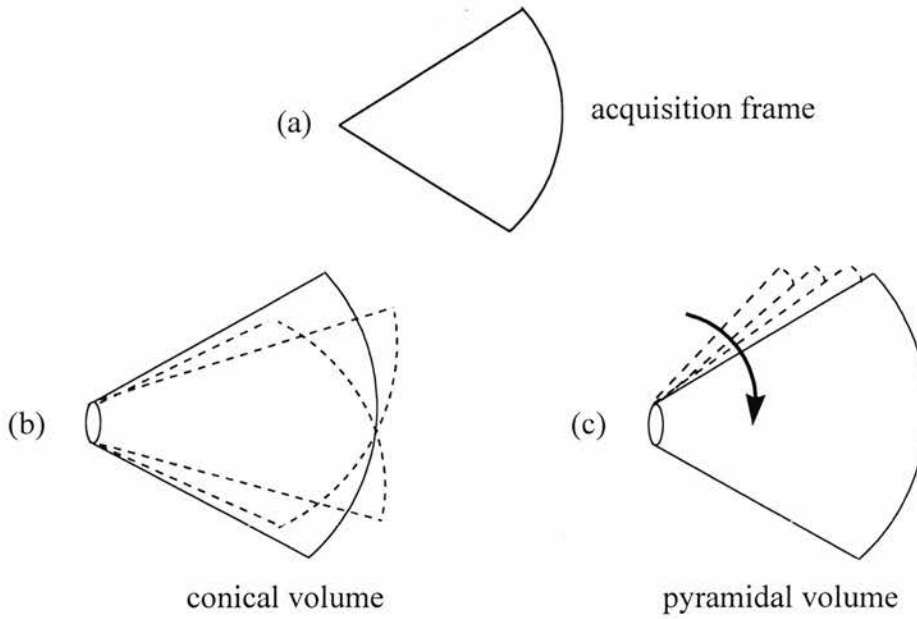


*Figure 2.3 : Illustration of the Rotational and the Fan scans. (a) The acquisition frame is a 2D sector image; (b) in the Rotational scan the acquisition plane is rotated stepwise and the acquired frames compose a conical volume; (c) in the Fan scan the acquisition plane is swept stepwise from one side to another in a direction perpendicular to the imaging sector. This fan-like motion results in a pyramidal volume.*

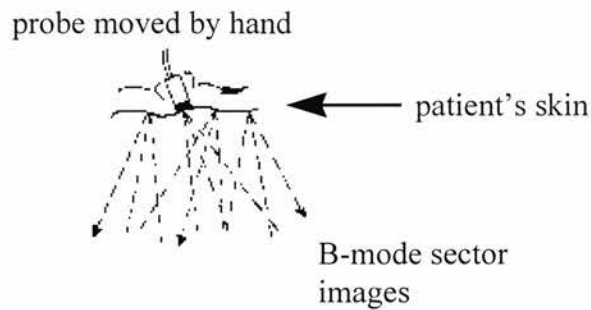


*Figure 2.4 : Compounded freehand and sector scans (from McDicken 1991).*

## **2.3 Scanning patterns for 3D forward-viewing IVUS**

Five three dimensional scanning patterns were examined in this work for use in forward-viewing IVUS. The investigation of the patterns was carried out with the aid of a mechanical scanning system which utilised a single element transducer mounted at the tip of a scaled-up catheter. Scaled-up vessel phantoms made from tissue mimicking material were used to simulate healthy and stenosed vessels. The transducer was scanned in a forward fashion so that the beam was directed ahead of the catheter tip. The acquisition geometries of the scanning patterns are described in the following paragraphs.

### **2.3.1 Conical scan**

With the transducer axis aligned at an angle  $\theta$  to the long axis of the catheter, the catheter is rotated over  $360^\circ$ . Thus, a conical surface is scanned. Keeping this acquisition geometry fixed, a set of conical surfaces is acquired by 'pulling-back' the catheter. The acquired volume has a conical shape (Figure 2.5). For this study the angle  $\theta$  was chosen to be  $15^\circ$ . A frame (conical surface) was composed of 125 lines, thus the angular step between successive lines on the conical surface was  $2.88^\circ$ . Sixty frames were acquired per volume at 0.9 mm increments.

This pattern is quite similar to the scanning technique of the side-viewing IVUS systems. The similarities refer to the pull-back of the catheter (Klein et al. 1992; Matar et al. 1994) and to the beam emission at a fixed angle. The major difference is that in the side-viewing systems the beam is emitted at approximately  $80^\circ$  to the catheter axis, while in the forward-viewing system of this study the beam was emitted at a much smaller angle, namely  $15^\circ$ .



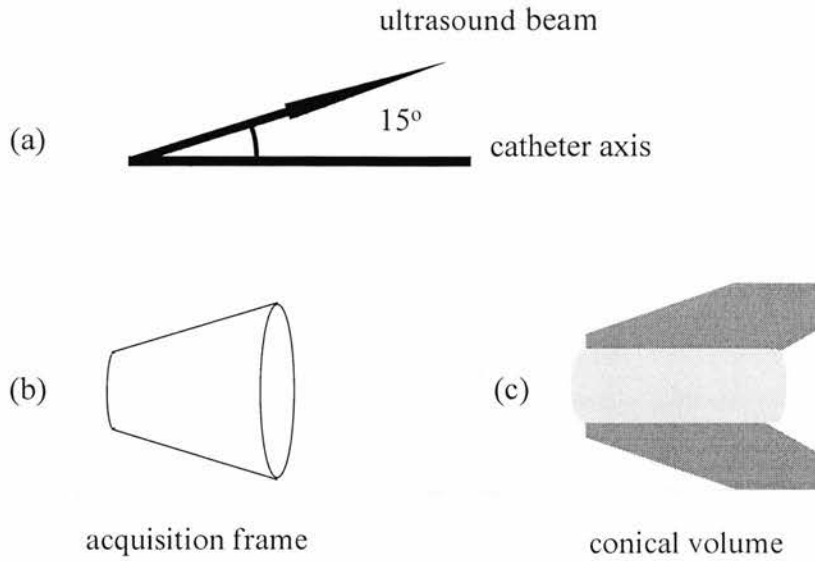


*Figure 2.5 : Illustration of the Conical scan. (a) The beam is maintained at a fixed angle  $15^\circ$  to the catheter axis. (b) During a frame acquisition the beam is rotated over  $360^\circ$  to scan a conical surface. (c) Using this frame acquisition geometry, a set of frames is acquired by 'pulling back' the catheter. The acquired volume has a conical shape with the data lying at the side parts of the volume (dark colour) while the middle volume area is 'hollow' (light colour).*

### 2.3.2 Spiral scan

During each frame acquisition the beam is emitted at a fixed angle  $\theta$  to the long axis of the catheter, which is rotated over  $360^\circ$ . Thus, a conical surface is scanned. A set of frames is acquired by varying the angle  $\theta$  from  $\theta_{\text{start}}$  (beam nearly parallel to the catheter axis) up to  $\theta_{\text{end}}$  in equal angular steps. This results in scanning a conical volume composed of a number of conical surfaces with one lying inside another (Figure 2.6).

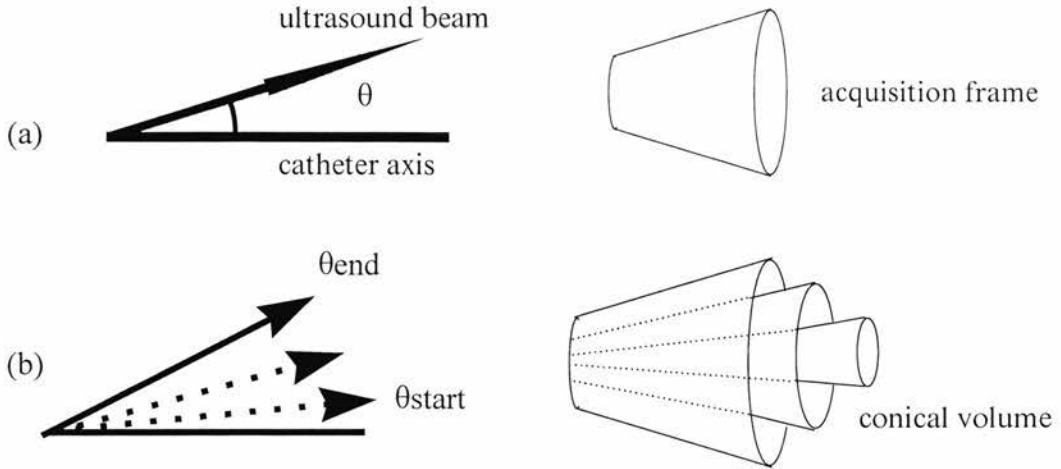


*Figure 2.6 : Illustration of the Spiral scan. (a) During a frame acquisition the beam is kept at a fixed angle  $\theta$  to the catheter axis and scans a conical surface. (b) A set of frames is acquired by varying the angle  $\theta$  from  $\theta_{start}$  up to  $\theta_{end}$  in equal steps. This results in scanning a conical volume composed of a number of conical surfaces with one lying inside another.*

This pattern was used by Back et al. (1994) in their forward-viewing IVUS work. In the study described here, each conical surface (frame) was composed of 125 lines at  $2.88^\circ$  angular steps. Angle  $\theta$  varied from  $0.6^\circ$  to  $36^\circ$ , in equal steps of  $0.6^\circ$ . The conical volume consisted of 60 frames and had a  $72^\circ$  cone angle.

### 2.3.3 Rotational scan

In this scanning pattern the beam is swept across a 2D plane to provide an acquisition frame. The acquisition plane is rotated in equal angular steps for a total of  $180^\circ$ , and for each rotational step a new frame is acquired. The set of acquired frames forms a conical volume (Figure 2.3). This pattern has been used by Evans et al. (1994), Ng et al. (1994) and Wiet et al. (1994) in their version of forward-viewing IVUS. It has also been widely used in other ultrasound applications such as

transesophageal echocardiography (Ofili and Nanda 1994; Roelandt et al. 1994b), transthoracic echocardiography (Ghosh et al. 1982; Ludomirsky et al. 1994; Ofili and Nanda 1994) and imaging of the gallbladder and the biliary tree (Fine et al. 1991). In this implementation, 110 lines were scanned across a  $66^\circ$  sector in equal steps of  $0.6^\circ$ , with the angular step between rotated sectors being  $1.8^\circ$ , i.e. the conical volume consisted of 100 frames (sectors) and had a  $66^\circ$  cone angle.

#### **2.3.4 Fan scan**

The beam is swept across a 2D plane as in the previous pattern, to provide an acquisition frame. The acquisition plane is swept in equal angular steps, from one side to another, in a direction perpendicular to the motion of the beam. For each sweep step a new frame is acquired. This 'fan-like' motion (Salustri and Roelandt 1995) results in scanning a pyramidal volume (Figure 2.3). This scanning pattern has also been widely used in other ultrasound applications such as transesophageal echocardiography (Martin et al. 1990), transthoracic echocardiography (Delabays et al. 1995) and imaging of abdominal organs (Gilja et al. 1994). In this study, 96 lines were scanned across a  $58^\circ$  sector in equal steps of  $0.6^\circ$ . The angular step between swept sectors was  $0.88^\circ$  and the volume consisted of 70 frames (sectors) arranged over a  $62^\circ$  angle.

#### **2.3.5 Compound scan**

This pattern involves placing the catheter in different concentric and eccentric positions inside the lumen of the vessel phantom. For each catheter location, any of the previously described scanning patterns can be performed. The acquired data sets are finally averaged to form the image. This pattern is not practical in terms of IVUS clinical applications. However, it was investigated in order to extend the understanding of the factors that affect image quality. In this study, three data sets

were obtained prior to compounding, from one concentric and two eccentric positions of the catheter in the phantom lumen (Figure 2.7).

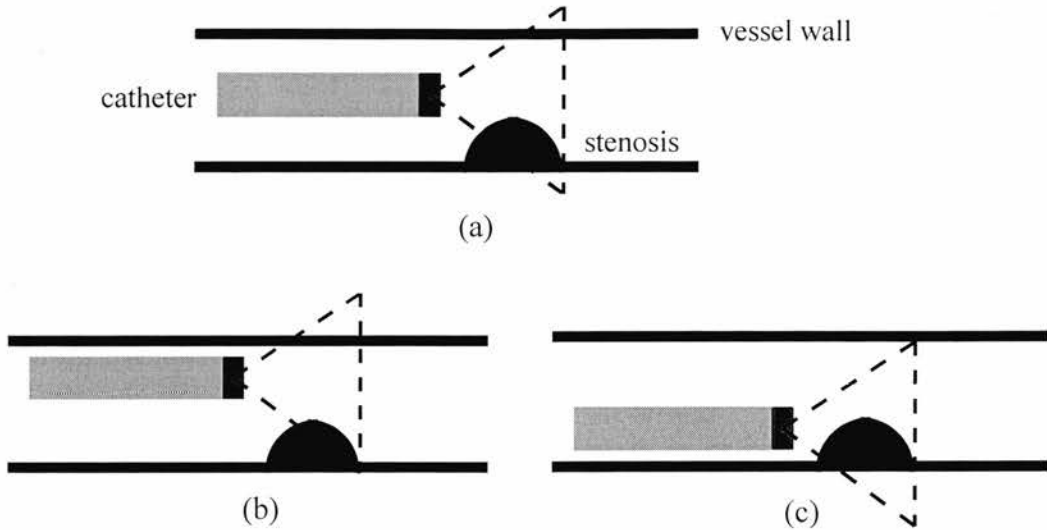


*Figure 2.7 : Illustration of the Compound scan. The catheter is placed in three different positions inside the lumen of the vessel phantom. Any of the previously described scanning patterns may be performed for each catheter location and the acquired data sets are averaged to form the image. This diagram shows the case of a stenosed vessel scanned from (a) a concentric catheter location, (b) an eccentric catheter location away from the stenosis and (c) an eccentric catheter location close to the stenosis. The dashed triangle denotes the scanned area ahead of the catheter.*

## 2.4 Scanning system

From the above description of the forward-viewing scanning patterns it becomes clear that a scanning system for implementing all these patterns should allow movement of the transducer in all directions as well as relative movement of the transducer within the vessel phantom. It was decided to implement the scanning patterns with the aid of stepper motors, since these motors would provide control and knowledge of the transducer position at any time, without the use of a position

sensing system. Six stepper motors were used in total providing six degrees of freedom for the transducer movement.

A diagram of the scanning system developed is shown in Figure 2.8a. Three stepper motors (SM1, SM2 and SM3) mounted on the side of a water tank, behind the catheter, provide the means to control the movement of the transducer. The motors SM1 and SM2 (model 23HS-108, McLennan, Surrey, UK) provide sweep motions of the transducer along two planes normal to each other, with the aid of two pairs of thin pulling wires (0.56 mm in diameter) threaded around the motor shafts. The third stepper motor, SM3 (model 34HS-109, McLennan, Surrey, UK), provides the rotational motion of the transducer (Figure 2.8b).

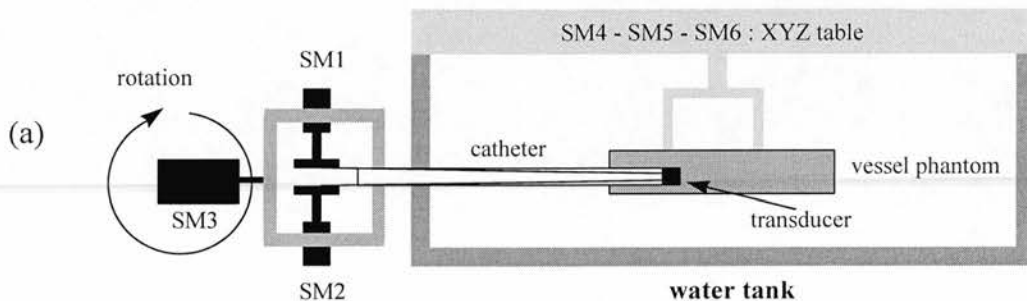


*Figure 2.8 : (a) Diagram of the mechanical scanning system which utilises six stepper motors for controlling the position of a single element transducer. The transducer is placed at the tip of a 'catheter'. The catheter is inserted in the lumen of a vessel phantom mounted on a supporting device inside a water tank.*

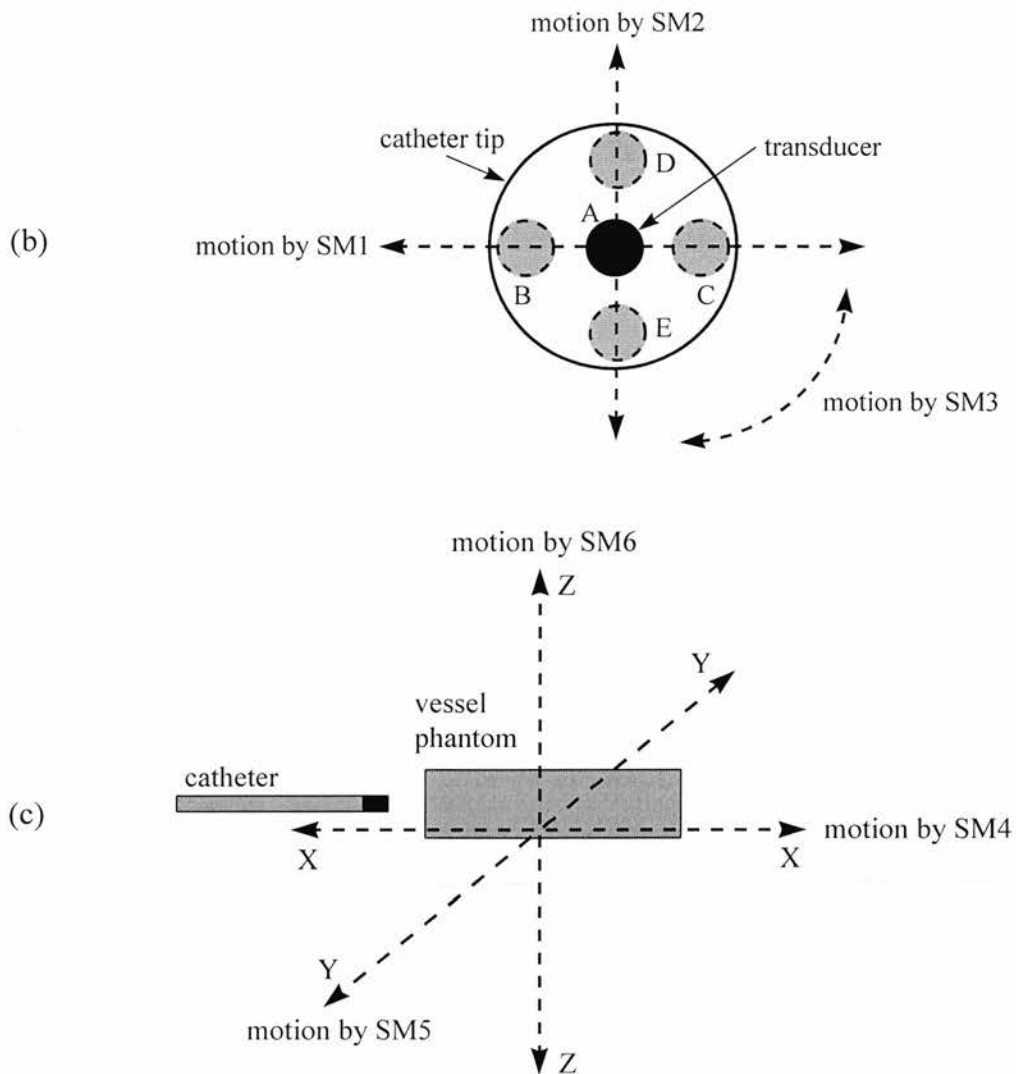


*Figure 2.8 (continued) : (b) Schematic diagram illustrating the three degrees of freedom for the movement of the transducer mounted on the catheter tip. Motor SM1 causes sweep motions of the transducer parallel to the direction defined by the positions B, A and C. Motor SM2 causes sweep motions of the transducer parallel to the direction defined by the positions D, A and E, and perpendicular to those caused by SM1. Motor SM3 causes rotational motions of the transducer similar to the one defined by positions B,D,C and E. (c) Schematic diagram illustrating the three degrees of freedom for the movement of the vessel phantom. Motors SM4, SM5 and SM6 move the phantom in three independent XYZ directions.*

The catheter is comprised of a scan head mounted on a plastic tubular shaft of 25 mm outer diameter. The scan head is designed to allow movement of the transducer in all directions. It consists of a plastic holder for the transducer, a PTFE sphere of 11 mm diameter, a pair of levers and a coupling pin. The design of the catheter and the scan head is illustrated in Figure 2.9. The transducer and its holder are mounted on the PTFE sphere by means of a coupling pin which runs through the sphere. The sphere is made to rotate in any direction by means of two rotation actuating levers operated by the pulling wires. Each of these levers has a semicircular shape with two ends attached to the sphere at diametrically opposite positions (12 and 6 o'clock positions for the first lever; 3 and 9 o'clock positions for the second lever). The levers cross each other forming a small square cage where the proximal end of the coupling pin is enclosed (Figure 2.9d). The pulling wires run along the lumen of the catheter and are clamped on the lever ends. When the motors rotate, the wires pull on the levers causing the coupling pin to move, which in turn, causes the sphere to rotate and the transducer to sweep. Rotation of motor SM1 sweeps the transducer up or down, while rotation of motor SM2 sweeps the transducer left or right.

The angular resolution of the transducer movements in the above two independent directions is defined by the angular resolution of the motors SM1 and SM2, the radii of the motor shafts and the radii of the levers controlling the movement of the sphere (Figure 2.9e). Let  $R_m$  be the motor shaft radius and  $R_l$  the lever radius. When the motor rotates over an angle of  $\theta_m$  degrees, the wire is pulled over a length  $L$  :

$$L = 2\pi R_m \cdot \frac{\theta_m}{360} \quad (2.1)$$

Assuming there is no slack on the wire and that it does not elongate under tension, the above motion causes an angular (sweep) motion of the transducer over an angle of  $\theta_l$  degrees so that

$$2\pi R_l \cdot \frac{\theta_l}{360} = L \quad (2.2)$$

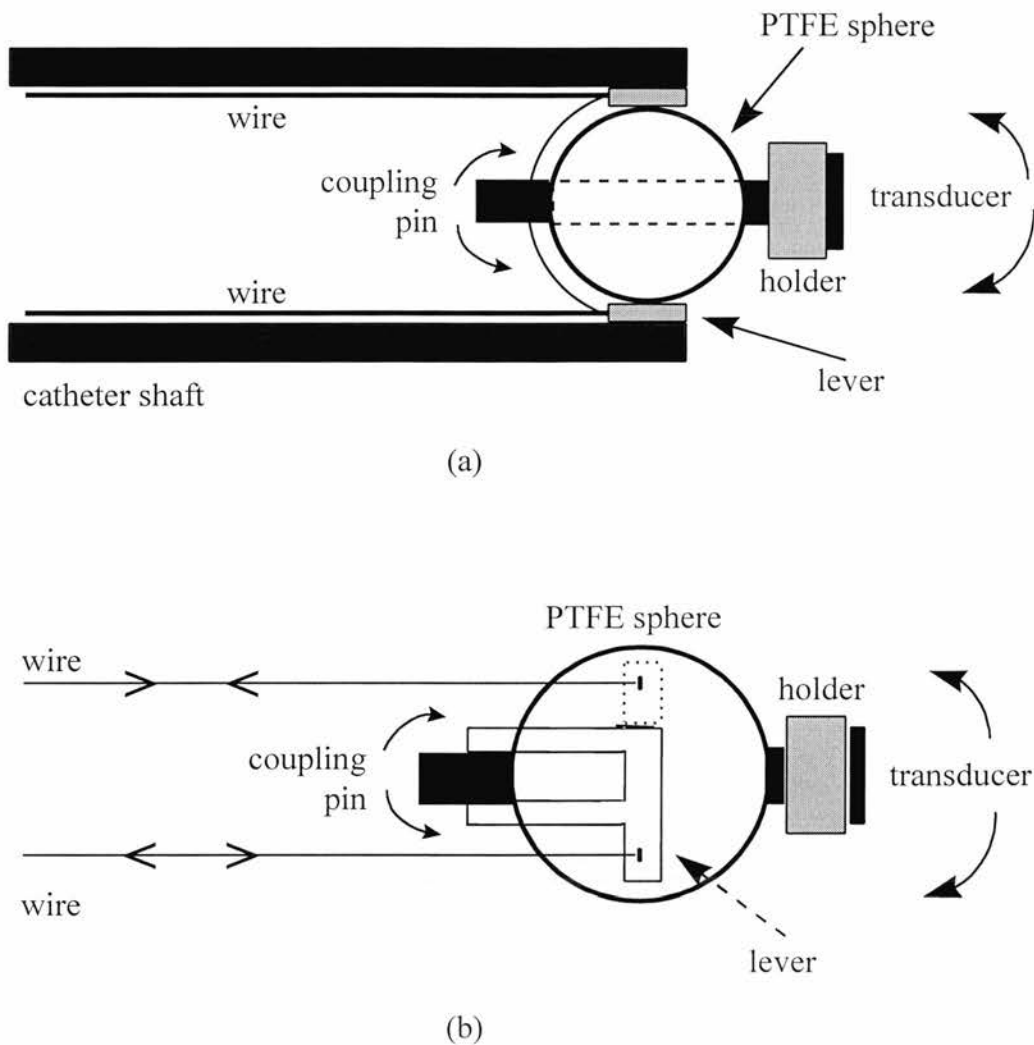


*Figure 2.9 : (a) Schematic diagram of the catheter which comprises of a scan head and a tubular shaft. The scan head consists of a plastic holder for the transducer, a PTFE sphere, a pair of levers and a coupling pin. Pulling wires connected to the motor shafts and to the levers of the scan head, run along the catheter lumen. (b) Schematic top view of the scan head. For clarity only one axis of motion is shown.*



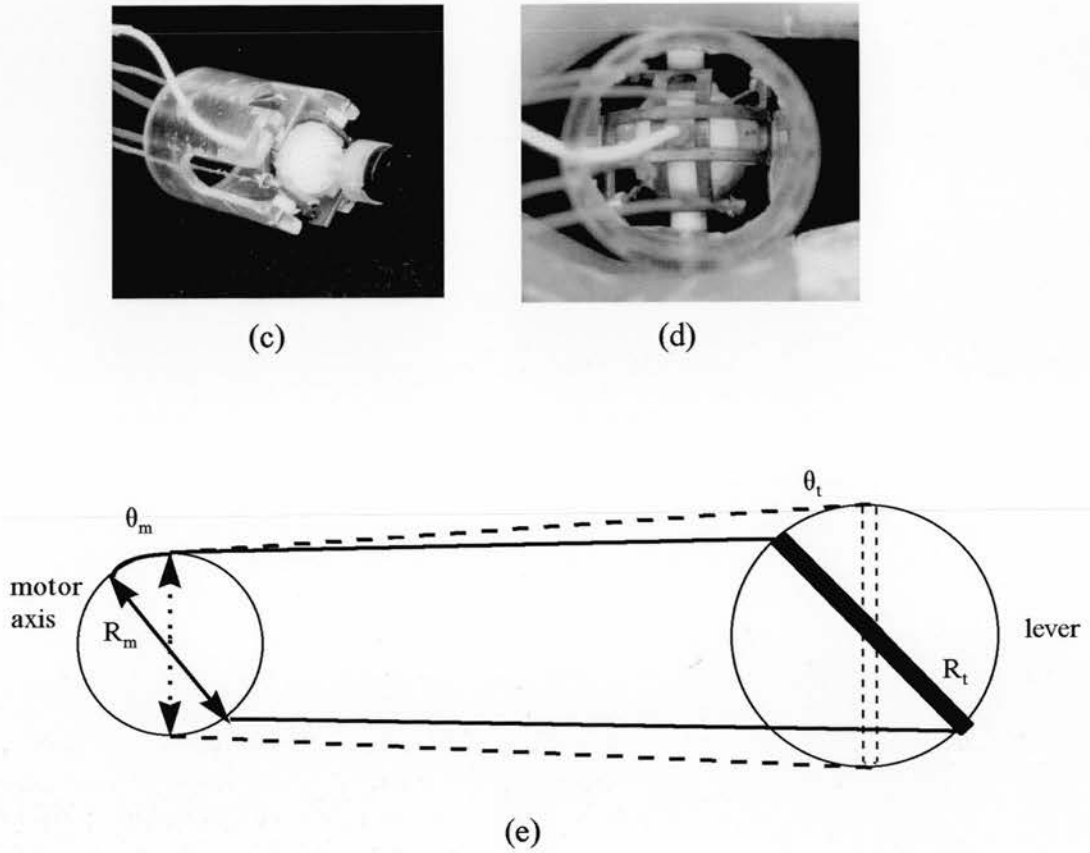


*Figure 2.9 (continued) : (c) Front view photograph of the scan head showing the transducer, the PTFE sphere and the rotation actuating levers with the pulling wires clamped on them. (d) Rear view photograph of the scan head showing the coupling pin enclosed by the levers. When the wires pull on the levers, the pin follows the direction of lever motion causing the transducer to sweep. (e) Principle of the angular motion of the transducer caused by rotation of stepper motors. The axis of the stepper motor (shown on the left) has a radius  $R_m$  and is connected with a pair of wires to the lever of radius  $R_t$  at the transducer end (shown on the right). Rotation of the stepper motor for an angle  $\theta_m$  causes a rotation of the lever for an angle  $\theta_t$ . Two different positions are shown in solid and dashed.*

Combining equations (2.1) and (2.2) results in

$$\theta_t = \frac{R_m}{R_t} \cdot \theta_m \quad (2.3)$$

The angular resolution of SM1 and SM2 ( $\theta_{m1}$  and  $\theta_{m2}$  respectively) is  $0.9^\circ$ . The radius of the SM1 shaft ( $R_{m1}$ ) is 4.7 mm and of the SM2 shaft ( $R_{m2}$ ) 5.4 mm. The radii of the corresponding levers  $R_{t1}$  and  $R_{t2}$  are 7 mm and 5.5 mm respectively. Substituting the above values in equation (2.3) it results in angular resolution of  $0.6^\circ$  for the sweep transducer motion caused by SM1, and angular resolution of  $0.88^\circ$  for the sweep motion caused by SM2.

Motor SM3 rotates the catheter together with the motors SM1 and SM2. A gearbox (model LP070-M1-10:1, Alpha Getriebbau GmbH, Igersheim, Germany) is fitted to SM3 in order to provide the necessary torque to rotate SM1 and SM2, as well as to improve the angular resolution of the rotation. The angular resolution of SM3 is  $0.9^\circ$ . With the use of the 10:1 ratio gearbox, the resolution of the rotational movement of the transducer is improved to  $0.09^\circ$ .

The vessel phantom is mounted on a supporting device inside the water tank. Three motors, SM4, SM5 and SM6 (model 23HS-104, McLennan, Surrey, UK) mounted on the tank frame, move the phantom supporting device in three independent directions, as in an XYZ axis system, with the use of ballscrews (Figures 2.8c and 2.10). In this way, it is possible to achieve relative movements between the catheter and the vessel phantom and most importantly to simulate the pull-back motion of the catheter, by moving the vessel phantom away from the catheter. Moreover, these three motors facilitate concentric and eccentric positioning of the catheter in the phantom lumen. The X and Z axis resolution is  $12.5 \mu\text{m}$ , with the Y axis resolution being  $17.5 \mu\text{m}$ .

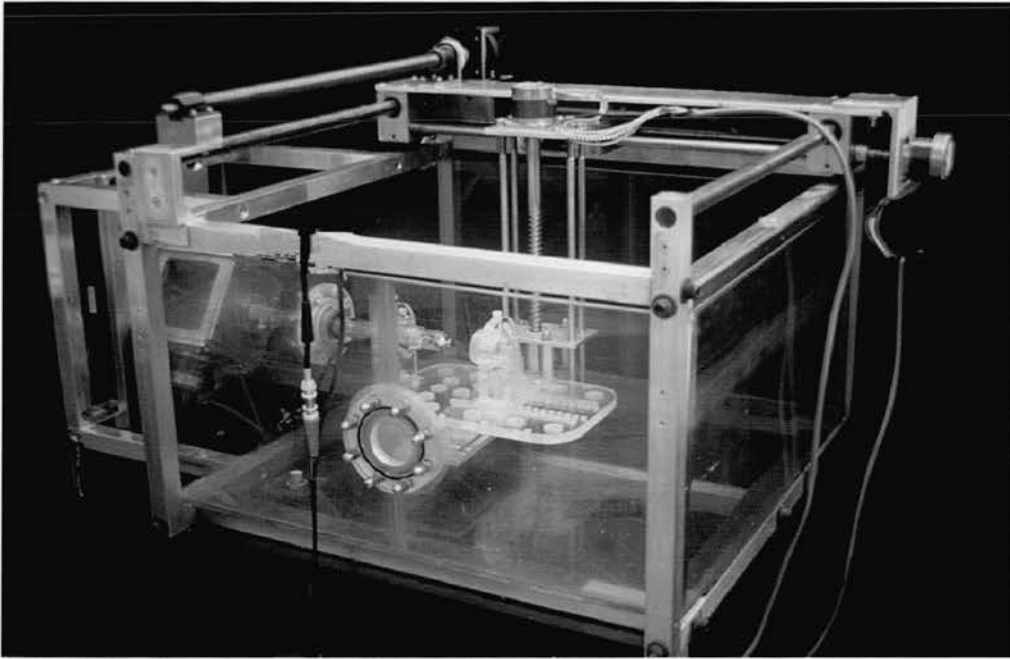


*Figure 2.10 : The water tank (60 cm long x 60 cm wide x 30 cm tall) fitted with a three axis XYZ motion system implemented with stepper motors and ballscrews. Also shown is the phantom supporting device in the centre of the tank as well as the catheter with the transducer.*

The phantom supporting device can also be manually orientated at an angle to the catheter. This allows the study of images obtained at non-parallel positions of the catheter to the long axis of the vessel.

The motors of the scanning system are controlled from a Pentium PC by means of a plug-in stepper motor controller card (model OMS-PC38-6, Oregon Micro Systems, Beaverton, Oregon, USA) and LabVIEW software (National Instruments, Austin, Texas, USA).

## **2.5 Data acquisition system**

### **2.5.1 Transducer**

The transducer used in this work was a single element disc-shaped PZT crystal. The outer diameter of the transducer was 9 mm and its central frequency was 7.5 MHz. A 0.2 mm active area needle hydrophone (HPM02/1, Precision Acoustics Ltd, Dorchester, UK) was used to assess the pulse length and to acquire a 6dB beam plot for this transducer (Figure 2.11).

The axial resolution of the system is approximately equal to 0.3 mm (half the pulse length). The lateral resolution is determined by the beam width and varies with the distance from the transducer face. The transducer is focused with the focal zone extending from 12 to 40 mm ahead of the transducer face. In this region the 6dB beam width is approximately 1 to 2 mm.

The axial resolution of the 30 MHz IVUS systems used for imaging coronary and peripheral arteries is reported to be around 75-80  $\mu\text{m}$ , and the lateral resolution to be 225-500  $\mu\text{m}$  (Foster et al. 1997; Hoskins and McDicken 1994; Li et al. 1994; Roelandt et al. 1993b). Comparing these values to the ones of the 7.5 MHz transducer used in this study, it can be observed that the axial resolution of the 7.5 MHz transducer is about 4 times poorer than that of the 30 MHz IVUS systems. The lateral resolution of the 7.5 MHz transducer is 4 to 10 times below that of the 30 MHz IVUS systems. These observations provided an indication of the appropriate size of the vessel phantoms in order to retain proportionality of resolutions and vessel dimensions between the system developed in this study and a typical IVUS system used for imaging coronary/peripheral arteries.

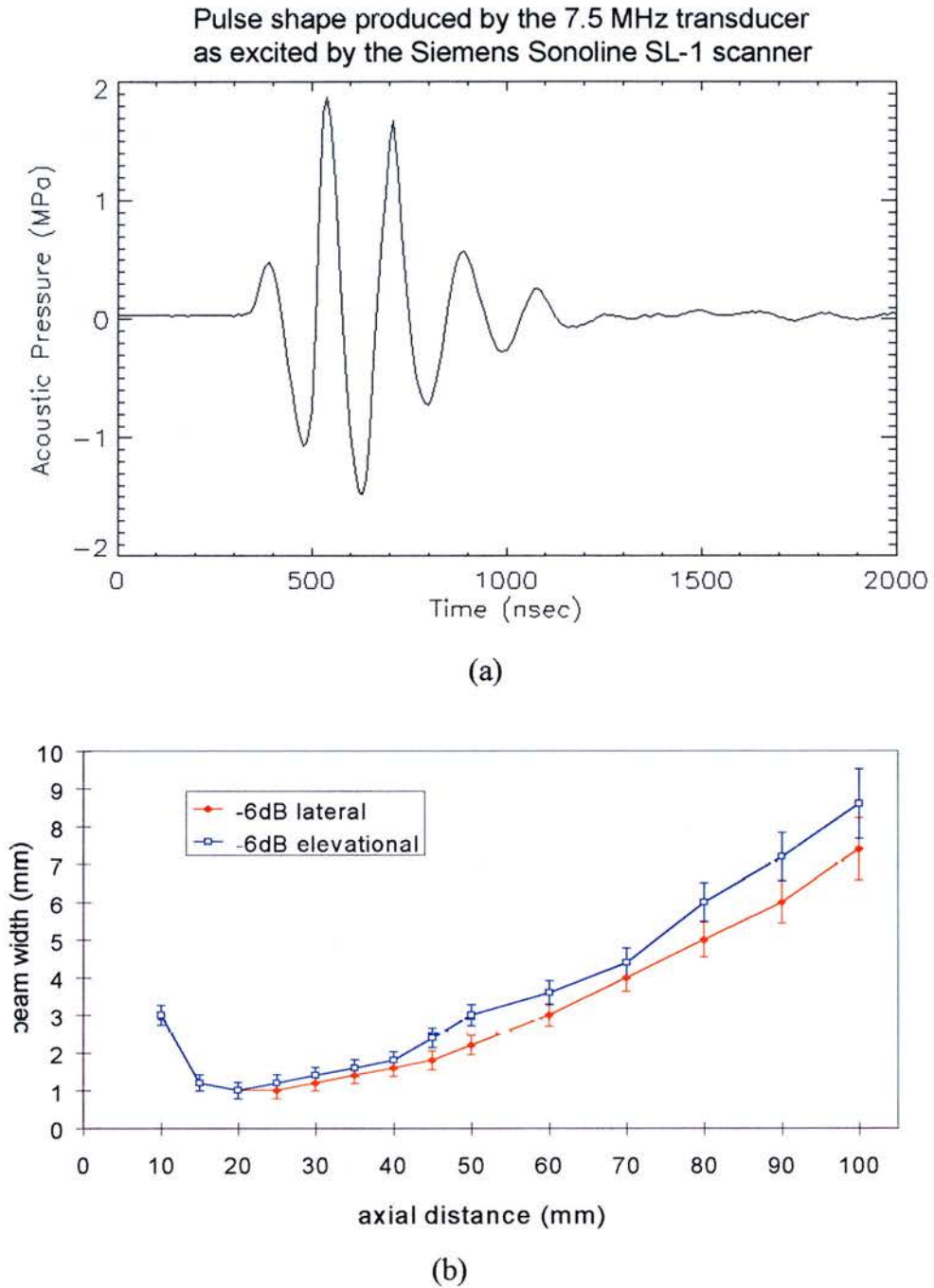


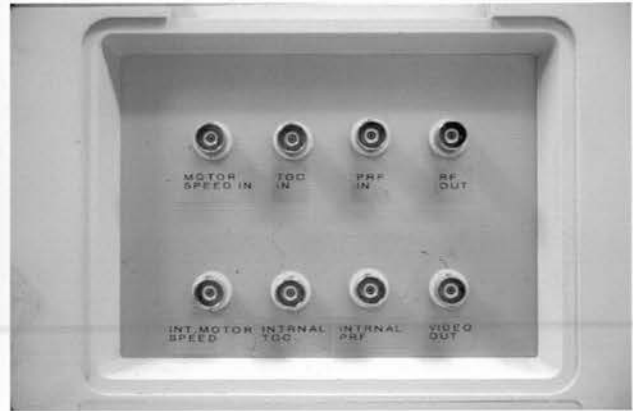
*Figure 2.11 : (a) Pulse shape, at 30 mm depth, of the single element 7.5 MHz transducer as excited by the Siemens Sonoline SL-1 scanner (this pulse shape is not an impulse response). (b) -6dB longitudinal plot of the beam shape (for peak-to-peak signal). The transducer is focused at a distance 12 to 40 mm from its face.*

### **2.5.2 Ultrasound scanner**

The transducer was connected to the M-mode input of an ultrasound scanner (Sonoline SL-1, Siemens Aktiengesellschaft, Erlangen, Germany), shown in Figure 2.12, which provided the electronic platform for transmitting and receiving the ultrasonic signal.



(a)



(b)

*Figure 2.12 : The Siemens Sonoline SL-1 ultrasound scanner (a), with a front panel (b) fitted for enabling access to the RF signal at the output of the receiver and for applying external PRF and TGC signals.*

According to Bijmens et al. (1994), there are certain advantages in using the received ultrasonic RF signal instead of the processed video signal for image display purposes. More specifically, use of the unprocessed RF signal preserves small and fast signal changes, which are otherwise lost when hardware is used to demodulate and log-compress the ultrasonic signal for display. Use of the RF signal has proven to

facilitate detection and tracking of the tissue-blood interface on reconstructed images (Pérez et al. 1992). Based on the above remarks, it was decided not to use the available video output of the ultrasound scanner. Instead, the receiver of the scanner was modified by the addition of a PCB buffer amplifier so that the RF signal was brought to a socket on the front panel of the scanner (Figure 2.12b). Image reconstruction and display were facilitated by software processing of the digitised RF signal. Another modification to the scanner provided the ability to bypass its fixed internal Pulse Repetition Frequency (PRF) rate and apply a variable external PRF instead. Finally, the scanner was further modified to accept an external Time Gain Compensation (TGC) signal generated by a circuit with a number of slide potentiometers controlled by the user. The external signals were applied via sockets on the front panel (Figure 2.12b).

### **2.5.3 Volume acquisition**

A diagram of the data acquisition system is given in Figure 2.13. The stepper motor controller card, plugged into the PC, is responsible for driving the motors in order to perform the required scanning patterns. The step signal of the motor which scans the beam to acquire a frame for a particular scanning pattern, is used to synchronise the data acquisition. An external programmable 'clock divider' circuit uses this step signal to generate a synchronous PRF signal which is the same rate or a sub-multiple of the stepper motor speed. This generated PRF is fed to the ultrasound scanner and to the external TGC generator circuit providing the TGC signal for the scanner. In this way, synchronisation of the ultrasonic lines with the motor steps is always achieved. The acquired RF signal is fed to a 12-bit 100 MHz A/D converter (model PDA12, Signatec Inc, Corona, California, USA), housed in the PC and controlled by LabVIEW software. The digitised data is archived on CD-ROM for off-line processing.



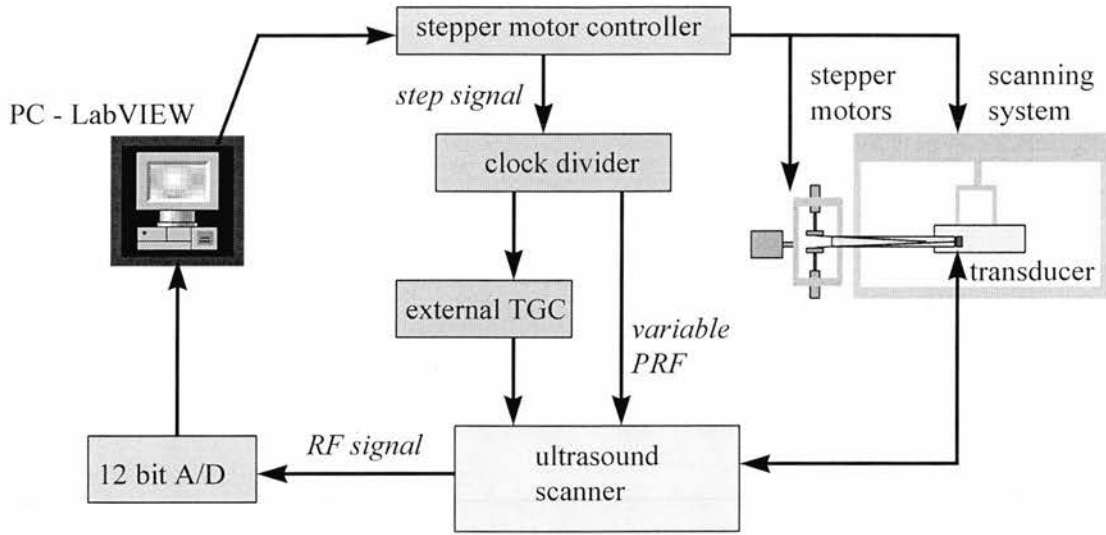


Figure 2.13 : The complete scanning and data acquisition system.

#### 2.5.4 Signal processing for image generation

The received RF signal  $x(t)$  is the real part of a complex analytical signal  $z(t)$  which contains amplitude and phase information and is known as the complex envelope. The relationship is described as

$$x(t) = \text{Re}\{z(t) \cdot e^{j2\pi f_0 t}\} \quad (2.4)$$

where  $f_0$  is the central frequency of the transducer (Figure 2.14).

The ultrasound image display is based on the amplitude of the complex signal. In order to derive this amplitude in the software based display approach adopted in this study, the originally received RF signal was shifted by  $90^\circ$  using the Hilbert transform. The resulting signal  $y(t)$  is the imaginary part of the complex envelope:

$$y(t) = \text{Im}\{z(t) \cdot e^{j2\pi f_0 t}\} \quad (2.5)$$

With both the real and the imaginary parts of the complex envelope available, its amplitude was calculated as

$$|z(t)| = \sqrt{x(t)^2 + y(t)^2} \quad (2.6)$$



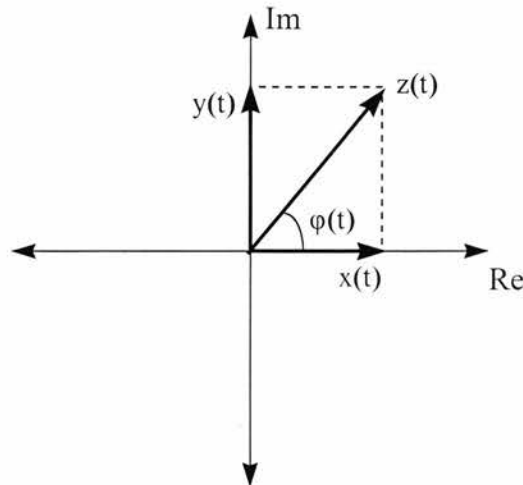


*Figure 2.14 : Diagram illustrating the relationship between the complex analytical signal  $z(t)$  and the measured RF signal  $x(t)$ . The phase  $\phi(t)$  of the complex signal is time-variant ( $2\pi f_0 t$ ). The amplitude of the complex signal is derived from the measured RF signal  $x(t)$  and its quadrature signal  $y(t)$ . The latter is obtained from the Hilbert transform of  $x(t)$ .*

The dynamic range of both  $x(t)$  and  $|z(t)|$  is well beyond the display capabilities of TV monitors and the perception of human vision. Therefore, there is a need to compress the dynamic range of the amplitude signal to a level appropriate for display on a monitor. Commercial scanners do this by log-compression through a logarithmic amplifier whose function resembles the natural logarithm. Consequently, in the software approach of this work, the amplitude signal was processed by a natural logarithm function. The resulting compressed signal was finally displayed on a window in the PC.

If the conical or spiral scanning pattern was used, the lines of an acquisition frame were displayed in a planar rectangular format for convenience of perception. If the rotational or the fan scan was used, then the lines acquired in a frame were scan converted to a sector scan display. The whole RF signal processing and image generation scheme was implemented in IDL programming (Research Systems, Boulder, Colorado, USA). IDL is a software package which offers interactive analysis of scientific and engineering data. It integrates an array orientated language

with tools for mathematical analysis, signal processing and image processing and visualisation in two and three dimensions.

## **2.6 Tissue mimicking material vessel phantoms**

Vessel phantoms made from tissue mimicking material were used in this study for evaluating the scanning patterns under examination. The vessel phantoms also served as test objects for assessing aspects of the experimental system.

### **2.6.1 Tissue mimicking material**

Tissue mimicking material (TMM) has recently been used for IVUS studies. These materials were either solutions of agar and gelatine in water with silicon carbide particles added to provide scattering (de Korte et al. 1997) or water-gelatine gel with silica powder added to act as scatterers (Ryan and Foster 1997).

In this study the agar based tissue mimicking material proposed by Tierlinck et al. (1997 and 1998) was used. This material consists of water, glycerol (Sigma, Poole, UK), Rodanol® Benzalkoniumchloride (Superfos Biosector A/S, Vedbaek, Denmark), agar (Struers Kebo Lab A/S, Albertslund, Denmark), aluminium oxide  $\text{Al}_2\text{O}_3$  powders of 3.0  $\mu\text{m}$  and 0.3  $\mu\text{m}$  particle size (Logitech Ltd, Glasgow, UK) and silicon carbide SiC powder 400 grain size (Logitech Ltd, Glasgow, UK).

Glycerol is added to water in order to raise the speed of sound from the level in water ( $1480 \text{ ms}^{-1}$ ) to the tissue level ( $1540 \text{ ms}^{-1}$ ). Rodanol® Benzalkoniumchloride is an antifungal agent added to prevent bacterial growth. The SiC powder is the main ingredient which adjusts backscatter. The two  $\text{Al}_2\text{O}_3$  powders adjust the attenuation to the level in soft tissue ( $0.5 \text{ dBcm}^{-1}\text{MHz}^{-1}$ ), and provide some backscattering too. Agar bonds all the ingredients together into a solid material. The relative proportion of the ingredients by weight is shown in Table 2.1.

*Table 2.1 : Composition of the tissue mimicking material (from Tierlinck et al. 1997).*

<b>TMM Ingredients</b>	<b>Weight proportion (%)</b>
Water	82.97
Glycerol	11.21
Rodanol® Benzalkoniumchloride	0.46
Agar	3.00
Al <sub>2</sub> O <sub>3</sub> - powder 3.0 µm	0.94
Al <sub>2</sub> O <sub>3</sub> - powder 0.3 µm	0.88
SiC - powder 400 grain	0.53

### **2.6.2 Specifications for the vessel phantoms**

Large vessel phantoms were constructed for use in conjunction with the scaled-up scanning system. It was desired to maintain a close proportion of resolutions and vessel dimensions between the system developed in this study and a typical IVUS system used for imaging human coronary and peripheral (femoral and iliac) arteries. The luminal diameters of human coronary arteries vary from 1.5 to 5.5 mm, with the mean values of the individual branches of the coronary tree being between 3 and 4 mm (Waller 1989a). The luminal diameters of femoral and iliac arteries range from 4 to 7 mm (mean 6 mm) and 8 to 10 mm (mean 8 mm) respectively (Gussenhoven et al. 1993a). According to the relative resolution figures mentioned in section 2.5.1, it was decided to construct vessel phantoms at approximately 6 to 8 times an average representative size of iliac, femoral and coronary arteries. Hence, the luminal diameter for the TMM vessel phantoms was chosen to be 45 mm.

Coronary and iliofemoral arteries are a muscular type of artery and their walls have a typical ultrasonic appearance which can be described as three-ringed, consisting of an inner echogenic, a middle echolucent and outer echogenic ring (Gussenhoven et al. 1989a; Lockwood et al. 1992; Potkin et al. 1990). It was desired

to simulate this three-ring ultrasonic appearance with the constructed vessel phantoms. The walls of the vessel phantoms were made of three layers, with the inner layer being echogenic, the middle 'relatively echolucent' and the outer echogenic.

The 'echolucent' material was achieved by varying the original recipe of the TMM. None of the scattering or attenuating powders (SiC and  $\text{Al}_2\text{O}_3$ ) were used for the 'echolucent' material. The only ingredients used were the liquids (water, glycerol and Rodanol®) and the agar. The latter ensured that the resulting structure was solid and not fluid, and did not introduce any significant backscatter.

The thickness of the media ranges between 157 to 304  $\mu\text{m}$  in normal coronary arteries (Waller 1989b) and between 600 to 800  $\mu\text{m}$  in normal iliofemoral arteries (Gussenhoven et al. 1993a). Proportionally, the thickness of the middle 'echolucent' layer in the constructed vessel phantoms was chosen to be 3.5 mm. The thickness of the inner and outer layer was 5 and 9 mm respectively. The TMM is quite delicate material when in thin layers. Hence, the outer layer was chosen much thicker than the other two layers, in order to protect the whole phantom structure from collapsing under its own weight and also to allow repeated use and handling.

### **2.6.3 Preparation of the vessel phantoms**

In order to make the echogenic layers and the stenoses, all the ingredients were mixed in a flask in the appropriate proportion by weight. The flask was tightly closed to prevent evaporation and placed in a water bath at about 96 °C temperature. The flask was kept in the bath for nearly two hours and the mixture was continuously stirred. Then the mixture was allowed to cool down to 42 °C, while still being stirred. After that, it was poured in a cylindrical mould to form the stenosis (if any) and the inner and outer wall layers. The mould consisted of a rod and two tubes concentrically aligned as shown in Figure 2.15a. The TMM was poured between the rod and the inner tube to form the inner wall layer and the stenosis (if any), and between the two tubes to form the outer wall layer. The rod and the tubes were

sprayed with lubricant oil so that the TMM did not stick to their surfaces. The mould was then air sealed and placed in the refrigerator for about two hours to solidify.

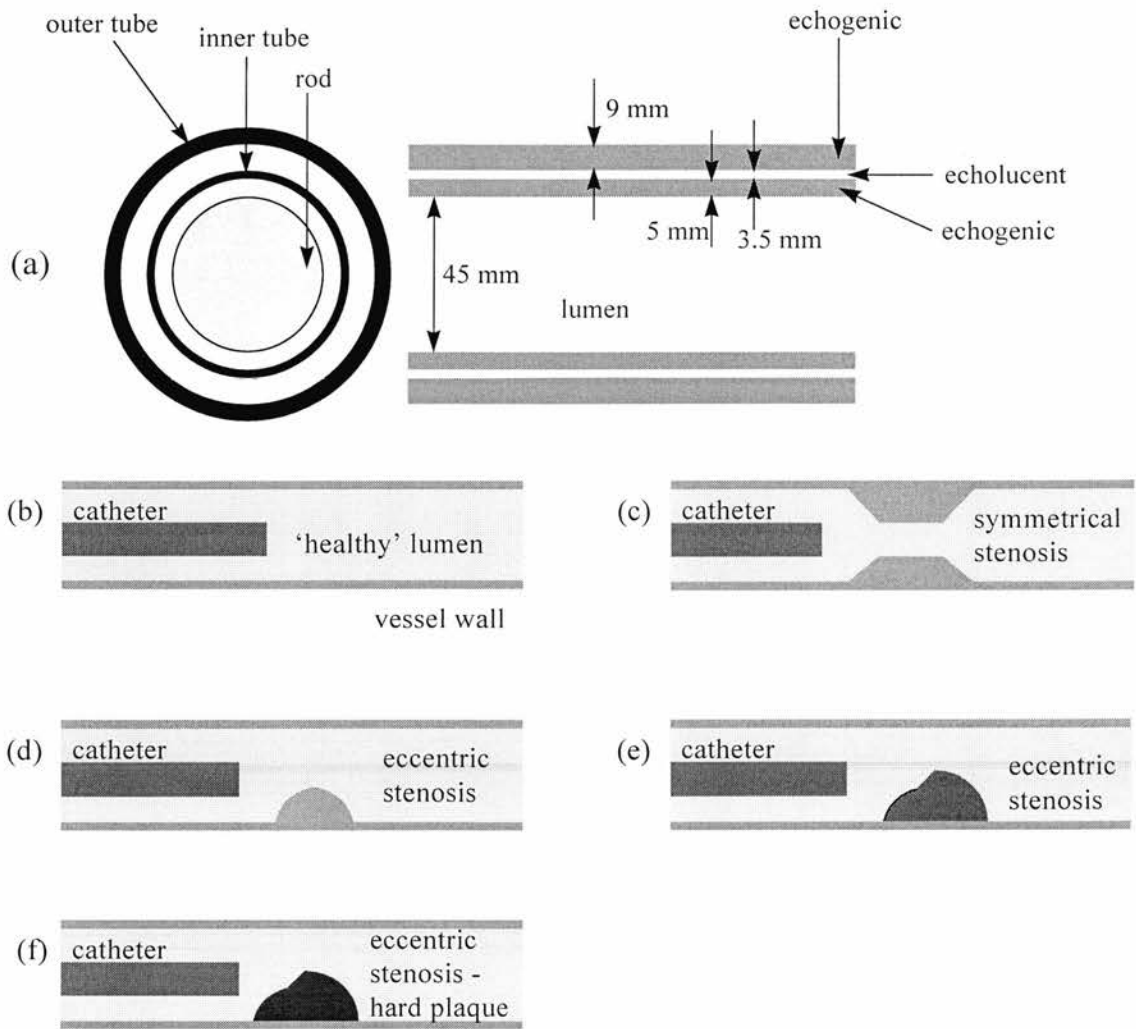


*Figure 2.15 : Vessel phantoms made of tissue mimicking material. (a) Diagram of the arrangement of the rod and the tubes used for moulding, along with wall structure and dimensions. (b) Diagram of the TMM phantom which simulates a healthy artery. (c) Simulation of a symmetrical cylindrical stenosis. (d) Simulation of a 'single hump' eccentric stenosis. (e) Simulation of a 'double hump' eccentric stenosis. (f) Same as in (e), but the stenosis is made of a more attenuating and scattering material in an attempt to mimic calcific plaque. Diagrams (b)-(f) also show a catheter inserted into the lumen of the vessel phantoms.*

The 'echolucent' material was prepared in a similar way to the original TMM. When the 'echolucent' material was at 42 °C and ready for pouring, the mould was taken from the refrigerator and the inner tube was removed with care. The 'echolucent' material was then poured into the place of the inner tube forming the middle wall layer. The mould was air sealed again and placed back in the refrigerator where it was left for several hours so that all the wall layers solidified together completely. After that, the rod and the outer tube were removed and the three layered vessel phantom was ready for use.

Phantoms mimicking a healthy vessel were made by using a solid rod of a constant diameter. When making phantoms to mimic stenosed vessels, rods made of two joined parts machined to a geometrical shape were used in order to form the stenosis (Figure 2.16). After solidification of all the materials, the two halves of these rods were removed from the opposite ends of the mould.

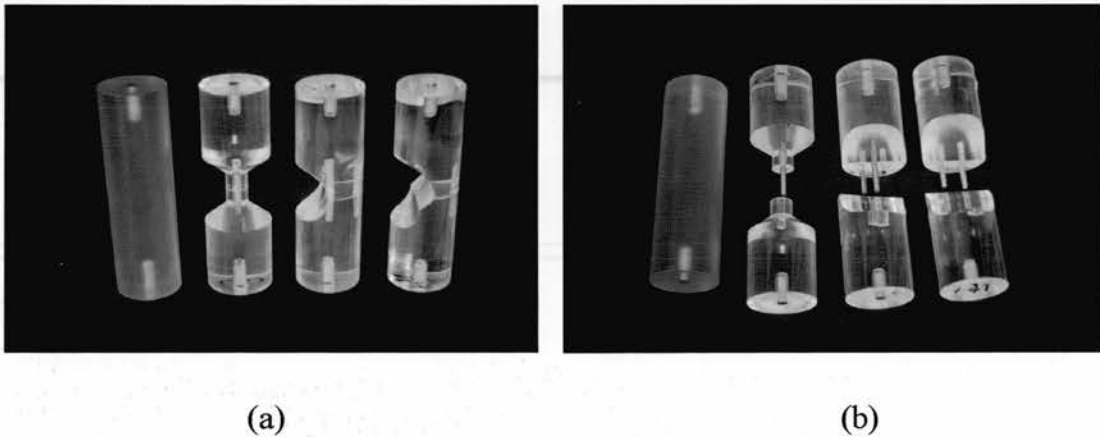


*Figure 2.16 : Rods used for moulding the TMM into vessel phantoms. The solid rod on the left part of the photographs is used for constructing the 'healthy' vessel phantom. The other rods, made from two joined parts, are used for constructing the stenosed vessel phantoms. Panel (b) shows these rods in 'exploded' view.*

Several shapes of stenoses were made and are shown in Figure 2.15. One of the vessel phantoms was constructed with a stenosis made from TMM with a 3-fold increased concentration of scattering and attenuating particles compared to the original recipe. This was an attempt to mimic the high level of reflection and acoustic shadowing seen in calcific plaques (Figure 2.15f).

The TMM used in this study has the tendency to swell when left in water, while it shrinks when in contact with air, outside water. Whenever the vessel phantoms were not placed in the water tank of the scanning system, they were stored in sealed containers in the refrigerator to prevent evaporation and deterioration. In this way, their useful life was extended to several months. During that time, the lumen diameter of the vessel phantoms, as measured by vernier calliper, did not deviate more than  $\pm 2\%$  from the manufactured size of 45 mm. At the end of their use, the vessel phantoms were cut into longitudinal and cross-sectional slices appropriate for photographs (Figure 2.17).

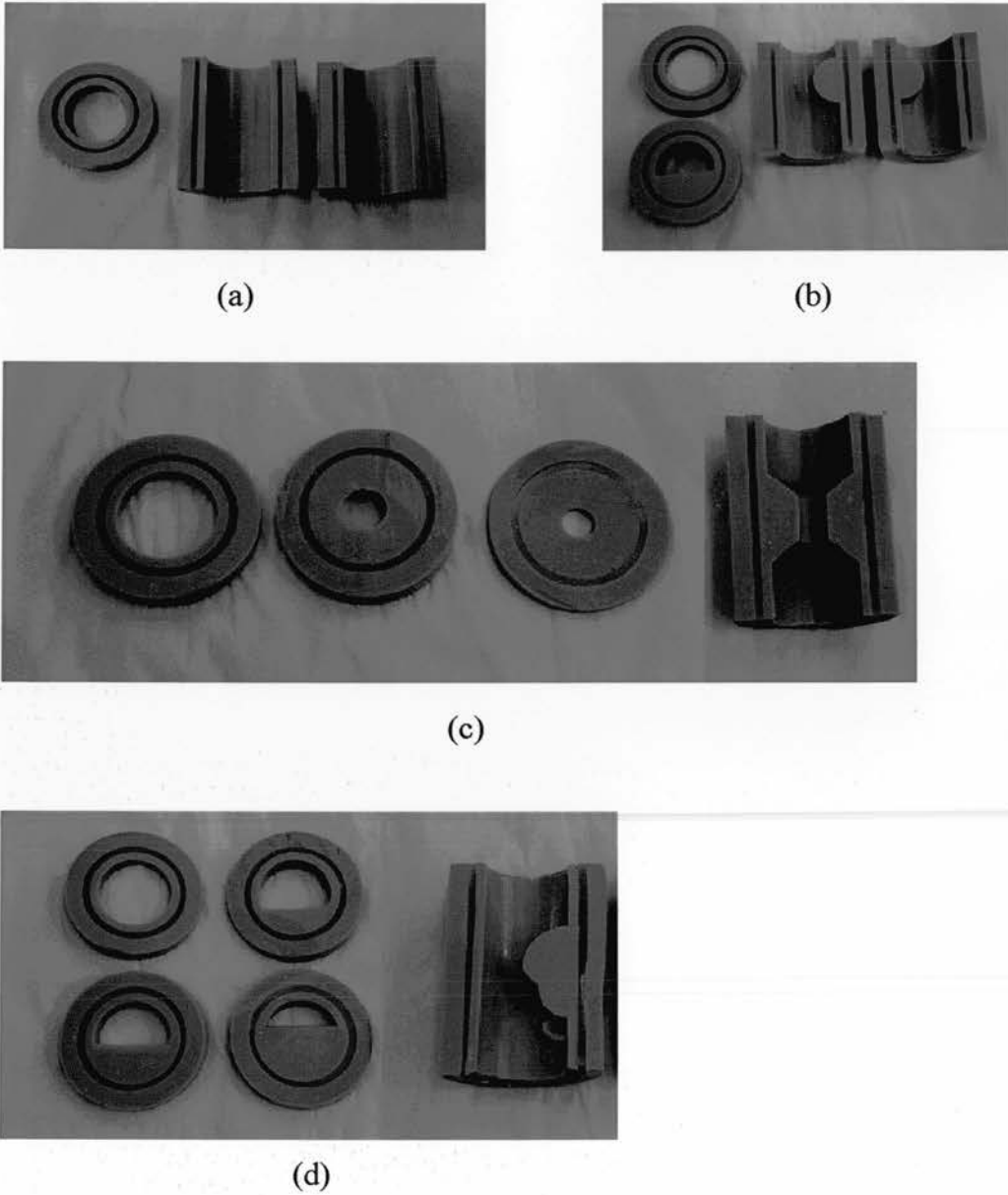


*Figure 2.17 : Photographs of longitudinal and cross-sectional slices of the various TMM vessel phantoms (not in scale). (a) 'Healthy' vessel phantom, (b) phantom with 'single hump' eccentric stenosis, (c) phantom with symmetrical cylindrical stenosis and (d) phantom with 'double hump' eccentric stenosis. The layered wall structure is evident in all slices of each phantom.*



## **CHAPTER 3**

### **EVALUATION OF THE EXPERIMENTAL SYSTEM**

#### **3.1 Introduction**

Chapter 2 described the design and development of a versatile mechanical scanning system for the implementation of a number of 3D scanning patterns for forward-viewing IVUS. Apart from the scanning system, the complete experimental set up also involved a data acquisition system and a software scheme for image production. These were also described in sections 2.5.3 and 2.5.4.

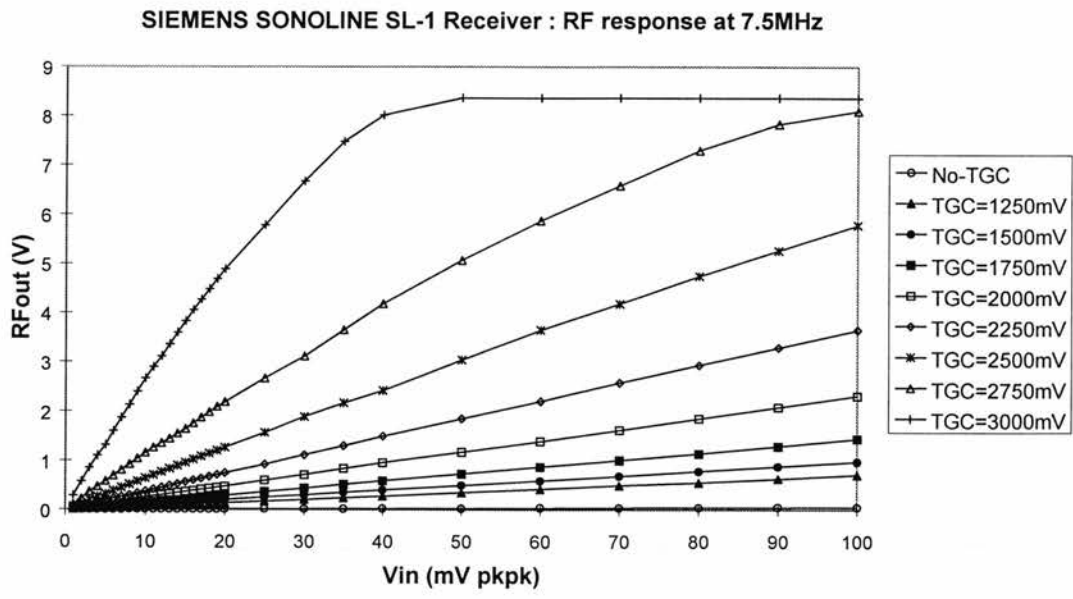
The current chapter evaluates the performance of various components of the experimental system. More specifically, the fidelity of the RF amplifier in the ultrasound scanner is examined in conjunction with the software procedure for producing frame images. The accuracy of the transducer motions provided by the scanning system is also assessed. Initial frame images acquired with the various scanning patterns are presented and system limitations are discussed.

#### **3.2 Linearity of the RF amplifier in the ultrasound scanner**

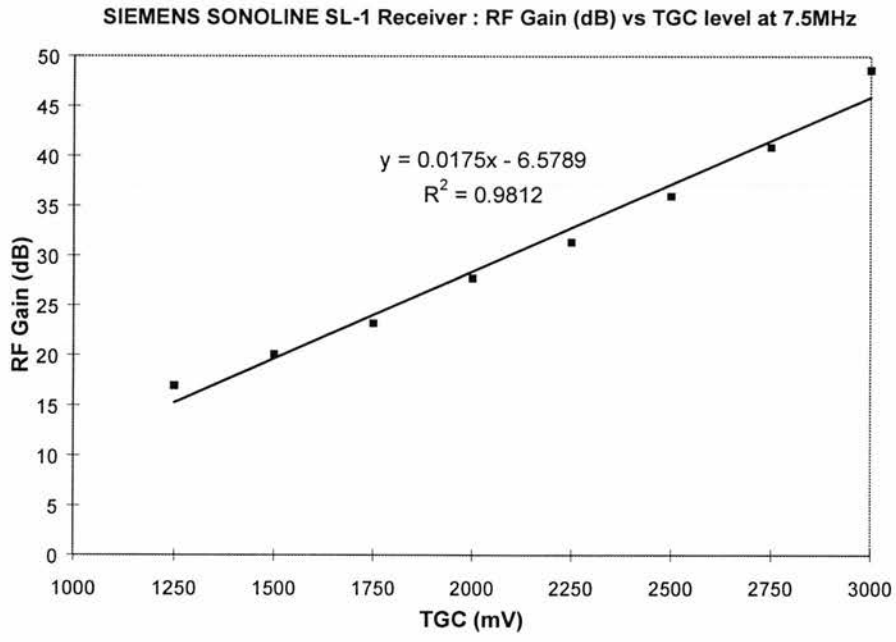
Since the system was based on processing the RF signal for producing and displaying images, it was important that the RF amplifier of the scanner had a linear response. In order to investigate this issue, sinusoidal signals of 7.5 MHz frequency and various amplitudes were fed into the M-mode input of the scanner. The amplified sinusoidal signals after the preamplifier stage, as well as at the RF output, were measured at different levels of externally applied TGC signal. The preamplifier has a

fixed gain, while the gain of the RF amplifier as a whole is determined by the voltage level of the applied TGC signal. The effective range of the TGC control signal for the Siemens Sonoline SL-1 scanner is between 0 and 3V.

From the measurements of the sinusoidal signals, the fixed amplification of the preamplifier stage was found to be approximately 17 dB. Knowing the amplification level at the preamplifier stage, it was possible to estimate the backscatter signal from the specific TMM by measuring the signal at the output of the preamplifier. For a variety of orientations and distances from the transducer face, the backscatter signals immediately after the transducer and before the preamplifier ranged up to 40 mV peak-to-peak. Thus, it was important that the RF amplifier of the scanner had a linear response at least for this range of input signals. Figure 3.1a shows the amplitude response of the scanner's RF amplifier for a range of sinusoidal input signals from 1 to 100 mV peak-to-peak, at different levels of TGC signal. It is clear that, with the exception of the highest TGC level which leads to early saturation, the amplitude response of the RF amplifier is linear (within 1%) for the above range of input signals. The relationship between the receiver gain in dB and the TGC level is also linear (within 1%) as shown by the interpolation line in Figure 3.1b. Hence, the RF amplifier of the particular scanner responds linearly both to externally applied TGC signals and to input signals which cover the range of the TMM backscatter.



(a)



(b)

*Figure 3.1 : (a) Amplitude response of the scanner's RF amplifier for a range of sinusoidal input signals of 7.5 MHz frequency, at different levels of TGC signal. (b) Gain of the RF amplifier as a function of the TGC signal, for an input signal of 13 mV peak-to-peak. A linear fit line is also shown.*

Based on the above observations, a distinction was expected between the different levels of backscatter arising from the echogenic and the 'echolucent' layers of the phantom wall. This was verified by observing an RF line penetrating the three-layered phantom wall. This line was part of a sector image obtained with the transducer inside the phantom lumen and the beam scanning a longitudinal plane. Figure 3.2a shows the segment of this RF line which corresponds to the phantom wall. The first part of the display (samples 0 to 300) is from the water path just before the phantom wall. The second part (samples 300 to about 2100) corresponds to the inner echogenic wall layer. Then samples 2100 up to about 3300 refer to the middle 'echolucent' layer and the remaining part of the RF line corresponds to the outer echogenic layer. It is clear that the echo from the 'echolucent' layer is much lower than the echoes from the two echogenic layers; in fact it is very close to the 'echo level' from water. It is also interesting to note that the echo level at the end of the inner layer is very similar to the one at the beginning of the outer layer. This distinction between the backscatter of the different layers is preserved throughout the successive stages of RF signal processing, namely the amplitude demodulation and the log-compression, as shown in Figures 3.2b and 3.2c respectively.

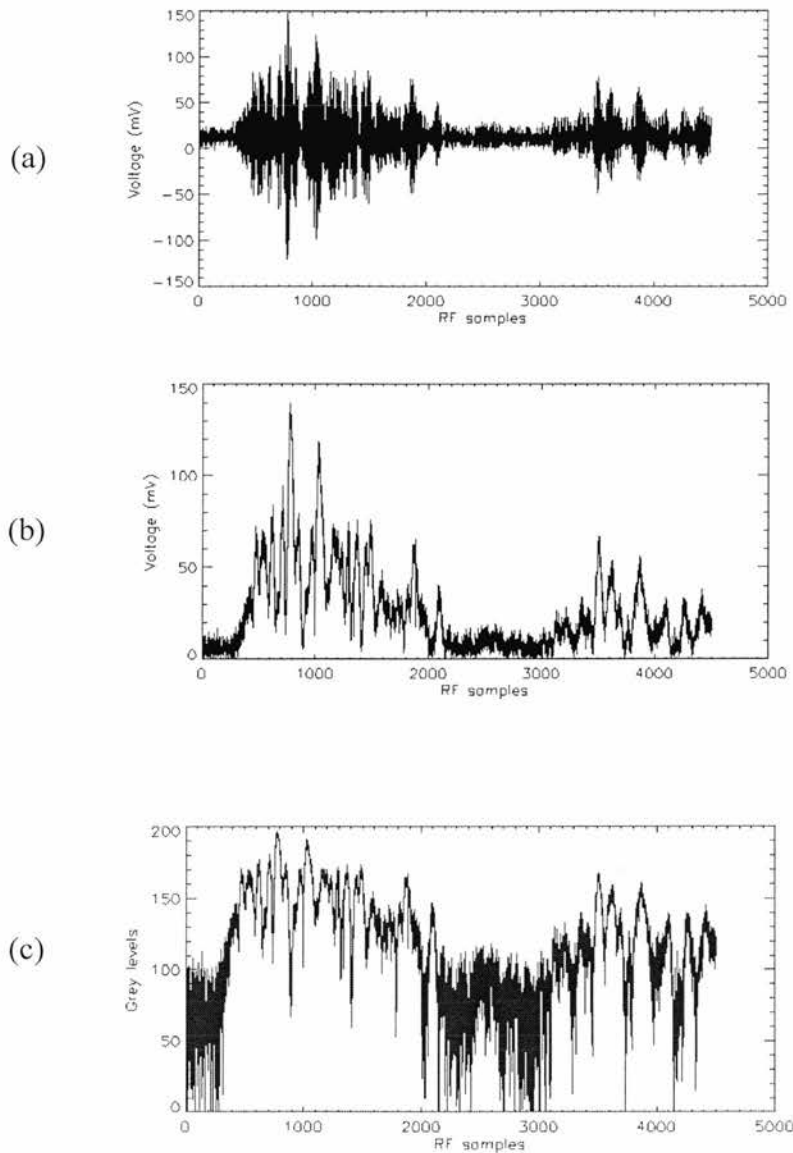


*Figure 3.2 : Echo signals corresponding to an ultrasonic line penetrating the three-layered wall of a TMM vessel phantom. (a) Received RF signal, (b) amplitude demodulated signal and (c) log-compressed signal. The first part of the display (samples 0 to 300) is from the water path just before the phantom wall. The second part (samples 300 to about 2100) corresponds to the inner echogenic wall layer. Samples 2100 up to about 3300 refer to the middle 'echolucent' layer and the remaining part of the RF line corresponds to the outer echogenic layer.*

### **3.3 Frame image production and display**

This section illustrates the sequence of RF signal software processing stages in the production of a frame image. The particular example used, refers to a sector image of the vessel phantom with the 'single hump' eccentric stenosis.

The display of the raw RF data frame (Figure 3.3a) is difficult to interpret, since the image has a dominant grey appearance due to the bipolar nature of the RF signal. The zero value of the signal corresponds to the middle of the grey level range, while negative values are displayed as darker levels and positive values as lighter levels. The rows of the rectangular image correspond to ultrasound lines. The shape of the structure can just be recognised, however it is clear that further processing is required in order to reach a meaningful display.

Similar comments apply to the display of the amplitude demodulated frame (Figure 3.3b). The signal is now unipolar with the zero value displayed as black level. The dynamic range of the demodulated signal exceeds that of the monitor display. As a result the top white levels of the display are allocated to the highest levels of the amplitude signal and the majority of the remaining signal levels are displayed at much fewer grey levels making it difficult to distinguish between them. The overall display on the screen looks somewhat darker than the RF frame, but it is still not any easier to detect tissue features and extract any meaningful information.

Logarithmic compression, by means of the natural logarithm  $y = \ln(x)$ , reduces the dynamic range of the signal to a level that can provide information for feature distinction and recognition of structure shapes. Such a log-compressed frame is shown in Figure 3.3c. The three layered wall structure can now be identified for the first time and a much better display of a stenosis in the lumen is available.

The final step is to scan convert this frame to a sector scan display. Sector scan conversion results in non-homogenous data density, leaving gaps in parts of the sector which need to be filled by interpolation. In the software approach followed in this study, the scan conversion was accomplished by relating the co-ordinates of each pixel in the sector image to co-ordinates in the rectangular image. Then the value of

the pixel in the rectangular image which was closest to the derived rectangular co-ordinates was allocated to the initial sector co-ordinates. In this way, all the pixels in the sector image were allocated a value and interpolation was accomplished. Figure 3.3d shows the sector scan converted image which corresponds to the rectangular image of Figure 3.3c. In the sector image the phantom walls appear parallel, as they actually are, the wall layers are distinguishable and the stenosis shape is clearly depicted.

This frame processing procedure is identical for the rotational and the fan scans. In the case of the conical and the spiral scans the sector scan conversion is not included and the frame processing ends in the rectangular display of the log-compressed image.

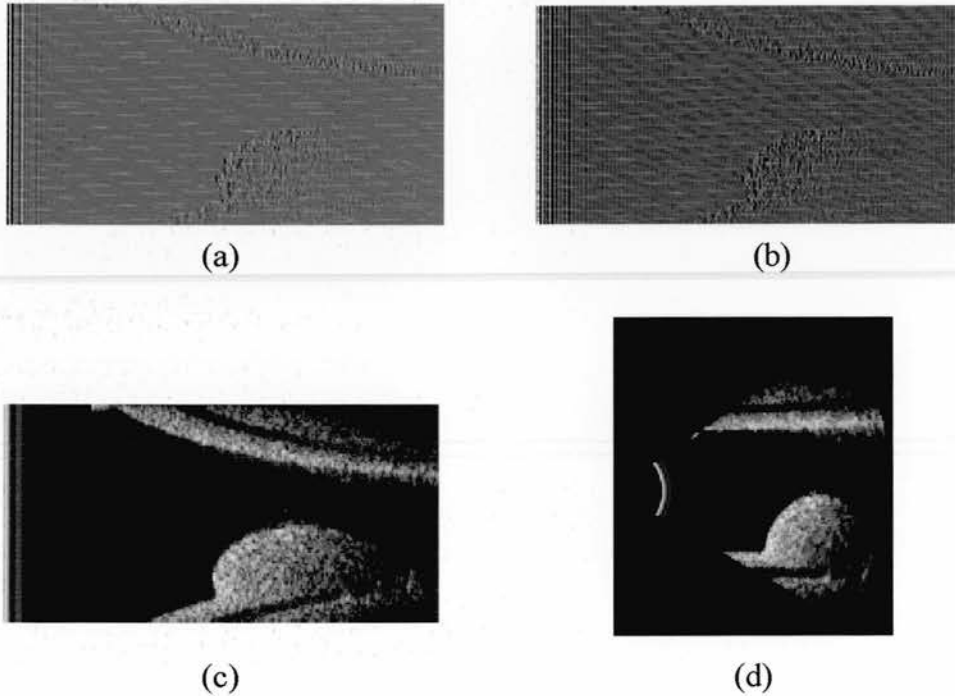


*Figure 3.3 : Software processing steps on an acquired RF frame in order to produce an image. (a) The acquired RF frame. The rows of the rectangular image correspond to ultrasound lines. (b) Amplitude demodulated frame. (c) Log-compressed image. This is the display format for the conical and spiral scans. (d) Sector scan converted image. This is the display format for the rotational and the fan scans.*

### 3.4 Geometrical accuracy of the scanning system

A crucial part of the overall system performance is that of the mechanical scanning system which implements the scanning patterns. The parameters needed to be evaluated were the accuracy of the transducer sweep motions controlled by motors SM1 and SM2 and the accuracy of the transducer rotation controlled by motor SM3 (Figure 2.8).

#### 3.4.1 Accuracy of the transducer sweep motions

A nylon filament phantom was used for assessing the accuracy of the sector scans by SM1 and SM2. This phantom was made of two flat perspex plates held parallel to each other and a number of nylon filaments connected at normal angles to these plates. The filaments were arranged on the surfaces of three imaginary concentric cylinders, at  $15^\circ$  angular steps. The cylinders' radii were 2, 4 and 6 cm, starting from the inner to the outer. There was also an additional filament which connected the common centres of the circles on the two plates. Schematic diagrams of this phantom are shown in Figure 3.4.

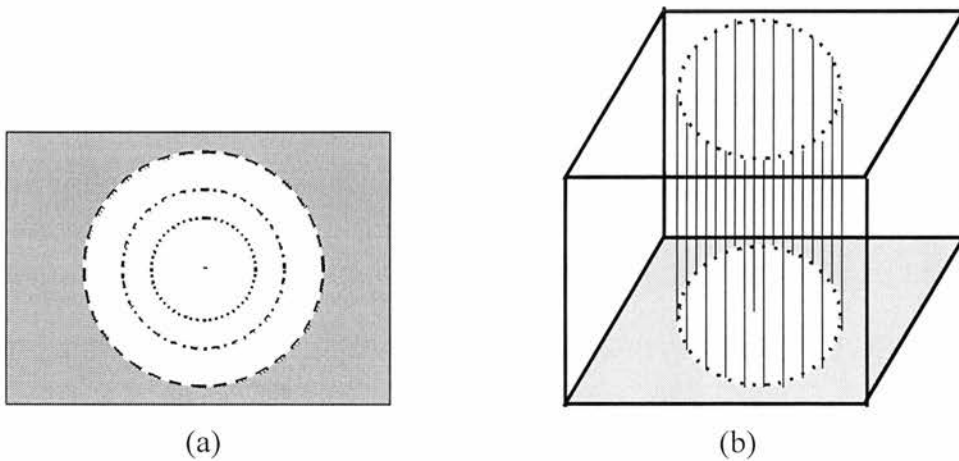
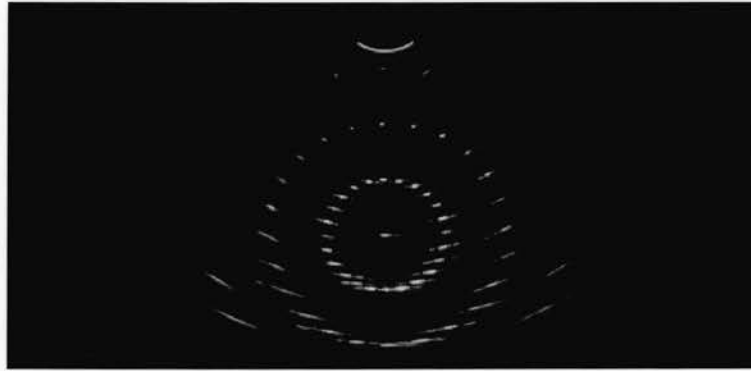


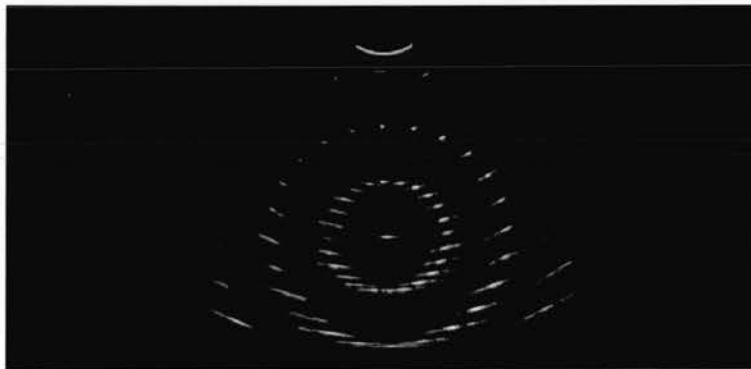
*Figure 3.4 : Nylon filament phantom used for assessing the accuracy of the sweep motions of the transducer. (a) Top schematic view, (b) schematic diagram where only one cylindrical surface is shown for clarity.*



The nylon filament phantom was placed in front of the transducer face in the water tank and a sector scan was performed with the aid of motor SM1, such that the scan plane was a cross-section of the cylindrical structure. The sector image was reconstructed according to the previously described procedure and is shown in Figure 3.5a. Similarly, a sector scan was performed by SM2 and the corresponding sector image is shown in Figure 3.5b. The field of view in these sector images includes the two inner circles and part of the outer circle.



(a)



(b)

*Figure 3.5 : (a) Image of the nylon filament phantom acquired with a sector scan performed by SM1, where the scan plane was a cross-section of the cylindrical structure. (b) Image acquired with a sector scan performed by SM2 in the same way as in (a).*

The 'design' diameters for the small and the large inner circle were 4 and 8 cm respectively. Measured diameters on the image of Figure 3.5a varied within  $\pm 2.5\%$ , from 3.9 to 4.1 cm for the small circle and from 7.8 to 8.1 cm for the large circle. Similar diameter sizes were also measured on the image of Figure 3.5b. Thus, the circular shapes of the phantom structures and their dimensions were well preserved in both sector images, evidence of the geometrical accuracy of the sweep motions of the scanning system.

In addition, these sector images provide information about the resolution of the scanning system. Resolution in the focal zone of the transducer is demonstrated by the echoes in the top arc of the large inner circle. The length of these echoes (axial resolution) was measured approximately 0.5 mm, while their width (lateral resolution) approximately 1 mm. Similarly, at the far end of the sector images, at distances 9 and 10 cm from the transducer face, the axial resolution was measured approximately 0.5 mm (for both distances), while the lateral resolution approximately 6 and 7.5 mm respectively. At these distances, the lateral resolution is degraded so much that neighbouring filaments cannot be resolved.

### **3.4.2 Accuracy of the transducer rotation**

The accuracy of the rotational motion of the transducer was assessed by scanning the TMM vessel phantom which simulated a healthy vessel. This phantom had a constant inner diameter. Thus, if the catheter was placed parallel to the long axis of the phantom and exactly in the centre of the lumen, the phantom wall should be at equal distances from the transducer face throughout a  $360^\circ$  rotation. For the assessment test, the catheter was placed as closely as possible in the centre of the lumen and parallel to the long axis of the phantom. The transducer beam was directed at a  $30^\circ$  angle to the long axis of the vessel phantom and rotated over  $360^\circ$ , exactly as in the case of acquiring a frame for the conical or the spiral scan. The acquired frame was processed according to the procedure described previously (in sections 2.5.4 and 3.3) and displayed as a rectangular image. This frame is shown in Figure 3.6, where

rows of the image correspond to ultrasound lines. Measured distances of the inner wall (at the middle part of the image) from the transducer face (bright line at the left part of the image) were equal within 3.3% over the full 360° rotation, and the three wall layers appear parallel to each other. This was taken as evidence of accurate transducer rotation by motor SM3.

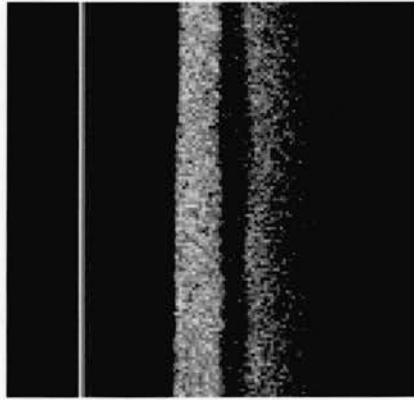


*Figure 3.6 : Reconstructed image of a conical surface scan of the 'healthy vessel' phantom providing evidence of accurate transducer rotation.*

### **3.5 Display of frames acquired with the various scanning patterns**

Having assessed the accurate performance of the experimental system, the set of TMM vessel phantoms constructed for this study were scanned. The slide potentiometers in the external TCG circuit were set for optimising the visualisation of the stenoses, if possible their complete extent, while keeping the noise in the images at reasonable levels. Sets of acquired frames are shown in sections 3.5.1 to 3.5.4 for the conical, the spiral, the rotational and the fan scans for the phantom simulating a vessel with a 'single hump' eccentric stenosis (Figure 2.15d). Frames of the conical and the spiral scans, although acquired as conical surfaces, are displayed as rectangular images for simplicity and easier understanding of the scanned features. The frames of the rotational and fan scans are displayed as sector images, exactly as they are acquired.

### **3.5.1 Frames acquired with the Conical scan**

During a pull-back conical scan, the first frame is the closest to the stenosis and the last one is the furthest away. The early frames provide the most information about the stenosis ahead of the catheter, while the subsequent ones display information about the proximal 'healthy' part of the vessel. All the frames image the vessel wall as in the current side-viewing IVUS systems (Figure 3.7).

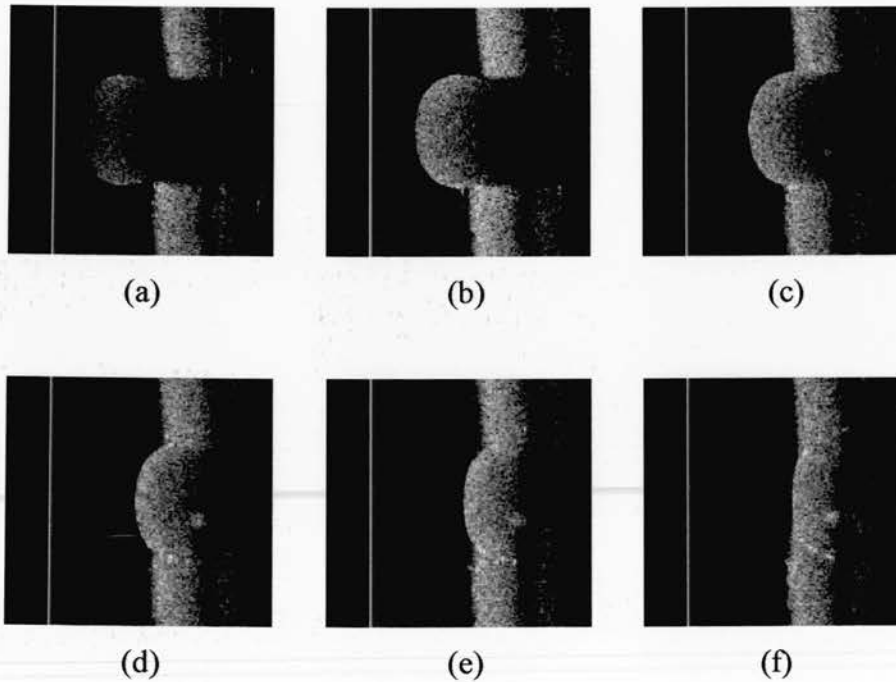


*Figure 3.7 : Series of frames acquired during a pull-back conical scan of the phantom simulating a vessel with an eccentric stenosis. Frame (a) is the closest to the stenosis and frame (f) is the furthest away from the stenosis. All the frames image the vessel wall.*

### **3.5.2 Frames acquired with the Spiral scan**

The spiral scan acquires frames with the catheter at a fixed position with respect to the vessel. The early frames provide information about any stenosis located at or near the centre of the lumen but no information about the vessel wall. As the ultrasound beam deviates from the long axis of the vessel, information about the vessel wall appears in the display progressively, while the information about the stenosis lying ahead reduces (Figure 3.8).

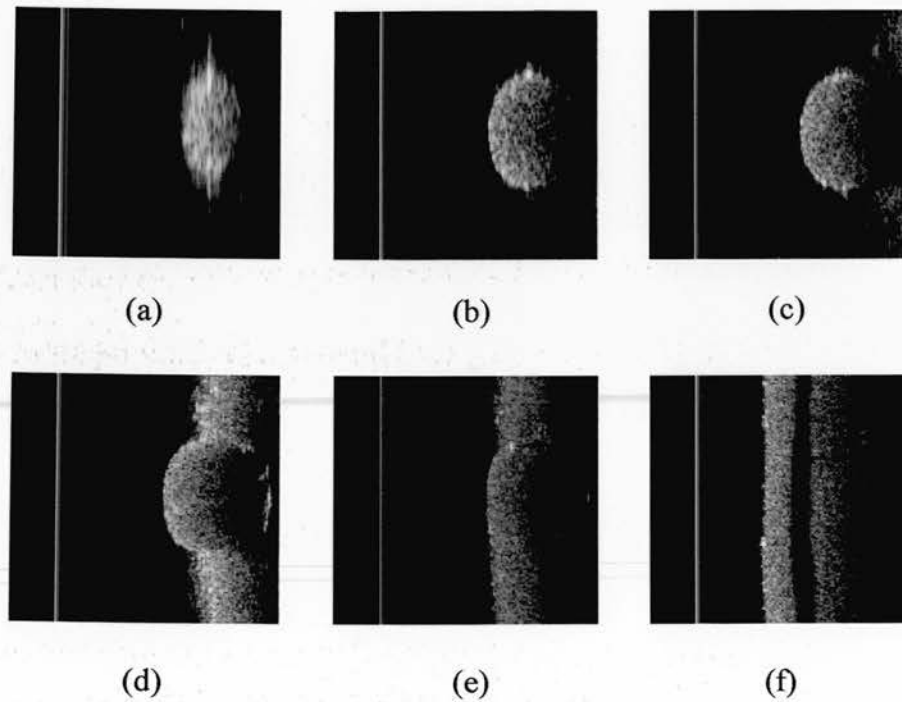


*Figure 3.8 : Series of frames acquired during a 3D **spiral scan** of the phantom simulating a vessel with an eccentric stenosis. Frames (a) and (b) image the stenosis only. Frames (c) and (d) image both the vessel wall and the stenosis, while frames (e) and (f) image the vessel wall only.*

### **3.5.3 Frames acquired with the Rotational scan**

The rotational scan also acquires frames with the catheter at a fixed position with respect to the vessel. Irrespective of the frame angular orientation, the displayed image includes information about the vessel wall and any stenosis present at the central or the side parts of the lumen. It is in fact a longitudinal image of the vessel at any particular angular orientation (Figure 3.9).

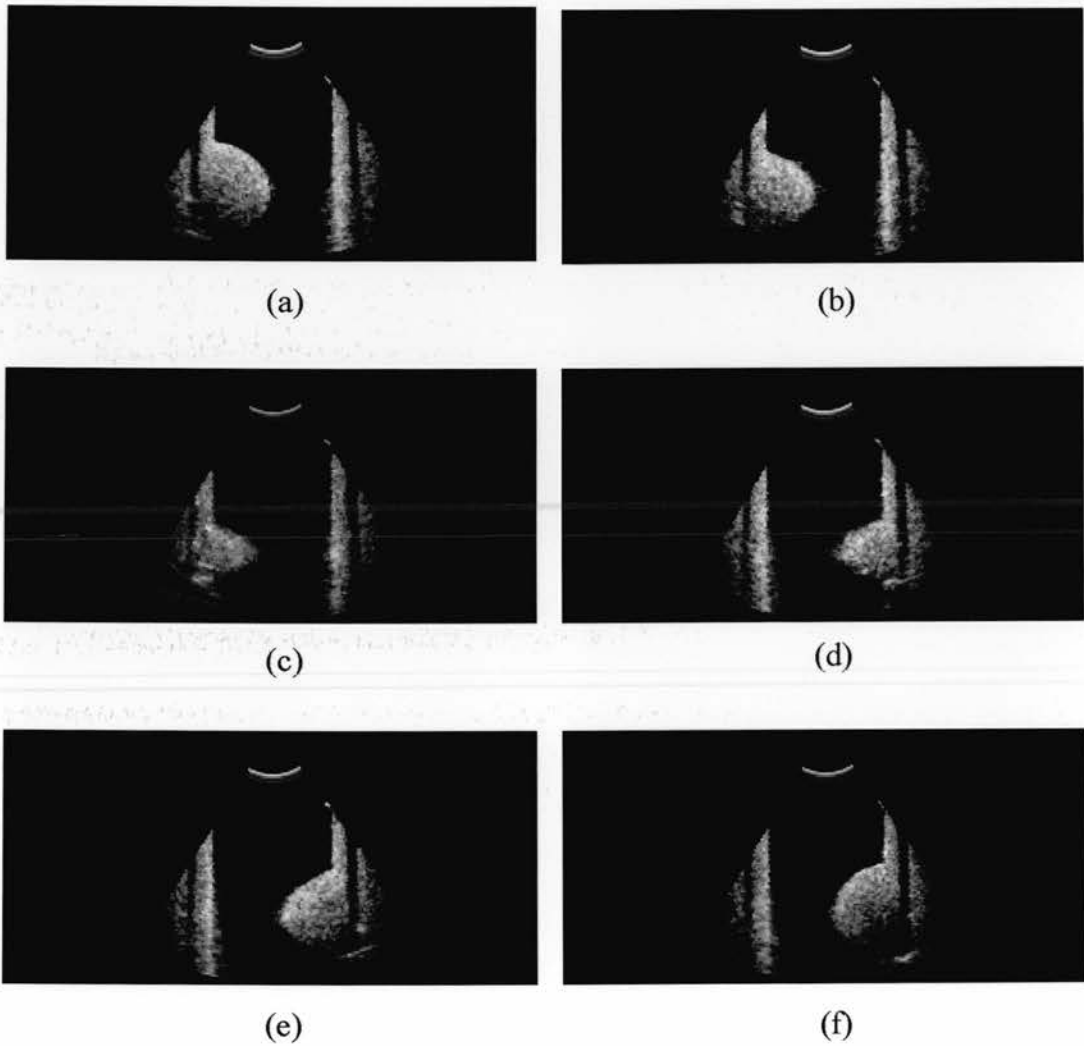


*Figure 3.9 : Series of frames acquired during a 3D **rotational** scan of the phantom simulating a vessel with an eccentric stenosis. Each frame is a longitudinal image of the phantom at the particular angular orientation of the catheter.*

### 3.5.4 Frames acquired with the Fan scan

The fan scan acquires frames with the catheter at a fixed position with respect to the vessel as in the case of the spiral and the rotational scans. The first frames display information about the vessel wall, and as the orientation of the acquisition frame progressively approaches the centre of the lumen, any existing stenosis appears on the display. Then the frame orientation starts to deviate from the lumen centre heading again for the vessel wall (Figure 3.10).

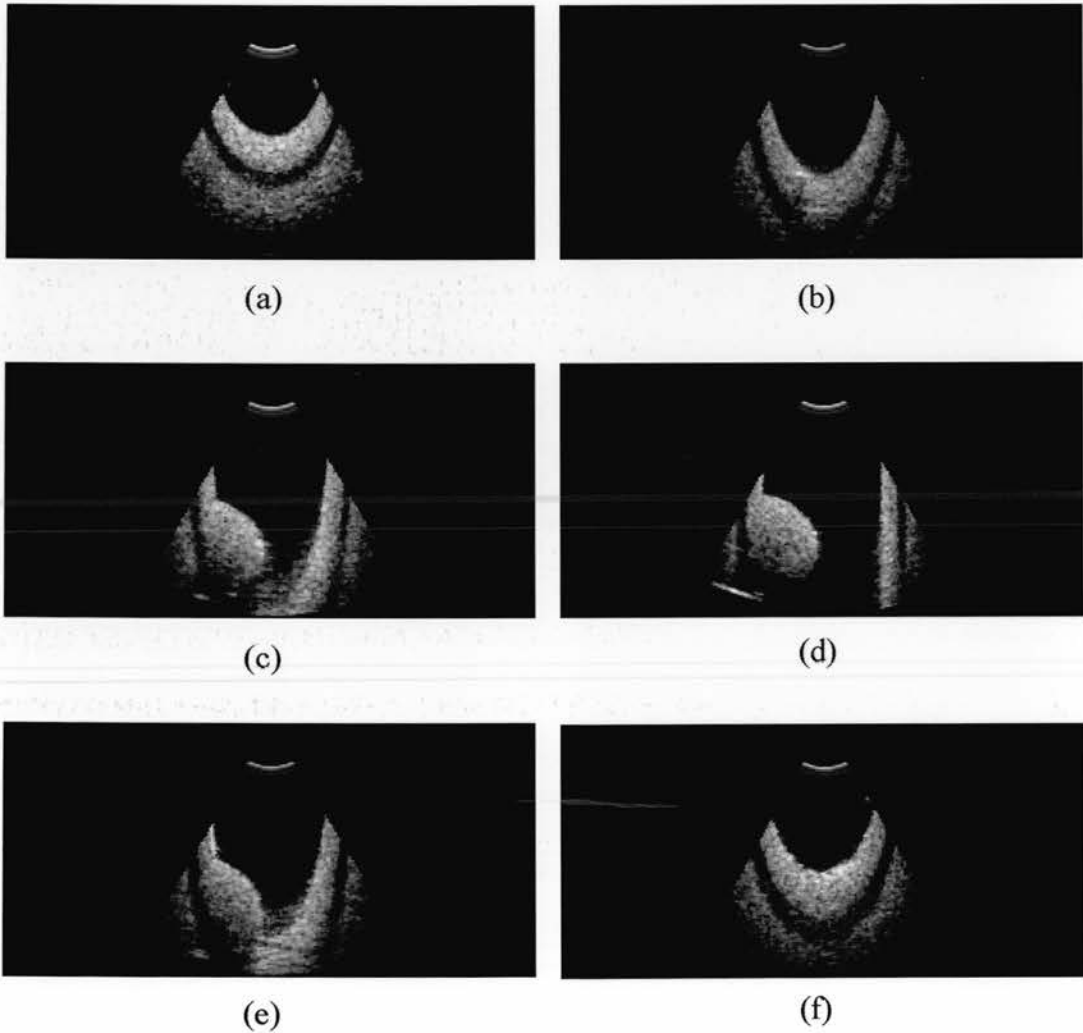


*Figure 3.10 : Series of frames acquired during a 3D fan scan of the phantom simulating a vessel with an eccentric stenosis. Frames (a), (b) and (f) image the vessel wall only. Frames (c), (d) and (e) image the stenosis as well as the vessel wall.*

## **3.6 System limitations**

### **3.6.1 Non-real-time operation**

The major limitation of the experimental system is that it cannot acquire and display in real-time. This restriction is imposed both by the mechanical scanning system as well as by the RF signal software processing scheme. The approach to construct a scanning mechanism that can move the transducer in any desired direction, introduced a compromise right from the outset. A dedicated system designed to scan in a fixed mode can be made to scan rapidly and work on a real-time basis. However, a versatile system which is required to scan in all directions, be reliable and accurate without suffering mechanical failures, involves a very delicate construction. The fact that the implementation is based on the use of pulling wires and on a sensitive mechanism of levers which move a sphere on which the transducer is mounted, demands a slow scanning speed in order to ensure long life for the wires and lever mechanism. It takes a few seconds to scan a single frame and consequently a few minutes (approximately 10 for the rotational scan) to complete a 3D volume acquisition. Furthermore, the system does not display images directly on a scanner's monitor. Instead, software is used for processing a large amount of RF data off-line in order to reconstruct and display the final image on a PC window. Each processed ultrasound line can be 10000 to 13000 samples long, depending on the desired depth for the field of view. In the case of the rotational scan for example, it takes approximately 30 seconds to perform all the described processing stages for the number of lines (110) of that length which compose a frame. Consequently, for the reconstruction of a volume consisting of 100 frames, 50 minutes are required.

As stated, the main objective was to build a versatile system that could be used *in vitro* for examining and assessing the potential of several 3D forward-viewing IVUS scanning patterns. Real-time performance was not set as a target, simply because at that stage the work was geared towards the understanding and evaluation of the scanning techniques. The use of TMM vessel phantoms *in vitro* did



not impose the time requirements of an *in vivo* examination. The phantoms did not change shape nor degraded during the time needed for a volume acquisition.

### 3.6.2 Field of view

A second limitation of the system is that the angular size of the field of view is not as large as those reported previously for forward-viewing IVUS systems (Evans et al. 1994, Ng et al. 1994). The system can provide a maximum of  $72^\circ$  sector image. This angle could have been larger, up to  $90^\circ$ , if only one sweep motion of the transducer had been required, i.e. only one of the two actions performed by motors SM1 and SM2. Because of the requirement to perform both of these sweep motions and consequently the need to include two lever mechanisms at the scan head, the space for free motion of the mechanical assembly at the catheter tip is limited. In the case of the rotational scan, the sector angle is further reduced to  $66^\circ$  to minimise fatigue in the pulling wires from repeated use. Moreover, in the fan scan the two sweep angles are even smaller:  $58^\circ$  and  $62^\circ$ . This can be explained by reference to Figure 3.11.

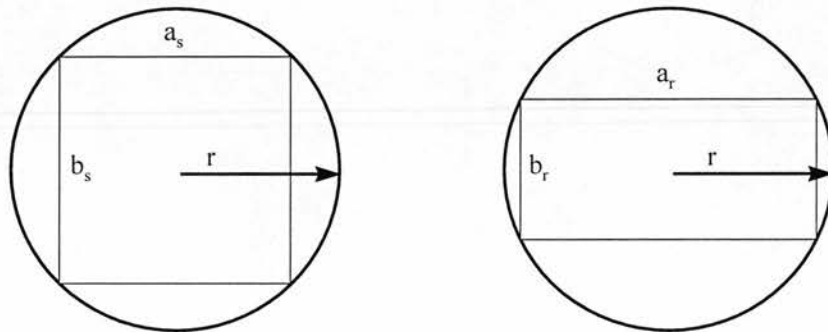


*Figure 3.11 : Explanation of the sweep angle limitations for the fan scan. When attempting to fit a square in a circle, the sides of the square ( $a_s$  and  $b_s$ ) are smaller than the diameter of the circle ( $2r$ ). When trying to fit a rectangle, its length ( $a_r$ ) can be close to the diameter size, however the width ( $b_r$ ) becomes correspondingly smaller.*

By relating the circle to a slice of the sphere on which the transducer is mounted, and the square or rectangle to the base of the pyramidal volume scanned by the fan scan, it is easy to imagine that the diameter  $2r$  corresponds to the maximum scan angle of the device and the sides ( $a_s$ ,  $b_s$ ) or ( $a_r$ ,  $b_r$ ) correspond to the two angles of the transducer sweep motions. Thus possible options include scanning a pyramidal volume with nearly equal angles (e.g.  $58^\circ$  and  $62^\circ$ ) or with very different angles (e.g.  $72^\circ$  and  $35^\circ$ ). It was decided to try and keep the pyramidal base close to a square shape, therefore the first of the above options was preferred.

### **3.7 Summary**

The construction and evaluation of an experimental scaled-up system, capable of implementing a number of scanning patterns for 3D forward-viewing IVUS imaging, have been described. The system makes use of the RF signal for off-line image reconstruction and display on a PC. Vessel phantoms made from tissue mimicking material are used to simulate healthy and stenosed arteries. The phantoms have a layered wall structure similar to that of human coronary arteries. The mechanical scanning system is accurate, preserving the geometry of the scanned objects, while the processing of the RF signal, initially by the RF amplifier and subsequently by software, enables accurate image reconstruction and display. The frame images initially acquired with the different scanning patterns, are of adequate quality to allow discrimination of the different layers at the phantom walls and appreciation of the stenoses' shapes. These images were an encouraging step to proceed towards the use of the various scanning patterns for 3D imaging.

## **CHAPTER 4**

# **IMAGE QUALITY OF THREE DIMENSIONAL FORWARD-VIEWING IVUS SCANNING PATTERNS**

### **4.1 Introduction**

The previous two chapters described the experimental scanning and imaging system and assessed its performance in acquiring, reconstructing and displaying frame images of vessel phantoms. The current chapter refers to the three dimensional issues of the system and presents images from 3D data sets acquired with the different scanning patterns under investigation. These data sets provide the basis for assessing the image quality achieved by these scanning patterns and allow comparative conclusions to be derived.

### **4.2 Three dimensional image reconstruction**

As described in section 2.5.4, image reconstruction and display are based on software processing of the RF signal sampled at the output of the scanner's receiver. This procedure is applied to the set of frames acquired during a volume scan, leading to a set of demodulated log-compressed images. For 3D reconstruction, the concept of two co-ordinate systems is used. Acquired data belongs to the source co-ordinate system  $\{B\}$ , while reconstructed data is in co-ordinate system  $\{A\}$ , referred as voxel space. During the 3D reconstruction procedure, the demodulated log-compressed

images are transformed from {B} to {A}, via translational and rotational operations. In the specific implementation of this study, the origins of {A} and {B} are identical and regarded as the centre of the sphere in the scanning head (section 2.4). The resolution of the voxel space is the same as the resolution of the frame images. In other words, the voxel can be regarded as a cube with dimensions equal to the pixel dimensions.

#### **4.2.1 Three dimensional reconstruction of the Conical and Spiral scans**

The demodulated log-compressed lines of each frame acquired with the conical or the spiral scan, are arranged at the specified angular steps of  $2.88^\circ$  onto conical surfaces in voxel space. In the case of the conical scan, these surfaces are of fixed cone angle ( $30^\circ$ ) and are translated to their appropriate positions in voxel space. As regards the spiral scan, the conical surfaces are placed at a fixed location in voxel space and their cone angle is varied (from  $1.2^\circ$  to  $72^\circ$ ).

#### **4.2.2 Three dimensional reconstruction of the Rotational and Fan scans**

The 2D sector images acquired with the rotational or fan scan are transformed from {B} to {A} by means of a transformation matrix  $T$  as described by Craig (1989). The whole transformation procedure is implemented as

$${}^A P = T \cdot {}^B P \quad (4.1)$$

where  ${}^A P$  is the position vector holding image point co-ordinates in voxel space {A},  $T$  is the transformation matrix and  ${}^B P$  is the position vector holding image point co-ordinates in source system {B}. In more detail equation (4.1) is written as

$$\begin{bmatrix} {}^A P_x \\ {}^A P_y \\ {}^A P_z \\ 1 \end{bmatrix} = \begin{bmatrix} R_{11} & R_{12} & R_{13} & D_x \\ R_{21} & R_{22} & R_{23} & D_y \\ R_{31} & R_{32} & R_{33} & D_z \\ 0 & 0 & 0 & 1 \end{bmatrix} \cdot \begin{bmatrix} {}^B P_x \\ {}^B P_y \\ {}^B P_z \\ 1 \end{bmatrix} \quad (4.2)$$

where  $R_{ij}$  are components of a matrix  $R$  representing rotations around the axes of  $\{A\}$ , and  $D_i$  are the components of the translation vector between the origins of  $\{A\}$  and  $\{B\}$ .

As mentioned above, the origins of  $\{A\}$  and  $\{B\}$  are identical, therefore all  $D_i$  are equal to zero. The sector images are firstly rotated around the X-axis of  $\{A\}$  by an angle  $\alpha$ , then around the Y-axis of  $\{A\}$  by an angle  $\beta$  and finally around the Z-axis of  $\{A\}$  by an angle  $\gamma$ . By adopting  $c\alpha$ ,  $c\beta$ ,  $c\gamma$ ,  $s\alpha$ ,  $s\beta$  and  $s\gamma$  as shorthand for  $\cos(\alpha)$ ,  $\cos(\beta)$ ,  $\cos(\gamma)$ ,  $\sin(\alpha)$ ,  $\sin(\beta)$  and  $\sin(\gamma)$  respectively, the matrix  $R$  is described as

$$R = R_z(\gamma) \cdot R_y(\beta) \cdot R_x(\alpha) = \begin{bmatrix} c\gamma & -s\gamma & 0 \\ s\gamma & c\gamma & 0 \\ 0 & 0 & 1 \end{bmatrix} \cdot \begin{bmatrix} c\beta & 0 & s\beta \\ 0 & 1 & 0 \\ -s\beta & 0 & c\beta \end{bmatrix} \cdot \begin{bmatrix} 1 & 0 & 0 \\ 0 & c\alpha & -s\alpha \\ 0 & s\alpha & c\alpha \end{bmatrix} \quad (4.3)$$

or finally as

$$R = \begin{bmatrix} c\beta c\gamma & s\alpha s\beta c\gamma - c\alpha s\gamma & c\alpha s\beta c\gamma + s\alpha s\gamma \\ c\beta s\gamma & s\alpha s\beta s\gamma + c\alpha c\gamma & c\alpha s\beta s\gamma - s\alpha c\gamma \\ -s\beta & s\alpha c\beta & c\alpha c\beta \end{bmatrix} \quad (4.4)$$

In the case of a conical volume acquired with the rotational scan, the angles  $\alpha_i$ ,  $\beta_i$ , and  $\gamma_i$  (in degrees) of rotation of frame  $i$  around the axes of system  $\{A\}$  are

- $\alpha_i = 0$
- $\beta_i = \left(i - \frac{N}{2}\right) \cdot d\theta$
- $\gamma_i = 90$

where  $N$  is the total number of acquired frames and  $d\theta$  is the angular step between rotated frames.

Similarly, for a pyramidal volume acquired with the fan scan, the angles (in degrees) of rotation of frame  $i$  around the axes of system  $\{A\}$  are

- $\alpha_i = \left(i - \frac{N}{2}\right) \cdot d\theta$
- $\beta_i = 90$

- $\gamma_i = 90$

where  $d\theta$  is now the angular step between swept sector frames and  $N$  is again the total number of acquired frames.

#### **4.2.3 Three dimensional reconstruction of the Compound scan**

The procedure for reconstructing a compounded volume is initially broken down to individual reconstructions of the 'component' volumes acquired at different catheter locations in the phantom lumen. The methods described in the previous two sections are used in this initial stage, according to what scanning pattern has been used for acquiring the component volumes. After that, there is an additional translational stage imposed on those component volumes which were acquired at eccentric catheter locations. This stage accounts for the offset from the concentric catheter location.

#### **4.2.4 Interpolation**

During the 3D reconstruction procedure, some voxels receive values from one or more frames. In the case of single contribution to a voxel from one frame only, the assigned voxel value is the pixel value from that frame. In the case of multiple contributions from more than one frame, the mean of the contributing pixel values is assigned as the final voxel value.

On the other hand, there are some voxels left with no assigned data values by the reconstruction procedure. These are treated as 'gaps' and are filled by interpolation. The interpolation algorithm used in this work fills the gaps with the mean value of the ultrasound data voxels lying in a local cubic neighbourhood centred around the gap. The size of the neighbourhood is initially 3x3x3 voxels. If no ultrasound data voxels are enclosed in it, the cube size is increased to 5x5x5, then to 7x7x7 etc., until at least one data voxel is enclosed (Barry et al. 1997; McCann et al. 1988; Nelson and Pretorius 1997).

### **4.3 Image display**

Three display formats have been used in this work: (a) volume visualisation, (b) display of 2D slices and (c) lumen cast display.

#### **4.3.1 Volume visualisation**

Two common techniques used for direct display of 3D medical data are *surface rendering* and *volume rendering* (Barillot 1993). Both of them project the volume data on a 2D display plane. Their relative merits and drawbacks depend on the specific application (Nelson and Elvins 1993; Udupa and Herman 1989).

Surface rendering operates on the principle that there are identifiable objects in the 3D data which are appropriately represented by their surfaces. Object surfaces are explicitly formed prior to creation of the display. Surface rendering uses only part of the 3D data for generating the display, in particular, only the data which belongs to the displayed surface. For this reason it is faster than volume rendering. This technique though, suffers from problems such as false positive and negative surface pieces, gaps in the surface and poor visualisation of small features.

Volume rendering makes use of the complete 3D data set in order to produce the display, therefore it is computationally more demanding than surface rendering. Object surfaces are not explicitly computed in this case. Each voxel in the 3D data set is assigned colour and opacity values, and contributes to the colour of the final image. The most common method of volume rendering is the *ray casting*. This involves a number of rays fired from a source point (the *eye*), through the volume, towards a display plane (the *screen*). One ray is fired for each pixel of the display *screen*. The colour and opacities of the voxels encountered by each ray are blended to produce the colour of the relative pixel on the *screen*. Volume rendering is suitable for visualising poorly defined objects such as diffuse structures. It creates a semitransparent display that permits visualisation of the inner volume structures which lie under outer surface layers.



It is this last specific property which makes volume rendering appealing in this study, where it is desired to visualise the stenosis located in the central part of the vessel phantom, underneath the different layers of the phantom wall. The reconstructed 3D data sets are visualised using the volume rendering facilities of IDL software package (Research Systems, Boulder, Colorado, USA). The average projection method is used, which assigns as final value of each pixel in the display image the average of the values of the voxels encountered by the corresponding rays. A number of volume rendering images are displayed in different orientations in space in order to enable a number of views which provide a comprehensive appreciation of the morphology of the stenosis in the phantom lumen.

#### **4.3.2 Display of two dimensional slices**

The reconstructed volumes can be sliced in any orientation to provide display of 2D images. In the case of intravascular imaging, display of cross-sectional and longitudinal slices is the most clinically useful display format. Thus, a simultaneous interactive display of such 2D images with the aid of the computer cursor has been developed in this work. A longitudinal slice through the middle of the vessel phantom is firstly displayed. The cursor is placed on it and can be moved within the borders of the display window. The cross-sectional slice which corresponds to the relative cursor co-ordinates at any time is then displayed in a different window and is updated every time the cursor is moved.

#### **4.3.3 Lumen cast display**

There is clinical interest in assessing and appreciating the residual lumen in a stenosed artery before and after interventional treatment. A way to facilitate this is to display a 3D lumen cast. In the current study, this is done by initially segmenting a set of successive cross-sectional slices from the reconstructed volume, along the length of the vessel phantom. The derived set of 2D lumen images is surface



rendered, resulting in a display which depicts the shape of the residual lumen and provides a view of luminal encroachments over the length of the phantom segment. Lumen cast images will be shown in the next chapter, following the description of image segmentation.

#### **4.4 Conditions for assessment of image quality**

The conical, spiral, rotational and fan scans were performed for each vessel phantom with the catheter placed in four different locations inside the phantom lumen. Three volume scans were performed with the catheter parallel to the long axis of the phantom: the first one with the catheter concentrically placed in the lumen (Figure 2.7a), the second with the catheter placed eccentrically (away from the stenosis in Figure 2.7b), and the third one with the catheter placed eccentrically in the opposite direction than before (close to the stenosis in Figure 2.7c). These three scan positions provided the data sets which were used for the reconstruction of the compound scan. In addition, the catheter was orientated at a 5° angle to the long axis of the phantom for a fourth volume scan as shown in Figure 4.1.

These different scan orientations allowed the assessment of image quality in ideal conditions (catheter parallel to the long axis of the vessel and centrally placed in the lumen) as well as conditions more likely to be encountered in clinical practice (eccentric position of the catheter in the lumen, or catheter at an angle to the long axis of the vessel).

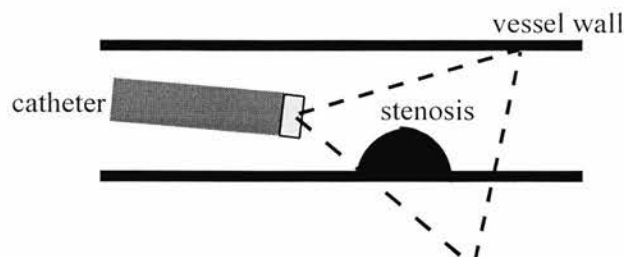


*Figure 4.1 : Volume scan with the catheter at an angle to the long axis of the phantom. The dashed triangle illustrates the field of view.*

The image quality was also assessed for cases of sparse data sets, where the line density per frame or the frame density per volume were reduced. This provided an indication of the robustness of a scanning pattern when used for acquiring limited amount of data and subsequently of its suitability for real-time application.

## **4.5 Image quality of data sets acquired with the various scanning patterns**

In this section, a number of images reconstructed from 3D data sets acquired with the various scanning patterns under investigation, are shown for all the types of vessel phantoms used in the study. The images presented in the subsections 4.5.1 to 4.5.3 refer to 3D data sets acquired with the catheter concentrically placed in the lumen and parallel to the long axis of the vessel phantom. The effects of non-central and non-coaxial catheter positions are discussed in a separate subsection (4.5.4) and so are the effects of using sparse data sets (subsection 4.5.5).

### **4.5.1 ‘Single hump’ eccentric stenosis**

This subsection presents images of the vessel phantom with the ‘single hump’ eccentric stenosis (Figure 2.15d). Figure 4.2 shows reconstructed 2D longitudinal slices of the phantom scanned with each scanning pattern. It can be seen that all the scanning patterns except the conical scan visualise the shape and the extent of the stenosis and discriminate the three layers at the phantom wall. The conical scan suffers from lack of information directly ahead of the catheter tip as well as poorer image quality at the phantom wall. These characteristics depend on the angle used in this scanning pattern between the ultrasound beam and the long axis of the phantom. Increasing this angle results in improved image quality at the phantom wall, but reduces the acquired and displayed information ahead of the catheter tip; the converse also applies. This effect is clearly illustrated in Figure 4.3 which shows reconstructed 2D longitudinal images of the same phantom scanned with the conical

pattern when the angle between the ultrasound beam and the phantom axis was set at 20°, 15° and 10°. Scanning with a 20° angle provides better image quality at the phantom wall than in the other cases, while scanning with 10° provides the most information about the stenosis lying ahead of the catheter. The 15° angle seems to be a good compromise and has thus been selected for use with the conical scan throughout this work.

Reconstructed cross-sectional images of the phantom scanned with each scanning pattern are shown in Figure 4.4. The three-layered wall structure is again identified and looks similar to the typical 'three-ring' appearance of the coronary arterial wall present when side-viewing IVUS is used. Observing these images, one can see different artifacts. These appear after interpolation and reflect the acquisition geometries of the different scanning patterns. There is an annular-ring artifact in the conical and spiral scan images, a radial artifact in the rotational scan image and a vertical banding artifact in the fan scan image. It is also interesting to see that the image quality of a compound scan composed of three spiral data sets (Figure 4.4e), is much better than the quality of the stand alone spiral scan (Figure 4.4b).

The volume rendering results in semitransparent images which allow visualisation of the stenosis in the lumen, through the phantom wall. These rendered volumes can be displayed in different orientations in space to allow a number of different views which can provide a better appreciation and perception of the structure inside the lumen. Their image quality is also comparable to the quality of the 2D reconstructed slices, in terms of discriminating the wall layers and identifying the shape and extent of the stenosis. In Figure 4.5, a rendered volume acquired with the spiral scan is displayed in a number of orientations rotated at 30° angular steps.

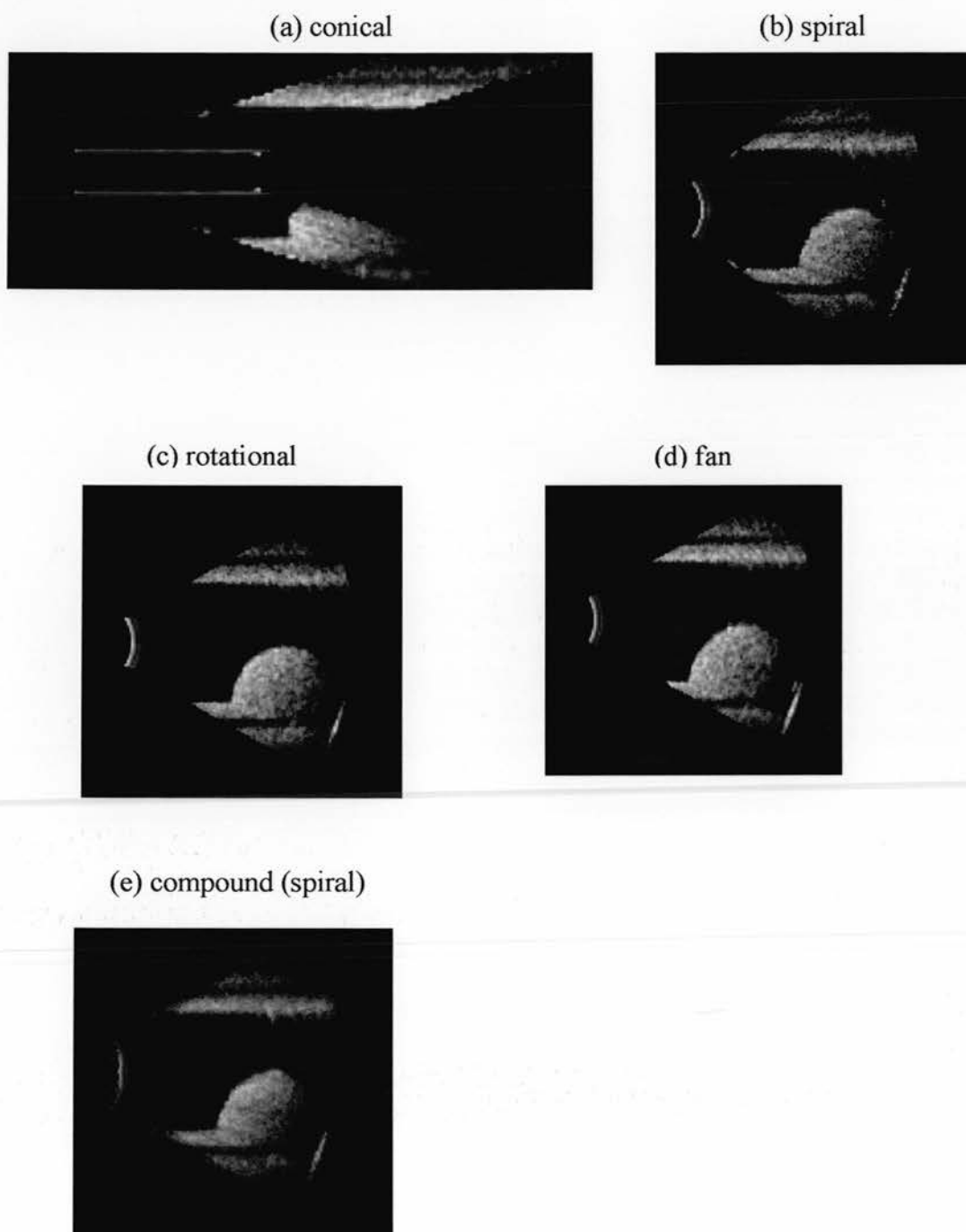


*Figure 4.2 : Reconstructed 2D longitudinal images of a vessel phantom with a 'single hump' eccentric stenosis scanned with each scanning pattern. The catheter was placed concentrically in the phantom lumen and parallel to the long axis of the phantom.*

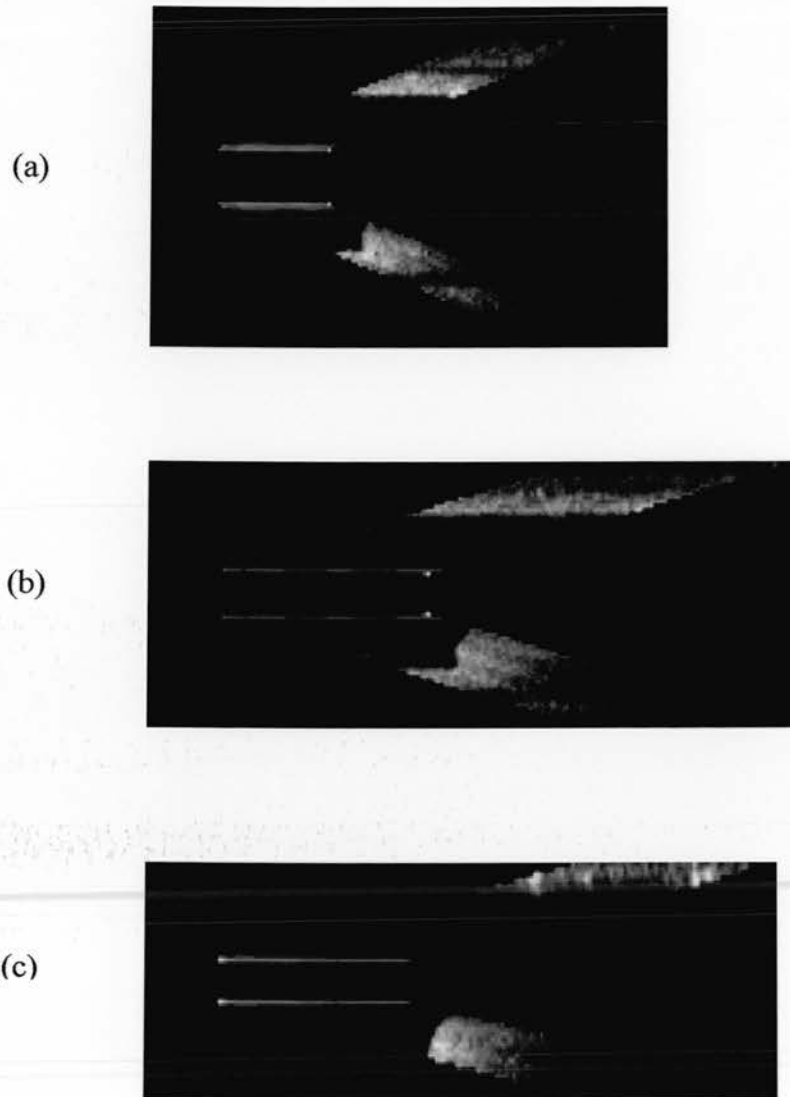


*Figure 4.3 : Reconstructed 2D longitudinal images of a phantom with a 'single hump' eccentric stenosis scanned with the conical scan using different angles between the ultrasound beam and the long axis of the phantom. The angles used were 20° in (a), 15° in (b) and 10° in (c).*

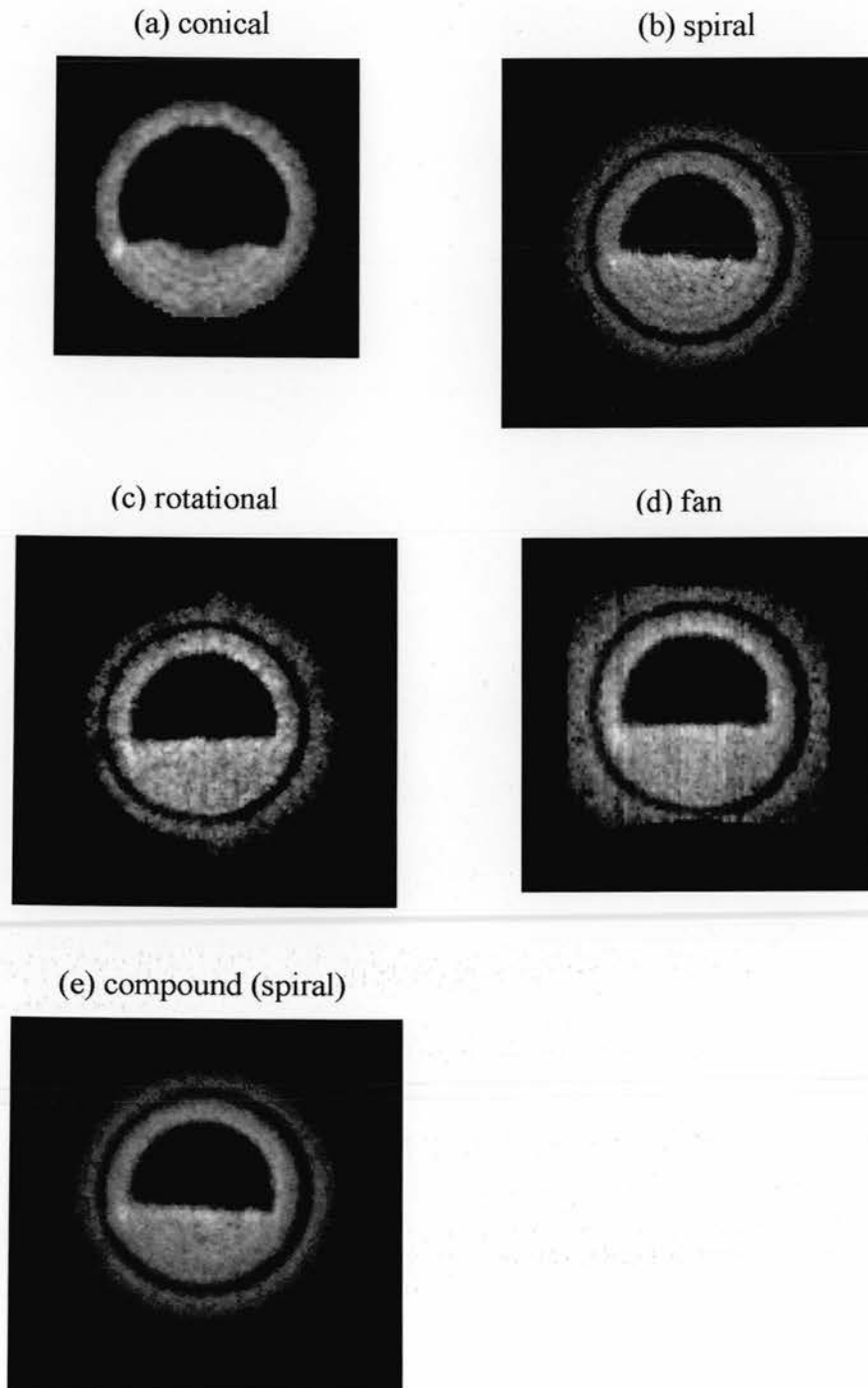


*Figure 4.4 : Reconstructed cross-sectional images of the vessel phantom with a 'single hump' eccentric stenosis scanned with each scanning pattern. The catheter was placed concentrically in the phantom lumen and parallel to the long axis of the phantom.*

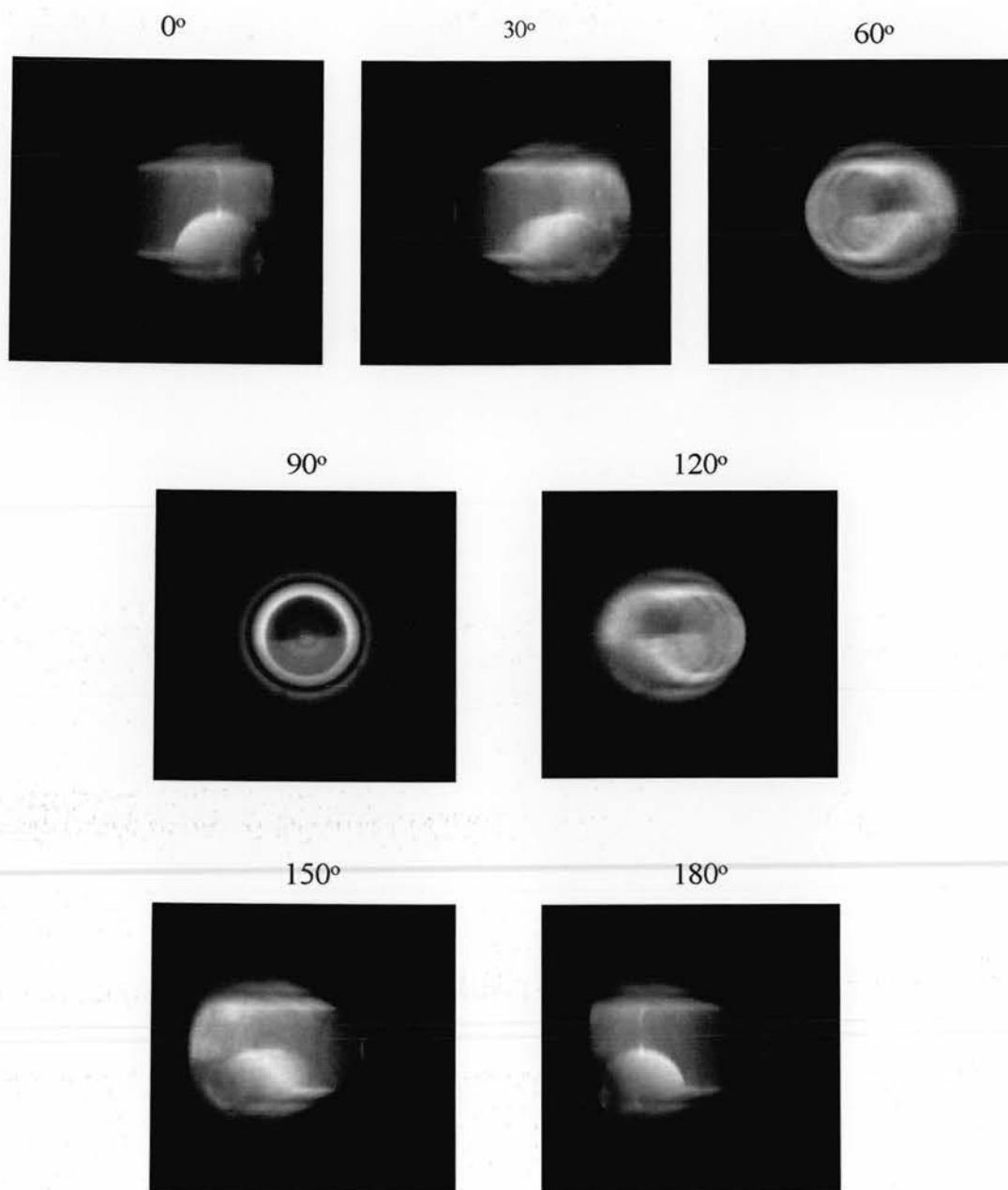


*Figure 4.5 : Rendered volume of the vessel phantom with a 'single hump' eccentric stenosis, scanned with the spiral scan when the catheter was placed concentrically in the phantom lumen and parallel to the long axis of the phantom. The volume is displayed in a number of orientations at 30° angular steps.*

#### **4.5.2 Symmetrical stenosis**

The vessel phantom with the symmetrical cylindrical stenosis (Figure 2.15c), provides stronger indication of the inability of the conical scan to fully visualise the structures ahead of the catheter. As seen from the reconstructed longitudinal images in Figure 4.6, the conical scan displays less than one third of the stenosis lying ahead of the catheter, while the other patterns visualise its full extent. When reconstructed cross-sectional images at the site of the narrow lumen channel are displayed as in Figure 4.7, it is seen that the spiral scan preserves the circular shape of the lumen and the outer phantom wall better than the rest of the scanning patterns. Once again the compound scan, composed in this case of three rotational data sets (Figure 4.7e), provides improved image quality compared to a stand alone rotational scan (Figure 4.7c).



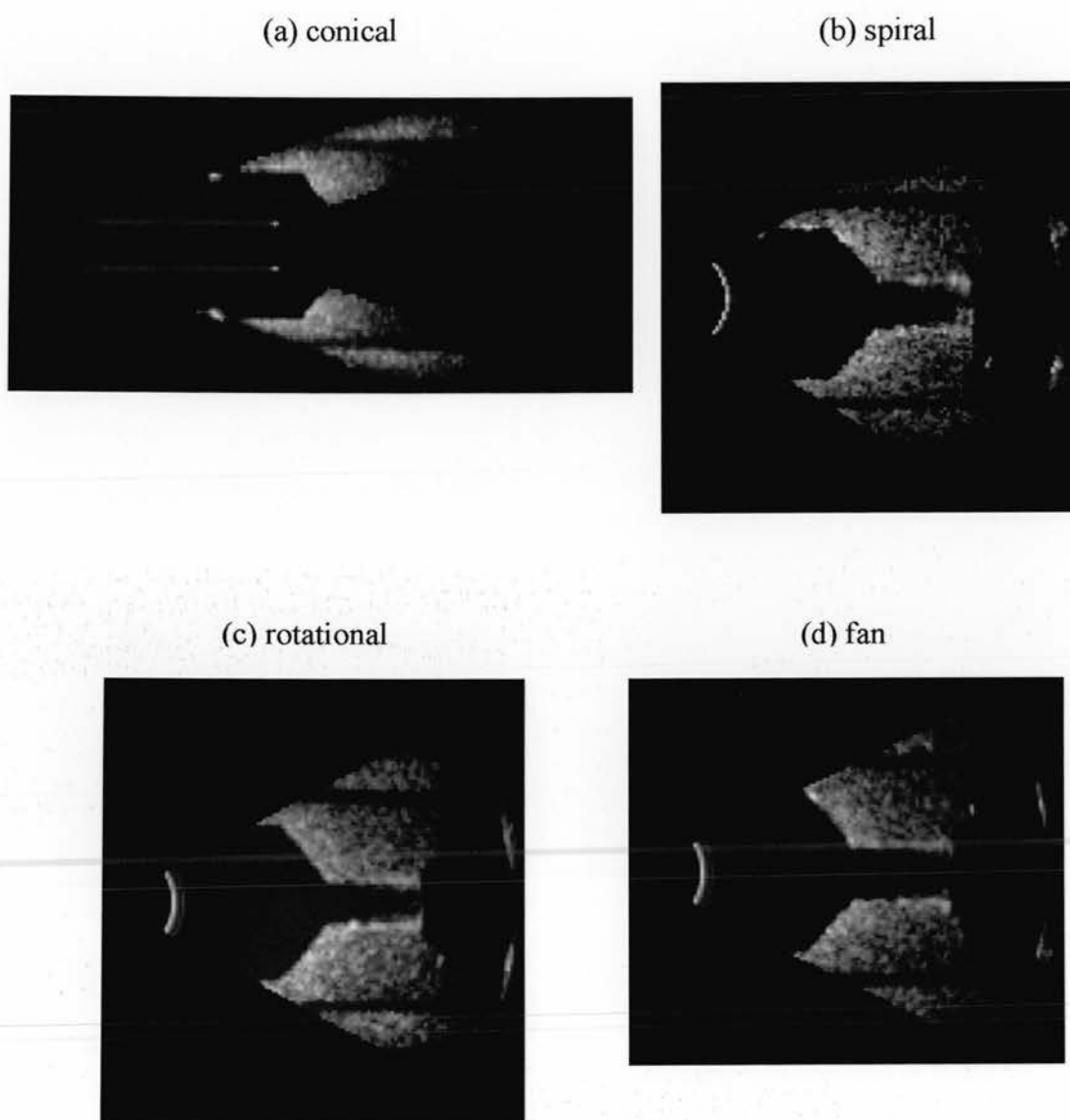


*Figure 4.6 : Reconstructed 2D longitudinal images of the vessel phantom with the symmetrical cylindrical stenosis, scanned with different scanning patterns. The catheter was placed concentrically in the phantom lumen and parallel to the long axis of the phantom. The conical scan displays less than one third of the stenosis lying ahead of the catheter, while the other patterns visualise its full extent.*

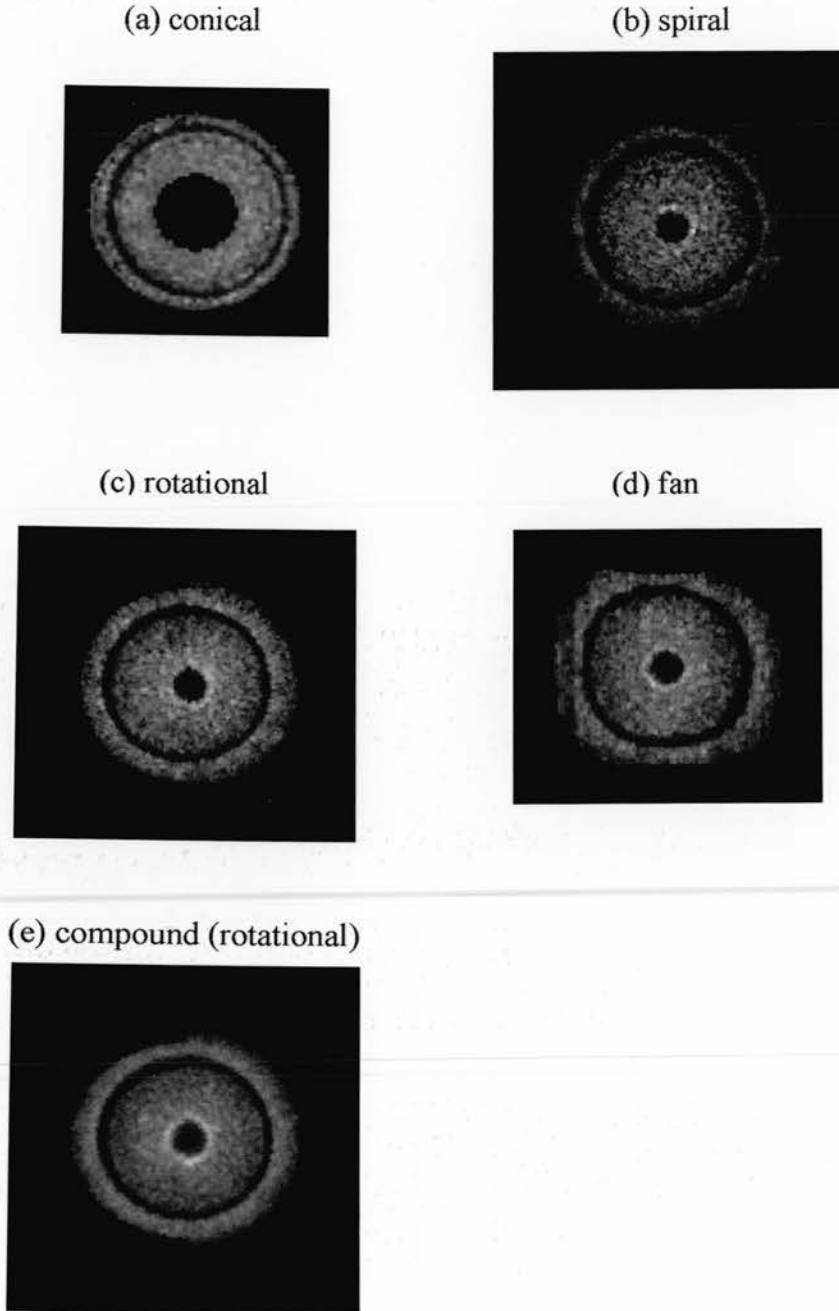


*Figure 4.7 : Reconstructed 2D cross-sectional images of the vessel phantom with the symmetrical cylindrical stenosis, scanned with each scanning pattern. The catheter was placed concentrically in the phantom lumen and parallel to the long axis of the phantom. The spiral scan preserves the circular shape of the lumen and the whole phantom better than the other patterns.*

### **4.5.3 ‘Double hump’ eccentric stenosis and ‘hard’ plaque material**

To appreciate the effects of the ‘hard plaque’, images of the phantom with a ‘hard double hump’ eccentric stenosis are compared to images of another phantom with a stenosis of exactly the same shape but softer composition (Figures 2.15f and 2.15e respectively). The ‘hard plaque’ provides strong acoustic shadowing, which persists even when the amplifier’s gain is increased. A typical example is given in Figure 4.8, where reconstructed longitudinal and cross-sectional images obtained with the rotational scan are shown for the two phantoms with stenoses of identical shape. Despite the higher gain setting in the case of ‘hard plaque’, the portion of the stenosis visualised in the longitudinal axis (Figure 4.8a) is less than in the case of the softer plaque and lower gain (Figure 4.8c). The echo from the front face of the ‘hard plaque’ is also much stronger, due to both the plaque material and the higher gain setting. The above are also obvious in the cross-sectional image (Figure 4.8b), where the acoustic shadowing appears in the lower part of the image (from the 3 to 9 o’clock) and the strong reflection reduces the apparent size of the visualised lumen area. The outer wall layer is still visible in this image, even though it is placed below the region of acoustic shadowing. This is due to the fact that this outer wall layer is reconstructed from beams which lie at the edge of the volume and do not propagate through the ‘hard plaque’. The above effects are observed for all the scanning patterns.

The acoustic shadowing effect as observed in forward-viewing IVUS is different than that in side-viewing IVUS. As regards 2D cross-sectional images, the acoustic shadowing in side-viewing IVUS obscures imaging of the vessel wall across a sector of the imaging plane located at the *same* site as the calcium deposits. In forward-viewing IVUS, calcium deposits visualised in a reconstructed cross-sectional image would cause acoustic shadowing seen at *subsequent* cross-sectional images. In addition, depending on the location of calcium, visualisation of the vessel wall might be possible as a result of ultrasound beams bypassing the calcium deposits.

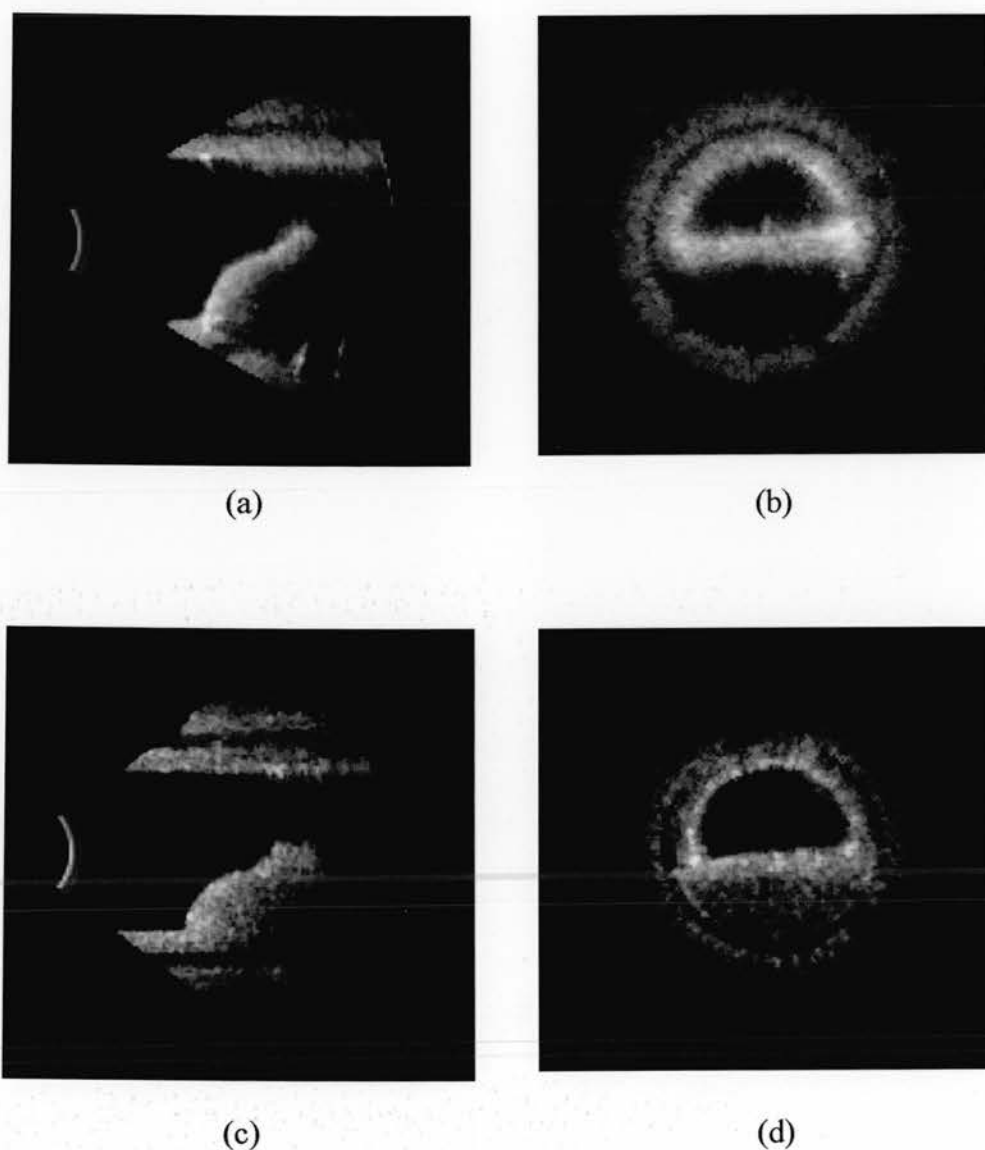


*Figure 4.8 : Reconstructed 2D longitudinal (a) and cross-sectional (b) images of the phantom with a 'double hump' eccentric stenosis consisting of 'hard plaque'; (c) and (d) are the corresponding images for the phantom with a 'double hump' stenosis of identical shape but softer composition. Strong reflection from the front surface as well as acoustic shadowing are observed for the 'hard plaque', as in the case of calcium in human arteries.*

#### **4.5.4 Eccentric and angulated positions of the catheter in the lumen**

Non-central and non-coaxial positions of the catheter in the vessel lumen affect the images obtained with side-viewing IVUS systems, both qualitatively and quantitatively (Chae et al. 1992; Di Mario et al. 1993; Finet et al. 1993; Nishimura et al. 1990).

Using the spiral, rotational and fan forward-viewing scanning patterns to scan the vessel phantoms with the catheter eccentric in the lumen but parallel to the long axis of the phantom, did not affect the apparent shape of the lumen, plaque and phantom wall (Figures 4.9 to 4.11). This was also further established by the reconstructed images of the compound scans which, as mentioned before, are composed of scans performed at eccentric and concentric catheter positions. There is no apparent image distortion or lumen size changes between the reconstructed single component and resulting compounded images in Figures 4.4b and 4.4e, or in Figures 4.7c and 4.7e either.

A unique observation appeared in the case of the conical scan. Even though there was no sign of distortion of the circular phantom shape due to non-central catheter locations, these different positions provided different orientations for the characteristic hollow part of the reconstructed volume seen in the conical scan. As a result, the visualised shape of the stenosis varied among these cases (Figure 4.12).

When the vessel phantoms were scanned with the catheter at an angle to their long axes, the reconstructed longitudinal images always provided evidence of the angular orientation and preserved the shape of the stenosis and the structure of the wall (Figure 4.13). No obvious distortion of the circular phantom shape was observed in reconstructed cross-sectional images (Figures 4.9c to 4.12c), probably due to the small extent of the angular orientation of the catheter.

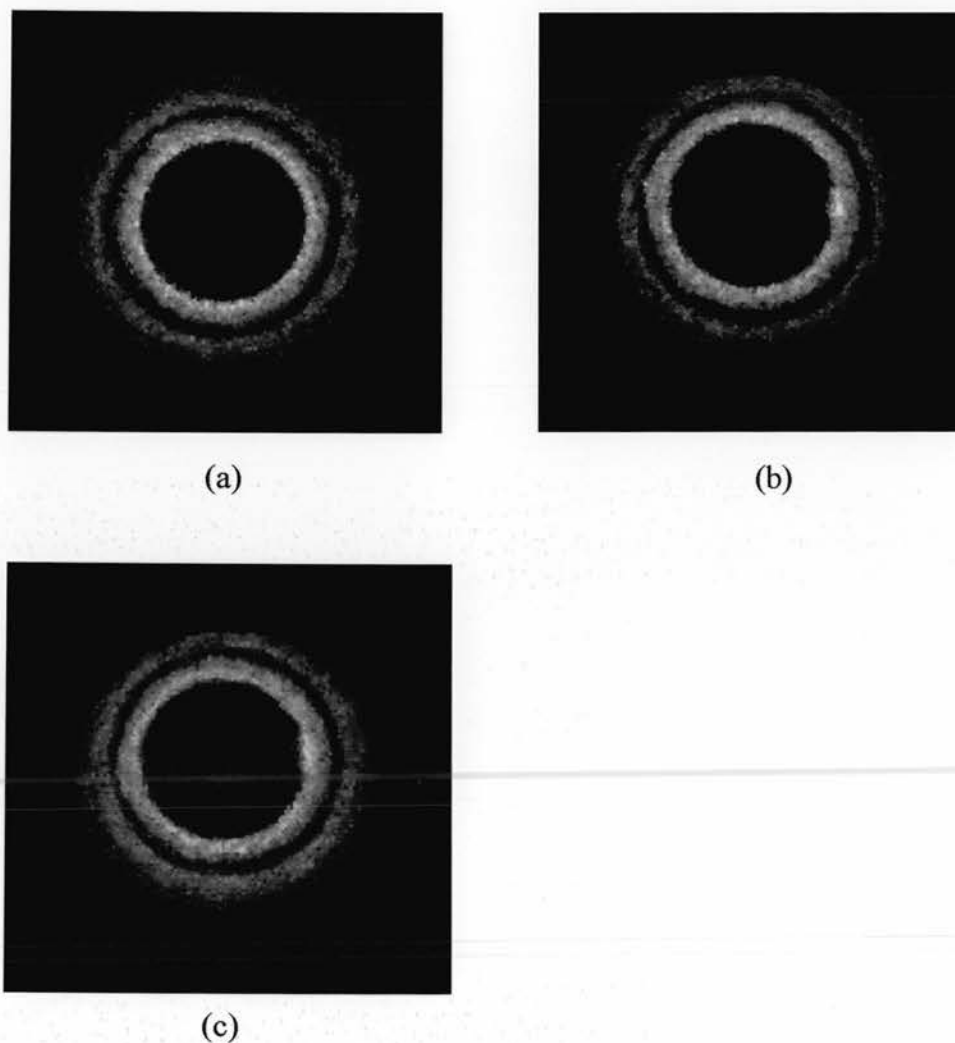


*Figure 4.9 : Reconstructed cross-sectional images of the 'healthy' vessel phantom scanned with the **spiral** scan. (a) Catheter concentric in the lumen and parallel to the long axis of the phantom. (b) Catheter eccentric and parallel to the long axis of the phantom. (c) Catheter at a 5° angle to the long axis of the phantom. No shape distortions of the lumen or the phantom wall are observed.*

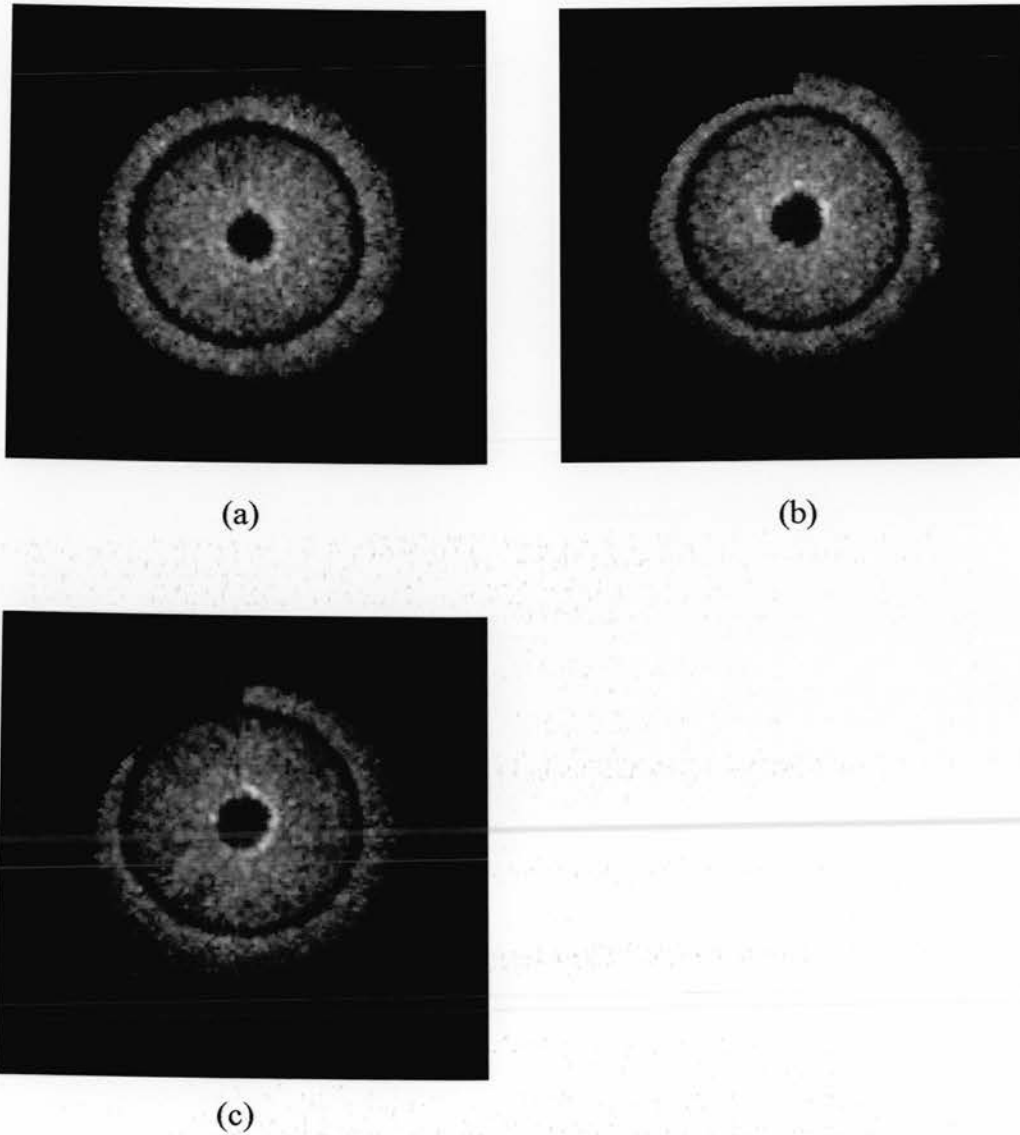
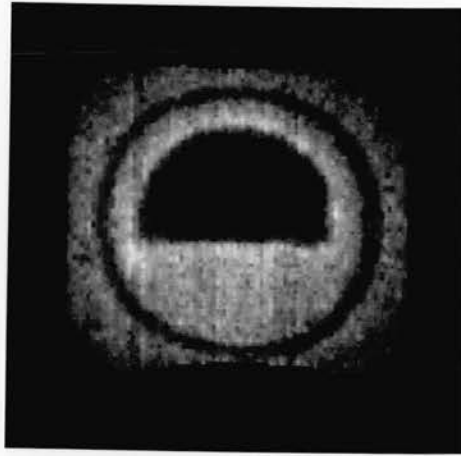
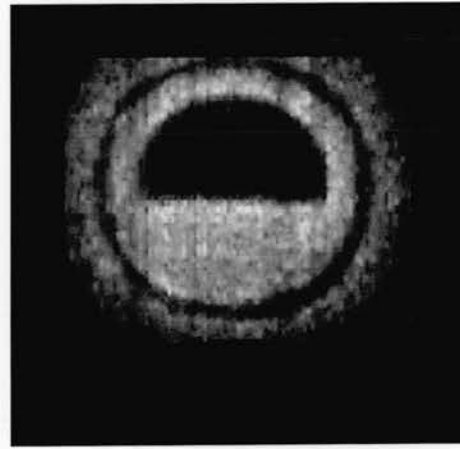


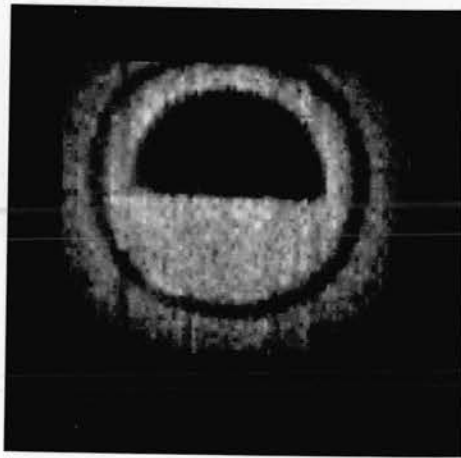
*Figure 4.10 : Reconstructed cross-sectional images of the phantom with the cylindrical symmetrical stenosis, scanned with the **rotational** scan; (a), (b) and (c) as in Figure 4.9. No shape distortions of lumen, plaque or phantom wall are observed. The 'shadow' from 10 to 12 o'clock in (c) is because that part of the image is outside the field of view.*



(a)



(b)



(c)

*Figure 4.11 : Reconstructed cross-sectional images of the phantom with a 'single hump' eccentric stenosis, scanned with the **fan** scan; (a), (b) and (c) as in Figure 4.9. No shape distortions of lumen, plaque or phantom wall are observed. The 'shadows' from 11 to 1 o'clock in (b) and (c) are because those part of the images are outside the field of view.*



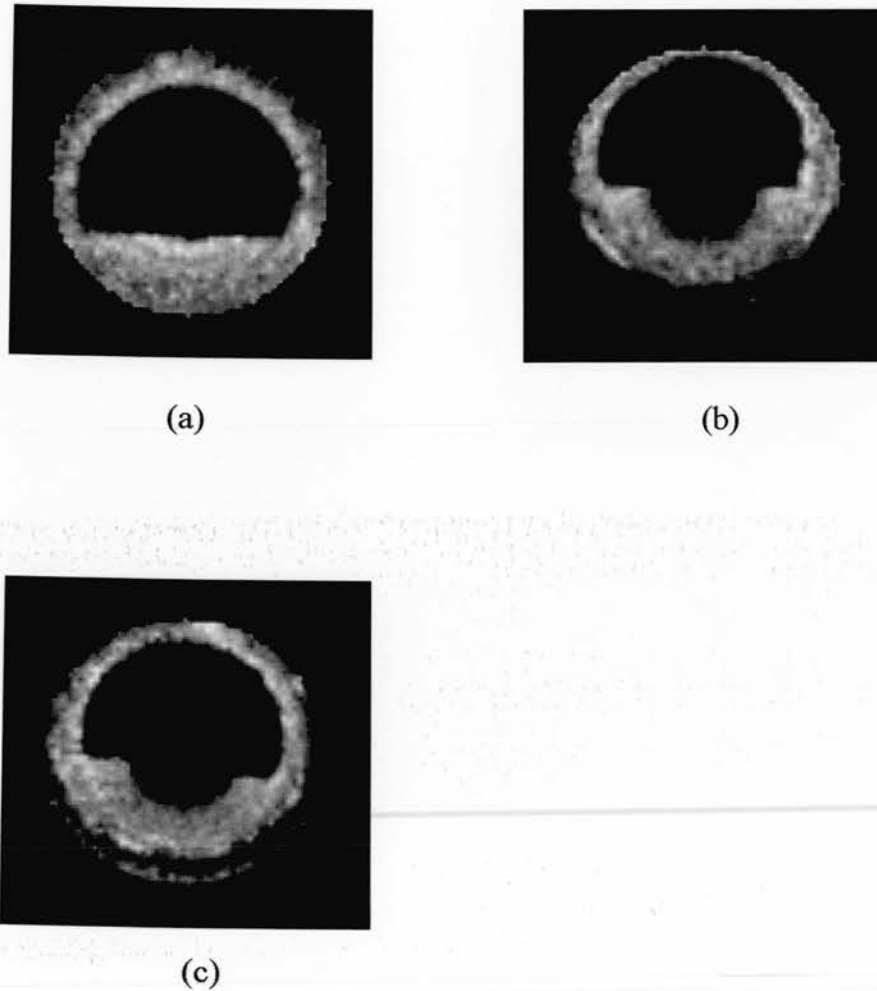
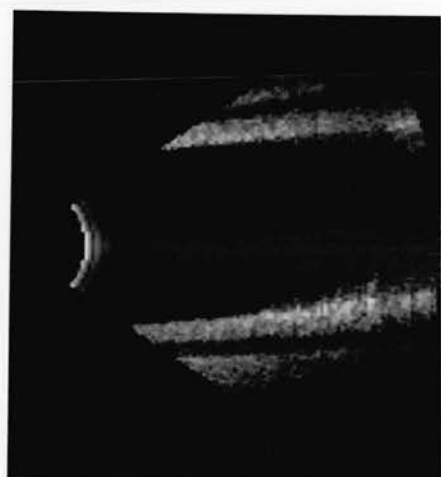
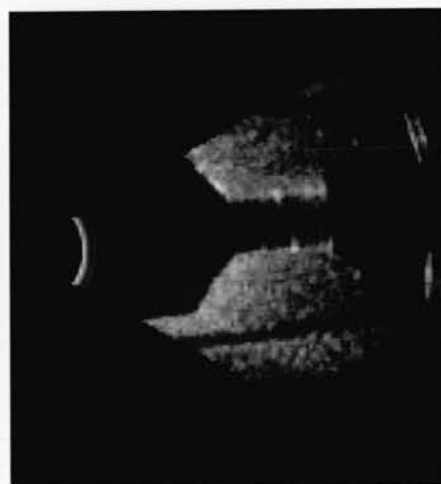


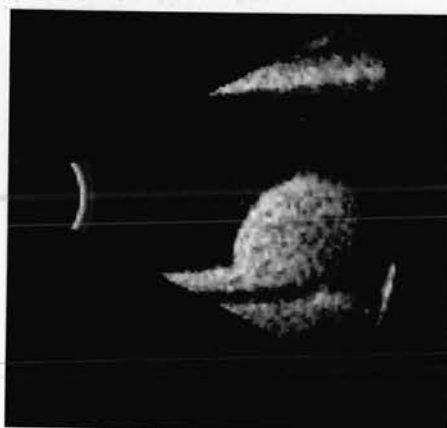
*Figure 4.12 : Reconstructed cross-sectional images of the phantom with a 'double hump' eccentric stenosis, scanned with the **conical** scan; (a), (b) and (c) as in Figure 4.9. Even though there is no sign of distortion of the circular phantom shape in the images derived from eccentric or angulated catheter positions, the different catheter positions provide different orientations for the characteristic hollow part of the reconstructed volume seen in this scanning pattern, affecting the visualised shape of the stenosis.*



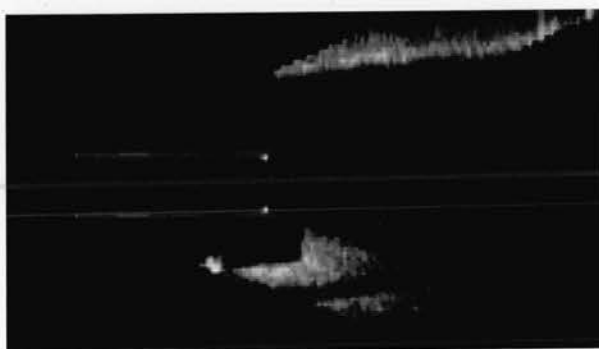
(a)



(b)



(c)



(d)

*Figure 4.13 : Reconstructed longitudinal images providing evidence of the angular orientation of the catheter and preserving the shape of the stenosis and the structure of the phantom wall. (a) 'Healthy' vessel phantom scanned by the spiral scan, (b) phantom with cylindrical symmetrical stenosis scanned by the rotational scan, (c) phantom with a 'single hump' eccentric stenosis scanned by the fan scan and (d) phantom with a 'double hump' eccentric stenosis scanned by the conical scan.*

#### **4.5.5 Effects of sparse data sets**

Real-time imaging is strongly desired in clinical practice. Most commercial imaging systems achieve real-time performance by scanning a reduced number of lines per frame or volume and relying on interpolation to fill the remaining gaps. The suitability for real-time application of the forward-viewing intravascular scanning patterns examined in this work was investigated by assessing the image quality they provided when used with sparse data sets. The original dense volume sets comprised of 60 frames with 125 lines each for the case of conical and spiral scans, 100 frames with 110 lines each for the rotational scan, and 70 frames with 96 lines each for the fan scan. Two parameters were varied: the line density per acquisition frame and the frame density per volume. Figures 4.14 to 4.17 illustrate the effects on the image quality for each scanning pattern individually, of a 3-fold reduction in the above densities.

As regards the conical scan, reduced frame density led to clearly visible pixels in the reconstructed longitudinal images (Figure 4.14c), while reduced line density in frames resulted in a star-like artifact in cross-sectional images due to large angular gaps between lines in the acquisition frames (Figure 4.14d).

In the case of the spiral scan, reduced frame density affected the homogeneous appearance of the plaque material (Figure 4.15c). The star-like artifact also appeared with reduced line density in frames, as in the conical scan (Figure 4.15d).

This artifact was also seen in the rotational scan, with the only difference that it arose from the reduced frame density leaving large angular gaps between acquisition frames (Figure 4.16d). When less lines were used per sector, the sector images appeared 'digitised'. This was observed for both the rotational (Figure 4.16c) and the fan (Figure 4.17c) scans. Finally, when the frame density was reduced in the fan scan, the vertical banding artifact mentioned previously became very strong as a result of large angular gaps between acquisition frames (Figure 4.17d).

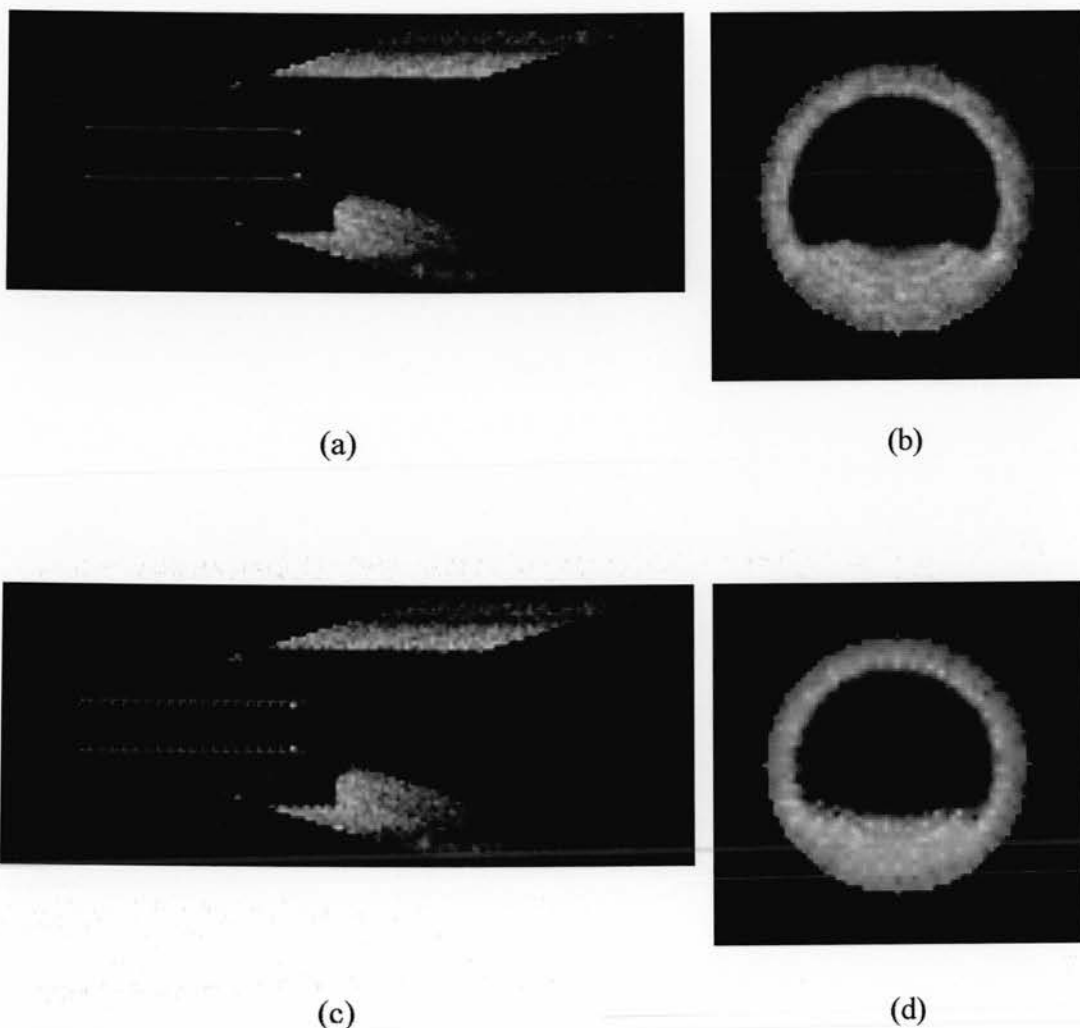


*Figure 4.14 : Effect of sparse data sets on the image quality of the **conical** scan. The images shown are for the phantom with the 'single hump' eccentric stenosis. (a) and (b) are reconstructed longitudinal and cross-sectional images respectively arising from dense data sets. (c) Reconstructed longitudinal image with reduced frame density per volume. Pixels are clearly visible in this image. (d) Reconstructed cross-sectional image with reduced line density per frame. A star-like artifact appears as a result of the large angular gaps between lines in the acquisition frames.*

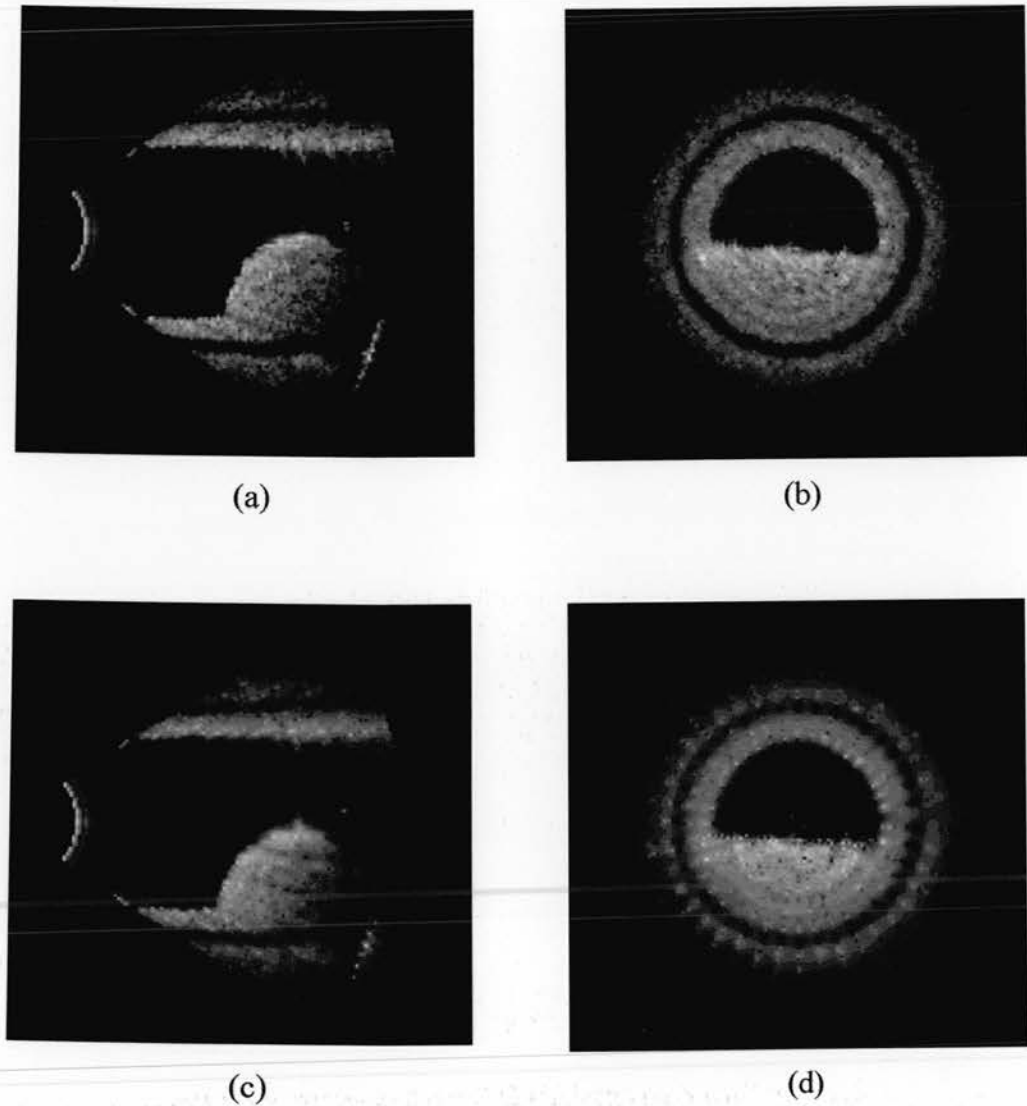


*Figure 4.15 : Effect of sparse data sets on the image quality of the spiral scan. The images shown are for the phantom with a 'single hump' eccentric stenosis. (a) and (b) are reconstructed longitudinal and cross-sectional images respectively arising from dense data sets. (c) Reconstructed longitudinal image with reduced frame density per volume. The plaque material looks less homogeneous compared to the image in (a). (d) Reconstructed cross-sectional image with reduced line density per frame. A star-like artifact appears as a result of the large angular gaps between lines in the acquisition frames.*

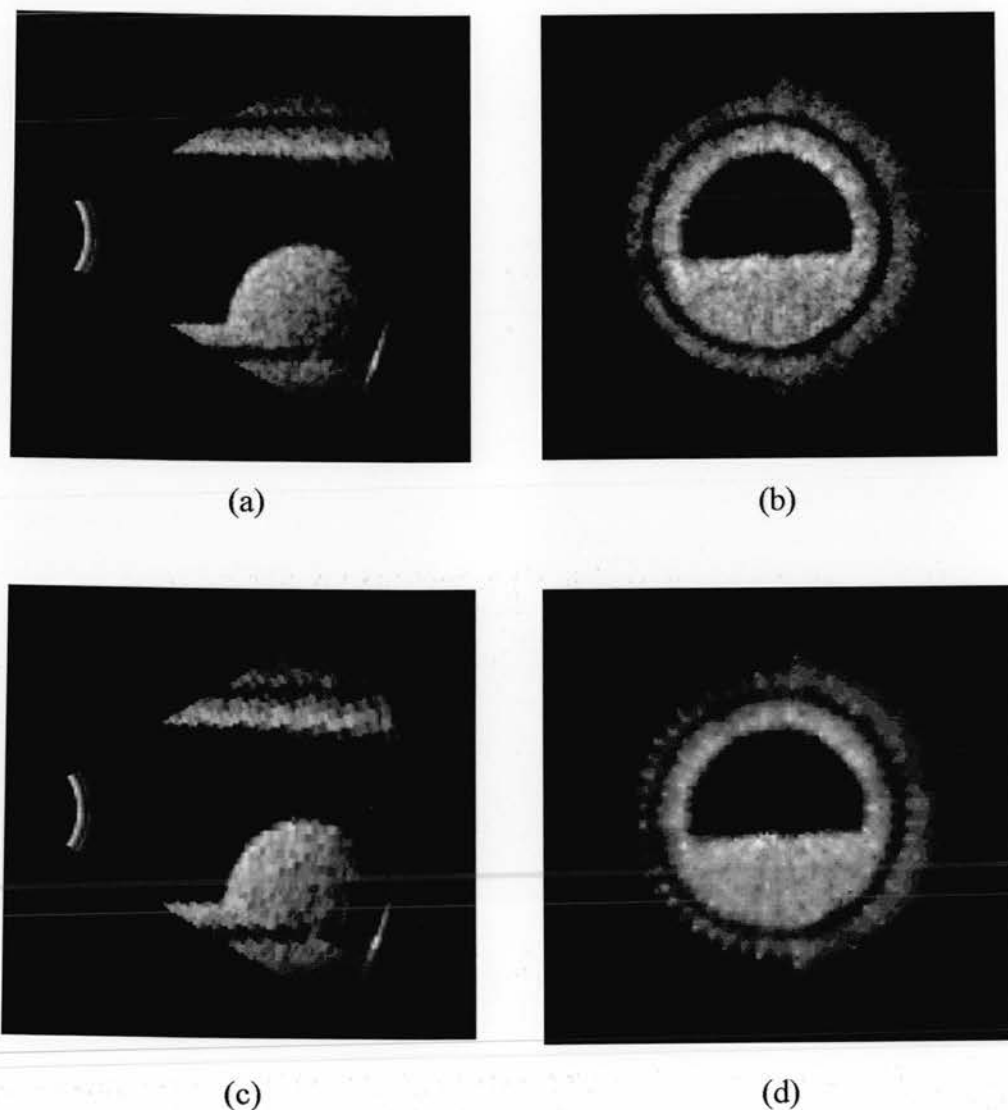


*Figure 4.16 : Effect of sparse data sets on the image quality of the **rotational** scan. The images shown are for the phantom with a 'single hump' eccentric stenosis. (a) and (b) are reconstructed longitudinal and cross-sectional images respectively arising from dense data sets. (c) Reconstructed longitudinal image with reduced line density per frame. The image looks 'digitised' compared to the image in (a). (d) Reconstructed cross-sectional image with reduced frame density per volume. A star-like artifact appears as a result of large angular gaps between frames.*

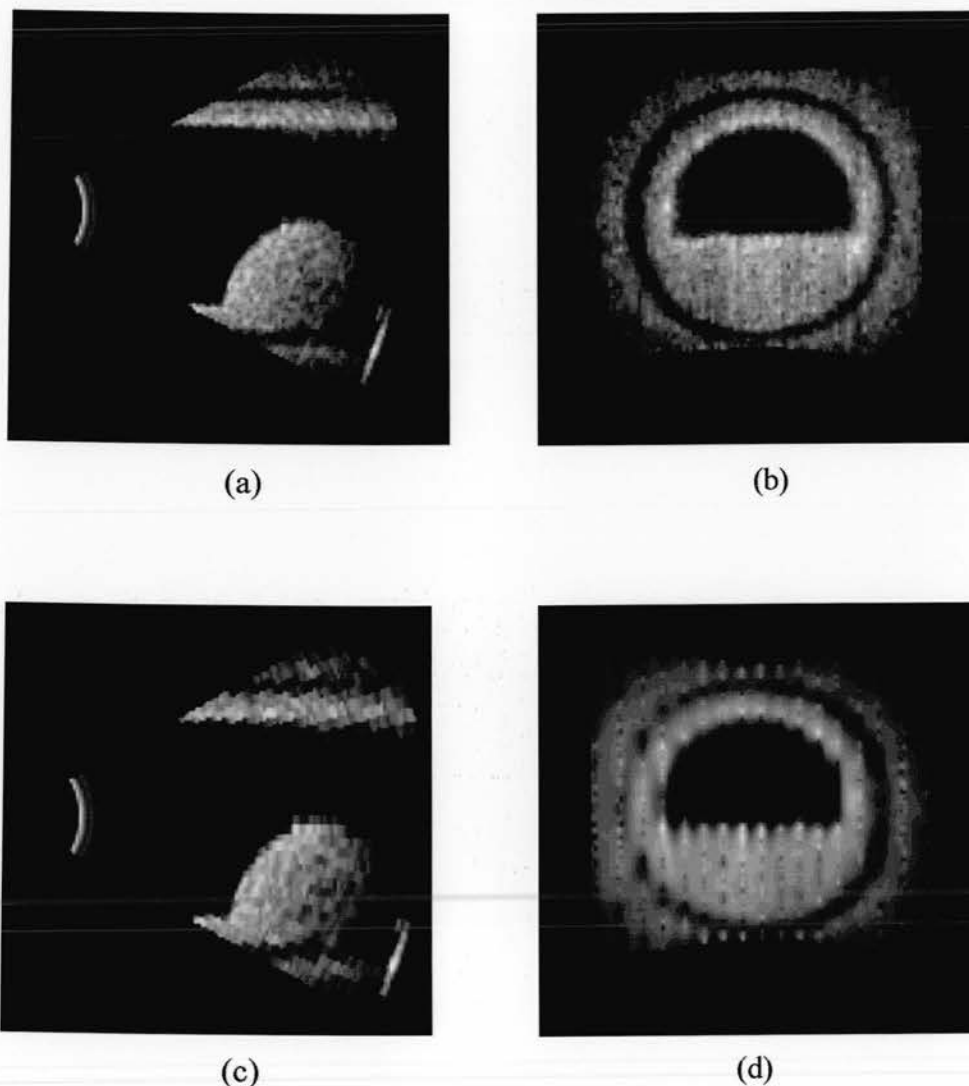


*Figure 4.17 : Effect of sparse data sets on the image quality of the **fan** scan. The images shown are for the phantom with a 'single hump' eccentric stenosis. (a) and (b) are reconstructed longitudinal and cross-sectional images respectively arising from dense data sets. (c) Reconstructed longitudinal image with reduced line density per frame. The image looks 'digitised' compared to the image in (a). (d) Reconstructed cross-sectional image with reduced frame density per volume. The vertical banding artifact is very strong as a result of large angular gaps between frames.*

The images shown in Figures 4.14 to 4.17, have not been subjected to any image processing at all. The effects of interpolating large gaps in voxel space were thus quite strong. Some image processing would certainly have improved the quality of these images (Al-Mejrad 1996), however it was desired to keep the comparisons on a raw basis as much as possible. Two medical physicists with experience in ultrasound imaging judged image sets of various data densities. They were not made aware of the scanning pattern used or the data density of the acquired volumes. The judgement of the images was concentrated on the assessment of the blurring caused by interpolation and the ability to identify the wall structure of the phantoms and the shape of the stenoses. There was a good agreement between the two physicists in discriminating images of acceptable quality according to the above criteria. The bottom line in data density was a 3-fold frame density reduction for the conical and spiral scans, a 2-fold frame density reduction together with a 2-fold line reduction for the rotational scan, and a 2-fold frame density reduction or a 2-fold line reduction for the fan scan. This helped to identify minimum requirements in terms of total number of ultrasound lines per volume for achieving adequate image quality with the examined scanning patterns. These requirements are given in Table 4.1. It can be seen that the fan scan needs a higher line density per acquired volume to match the quality of the other scanning patterns, therefore it may be less suited than the other patterns for real-time application.

*Table 4.1 : Minimum requirements in number of ultrasound lines per volume for the examined forward-viewing intravascular scanning patterns in order to achieve adequate image quality.*

<b>Scanning pattern</b>	<b>Total lines in scanned volume</b>	<b>Line density (lines per cm<sup>3</sup>)</b>
Conical	2500	9.5
Spiral	2500	6.2
Rotational	2750	8.5
Fan	3360	10.4



## **4.6 Discussion**

### **4.6.1 Image quality of the Compound scan**

The compound scan appeared to produce the best image quality among all the scanning patterns, as seen clearly from the cross-sectional images (Figures 4.4 and 4.7). Nevertheless, this scanning pattern is not practical for clinical applications. There is limited steerability, from outside the patient's body, of an IVUS catheter lying inside a vessel. It is very difficult, or even impossible, to position the catheter at different locations within the same site of a narrow vessel such as the coronary artery, and then perform individual 3D scans for each one of them. In addition to that, the acquisition and processing time would increase significantly exceeding the allowance of a real-time interventional procedure. Therefore, this pattern was not regarded as a potential practical tool for a future application, but rather as a research tool for assessing factors which affect the image quality. Interestingly, it appeared that even a small number of different acquisition orientations (only three in this work as shown in Figure 2.7) improved the image quality of the scanned volume significantly. This can be explained by considering the angular dependence of backscatter. Returned echo signals are stronger for angles of incidence of the ultrasound beam with tissue closer to  $90^\circ$ , and weaker for smaller angles of incidence. In effect, compounding helps achieve enhanced angles of incidence from alternative directions, hence stronger echo signals, the contribution of which at the signal averaging stage results in improved image quality.

### **4.6.2 Image quality of the Conical scan**

The conical scan suffered from limited field of view ahead of the catheter tip. In cases like that of the phantom shown in Figure 4.6, more than half of the stenosis could not be imaged at all. This scanning pattern also resulted in the worst image quality at the phantom wall, making the discrimination among the wall layers

difficult. Its performance on these aspects depended on the scan angle used between the ultrasound beam and the long axis of the phantom. The wider this angle, the better the image quality at the phantom wall, but lesser the displayed information ahead of the catheter tip, and vice versa (Figure 4.3). A 15° angle was chosen as a preferred compromise between these two conflicting requirements.

Moreover, the conical scan was affected by the orientation of the catheter in the lumen during acquisition. Although there was no apparent distortion of the circular phantom shapes in the images derived from eccentric or angulated catheter positions, these different positions located the characteristic hollow part of the reconstructed volume differently. This resulted in visualising different parts and shapes of the stenosis in each case (Figure 4.12).

The conical scan is effectively a pull-back technique like the one used for 3D imaging with the side-viewing IVUS systems. It is therefore expected, that its clinical application would be affected by the same artifacts which appear in the current side-viewing systems (Di Mario et al. 1995a; Roelandt et al. 1994a). For example, bends in the catheter can cause uneven spacing of acquisition frames during pull-back, affecting the 3D reconstruction. Furthermore, non-uniform rotation of the catheter and vessel curvatures can introduce image distortion leading to over or underestimation of plaque size. Finally, motion of the catheter in the lumen during the cardiac cycle combined with systolic-diastolic changes in vessel dimensions would introduce a characteristic saw-shaped appearance of the vessel (Di Mario et al. 1995a). There are ways of reducing the above artifacts, however they involve use of more complicated and expensive instrumentation. Biplane angiography could be used simultaneously with IVUS, for tracking the correct path and orientation of the catheter tip in the lumen of tortuous vessels during pull-back, enabling correct orientation of the acquired images in the 3D space (Klein et al. 1992; Prause et al. 1996; Slager et al. 1997). ECG gated acquisition would be required to eliminate the saw-shaped appearance of the vessel and allow accurate analysis of vessel dimensions (Bruining et al. 1996), but at the cost of increased examination time and radiation exposure in the catheterisation laboratory.

### **4.6.3 Image quality of the Spiral, Rotational and Fan scans**

The spiral, rotational and fan scans provided full visualisation of the shape and extent of the stenoses and were capable of discriminating phantom wall layers. Display of reconstructed images with no image processing imposed on them at all, revealed interpolation artifacts which resembled the acquisition geometries of these scanning patterns. More specifically, annular-ring artifacts for the spiral scan, radial artifacts for the rotational scan and vertical banding artifacts for the fan scan were observed due to undersampling of the volumes of interest.

The clinical significance of these artifacts, if any, has yet to be assessed. In terms of image quality though it seems that the vertical banding artifact has the strongest impact. Looking at reconstructed cross-sectional images from a fan scan, the intensity is higher at the centre of the images than it is at the sides (Figures 4.4d and 4.7d). This is partly explained by the fact that for every cross-section in the volume, the central pixels of that section are closer to the transducer than the pixels at the sides. Hence, the ultrasonic beams which correspond to the central pixels have experienced less attenuation due to shorter path lengths than the beams which correspond to the pixels at the sides of the cross-section (Figure 4.18). This effect is not completely balanced by the TGC settings and, eventually, provides the central pixels (voxels originally) with higher intensity values and forms the central band of higher intensity.

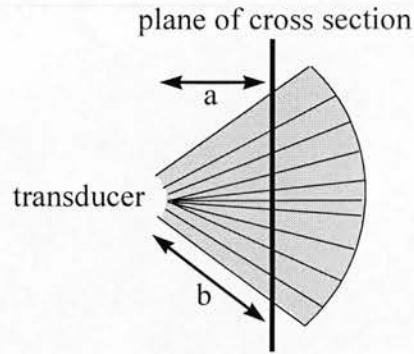


*Figure 4.18 : Illustration of the non-uniform path lengths and frame density in a fan-scanned volume. The thin lines represent the frame orientations and the thick vertical line is a section plane providing a cross-sectional image. The frame density is higher in the middle of the volume and closer to the transducer. Distance 'a' of the central part of the cross-section from the transducer face is smaller than the distance 'b' of the side parts.*

Another factor which contributes to the above artifact is the frame density in a fan-scanned volume. This density is not uniform; it is higher in the central part of the volume and lower at the sides (Figure 4.18). As a result, there are more data voxels in the middle of the volume to contribute to the interpolation of relatively small gaps, while at the sides there are less data voxels and larger gaps. The interpolation algorithm initially looks for data voxels in a 3x3x3 cubic neighbourhood centred around the gap. If no data voxels are found then the size of the cube is increased to 5x5x5, then to 7x7x7 etc., until at least one data voxel is enclosed. The higher the frame density in a region of the volume, the smaller the size of the cubic neighbourhood in the interpolation procedure, thus the more accurate the interpolated value is. On the other hand, the lower the frame density in a region of the volume the larger the size of the cubic neighbourhood. This means that voxels which may be away from the gap and might not always be related to the structures in the immediate proximity of the gap, can contribute to the interpolated value. These voxels might

also have lower intensity values, for the reason explained previously, thus reducing the interpolated intensity value.

An interesting observation arose from scanning the phantom with the symmetrical cylindrical stenosis. Reconstructed cross-sectional images revealed that the circular shape of the stenosis and the phantom was best imaged by the spiral scan (Figure 4.7). This pattern seems to be the most suitable for imaging cylindrical structures due to its operational principle: acquisition on a conical surface which has cylindrical symmetry.

The rotational scan requires a perfect match of orientations between the first and last acquisition frames. If this does not happen, then a shift between the two halves of the image may appear. Such a slight shift can be seen in Figure 4.7c and is due to some slack in the pulling wire in the mechanical system during the scan of that particular phantom.

#### **4.6.4 Potential for real-time imaging**

In real-time imaging, sparse data sets are acquired for a volume reconstruction and in such case the effect of the previously mentioned artifacts on image quality could become significant. In particular, the vertical banding artifact of the fan scan combined with even larger gaps between acquisition frames degrades the image quality seriously (Figure 4.17) and more severely than the artifacts in the other patterns. The way to reduce its effect is to increase the number of frames per volume and effectively scan more lines. According to the information shown in Table 4.1, and taking into account that the pulse repetition frequency (PRF) in most intravascular scanners ranges from 5 to 10 kHz, the fan scanning pattern cannot scan as many volumes per second as the other scanning patterns, therefore it is less suited for accurate real-time application.

The spiral and rotational scans have the potential to complete a volume acquisition in a relatively short period of time, e.g. 300 msec, such that all the lines are acquired within the same part of the cardiac cycle, preferably the diastole during

which vascular motion is reduced. This could effectively ensure fixed position for the catheter tip during volume acquisition and possibly avoid motion artifacts arising from systolic-diastolic changes in vessel dimensions (Roelandt et al. 1994a). Consequently, the need for complicated position registration could be eliminated.

#### **4.6.5 Scanning with non-central and non-coaxial catheter positions**

In side-viewing IVUS systems, the image quality and the accuracy of lumen size measurements are affected by non-central and non-coaxial positions of the catheter in the vessel lumen. Investigations have shown that when the catheter is eccentrically placed but still parallel to the long axis of the vessel, the circular shape of the image is preserved (Di Mario et al. 1993; Finet et al. 1993) and there is practically no change in the measured luminal dimensions (Chae et al. 1992). However, the intensity around the wall is no longer uniform, as in the case of central and coaxial catheter positions. Higher intensity is observed at the wall beside the catheter and exactly opposite from it, while lower intensity is observed at the lateral parts of the wall and this can affect the visualisation of plaque (Di Mario et al. 1993). Finet et al. (1993) have given a thorough explanation for the non-uniform intensity effect in side-viewing IVUS. According to their report, the decrease of intensity arises from non-normal angles of incidence of the ultrasound beam with the vessel wall. In the case of conventional side-viewing IVUS imaging, when the catheter is central in the lumen and a circular cross-section is assumed, the beam is nearly normal to the vessel wall for the whole 360° rotation of the catheter. This results in maximum reflection from the whole wall circumference. However, when the catheter is moved at an eccentric position, the angle of beam incidence varies throughout the rotation. The beam is normal to the vessel wall only at the two diametrically opposed points of the vessel diameter passing through the transducer. Thus at these two points the reflection is maximum, while it is reduced at all other points around the wall.

In forward-viewing IVUS the beam is always directed at non-normal angles to the whole of the vessel wall and to the majority of the lumen structures lying



ahead of the catheter tip. This applies to different orientations of the catheter in the lumen, hence no major intensity fluctuations would be expected, like the ones encountered in side-viewing systems between areas of normal and non-normal beam incidence. When the spiral and the two sector scanning patterns were used to scan the various vessel phantoms with the catheter eccentrically placed in the lumen but still parallel to the long axis of the phantom, the image quality did not seem to be significantly affected. No obvious intensity changes were observed, something which verified the above hypothesis.

When the catheter of a side-viewing IVUS system lies at an angle  $\theta$  to the long axis of the vessel, the imaging plane is no longer normal to the vessel wall and the shape of the displayed cross-section becomes elliptic, leading to overestimation of the lumen dimensions (Chae et al. 1992; Geselschap et al. 1998; Thrush et al. 1997). The short axis of the ellipse is equal to the vessel diameter, while the long axis is increased by  $1/\cos\theta$  leading to proportional increase in the measured lumen size. Moreover, the intensity can be significantly decreased at sectors of the wall, causing echo dropouts on the display (Di Mario et al. 1993).

When the forward-viewing scanning patterns were used at angulated catheter positions, the reconstructed longitudinal images always provided correct evidence of the angular orientation of the catheter and depicted the shape of the stenosis and the structure of the wall (Figure 4.13). In imaging small vessels such as coronary arteries *in vivo*, the angulation of the catheter in the vessel is restricted to only 2 or 3° degrees, because of the relatively small vessel to catheter diameter ratio and the long path of the catheter in the arterial system (Finet et al. 1993). The angle chosen in this work was slightly larger than the above values, namely 5°. It did not prove large enough to cause shape distortion in images, as noted from the comparison of reconstructed cross-sectional images obtained from scans with angulated catheter positions to equivalent images arising from scans with parallel catheter positions (Figure 4.9 to 4.11).

Overall, the effects of non-central and non-coaxial catheter positions on the image quality, seem to be less striking for forward-viewing IVUS than for side-viewing IVUS. This is likely to be an advantage of the forward-viewing IVUS in performing serial studies, where of course the catheters can never be placed identically in the lumen. The only exception to this is the conical scan, for the reasons mentioned in section 4.6.2.

## **4.7 Conclusion**

Following the assessment of image quality in a number of 3D data sets acquired with the various scanning patterns under investigation, it becomes evident that compounding has a great impact in improving the image quality. Nevertheless, image compounding is not clinically practical.

Referring to the remaining practical options, the conical scan proved to be the least favourable in terms of image quality and size of field of view. The quality provided by the fan scanning pattern is greatly affected when the frame density in the scanned volume is reduced. Subsequently, the fan scan is not very promising for real-time application. On the other hand, the rotational and the spiral scans produce the best image quality after the compound scan and have the potential for real-time imaging. Based on the above remarks, the spiral and rotational patterns are the preferred choices for forward-viewing IVUS as far as image quality and practical real-time application are concerned.



## **CHAPTER 5**

# **QUANTITATIVE ACCURACY OF THREE DIMENSIONAL FORWARD-VIEWING IVUS SCANNING PATTERNS**

### **5.1 Introduction**

Quantitative IVUS is used in clinical practice for assessing the extent of atherosclerosis before and after interventional treatment. Area and volume measurements are facilitated by image segmentation of 2D cross-sectional images, whereby the contours of vessel structures are identified. Lumen area measurements for example, are based on measuring the area enclosed by the luminal contour, i.e. the border between the lumen and the inner wall surface.

This chapter refers to the accuracy of the examined forward-viewing IVUS scanning patterns when used for quantitative applications. At first, a review of image segmentation techniques used in IVUS is presented along with background theory of edge detection. The software scheme developed for lumen area measurements is described and results of the quantitative analysis are presented and statistically compared.

## **5.2 Image segmentation in side-viewing IVUS**

A variety of algorithms have been applied to segmentation of side-viewing IVUS images. These can be classified as manual, automatic and semiautomatic.

The manual segmentation was the first approach used to analyse IVUS images. It requires extended user input, as the user tracks the lumen border manually frame by frame. It is a tedious and time consuming approach and leads to large intra-observer and inter-observer variability (Bouma et al. 1996; Potkin et al. 1990). The impracticality of manual segmentation directed the research towards more automated approaches.

Fully automated segmentation algorithms based on thresholding have extensively been used, especially in the early days of 3D IVUS. In these techniques, a pixel (in 2D images) or a voxel (in 3D images) is classified as part of a structure if its intensity value is between a minimum and a maximum value defined by the operator (Cavaye et al. 1991; Hu and Hu 1995; Rosenfield et al. 1991; Rosenfield et al. 1992). The performance of these methods is hugely dependent on the selected threshold values and is greatly affected by the presence of image artefacts like the ones arising from calcific plaque. An alternative automated approach is the use of acoustic quantification (Hausmann et al. 1994; von Birgelen et al. 1996d). The application of this method is affected by the quality of the acquired IVUS images and by non-central positions of the IVUS catheter in the lumen (Hausmann et al. 1994; von Birgelen et al. 1996b and 1997). These are probably the reasons why this technique has not become more popular.

Lately, semiautomatic segmentation methods have been favoured. They require user input only at the beginning of the procedure. Border detection is based either on adaptive region growing (Brathwaite et al. 1996) or on dynamic contour models which operate by minimising the energy of dynamic cost functions (Li et al. 1993; Sonka et al. 1995a and 1995b). The latter approach is most commonly used and is based on initial information provided by the user to detect the lumen border in an initial image. This initially detected border is then used as input for detecting the

borders in subsequent images. The user input can be either in the form of regions of interest in an initial cross-sectional image (Sonka et al. 1995a and 1995b) or in the form of initial border points along two longitudinal slices of the reconstructed volume, which serve as starting points for tracking the longitudinal lumen borders, which in turn provide starting points for tracking the cross-sectional lumen borders (Li et al. 1993; Li 1997).

### **5.3 Considerations for image segmentation in forward-viewing IVUS**

In a comparative study on side-viewing IVUS data (Bouma et al. 1996), the dynamic contour models have shown better performance than the region growing and thresholding methods, and have also appeared to be comparable or even preferable to manual segmentation methods. This was further established by van der Lugt et al. (1998), who showed that a contour analysis system provided area measurements in agreement with manual border tracing and showed low inter-observer and intra-observer variability. Based on these findings, a dynamic contour model was chosen for the purposes of image segmentation and lumen area measurements in this study of forward-viewing IVUS. The model was applied to 2D cross-sectional slices reconstructed from the acquired 3D data sets.

Dynamic contour models require an edge image as input which can be provided by gradient operators. According to Bovik (1988), standard gradient operators (such as Sobel or Roberts edge detectors) perform poorly in the presence of speckle in ultrasound images. This is because the local variance of the speckle varies with the local image intensity. In fact, the speckle intensity is multiplicative with the underlying image intensity, causing the statistics of the image gradient to vary in turn with the image intensity too. On the other hand, second derivative operators have the advantage of being invariant to the image intensity over uniform reflectance regions, therefore they are more suitable for edge detection in speckled images.

### **5.3.1 Edge detection**

Whenever there is an intensity change in the original 2D image  $I(x,y)$ , a zero crossing occurs at the output of the second directional derivative of the image intensity. In order to characterise intensity edges, the directional derivative should be taken into the orientation formed locally by the zero crossings. Marr and Hildreth (1980) introduced the use of the computationally efficient Laplacian operator

$$\nabla^2 f = \frac{\partial^2 f}{\partial x^2} + \frac{\partial^2 f}{\partial y^2} \quad (5.1)$$

which is orientation independent. There is a difference between the zeros of the second directional derivative and those of the Laplacian, however this difference is small if the intensity surface of the image has small curvature.

Differentiation of a noisy function such as ultrasound backscatter is an ill-posed problem and can be regularised by the use of smooth low pass filters (Torre and Poggio 1986). According to Marr and Hildreth (1980), the optimal filter should be smooth and localised both in the frequency and time domain, having small frequency and spatial variances. These two requirements are conflicting and there is only one distribution which optimises their relationship, the Gaussian, which for the 2D case is described as

$$G(x,y) = \frac{1}{2\pi\sigma^2} \exp\left(-\frac{(x^2 + y^2)}{2\sigma^2}\right) \quad (5.2)$$

where  $\sigma$  is the space constant.

When images are smoothed with a 2D filter such as the Gaussian in equation (5.2), their intensity curvature is reduced and the Laplacian  $\nabla^2$  performs almost as well as the second directional derivative (Torre and Poggio 1986). Based on the above, and according to what Marr and Hildreth (1980) have proposed for edge detection, the original 2D image  $I(x,y)$  is firstly convolved with a 2D Gaussian filter  $G(x,y)$  and then the Laplacian  $\nabla^2$  operator is performed on the Gaussian filtered image :

$$\nabla^2(G(x,y) * I(x,y)) \quad (5.3)$$

which is equal to

$$(\nabla^2 G(x,y)) * I(x,y) \quad (5.4)$$

where

$$\nabla^2 G(x,y) = \left( \frac{1}{2\pi\sigma^4} \right) \left( 2 - \frac{(x^2 + y^2)}{\sigma^2} \right) \exp\left( -\frac{(x^2 + y^2)}{2\sigma^2} \right) \quad (5.5)$$

is the Laplacian of Gaussian operator (LoG) and the \* represents convolution.

Edge detection can thus be based on finding the zero crossings of the convolution of the LoG operator with the original image  $I(x,y)$ . Zero crossings are the points where the response of the above operation goes through a zero value in a local 3x3 neighbourhood. It is possible to decompose the LoG operator into a summation of two separable filters (Huertas and Medioni 1986):

$$\nabla^2 G(x,y) = h_{12}(x,y) + h_{21}(x,y) \quad (5.6)$$

or

$$\nabla^2 G(x,y) = h_1(x)h_2(y) + h_2(x)h_1(y) \quad (5.7)$$

with

$$h_1(z) = \frac{1}{\sqrt{2\pi}\sigma^2} \left( 1 - \frac{z^2}{\sigma^2} \right) \exp\left( -\frac{z^2}{2\sigma^2} \right) \quad (5.8)$$

$$h_2(z) = \frac{1}{\sqrt{2\pi}\sigma^2} \exp\left( -\frac{z^2}{2\sigma^2} \right) \quad (5.9)$$

in order to simplify the software implementation of the convolution  $\nabla^2 G * I$ . The gradient of the edge is calculated at the zero crossings in 4 directions (horizontal, vertical and two diagonals) and the maximum gradient is used as edge strength.

By applying this procedure to a set of successive 2D cross-sectional slices of the reconstructed volume, a set of 2D edge images is derived and can be used as input for a dynamic contour model.

### 5.3.2 'Snake' dynamic contour model

A contour model extensively used in image segmentation, is the 'snake' model firstly proposed by Kass et al. (1988). A snake is an energy minimisation controlled continuity spline which operates under the influence of image forces and internal energy forces. The contour is represented by a vector  $v(s) = (x(s), y(s))$ , having the arc length  $s$  as a parameter. The energy of the spline is given as

$$E = \int_0^1 E_{snake}(v(s))ds = \int_0^1 (E_{int}(v(s)) + E_{image}(v(s)))ds \quad (5.10)$$

where  $E_{int}$  represents the internal energy of the contour and  $E_{image}$  represents the image forces. The internal energy of the spline can be written as

$$E_{int} = (\alpha(s)|v_s(s)|^2 + \beta(s)|v_{ss}(s)|^2) / 2 \quad (5.11)$$

and consequently the energy of the snake is described as

$$E = \int_0^1 (\alpha(s)E_{cont} + \beta(s)E_{curv} + \gamma(s)E_{image})ds \quad (5.12)$$

The first term (*continuity* energy) represents the elasticity of the curve and the values of the coefficient  $\alpha$  determine the extent to which the spline is allowed to stretch at a specific point. The second term (*curvature* energy) represents the rigidity of the curve with the values of coefficient  $\beta$  determining the extent to which the spline is allowed to bend at a point. If  $\alpha$  is zero at a point of the curve then a discontinuity can occur at that point; if  $\beta$  is zero then a corner can develop there. The mechanical properties of the snake are, in other words, dependent on the values of  $\alpha$  and  $\beta$  which can be user specified or dynamically changed throughout the energy minimisation procedure.

The image forces are the edge strengths as determined by the edge image according to equation (5.4). Minima of  $E_{image}$  lie on zero crossings of  $\nabla^2 G * I$ . This means that the snake is attracted to zero crossings which, as mentioned in section 5.3.1, define edges of the original image.

In the current study, the implementation of a snake model for tracking the luminal contour in 2D cross-sectional forward-viewing IVUS images, is according to

the ‘greedy algorithm’ proposed by Williams and Shah (1992). The user inserts a number of points  $v_i(x_i, y_i)$  for the snake around and close enough to the lumen border on the edge image, and defines the initial values of the parameters  $\alpha_i$ ,  $\beta_i$  and  $\gamma_i$  for each point. The continuity term is given by

$$E_{cont} = \bar{d} - |v_i - v_{i-1}| = \bar{d} - \sqrt{(x_i - x_{i-1})^2 + (y_i - y_{i-1})^2} \quad (5.13)$$

where  $\bar{d}$  is the average distance between the points, while the curvature term is given by

$$E_{curv} = |v_{i-1} - 2v_i + v_{i+1}|^2 = (x_{i-1} - 2x_i + x_{i+1})^2 + (y_{i-1} - 2y_i + y_{i+1})^2 \quad (5.14)$$

Typical initial values for the parameters are  $\alpha=1$ ,  $\beta=1$  and  $\gamma=1.2$ . The algorithm iterates and during each iteration the energy for each point and for its local 3x3 neighbourhood is calculated. The point in the neighbourhood resulting in the lowest energy level is then selected as the new location of the initial point. The curve progressively shrinks and converges onto the lumen border. The user needs only to provide starting snake points for the first image. The converged points from that image are used as starting points for the subsequent image and so on. Once the snake tracks the lumen edge, it locks on to it and follows its shape from image to image (Kass et al. 1988).

## **5.4 Quantitative measurements and analysis**

### **5.4.1 Lumen area and volume measurement**

In each segmented 2D cross-sectional image, spline interpolation is used to connect the snake points and display a closed continuous curve. The number of pixels enclosed by the curve is counted by software and converted to area size in  $\text{mm}^2$ . In this way, the lumen area is measured for a number of successive slices



corresponding to a segment of the vessel phantom, and can be integrated to provide an estimation of the lumen volume of the particular phantom segment according to

$$V = H \cdot \sum_{i=1}^N A_i \quad (5.15)$$

where  $V$  is the lumen volume of the vessel phantom segment,  $A_i$  is the lumen area in cross-sectional image  $i$ ,  $H$  is the thickness of the cross-sections (equal to a pixel dimension), and  $N$  is the total number of segmented 2D cross-sectional images.

### **5.4.2 Statistical analysis**

The 5° angle of the non-coaxial position of the catheter used in this work was too small to cause significant errors in measuring luminal dimensions (Geselschap et al. 1998; Thrush et al. 1997). Therefore, it was considered adequate to concentrate on the assessment of quantitative accuracy for catheter positions parallel to the long axis of the vessel phantom, both concentric and eccentric.

The accuracy of lumen area measurements was examined for the spiral, the rotational and the fan scan. As regards the conical scan, due to the partial lack of information ahead of the catheter tip, there is no confidence whether the lumen border is fully visualised or not. Hence, this scanning pattern could not be included in the tests for quantitative accuracy.

A total of 30 3D data sets were quantitatively assessed for the combination of 5 vessel phantoms, 2 catheter positions (concentric and eccentric in the lumen while parallel to the phantom long axis) and 3 scanning patterns (spiral, rotational and fan). The segmentation procedure was repeated five times for each of the 3D data sets. At each repetition, a different set of valid starting points was provided as input to the snake algorithm. In this way, five lumen measurements were obtained and their mean was used to plot a representative lumen profile for each 3D data set.

All experiments were carried out at 22-23°C. The data sets for each particular phantom were acquired within two hours. Prior to that, the vessel phantom was allowed to soak in the water tank for approximately 30 minutes in order to reduce its



swelling during acquisition, as well as ensure a lumen surface free of air bubbles. During the actual data acquisition time, the increase in phantom lumen area due to swelling was not greater than 2%. The known manufacturing dimensions of the vessel phantoms were used to allow a straightforward calculation of 'design' lumen areas at the sites of measurement, assuming parallel positions of the catheter. The measured lumen profiles were plotted against the 'design' ones for comparison purposes. The differences between measured and 'design' lumen areas were also calculated and plotted as percentage error plots. Paired t-tests between the measured lumen areas were performed to indicate significant or non-significant differences arising from the use of the different scanning patterns. A p value of 0.05 defined the significance level. The maximum absolute lumen area error, the RMS lumen area error throughout the set of segmented cross-sectional slices, and the percentage volume error were used as accuracy indices.

Finally, the effect of catheter positions on the measurements of lumen area was assessed by paired t-tests between the data sets arising from concentric and eccentric catheter positions in the phantom lumen.

## **5.5 Results**

### **5.5.1 Segmented images and lumen cast display**

The snake algorithm successfully tracked the luminal border in the majority of the images, irrespective of the shape and size of the stenosis. Examples of luminal border detection on cross-sectional images are shown in Figure 5.1.

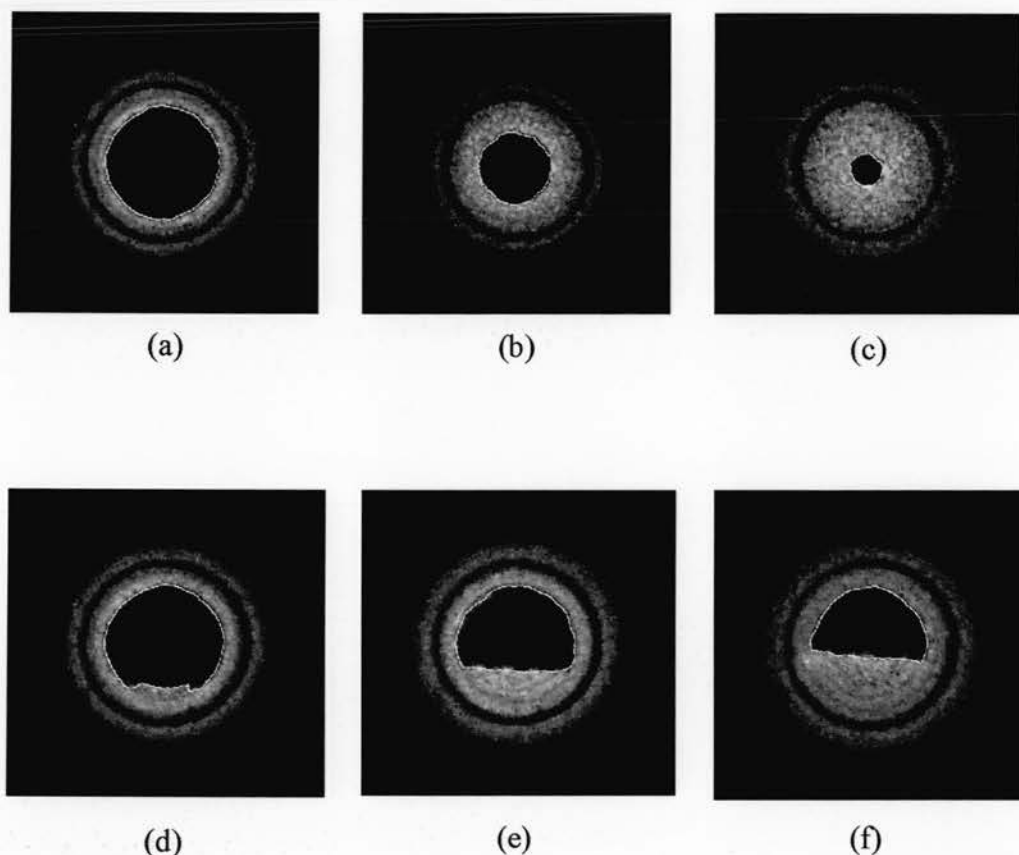


*Figure 5.1 : Detection of luminal border on reconstructed 2D cross-sectional images of the vessel phantom with the symmetrical cylindrical stenosis (a, b and c) and the vessel phantom with the 'single hump' eccentric stenosis (d, e and f).*

Only at large distances from the focal zone of the transducer, did the algorithm fail to provide reliable segmentation. This was due to poor quality of the reconstructed 2D images caused by degraded lateral resolution and decreased signal to noise ratio at those depths. For the successfully segmented length of the phantoms, the lumen cast was displayed (Figure 5.2).

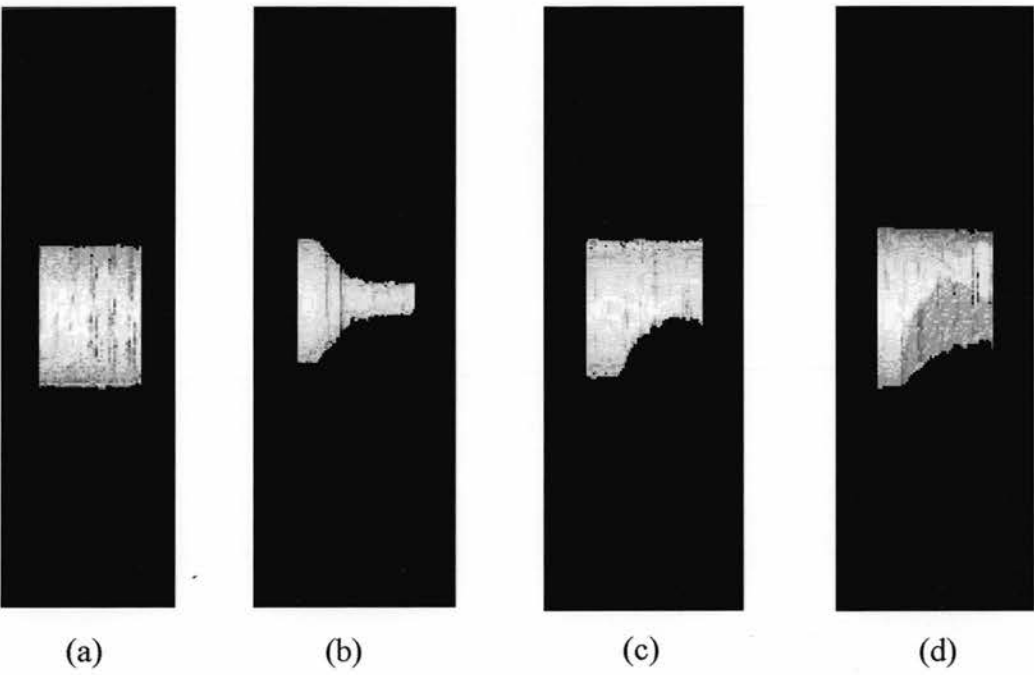


*Figure 5.2 : Lumen cast displays: (a) 'Healthy' vessel phantom, (b) Phantom with symmetrical cylindrical stenosis, (c) Phantom with eccentric stenosis, and (d) same phantom as in (c) but displayed at different orientation in space.*

### **5.5.2 Accuracy of lumen area measurements**

Lumen profile plots were created by measuring the lumen area throughout a set of successfully segmented successive cross-sectional slices, starting from near the transducer (left part of the longitudinal images in Figures 5.3a to 5.7a) and moving deeper into the vessel phantom away from the transducer (right part of the longitudinal images in Figures 5.3a to 5.7a). Lumen profile plots are shown in Figures 5.3b to 5.7b for concentric catheter positions and for various vessel phantoms used in this work, while the corresponding error plots are shown in Figures 5.3c to 5.7c.

At the first instance, looking at the profile plots for the ‘healthy’ vessel phantom (Figure 5.3), the curves derived from the scanned data sets seem to be close to the ‘design’ lumen area and the maximum errors are in the range of 7%.

The situation changes, when observing the curves referring to phantoms with stenoses. It can be seen that for parts of the scanned volume lying at short to medium range distances from the transducer face, the experimental curves are in agreement with the ‘design’ ones within the levels seen for the ‘healthy’ phantom. However, for parts of the volume lying at large distances beyond the focal zone of the transducer, the deviations of the measured areas from the ‘design’ ones are increased, especially for the spiral scan. As seen from the error plots, the size and composition of the stenosis affect the magnitude of the error in lumen area measurements.

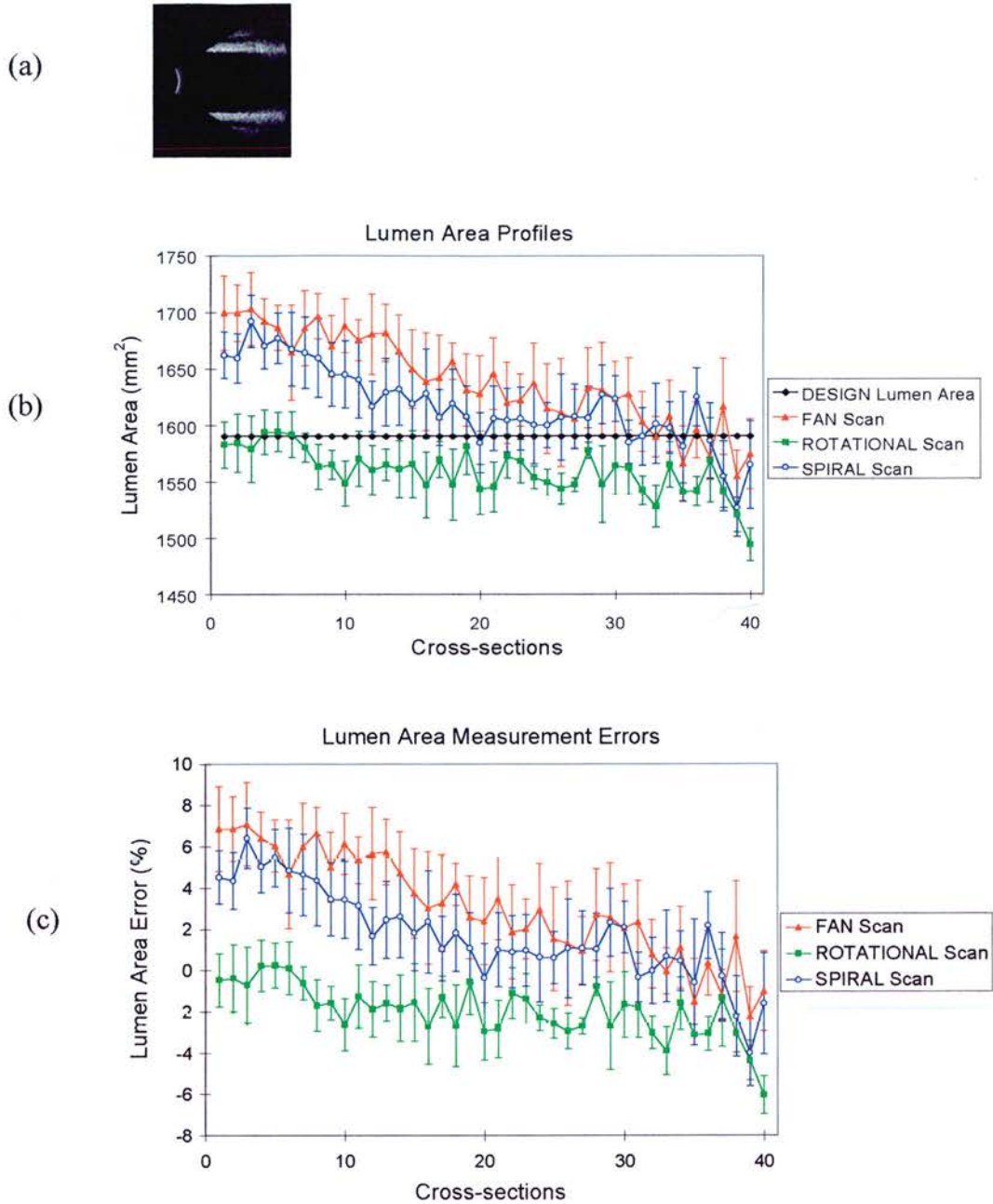


*Figure 5.3 : Lumen area profiles (b) derived from the 3D data sets acquired by the fan, rotational and spiral scans for the ‘healthy’ vessel phantom shown in (a). Lumen area is measured at 2D cross-sections starting near the transducer and moving deeper into the phantom, from left to right on the image in (a). Equivalent error plots are given in (c). Error bars denote two standard errors. The catheter is concentric in the lumen and parallel to the long axis of the phantom.*

For the eccentric stenoses, both the 'single hump' (Figure 5.4) and the 'double hump' shape (Figure 5.5), the errors for the sector scans (fan or rotational) are mostly within the 10-15% level. For the same phantoms, the spiral scan errors can reach magnitude levels of 23-30%.

The phantom with the 'hard plaque' and the higher gain setting used for scanning it, provide more unfavourable conditions for measuring lumen dimensions. The ultrasound beam is effectively broader due to the higher gain setting and higher backscatter from the 'hard plaque', resulting in lumen narrowing on the ultrasonic images. Thus, lumen areas measured in the cross-sections are underestimated, with the errors (Figure 5.6) being higher than those seen for the phantom with a stenosis identical in shape but of softer material (Figure 5.5). The error magnitude is now up to 45% for the spiral scan, up to 30% for the fan scan and 20% for the rotational scan. Once again, the sector scans look more accurate than the spiral scan. More significantly, the rotational scan looks to be affected less than the fan scan. In fact its error levels are not much greater than they were for the phantom of Figure 5.5.

The phantom with the symmetrical cylindrical stenosis seems to provide two areas of interest for performance tests of the scanning patterns. The first is the area before the narrow lumen channel, where the patterns appear to be accurate within a range of 20%. The second is within the narrow lumen channel itself, where the accuracy is worse. The deeper in this channel, the stronger the underestimation of luminal dimensions. The sector scans produce errors with magnitudes up to 30-40%, while the spiral scan results in error levels of 50-60% for the longest distances from the transducer face, deep in the channel (Figure 5.7).

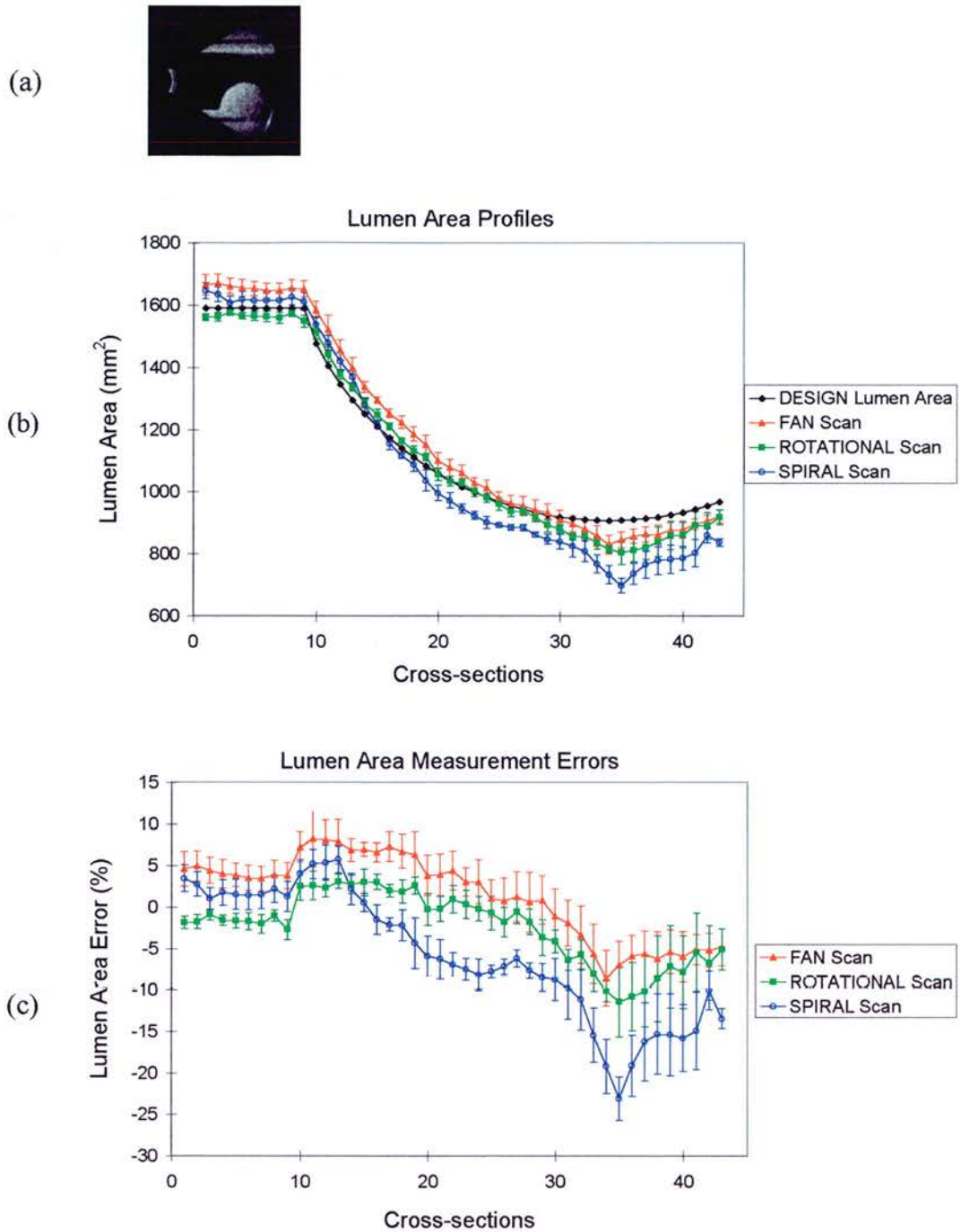


*Figure 5.4 : Lumen area profile (b) and error plots (c) as in Figure 5.3, for the vessel phantom with the 'single hump' eccentric stenosis (a). Error bars denote two standard errors. The catheter is concentric in the lumen and parallel to the long axis of the phantom.*



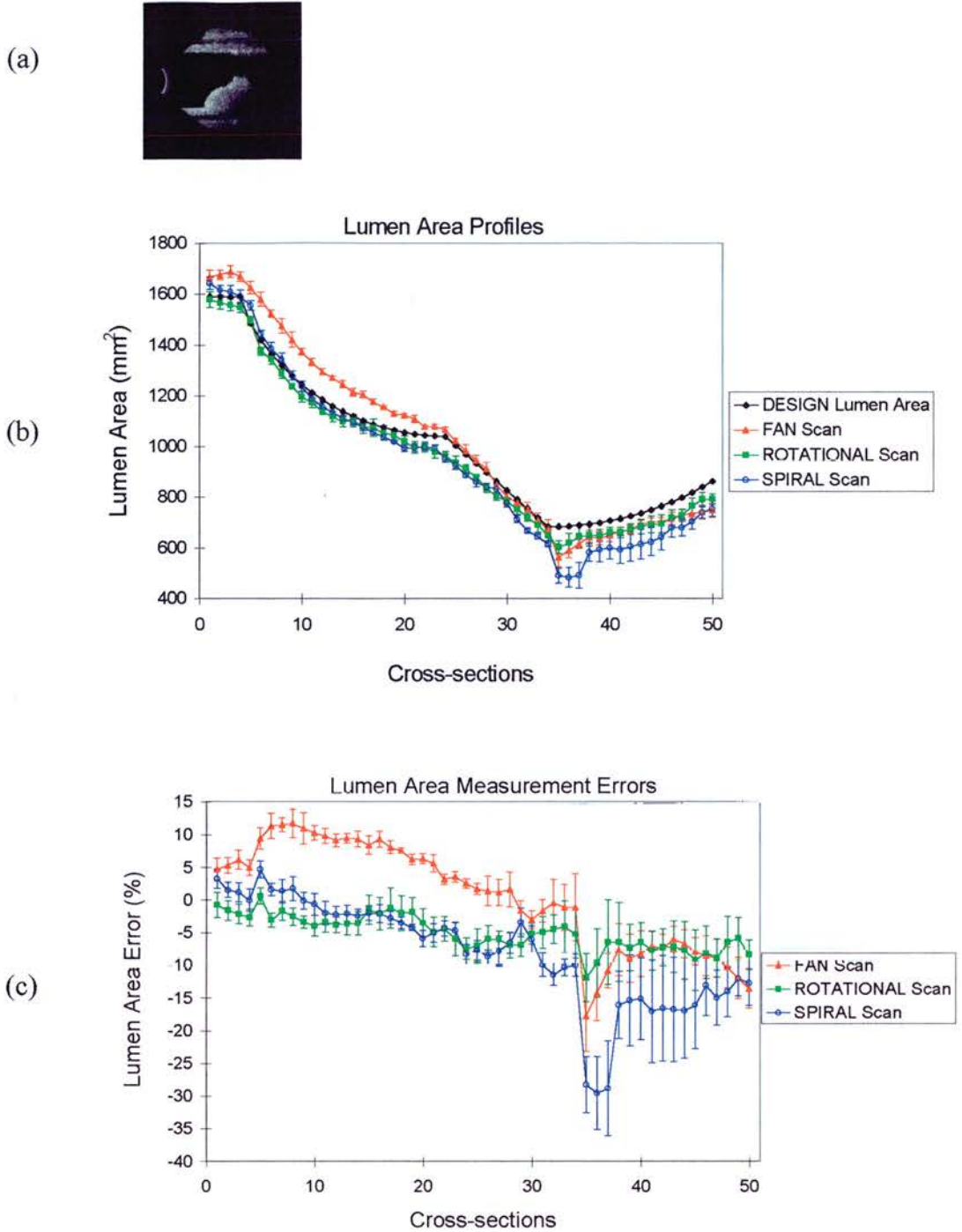


*Figure 5.5 : Lumen area profile (b) and error plots (c) as in Figure 5.3, for the vessel phantom with the 'double hump' eccentric stenosis (a). Error bars denote two standard errors. The catheter is concentric in the lumen and parallel to the long axis of the phantom.*



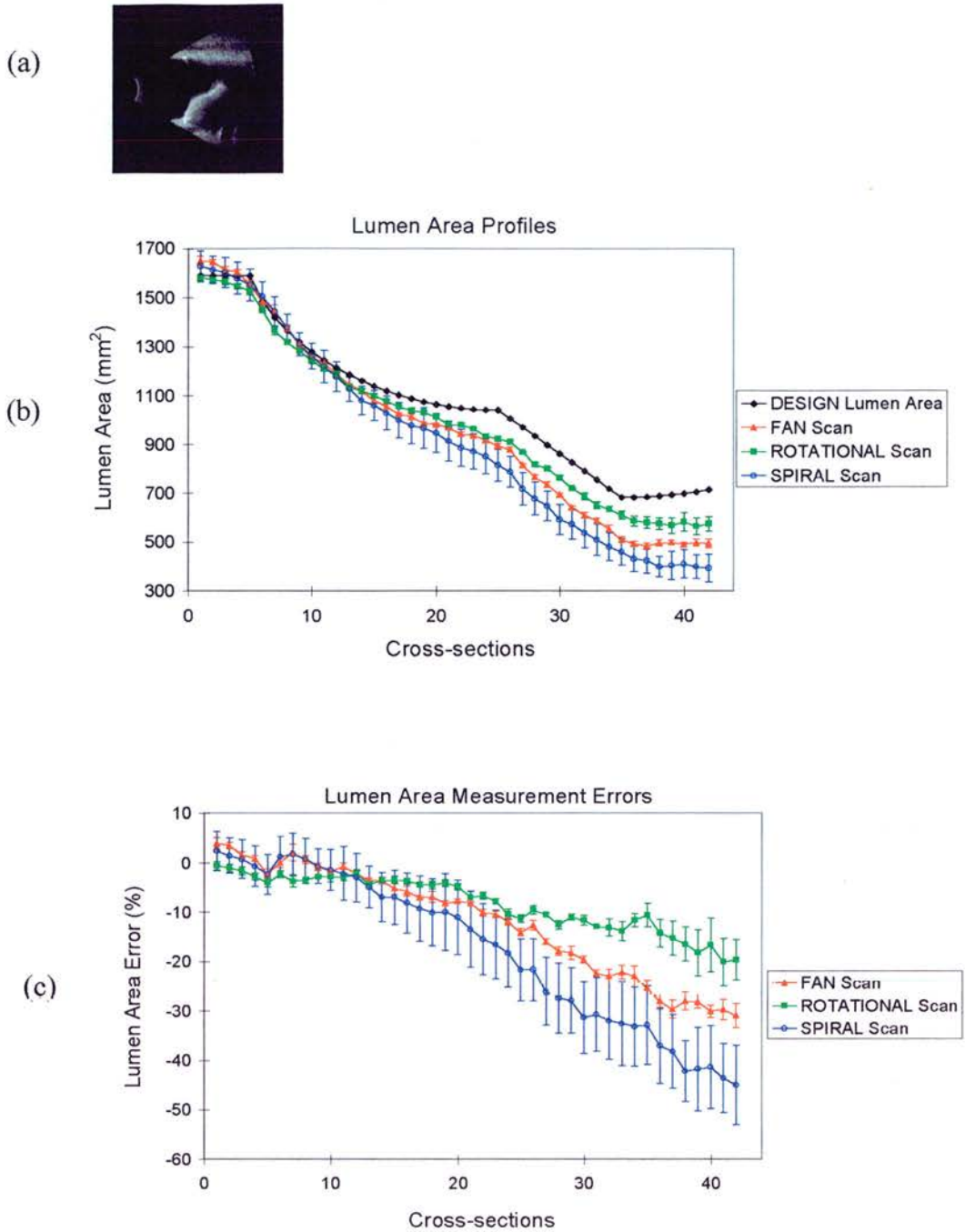


*Figure 5.6 : Lumen area profile (b) and error plots (c) as in Figure 5.3, for the vessel phantom with the 'hard double hump' eccentric stenosis (a). Error bars denote two standard errors. The catheter is concentric in the lumen and parallel to the long axis of the phantom.*

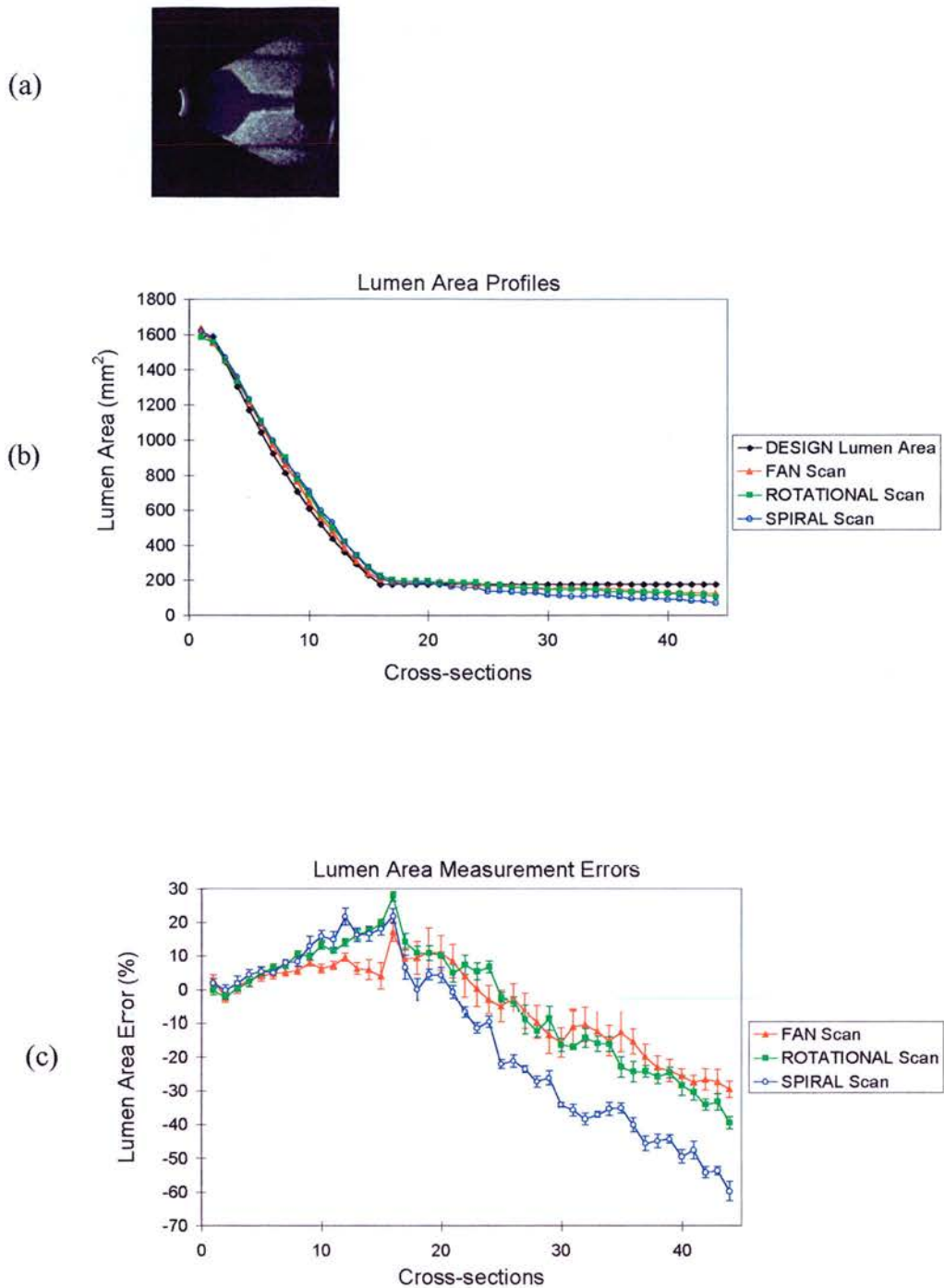


*Figure 5.7 : Lumen area profile (b) and error plots (c) as in Figure 5.3, for the vessel phantom with the symmetrical cylindrical stenosis (a). Error bars denote two standard errors. The catheter is concentric in the lumen and parallel to the long axis of the phantom.*

The observations mentioned so far are for volumes scanned with the catheter concentric in the lumen and parallel to the long axis of the vessel phantom. When volumes acquired with eccentric and parallel catheter positions were used for quantitative analysis, the results appeared similar. The trend was to slightly underestimate the luminal dimensions in comparison with the values derived with concentric catheter positions. This was true for all the vessel phantoms scanned with the rotational scan. It was also true for the fan and the spiral scans, apart from the phantom with the 'single hump' eccentric stenosis where overestimation of luminal dimensions was observed instead. When paired t-tests were performed on a cross-section by cross-section basis on the lumen area measurements derived from the data sets acquired with concentric and eccentric catheter positions, the rotational scan proved the most consistent of all. For 3 out of 5 vessel phantoms, the differences of luminal dimensions were not significant at 5% level for this pattern. In the case of the fan scan, the differences were not significant for one phantom only, while for the spiral scan the differences appeared significant at 5% level for all the phantoms. Differences between the corresponding volume estimations varied from practically 0 to 7%, with the spiral scan providing the highest difference levels (Table 5.1).

The quantitative accuracy of the scanning patterns over segments of vessel phantoms can be described by the RMS lumen area errors and the percentage volume errors. Table 5.2 lists these errors between experimental data acquired using the rotational, fan and spiral scanning patterns at concentric/eccentric catheter positions, and the 'design' values known from the manufacturing of the vessel phantoms. The rotational scan appears to have the smallest RMS lumen area errors in almost all of the cases, while the spiral scan usually produces the worst error levels of the three. The fan scan performs in between. In the majority of the data sets, differences between lumen area measurements provided by the different scanning patterns are significant at 5% level (Table 5.3). The errors in volume estimation appear smaller than the errors in individual lumen area estimations, due to cancelling out of over and underestimated measurements throughout the 2D image sets. Volume errors are

mostly below 10% and once again the rotational scan performs more accurately than the other two.

*Table 5.1 : Comparison of lumen area and volume measurements between data sets acquired at concentric and eccentric catheter positions. S and NS denote significant and non-significant difference at 5% level respectively.*

<b>Vessel Phantom</b>	Eccentric vs Concentric Paired t-test (p=0.05) on Lumen Area measurements			Volume Difference (%) $\frac{(Eccentric - Concentric)}{Concentric} \times 100\%$		
	<i>Rotational Scan</i>	<i>Fan Scan</i>	<i>Spiral Scan</i>	<i>Rotational Scan</i>	<i>Fan Scan</i>	<i>Spiral Scan</i>
'Healthy'	NS	NS	S	-0.05	-0.36	-0.89
Single hump eccentric stenosis	S	S	S	-1.39	4.04	7.03
Double hump eccentric stenosis	NS	S	S	-0.93	-0.75	-2.45
'Hard' plaque	S	S	S	-1.94	-2.23	-5.71
Symmetrical stenosis	NS	S	S	-4.65	-3.22	-4.99

*Table 5.2 : Errors between lumen area and volume measurements based on experimental data acquired using the rotational, fan and spiral scanning patterns at concentric/eccentric catheter positions, and the 'design' values known from the manufacturing of the vessel phantoms.*

Catheter Location	Vessel Phantoms	Lumen Area RMS Error (mm <sup>2</sup> )			Volume Error (%)		
		Rotational	Fan	Spiral	Rotational	Fan	Spiral
<b>Concentric</b>	'Healthy'	37.2	63.3	44.2	-2.0	3.1	1.7
	Single hump eccentric stenosis	47.2	62.0	92.0	-0.3	3.9	-4.4
	Double hump eccentric stenosis	48.7	83.8	86.7	-3.5	3.2	-5.3
	'Hard' plaque	81.4	127.8	185.0	-5.9	-8.3	-12.9
	Symmetrical stenosis	43.9	32.4	61.4	1.1	0.2	-2.4
<b>Eccentric</b>	'Healthy'	36.6	43.0	37.0	-1.8	2.2	1.3
	Single hump eccentric stenosis	52.2	104.8	59.6	-1.7	7.7	3.0
	Double hump eccentric stenosis	70.7	86.4	109.7	-4.4	3.3	-7.6
	'Hard' plaque	106.7	114.8	127.5	-6.8	-4.8	-6.1
	Symmetrical stenosis	26.6	32.4	47.4	-2.3	-3.0	-8.4

*Table 5.3 : Paired t-tests between lumen area measurements derived from the different scanning patterns. S and NS denote significant and non-significant difference at 5% level respectively.*

Catheter Location	Vessel Phantoms	Paired t-tests p=0.05		
		<i>Rotational vs Fan</i>	<i>Rotational vs Spiral</i>	<i>Fan vs Spiral</i>
<b>Concentric</b>	'Healthy'	S	S	S
	Single hump eccentric stenosis	S	S	S
	Double hump eccentric stenosis	S	S	S
	'Hard' plaque	S	S	S
	Symmetrical stenosis	<b>NS</b>	S	S
<b>Eccentric</b>	'Healthy'	S	S	S
	Single hump eccentric stenosis	S	S	S
	Double hump eccentric stenosis	S	S	S
	'Hard' plaque	S	<b>NS</b>	S
	Symmetrical stenosis	<b>NS</b>	S	S

## **5.6 Discussion and Conclusion**

The accuracy of quantitative measurements on data sets acquired with the forward-viewing scanning patterns varied with the distance of the region of measurement from the transducer face. The presence of a stenosis and its size and composition also influenced the measurements of lumen area. The best agreement between experimentally measured and 'design' lumen areas were observed for the 'healthy' phantom, with error levels below 10%. Similar error levels were also seen in phantoms with stenoses, but only for regions near the transducer or around its focal area. However, for regions lying further away, beyond the focal zone, the errors increased. The presence of stenosis increased the attenuation of ultrasound beams penetrating the plaque material and subsequently reduced the signal-to-noise ratio (SNR). This, in conjunction with broader beam in the area beyond the focal zone (i.e. poorer resolution) reduced the quality of the reconstructed images and led to underestimation of lumen areas on the ultrasound images.

The worst effects were seen on the data sets acquired with the spiral scan. This pattern suffered from severe underestimation of luminal dimensions at distances away from the transducer focus, especially in the regions where the lumen was at its narrowest. In these cases, the measured lumen areas were 40 or even 60% lower than the 'design' areas. The sector scans performed better than the spiral scan on this aspect. The reason may be found in the different principle of interpolation and reconstruction used for the sector scans and the spiral scan. The sector scans permitted scan conversion of the acquired frames onto 2D sector images, during which a first 'bilinear' interpolation stage was performed in two dimensions. Then the sector images were placed in their appropriate orientation in voxel space and a second interpolation stage was performed in three dimensions based on the principle of 'local cubic neighbourhood'. On the other hand, each individual frame acquired with the spiral scan is itself a 3D conical surface of limited thickness. It was not practical to perform a first interpolation stage in three dimensions to fill the gaps on such a thin 3D surface alone. Instead, all the lines from all the acquired frames were



directly arranged on conical surfaces placed in appropriate positions in voxel space and after that, the ‘local cubic neighbourhood’ interpolation was performed in three dimensions. It appears that the additional 2D interpolating stage in the sector scans contributed towards a more accurate interpolation and reconstruction at boundaries of structures, which proved beneficial for area measurements.

Overall, the rotational scan proved the most accurate pattern. In the majority of the examined data sets, it came up with the smallest absolute and RMS lumen area errors, as well as volume errors (Table 5.4). Moreover, it seemed to be the least affected from non-central catheter positions in the lumen (Table 5.1).

In clinical applications, accurate measurement of the minimum lumen size in a vessel segment is of great importance, since it forms the basis for selecting the size of the treatment device. If forward-viewing IVUS were to be used for decision making in such a situation, then according to the above observations, the most suitable tool would be a system based on the rotational scan.

*Table 5.4 : Ranking of quantitative accuracy performance of the rotational, fan and spiral scanning patterns. The numbers indicate how many times out of the total each pattern is classified in the specific rank of accuracy.*

Rank position	RMS accuracy			Volume accuracy		
	<i>Rotational</i>	<i>Fan</i>	<i>Spiral</i>	<i>Rotational</i>	<i>Fan</i>	<i>Spiral</i>
1 <sup>st</sup>	9	1	0	4	4	2
2 <sup>nd</sup>	1	6	3	5	3	2
3 <sup>rd</sup>	0	3	7	1	3	6



## CHAPTER 6

# A THREE DIMENSIONAL FORWARD-VIEWING IVUS IMAGING SYSTEM

### 6.1 Introduction

Up to this point, a number of scanning patterns have been investigated for use in 3D forward-viewing IVUS imaging. The patterns were implemented with the aid of a versatile scaled-up mechanical scanning system. Scaled-up tubular vessel phantoms made of tissue mimicking material were used as test objects. The phantoms simulated cases of healthy vessel, symmetrical and eccentric stenoses as well as hard plaque. A large number of images were acquired to allow an extensive assessment of the image quality provided by the scanning patterns and the factors which affect it. The scanning patterns were also evaluated with regard to the accuracy of quantitative measurements of lumen area and volume.

In this chapter, issues relating to clinical use and miniaturised construction will also be taken into consideration in order to complete the frame of comparison among these patterns and help identify the most promising one for practical clinical application. Following that, the design and development of a small scale system for three dimensional forward-viewing IVUS imaging of human arteries *in vitro* will be described. This new imaging system is based on a mechanical device implementing the scanning pattern regarded as the most suitable one.

## **6.2 Clinical utility of the various scanning patterns**

Frames of the conical and the spiral scans are acquired on 3D conical surfaces, however, it is more convenient to display them as 2D rectangular images for simplicity and easier understanding of the scanned features. The rotational and fan scans acquire data on 2D sector planes and the individual acquisition frames can be displayed as sector images, exactly as they are acquired. In this aspect the sector scans are more advantageous over the conical and spiral scans.

During a pull-back conical scan, the early frames provide the most information about the stenosis ahead of the catheter, while the subsequent ones display information about the proximal 'healthy' part of the vessel (Figure 3.7). All the frames image the vessel wall, however the visualisation of the stenosis is incomplete, as already mentioned in section 4.6.2.

The spiral scan acquires frames with the catheter at a fixed position with respect to the vessel. During acquisition the angle between the beam and the long axis of the vessel is increased, frame after frame. The early frames provide information about any stenosis located at or near the centre of the lumen but no information about the vessel wall. As the ultrasound beam deviates from the long axis of the vessel, information about the vessel wall appears in the display progressively, while the information about the stenosis lying ahead reduces (Figure 3.8). It is clear that the information provided by an individual frame acquired with the spiral scan is not always adequate for clinical use and it becomes essential to complete the whole volume acquisition and reconstruction before any display of clinically useful data.

The fan scan acquires frames with the catheter at a fixed position with respect to the vessel as in the case of the spiral scan. The early frames display information about the vessel wall, and as the orientation of the acquisition frame progressively approaches the centre of the lumen, any existing stenosis appears on the display. Then the frame orientation starts to deviate from the lumen centre heading again for the vessel wall. As seen from the images in Figure 3.10, only the frames in the

central region of the acquired volume can provide an image of immediate clinical use from a forward-viewing perspective. Hence, as for the spiral scan previously, it is necessary to acquire and reconstruct the whole volume in order to obtain more clinically useful data for display.

The rotational scan also acquires frames with the catheter at a fixed position with respect to the vessel. Irrespective of the frame angular orientation, the displayed image includes information about the vessel wall and any stenosis present at the central or the side parts of the lumen. In fact, this particular scanning pattern always provides a 2D image of a longitudinal slice of the vessel at any particular orientation of the acquisition plane (Figure 3.9). In other words, the rotational scan is capable of displaying clinically useful data for every acquired frame on a real-time 2D basis. This is a very significant feature, unique to this scanning pattern, and clearly a very strong advantage for immediate clinical use, even on two dimensions.

### **6.3 Manufacturing issues for forward-viewing IVUS catheters**

One of the reasons why forward-viewing IVUS systems have not been commercially available on a wide scale so far is the difficulty of manufacturing a small catheter of similar dimensions to the side-viewing ones. Only recently, the first flexible forward-viewing IVUS catheter of quite a small size (5 Fr) suitable for intracoronary use appeared (Liang and Hu 1997a). This catheter has a relatively simple rotating mirror design, which allows it to be used in conjunction with the mechanical motor drives designed for side-viewing catheters. However, the device scans a curved sector, which results in distortion of geometrical features. In addition, its use in 3D acquisition and reconstruction has yet to be demonstrated.

From all the forward-viewing scanning patterns examined in this study, the easiest by far to implement on a miniature device is the conical scan. The design of a catheter based on this pattern would differ very little from the typical design of mechanical side-viewing catheters. In fact, the only difference would be the

positioning of the transducer at an angle at the catheter tip, as opposed to the nearly flat positioning in the side-viewing catheters. In this way, the current technology of flexible drive shafts could be used directly, with no modifications, resulting in a relatively inexpensive disposable device.

The manufacturing complications are much greater for the other forward-viewing patterns. The spiral and the rotational scans require one sweeping and one rotational mechanism, while the fan scan requires two sweeping mechanisms. The spiral and the rotational scans could benefit from the existing rotational mechanism technology used in the side-viewing devices. The construction of a miniature sweeping mechanism though, is a challenge. The requirement for two of such mechanisms for the implementation of the fan scan means that this specific pattern might be the most difficult and most expensive to miniaturise at the catheter scale.

A number of United States patents have proposed ways of constructing mechanisms for ultrasound imaging ahead of the catheter tip, employing cables (Gardineer and Vilkomerson 1994), pin-slot arrangements (Maroney et al. 1994), or shape memory alloys (Imran 1995; Kazi et al. 1995). These designs provide some promise for overcoming the problem of implementing a miniature scanning mechanism at the catheter tip.

Recently, improvements in micro-motor technology have allowed the manufacturing of an experimental side-viewing IVUS catheter with a micro-motor incorporated at its tip to provide the scanning motion for the beam of a single element transducer (Erbel et al. 1997; Lancée et al. 1995). Images acquired with this prototype device showed good quality, comparable to that of conventional IVUS systems. The particular micro-motor was 1 mm in diameter and 2 mm long. In addition to that, silicon technology micro-gears able to move objects as heavy as 0.5 kg with a nm range displacement resolution have been manufactured (Sandia National Laboratories, New Mexico, USA). This is a very promising field and could well be used for the development of a miniature forward-viewing IVUS catheter. Micro-motors combined with silicon technology micro-gears could be the solution for a miniature sweeping mechanism at the catheter tip in order to scan the beam

across a sector. An illustration of how such a construction could be materialised is shown in Figure 6.1.

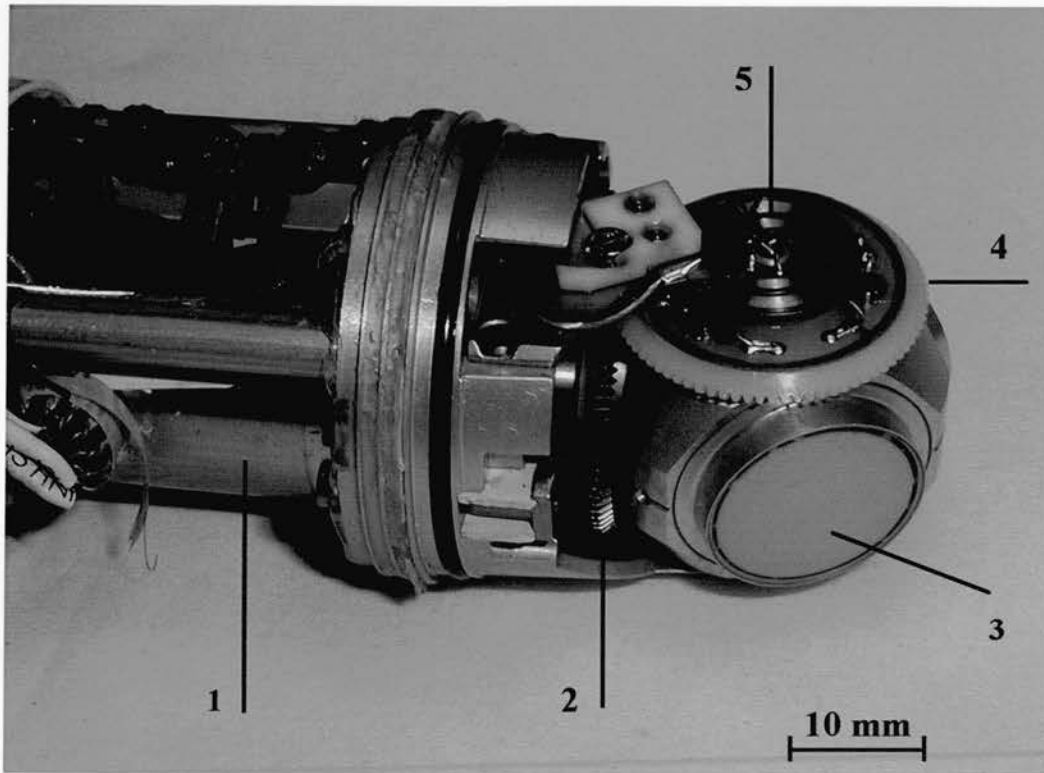


*Figure 6.1 : Photograph of a Siemens (non-micro scale) transthoracic mechanical scanner probe. The design principle of this device could be used in a miniature forward-viewing IVUS catheter. A micro-motor (1) could drive a small high frequency transducer (3) by means of micro-gears (2 and 4). Slip rings (5) would be employed for electrical coupling of the transducer.*

Latest developments in miniature arrays have led to improvements in image quality with the use of higher number of piezoceramic elements. Current side-viewing phased array IVUS systems operate with 64 PZT elements placed on the circumference of 3.5 Fr catheters (EndoSonics Corporation, Rancho Cordova, California, USA) or 2.9 Fr catheters (Intravascular Research Limited, Middlesex, UK). This technology could be considered as an alternative for the implementation of

the rotational scan in particular. A phased array could be placed at the catheter tip imaging a sector plane ahead of the catheter. It could also be combined with a typical drive shaft system to rotate the sector plane in order to scan a conical volume. The available space for an array at the tip of a catheter 3-4 Fr in diameter would be approximately  $\pi$  times less than the available space around the circumference of the catheter. This means that with the current manufacturing technology, only 20 elements or so could be placed at the catheter tip. The image quality and the steering ability provided by such a number of array elements may not be adequate (Whittingham 1991), nevertheless, the development rate of this technology does not exclude the possibility of placing larger numbers of elements at the catheter tip in the future.

#### **6.4 Choice of scanning pattern for forward-viewing IVUS**

Table 6.1 provides information on how the various forward-viewing scanning patterns are comparatively ranked according to all the issues mentioned so far, i.e. image quality, accuracy of quantitative measurements, clinical utility and miniaturised construction.

*Table 6.1 : Comparative ranking of forward-viewing scanning patterns. Four crosses denote top ranking, while one cross denotes bottom ranking. 'N/A' denotes not applicable.*

	<b>Conical Scan</b>	<b>Spiral Scan</b>	<b>Rotational Scan</b>	<b>Fan Scan</b>
<b>Image Quality</b>	+	++++	+++	++
<b>Quantitative Accuracy</b>	N/A	++	++++	+++
<b>Clinical Utility</b>	+	++	++++	+++
<b>Miniaturisation</b>	++++	+++	+++	+

According to this tabulated data, it is believed that the most promising tool for forward-viewing IVUS imaging is a system implementing the *rotational* scan. This pattern provided good image quality (chapter 4), was shown to be the most accurate in *in vitro* quantitative measurements (chapter 5), and is capable of displaying real-time 2D clinically useful information. The construction of a small flexible forward-viewing catheter for *in vivo* use, based on the rotational scanning pattern, is still a challenging task. However, the latest technology developments provide hope that the production of such a system may be possible in the near future.

## **6.5 Design of a three dimensional forward-viewing IVUS imaging system**

It was decided to construct a small scale catheter, the smallest possible within the departmental facilities, for use in 3D forward-viewing IVUS imaging of human arteries *in vitro*. The catheter would involve use of real IVUS transducers and would implement the preferred rotational scanning pattern. In this way, a valuable assessment would be performed on the use of the rotational scan for 3D forward-viewing IVUS imaging of real arterial structures.

### **6.5.1 The intravascular ultrasound scanner**

The scanner used for the *in vitro* study was a Hewlett-Packard Sonos Intravascular imaging system (Hewlett-Packard, Andover, Massachusetts, USA) shown in Figure 6.2. This system is designed to operate with 12.5, 20 and 30 MHz side-viewing catheters. It consists of appropriate electronics for transmission, reception and scan conversion, a control panel, a patient interface unit, two monitors, a Super-VHS video cassette recorder and a black & white printer. The intravascular images are obtained by connecting a catheter to the patient interface unit. This unit provides mechanical rotation of the catheter as well as coupling of the transducer with the transmission-reception electronics. In this way, cross-sectional images from



inside the arteries are displayed on the monitors. The system also allows a number of measurements to be performed including calculation of lumen diameter, circumference, cross-sectional area, plaque area, percent stenosis by diameter as well as percent stenosis by area.

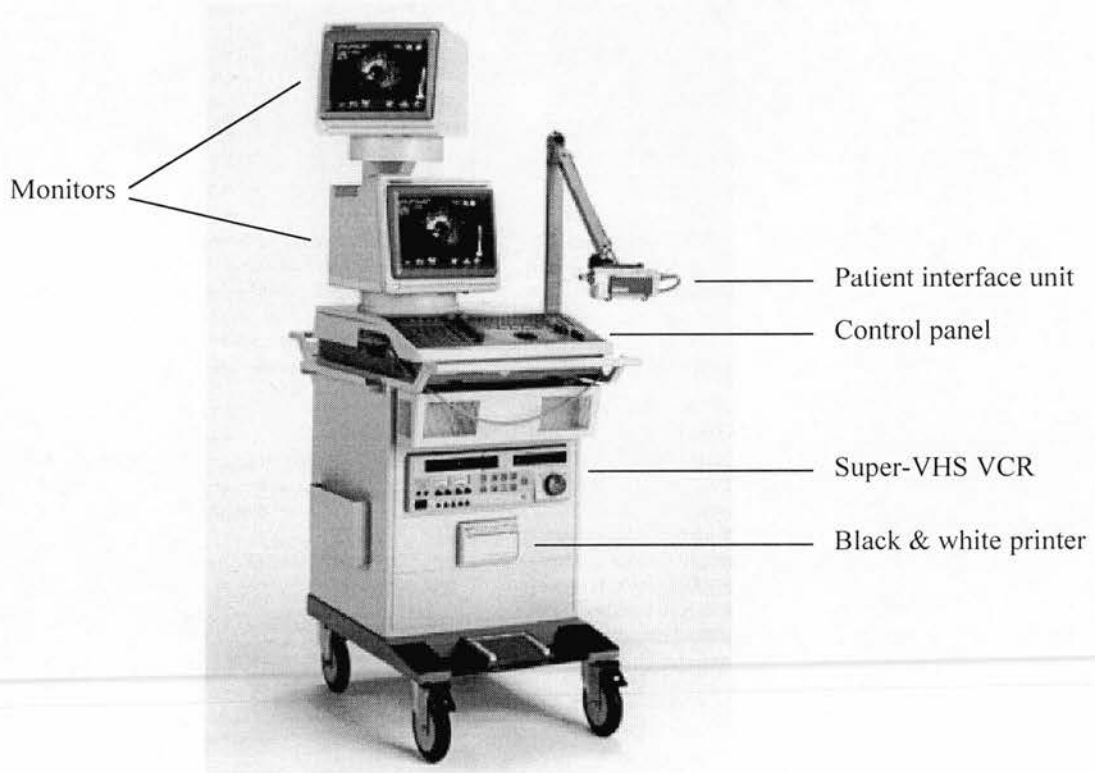


*Figure 6.2 : The Hewlett-Packard Sonos Intravascular imaging system (copyright Hewlett-Packard, Andover, Massachusetts, USA).*

An additional feature of the particular scanner used in this work was an output port allowing direct access to the RF signal as well as to the line and frame synchronisation pulses. Moreover, the manufacturer of the scanner had provided software instructions for disabling the motor rotation in the patient interface unit while allowing transmission and reception of ultrasound signals. In essence, this permits use of the transducer for A-mode imaging. The above additional features were in fact those which enabled the use of the scanner in forward-viewing imaging.



## **6.5.2 Design of the forward-viewing IVUS catheter**

The design considerations for the forward-viewing IVUS catheter can be distinguished into the ones regarding the transducer and those regarding the catheter body. All of them are described below in detail.

### **6.5.2.1 Transducer design considerations**

The transducer used in this *in vitro* study was a 30 MHz single element PZT crystal located at the tip of a 3.5 Fr side-viewing catheter (Boston Scientific Co, Watertown, Massachusetts, USA). Part of the plastic sheath near the catheter tip was cut with a blade and removed until the transducer along with another 5 cm of the distal part of the catheter shaft were exposed. The shaft of this particular catheter consists of two layers of six-strand stainless steel coils which are helically wound in opposite directions with respect to each other (ten Hoff 1993). The outer layer of the exposed distal part of the shaft was filed and removed very carefully in order to increase the flexibility and reduce the diameter of that distal part of the catheter. In this way, it was possible to bend the shaft at a point near the transducer, without damaging the device, and subsequently mount the transducer on the catheter body described in the next section.

The casing surrounding the transducer element and the catheter shaft is approximately 0.85 mm wide and 2 mm long. The length of this casing is the major factor that defines the size of the forward-viewing catheter, as it has to be fully accommodated at the tip of the forward-viewing catheter.

In these particular 30 MHz side-viewing catheters, the ultrasound beam is not emitted at exactly normal angle to the long axis of the catheter. According to data supplied by the manufacturer, the beam is emitted at a 12° forward deviation from the normal direction, something which had also been verified during previous work in the Department of Medical Physics and Medical Engineering (Spencer et al. - unpublished data). This is an important feature which needs to be accounted for when designing a device that makes use of a transducer from these side-viewing catheters.

### **6.5.2.2 Catheter body design considerations**

A stiff catheter has been constructed for use with the system of stepper motors described in section 2.4 (Figure 2.8). In the case of the *in vitro* study, only the rotational scan is employed and consequently only two motors are required for its implementation: motor SM1 for sweeping the beam across a sector plane and motor SM3 for rotating the sector plane.

The catheter comprises a small scan head mounted at the end of a stainless steel tube as shown in Figure 6.3. The part of the catheter which is intended for insertion inside arteries has an outer diameter of 3.8 mm and a wall thickness of 0.4 mm. The scan head is designed to allow a sweep motion of the transducer across a sector. It consists of a plastic wheel of 3 mm diameter and 3 mm width, upon which the transducer is mounted. The transducer is firmly placed, with use of super glue, inside a groove on the circumference of the wheel. The groove is orientated at a 12° angle to the axis of the wheel in order to compensate for the directional deviation of the transducer beam mentioned in the previous section. In this way, the resulting beam direction is aligned with the axis of the forward-viewing catheter (Figure 6.3b). The wheel is mounted on the stainless steel tube with a pair of pins. In addition to providing support, these pins allow rotation of the wheel around its axis. The wheel is made to rotate by means of a pair of very thin pulling wires (0.27 mm diameter Microcable, Carl Stahl, Süssen, Germany). The pulling wires are clamped on diametrically opposite sites of the wheel, run along the lumen of the catheter and are threaded around the motor shaft. When motor SM1 rotates, the wires pull on the wheel causing it to rotate. This motion, in turn, causes the attached transducer to sweep. The principle of operation has been illustrated earlier in Figure 2.9e and the prototype forward-viewing catheter is shown in Figure 6.4.

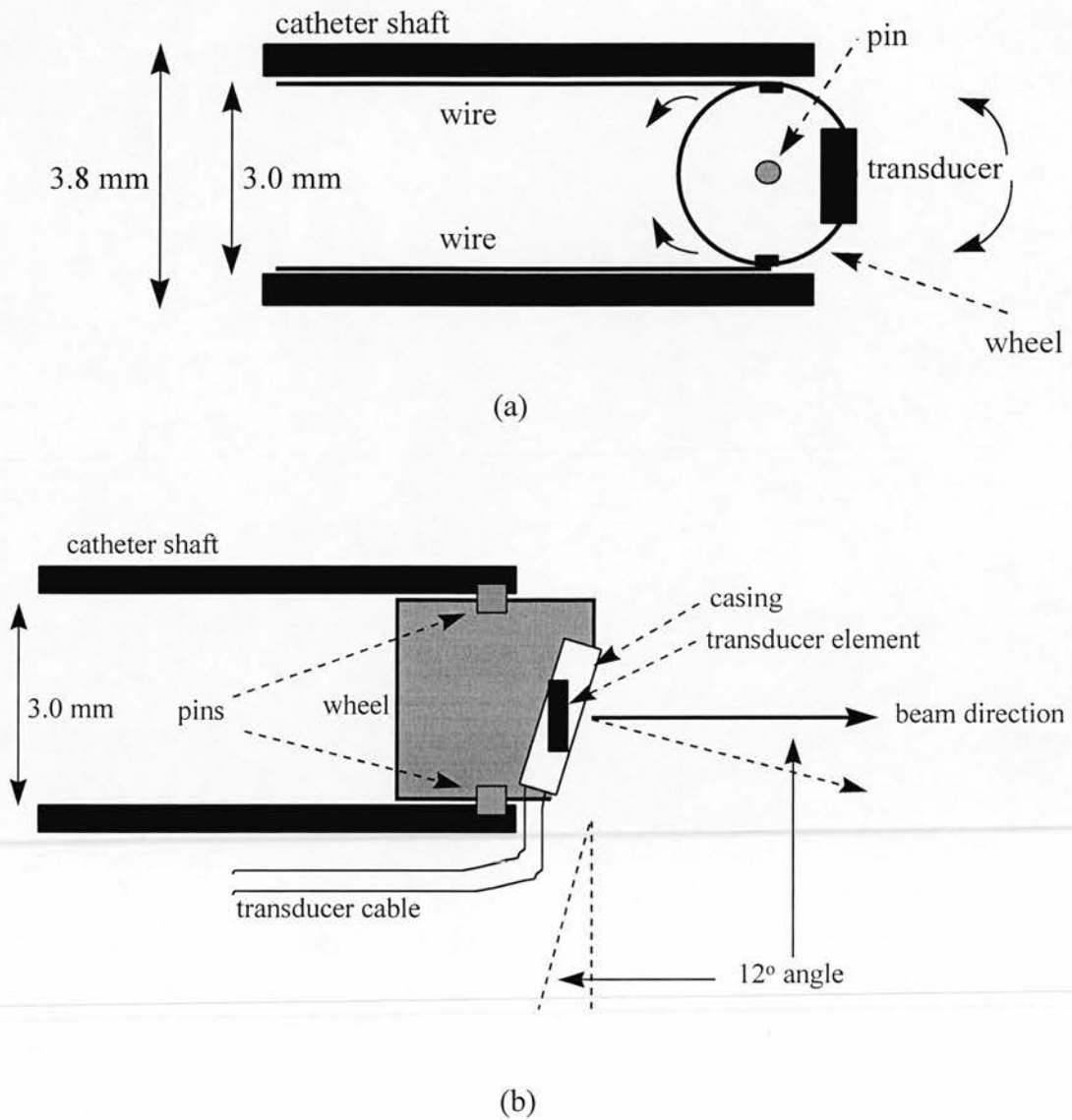


*Figure 6.3 : (a) Schematic top view of the forward-viewing catheter which comprises a scan head and a stiff tubular shaft. The scan head consists of a plastic wheel on which the transducer is mounted and coupling pins. Pulling wires run along the catheter lumen and are connected to a motor shaft and to the wheel of the scan head. (b) Schematic side view of the scan head showing the angled positioning of the transducer so that the beam is directed parallel to the axis of the catheter.*

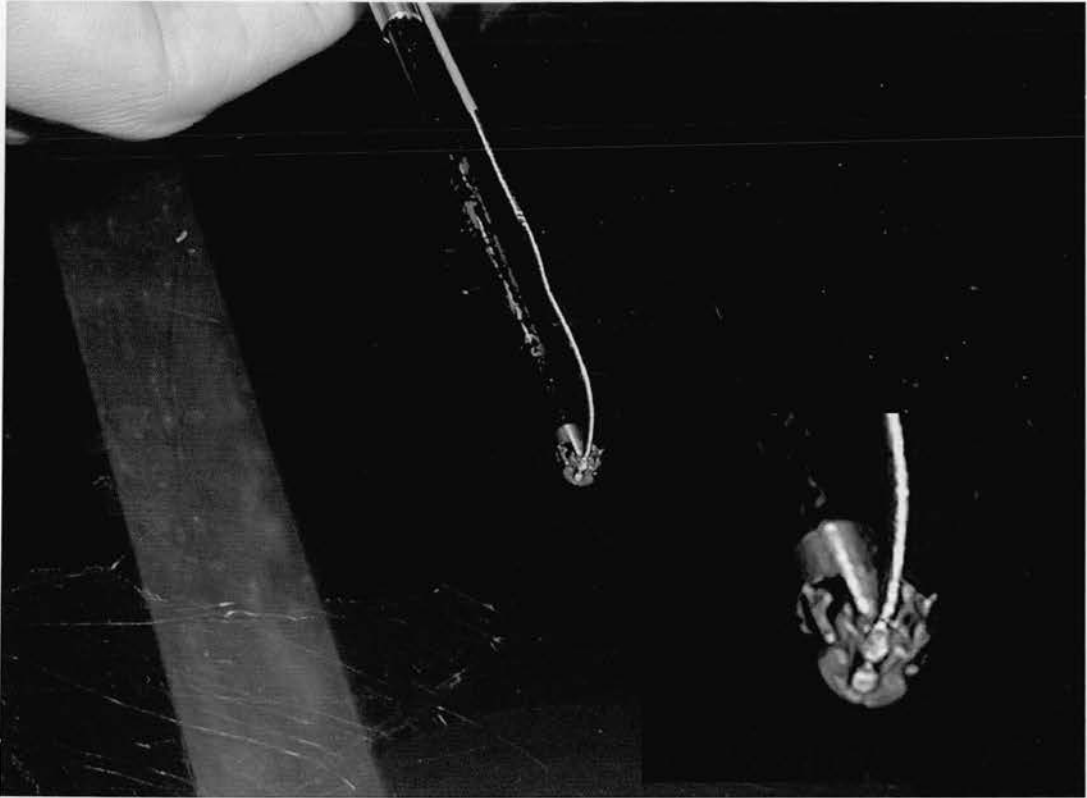


*Figure 6.4 : The forward-viewing IVUS catheter. Shown in this photograph are the catheter shaft, the wheel with the transducer attached on it, the transducer cable running parallel to the catheter and the pulling wires clamped on the wheel. A zoomed photograph of the probe head is also inserted in the lower right corner.*

Assuming there is no slack on the wires and that they do not elongate under tension, the angular resolution of the transducer sweep is given by equation 2.3. According to the manufacturer of the microcable used as pulling wire, its lifetime would be relatively short if the radius of motor shaft was less than 8 times the diameter of the microcable, i.e. less than 2.16 mm. Therefore, in order to avoid fatigue and failure of the pulling wires, it was decided to increase the radius of the motor shaft to 5 mm. A 5:1 ratio gearbox (model IP57-M01-5, McLennan, Surrey, UK) was also fitted on motor SM1 to improve its angular resolution from  $0.9^\circ$  to  $0.18^\circ$ . This modification was regarded as necessary in order to compensate for the

increase in motor shaft radius by keeping the product  $R_m\theta_m$  at low levels. By substituting the above values along with the wheel radius (1.5 mm) in equation 2.3, the angular resolution of the transducer sweep was calculated as  $0.6^\circ$ .

### **6.5.3 Data acquisition and image reconstruction**

The ultrasound scanner used in this study was designed for real-time side-viewing IVUS imaging. However, the ability to disable the side-viewing catheter rotation while continuing to transmit and receive ultrasonic signals, along with the feasibility of sampling the RF signal from an output port, allowed the use of the scanner for non-real-time forward-viewing imaging. The original side-viewing catheter was in that case used only as a cable connecting the transducer to the scanner, and an A-mode RF line was available at the output port for each individual transducer orientation. According to the manufacturer of the scanner, there was no non-linear processing of the RF signal prior to the point of access. The TGC circuitry came before the RF output, allowing gain control along the RF lines.

The data acquisition system used for *in vitro* imaging of human arteries was similar to that described in section 2.5.3. It involved a Pentium PC for controlling the equipment by means of LabVIEW software. A schematic diagram of the new data acquisition system is given in Figure 6.5. The main difference from the system used in conjunction with the TMM vessels, was that in the new system the acquisition sequence was mastered by the rate of RF line digitisation in the A/D converter (model PDA12, Signatec Inc, Corona, California, USA). In essence, following the capture of each individual RF line, the stepper motor controller card (model OMS-PC38-6, Oregon Micro Systems, Beaverton, Oregon, USA) was allowed to direct the stepper motor SM1 to advance the transducer to its next orientation in the sector plane. The transducer remained there until a new RF line was captured for that new orientation. The digitised data was archived on CD-ROM for off-line processing.

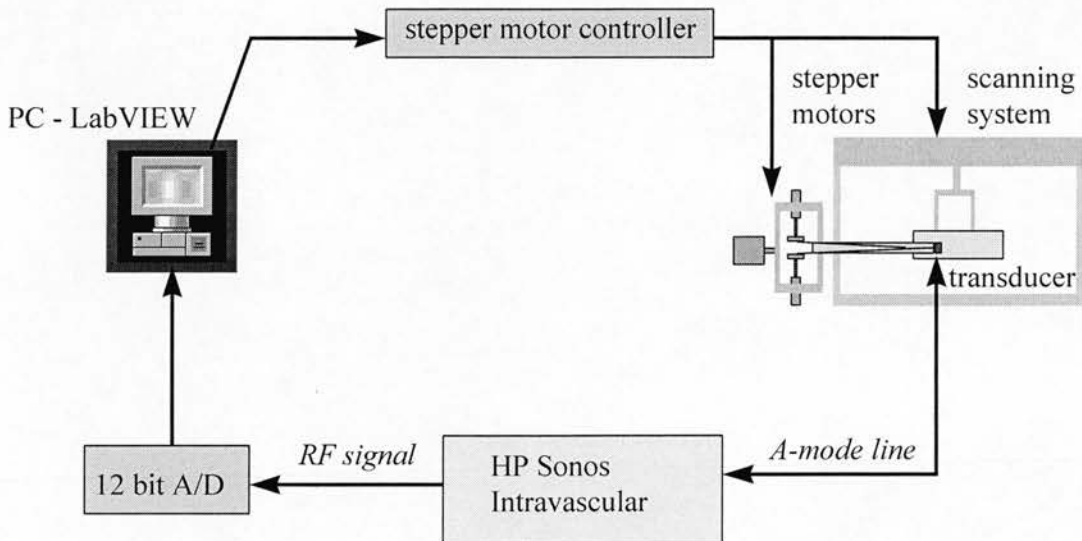


*Figure 6.5 : The data acquisition system used for the in vitro imaging of human arteries.*

Images were produced by software processing of the RF data, according to the scheme described earlier in section 2.5.4. The acquired RF lines were demodulated using Hilbert transform, log-compressed and scan converted to produce the 2D sector images. Following that, three dimensional reconstruction was performed according to the procedure described in section 4.2.2. The whole processing scheme was again implemented in IDL programming.

## 6.6 Resolution of the forward-viewing IVUS system

The active element of the 30 MHz transducer is disc shaped with 0.66 mm diameter. A 0.075 mm active area needle hydrophone (HPM075/1, Precision Acoustics Ltd, Dorchester, UK) was used to assess the pulse characteristics and acquire beam plots for this transducer.

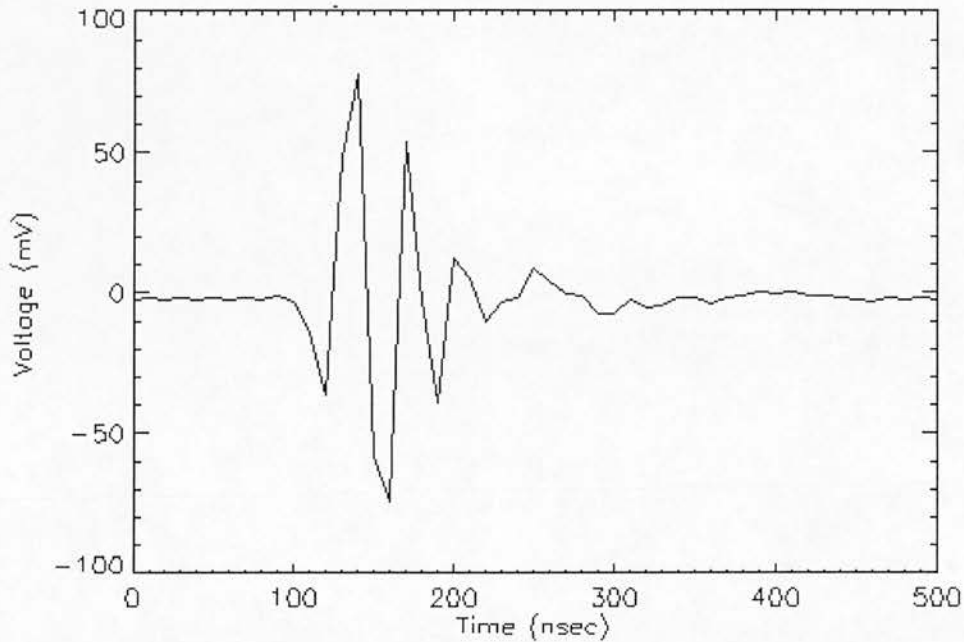


*Figure 6.6 : Pulse length of the single element 30 MHz IVUS transducer. 100  $\mu\text{m}$  of return echo distance correspond to approximately 130 nsec.*

As revealed from the hydrophone measurements, the transmitted pulse is approximately 3 cycles long (Figure 6.6) and has a central frequency of 28 MHz (Figure 6.7). The axial resolution of the system is approximately 45-50  $\mu\text{m}$  (half the pulse length). The transducer is unfocused and, according to equation 1.1, the near field zone extends up to 2 mm ahead of the transducer face. When this transducer was used for forward-viewing IVUS imaging, major parts of the imaged features were at distances greater than 2 mm from the transducer. In other words, they were lying in the transducer's far field, where the beam was broader and the lateral and elevational resolutions poorer than in the near field. The 6 dB resolutions in the far field are shown in Figure 6.8, where one can notice marked degradation at distances greater than 6 or 7 mm from the transducer face.



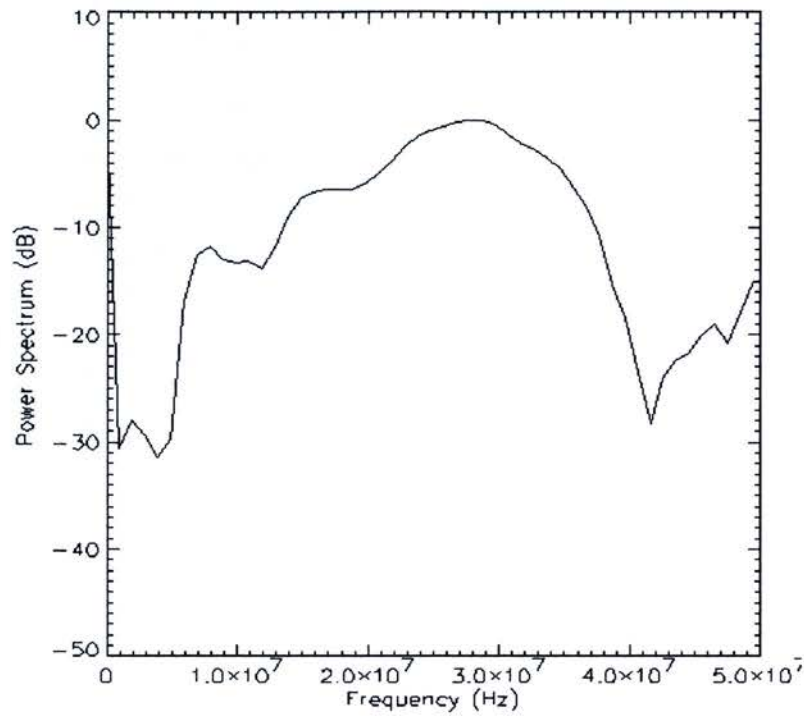


*Figure 6.7 : Relative power spectrum of the pulse transmitted from the 30 MHz IVUS transducer.*

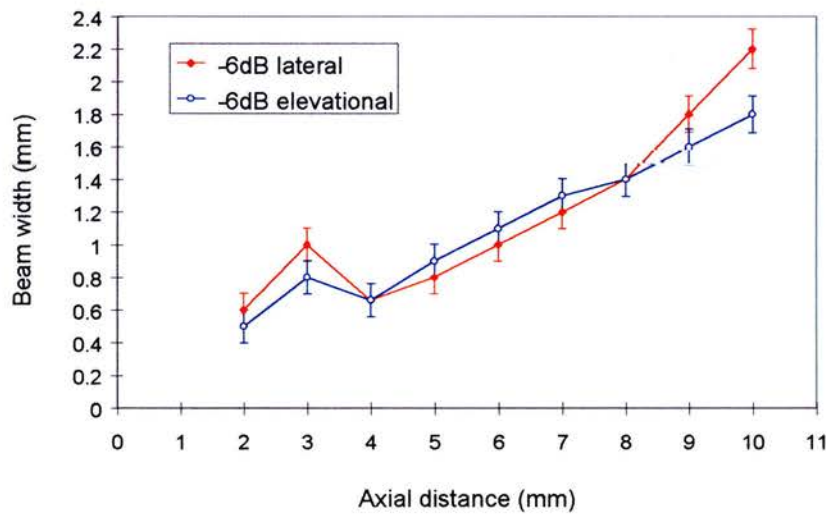


*Figure 6.8 : -6dB (for peak-to-peak signal) longitudinal plots of the lateral and elevational resolutions in the far field of the single element 30 MHz IVUS transducer.*



## **6.7 Geometrical accuracy of the forward-viewing IVUS system**

The scanning accuracy of the forward-viewing IVUS system was dependent on two main technical factors: (i) the accuracy of the transducer sweep motion, and (ii) the accuracy of the catheter rotation.

### **6.7.1 Accuracy of the transducer sweep motion**

A silk filament phantom was used for assessing the accuracy of the sector scan by motor SM1. This phantom was made of two flat perspex plates held parallel to each other and eight silk filaments connected at normal angles to these plates. The filaments were arranged on the surface of an imaginary cylinder at  $45^\circ$  angular steps. The cylinder's diameter, as measured across opposite filaments, was  $4.95 \pm 0.17$  mm. A schematic diagram of this phantom is shown in Figure 6.9.

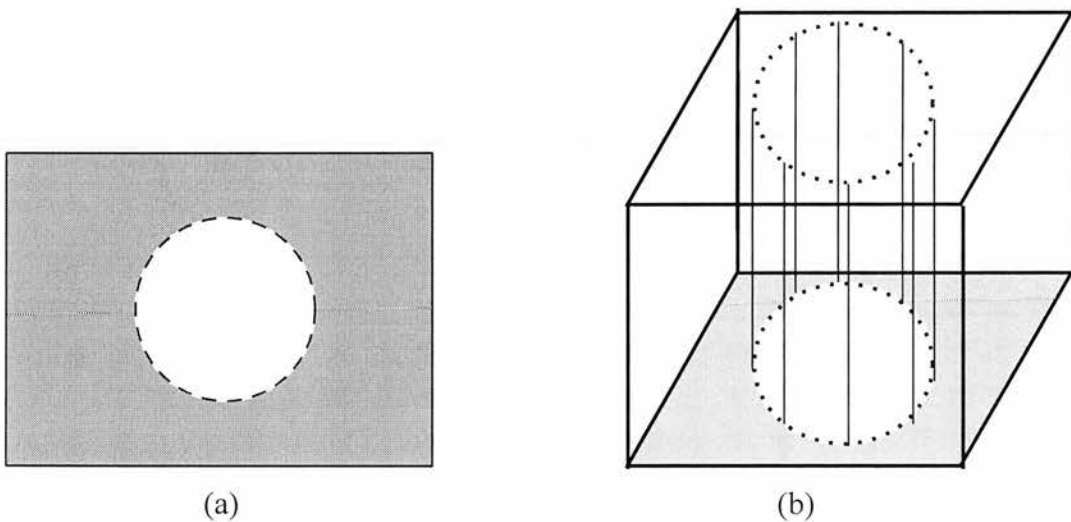


*Figure 6.9 : Silk filament phantom used for assessing the accuracy of the transducer sweep motion in the forward-viewing IVUS system. (a) Top view, (b) schematic diagram.*

The phantom was placed in front of the transducer's face in the water tank of the scanning system. A sector scan was performed with the aid of motor SM1, such that the scan plane was a cross-section of the cylindrical structure. The resulting

sector image is shown in Figure 6.10. Measured phantom diameters on that image varied within -3 to -7% of the average design value, from 4.6 to 4.8 mm. Thus, the circular shape of the phantom structure was well preserved in the sector image, evidence of the geometrical accuracy of the sweep motion of the scanning system.

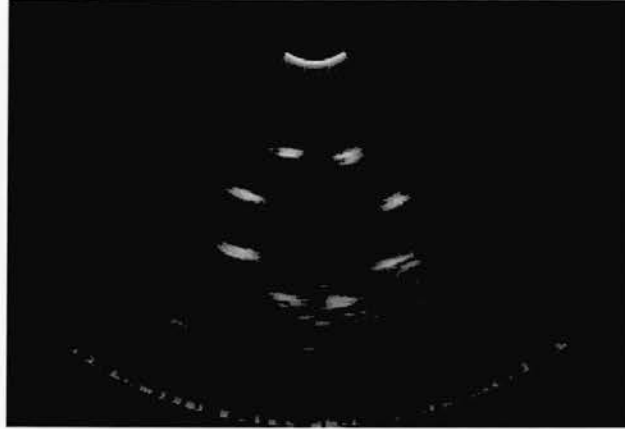


*Figure 6.10 : Image of the silk filament phantom acquired with a sector scan performed by SM1, where the scan plane was a cross-section of the cylindrical structure.*

### **6.7.2 Accuracy of the catheter rotation**

The accuracy of the catheter rotation was assessed by scanning one end of a perspex tube placed in front of the catheter tip. The inner diameter of that end of the tube was 4 mm. The catheter was aligned as accurately as possible with the centreline of the tube and a 3D rotational scan was performed. After the acquired data was reconstructed in three dimensions, a cross-sectional slice from the part of the volume corresponding to the end of the tube was displayed as in Figure 6.11. The image of the end of the tube in that figure is quite circular and measured inner diameters varied within -5 to -12% of the actual size (from 3.5 to 3.8 mm), revealing reasonably accurate catheter rotation by motor SM2. Deviations from perfect circular shape and

the actual dimensions are attributed to gradual degradation of the catheter rotation with repeated use.



*Figure 6.11 : Reconstructed cross-sectional image of one end of a perspex tube placed in front of the catheter tip.*

## **6.8 System limitations**

### **6.8.1 Non-real-time operation**

The major limitation of the system is that it cannot acquire and display in real-time. This restriction is mainly imposed by the operational mode of the ultrasound scanner in the forward-viewing system. In essence, the scanner can only be used as a transmitter-receiver without taking advantage of its features that provide real-time imaging when used in the original side-viewing IVUS mode. There is no capability for internal processing of the acquired data to produce and display images, therefore these tasks need to be performed off-line. In addition to the above, a slow scanning speed is used to ensure long life for the pulling wires and scan head mechanism.

For the purposes of this study, the non-real-time operation of the system is not a problem. When imaging *in vitro*, the arteries can be held at fixed positions with respect to the catheter throughout the duration of a volume acquisition. In this way, registration artifacts can be avoided and it is feasible to image the actual morphology and geometry of the artery accurately.

### **6.8.2 Field of view**

A second limitation of the system can be the angular size of the field of view. Although it was possible to sweep the transducer across sectors as wide as 100°, it was decided to restrict the system operation within a 72° sector in order to preserve the pulling wires and the scan head mechanism during prolonged use. This angle is not as large as other ones reported previously for forward-viewing IVUS systems (Evans et al. 1994, Ng et al. 1994). However, this was only due to a conservative approach concerning the maintenance of the system and not an intrinsic system limitation.

## **6.9 Summary**

In this chapter the comparison between a number of scanning patterns for forward-viewing IVUS imaging was concluded, indicating the *rotational* scan as the most promising scanning technique. Based on this outcome, a small scale mechanical catheter was designed and constructed, implementing the rotational scan for 3D forward-viewing IVUS imaging of human arteries *in vitro*. The catheter utilised a single element 30 MHz IVUS transducer and was interfaced to an intravascular ultrasound scanner. Use of test phantoms showed that the new scanning system was accurate, preserving the geometry of scanned objects. Image scan conversion and 3D reconstruction were achieved by off-line processing of the RF signal available at an output port of the scanner.

## CHAPTER 7

# FORWARD-VIEWING IVUS IMAGING OF ARTERIES *IN VITRO*

### 7.1 Introduction

The previous chapter provided a description of the catheter and the imaging system developed for forward-viewing IVUS imaging. In addition to that, the fidelity and performance of the system were discussed. The current chapter demonstrates the use of the above system in imaging human arteries *in vitro*. A number of forward-viewing images were acquired from normal and diseased arteries and were correlated with histological analysis and corresponding images acquired with a side-viewing IVUS system. This provided the basis for assessing the image quality and dimensional accuracy achieved by a forward-viewing IVUS system based on the rotational scan, and allowed conclusions to be derived on the practical utility of such a system.

### 7.2 *In vitro* imaging protocol

Vessel specimens from carotid and femoral arteries were obtained from adult human post-mortem material derived from hospital autopsies that had written permission to keep tissue for medical education, research and the treatment of other patients. Immediately after resection from the human body, the vessels were placed

into 10% buffered aqueous solution of formaldehyde (formalin) to reduce biohazard risks. These items were transferred to the University of Edinburgh Department of Medical Physics and Medical Engineering for the purposes of the IVUS study. The arterial specimens were placed in water baths and imaged with both side-viewing and forward-viewing IVUS systems. All experiments were carried out at room temperature (22 °C). The individual imaging procedures are described below.

### **7.2.1 Side-viewing IVUS imaging**

The arteries were mounted on the scanning rig shown in Figure 7.1. The tank was filled with water and a 3.5 Fr, 30 MHz side-viewing mechanically rotated IVUS catheter (Boston Scientific Co, Watertown, Massachusetts, USA) was inserted into the tank and the vessel via a watertight valve. The catheter was advanced as close as possible to the distal end of the vessel, lumen area permitting. The assembly of the catheter and the ultrasound scanner's patient interface unit, was attached to an automatic pull-back device (Boston Scientific Co, Sunnyvale, California, USA), which was set to operate at the speed of 0.5 mm sec<sup>-1</sup>.

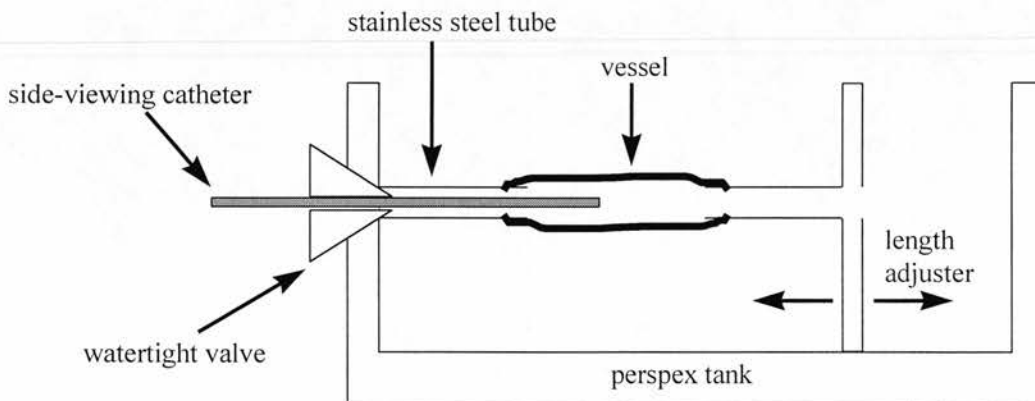


*Figure 7.1 : Scanning rig used for side-viewing IVUS imaging of arteries in vitro.*

RF ultrasound lines available at the output port of the ultrasound scanner (Sonos Intravascular, Hewlett-Packard, Andover, Massachusetts, USA) were captured by a 12-bit digitiser (model PDA12, Signatec Inc, Corona, California, USA) at 100 MHz sampling rate. Each acquisition frame, i.e. 360° cross-sectional image, consisted of 240 ultrasound lines. The acquisition software was configured to capture and store one frame per second. In this way, cross-sectional images were obtained at 0.5 mm increments along the vessel length, until the catheter reached the most proximal part of the vessel. The digitised RF data was archived on CD-ROM for off-line processing and production of 2D images according to the procedure described earlier in section 2.5.4.

### **7.2.2 Forward-viewing IVUS imaging**

The arterial specimens were placed in a small water tank and secured in a fixed position with the aid of pins. The small tank was in turn placed inside the larger tank of the scanning system (Figure 2.10) and was positioned by means of the 3-axis system so that the vessel was advanced over the forward-viewing catheter (Figure 7.2).

A conical volume was acquired for each vessel using the rotational scanning pattern. The same ultrasound scanner and data acquisition card were employed as in the case of side-viewing IVUS imaging. The data acquisition procedure has been described in section 6.5.3. Each conical volume consisted of 50 sector frames with the angular step between the frames being constant and equal to 3.6°. Each frame consisted of 120 ultrasound lines arranged across a 72° sector in equal angular steps of 0.6°. The digitised RF data was archived on CD-ROM for off-line processing and production of 2D images according to the procedure described in section 2.5.4. The scanned segments of the vessels were marked with needles for histological location.

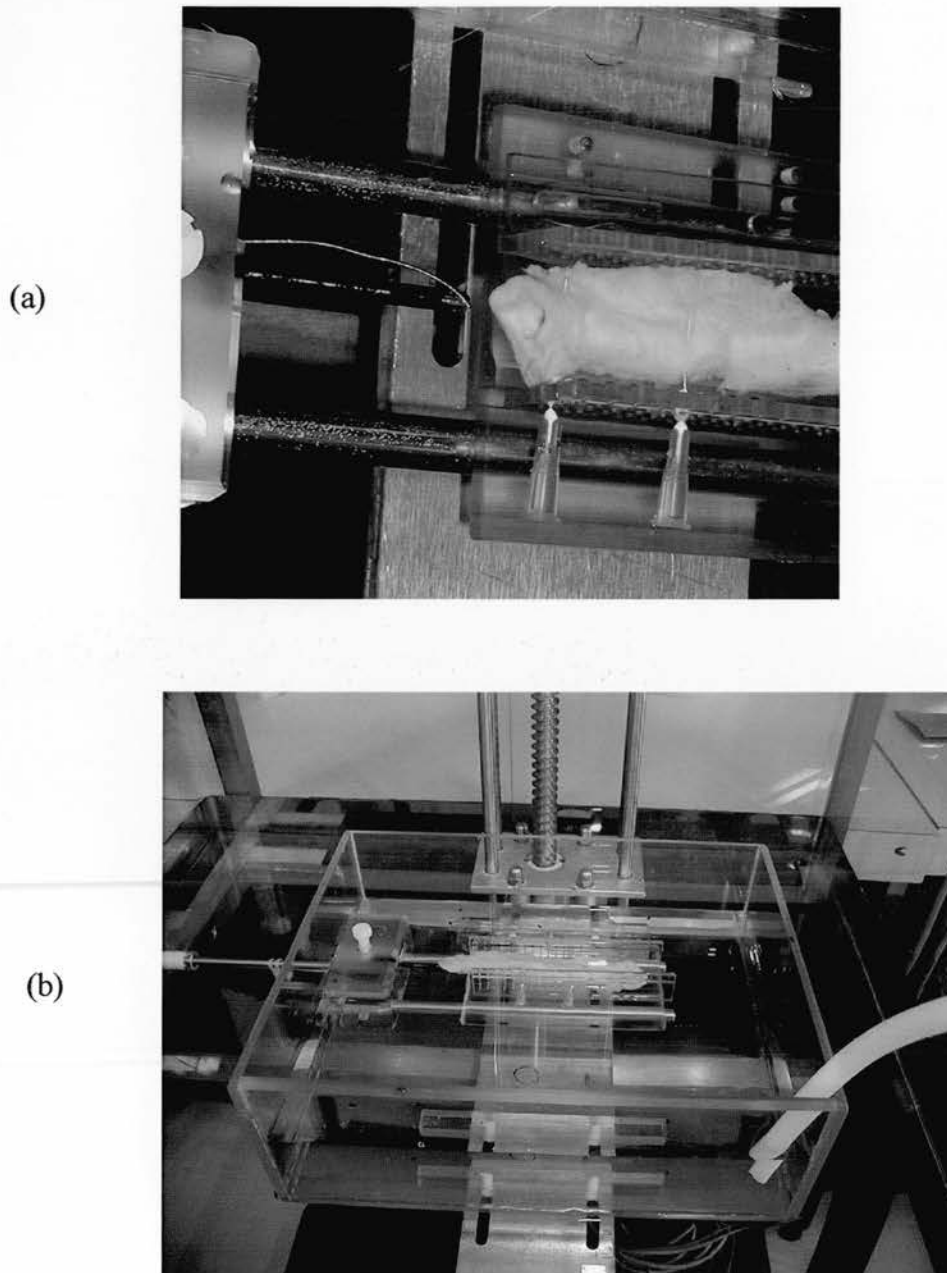


*Figure 7.2 : (a) Artery mounted in a fixed position in a water tank, with the aid of pins, and placed in front of the forward-viewing IVUS catheter. (b) Arrangement of the water tanks showing the catheter inserted into the vessel.*



### **7.2.3 Histological analysis**

After completion of the imaging procedures, the arterial specimens were transferred to the University of Edinburgh Department of Pathology. The vessel segments that were scanned by the IVUS imaging systems were dissected to allow correlation of ultrasound images with histology. The dissection method created cross-sectional slices approximately 2 mm in depth to allow sufficient material for later paraffin embedding. For example, a 10 mm length of vessel generated 5 cross-sectional slices.

The cross-sectional slices were initially X-rayed to localise vessel wall calcification. Subsequent to that, each cross-sectional slice was decalcified and embedded in paraffin to create a paraffin block. Each embedded paraffin block was then sliced using pathology microtome devices. Four histological cross-sections were created per cross-sectional slice, each section being 4.0  $\mu\text{m}$  in thickness. In total, twenty histological 4.0  $\mu\text{m}$  thick cross-sections were available from a 10 mm long vessel segment. Each section was subsequently stained with haematoxylin and eosin.

Photography was performed on the histological sections to record the entire vessel wall circumference and associated lumen. Following that, the film was processed to generate 35 mm photographic slides which were subsequently scanned in a slide scanner to produce digital images. The histological sections were used for morphological and dimensional correlation with ultrasound images.

## **7.3 Imaging results**

Three dimensional data sets were successfully acquired with the forward-viewing catheter. Cross-sectional slices (2D images) could be derived and displayed from the reconstructed forward-viewing volumes. These images were similar to the 2D images acquired with the side-viewing system and could be directly correlated to the histological cross-sections.

Initially, gain settings in the ultrasound scanner were selected for optimisation of side-viewing IVUS imaging. The backscatter signal in forward-viewing IVUS is weaker than in side-viewing, due to the non-normal beam incidence on the vessel wall. When the side-viewing gain settings were used for forward-viewing imaging, the achieved penetration through the atherosclerotic walls was severely limited. In order to optimise the acquired forward-viewing images in terms of display contrast and penetration depth, the overall amplifier gain in the ultrasound scanner was set 6 dB higher than the value used for side-viewing imaging. This improved the quality of the forward-viewing IVUS images significantly and allowed imaging at depths ranging from 3.1 to 6.8 mm distal to the catheter tip, depending on the amount of atherosclerotic tissue present in front of the catheter.

For relatively normal arterial segments, or with minimal disease, the vessel walls in the two dimensional frames acquired with the forward-viewing catheter appeared relatively thin and smooth (Figure 7.3).

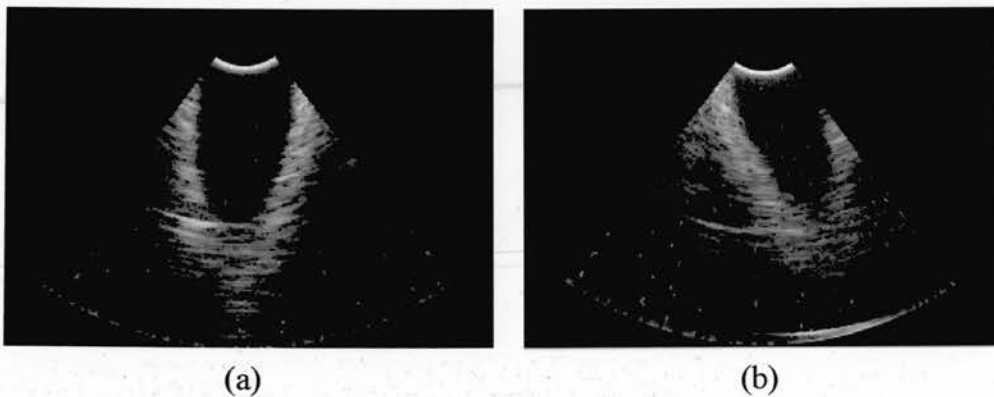


*Figure 7.3 : Forward-viewing IVUS longitudinal images (acquired frames) of a relatively disease free carotid artery. Frame (b) indicates that the forward-viewing catheter is deflected at an angle with respect to the axis of the vessel, i.e. the axis of the sector scan is offset from the axis of the vessel. This orientation is responsible for the echo between the distal parts of the vessel walls shown in frame (a). This echo is from the vessel wall located at  $90^\circ$  with respect to the orientation of frame (a) and not from any stenosis.*

The lumen shape as shown in cross-sectional images from the reconstructed forward-viewing volume, correlated well with histology (Figure 7.4).

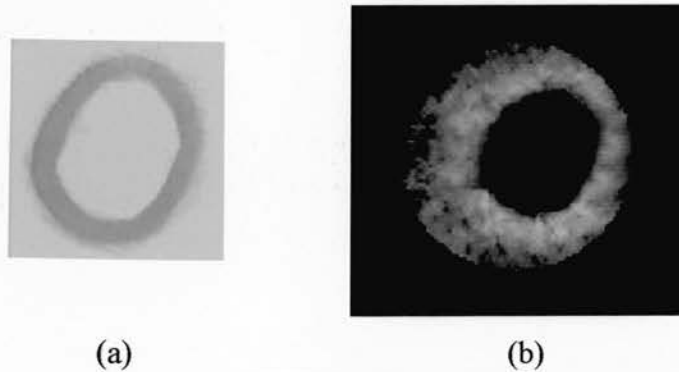


*Figure 7.4 : Histological (a) and forward-viewing IVUS (b) cross-sections of a relatively disease free carotid artery.*

The apparent discrepancy in vessel wall thickness between histology and forward-viewing IVUS, is due to three reasons. The first one is the angulated catheter orientation with respect to the vessel axis (seen in Figure 7.3b). Cross-sections of the reconstructed IVUS volume are in fact oblique sections of the vessel anatomy; at such sections the wall thickness is greater than at perfect cross-sections. Secondly, part of the right vessel wall is outside the catheter's field of view (seen also in Figure 7.3b). This causes the right vessel wall to appear thinner than the left one in the cross-sectional ultrasound image, to an extent greater than that seen in the histological section. The third reason is the lateral resolution of the transducer. The displayed cross-section corresponds to a distance lying in the far field of the transducer, where the lateral resolution is sub-optimal (in the range 0.8 to 1 mm). As a result, wall echoes are broader, occupying space originally belonging to the lumen. Lumen area measurements, shown later in section 7.4, verify the luminal 'narrowing' caused by this effect.

Regarding imaging of vessels with various degrees of atherosclerosis, the forward-viewing IVUS system was proven capable of displaying luminal stenoses and occlusions in acquired two dimensional frames (Figure 7.5).

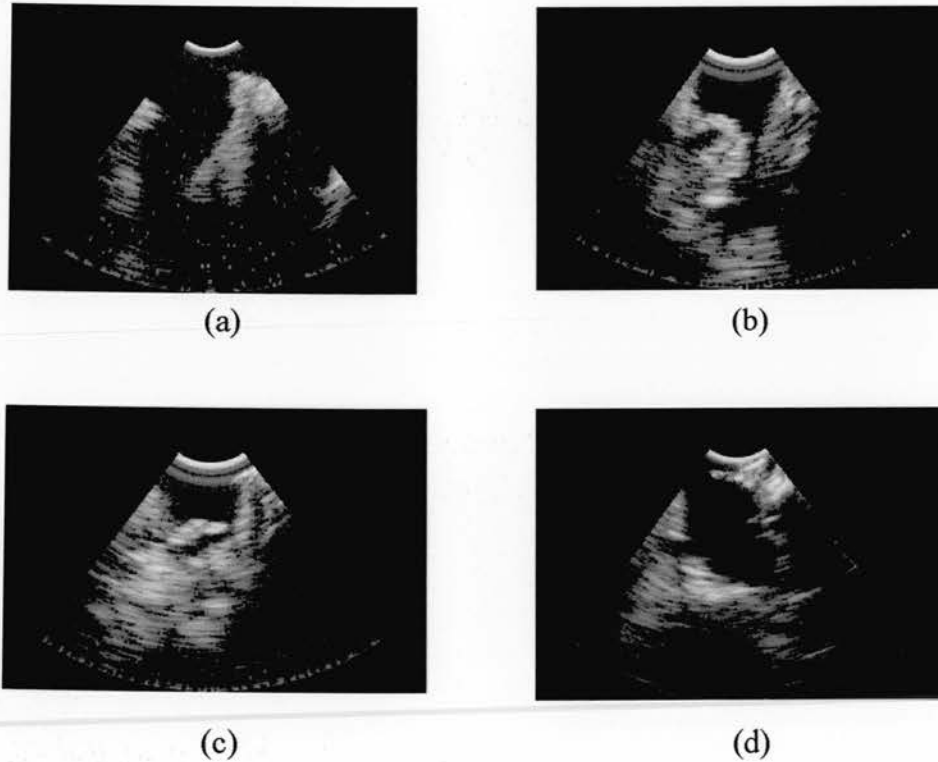


*Figure 7.5 : Forward-viewing IVUS longitudinal images (acquired frames) from a carotid artery with an eccentric stenosis (a), and a femoral artery with very severe (b) and total occlusions (c and d).*

In Figures 7.5b and 7.5c, the layered wall structure can be identified in parts of the right vessel wall, where the media appears as an echolucent layer between two parallel echogenic layers. Areas of bright echoes in the proximity of the catheter axis are indicative of fibrous and/or calcific plaque. In Figure 7.5d in particular, a strong echo at the site of the right wall followed by acoustic shadowing at further distances from the transducer, is evidence of calcium deposits. Acoustic shadowing due to calcium is always present at reconstructed cross-sectional images corresponding to regions beyond the calcium location (Figure 7.6).

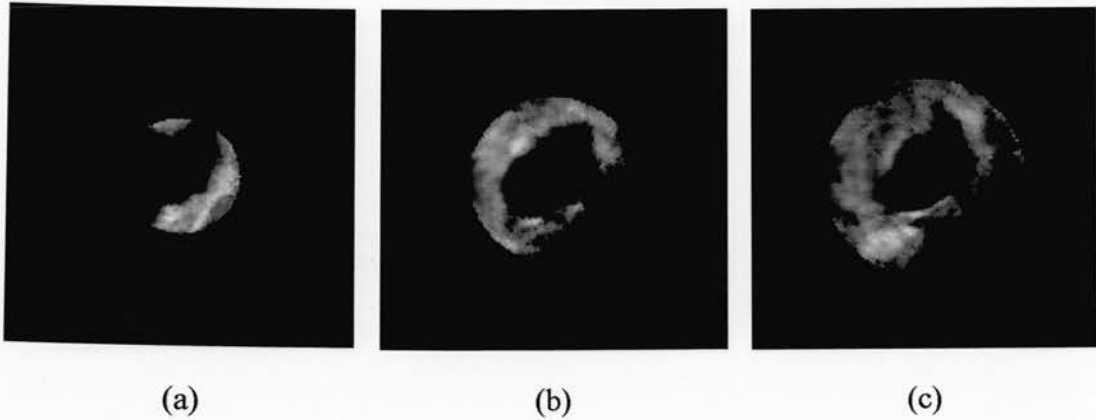


*Figure 7.6 : Reconstructed cross-sectional forward-viewing IVUS images of a diseased femoral artery at 1.5 mm (a), 2.8 mm (b) and 3.7 mm (c) distal to the catheter tip. Calcium deposits indicated by bright echoes between 3 and 6 o'clock in (a) cause acoustic shadowing in the same regions in (b) and (c). The 'echo-free' sector between 7 and 11 o'clock in (a) is part of the lumen; the corresponding part of the vessel wall is outside the catheter's field of view.*

In the case of diseased vessels, the reconstructed cross-sectional forward-viewing IVUS images revealed lumen shapes in agreement with histological sections and 2D images acquired with side-viewing IVUS, as illustrated in Figures 7.7 to 7.10.

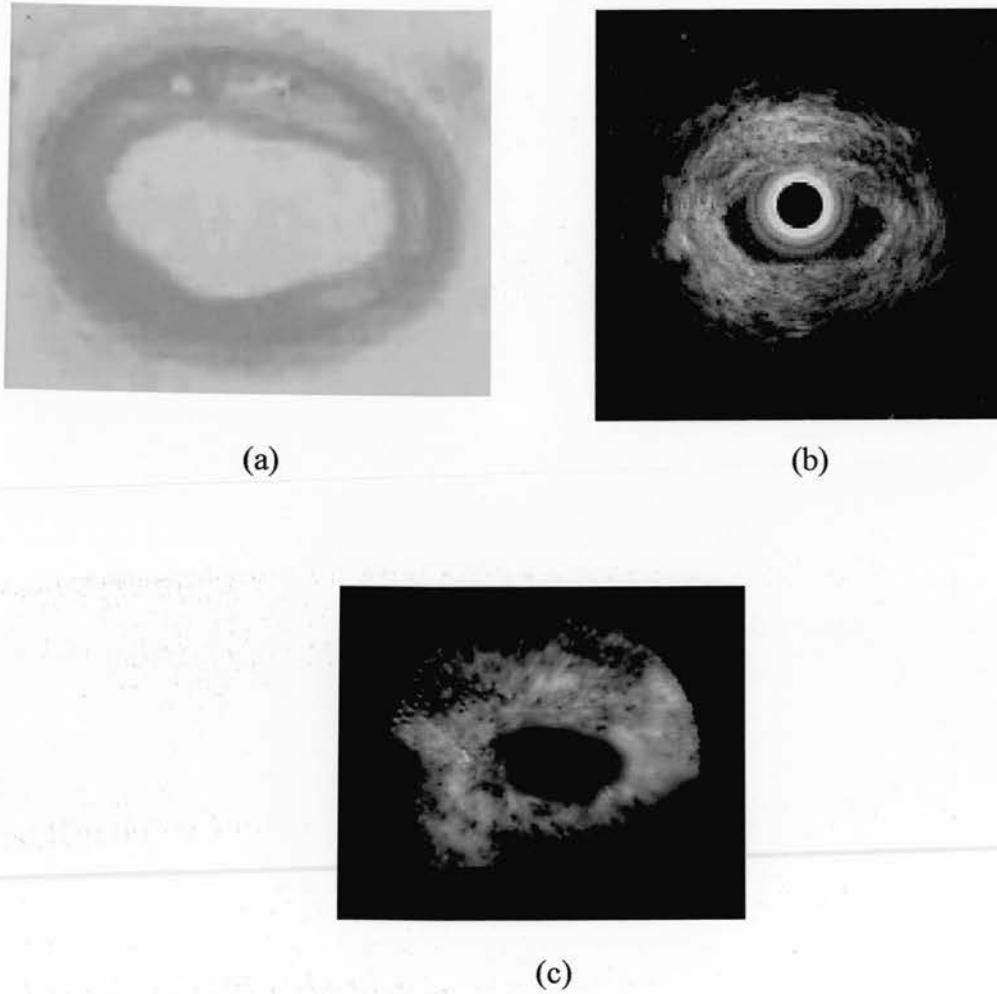


*Figure 7.7 : Histological (a), side-viewing IVUS (b) and forward-viewing IVUS (c) cross-sections of a diseased carotid artery. The residual lumen shape as depicted by both IVUS systems, is in good morphological agreement with histology. A calcium deposit inside the vessel wall, seen at around 12 o'clock in the histological section, is indicated by bright echoes at the same location in both IVUS images.*

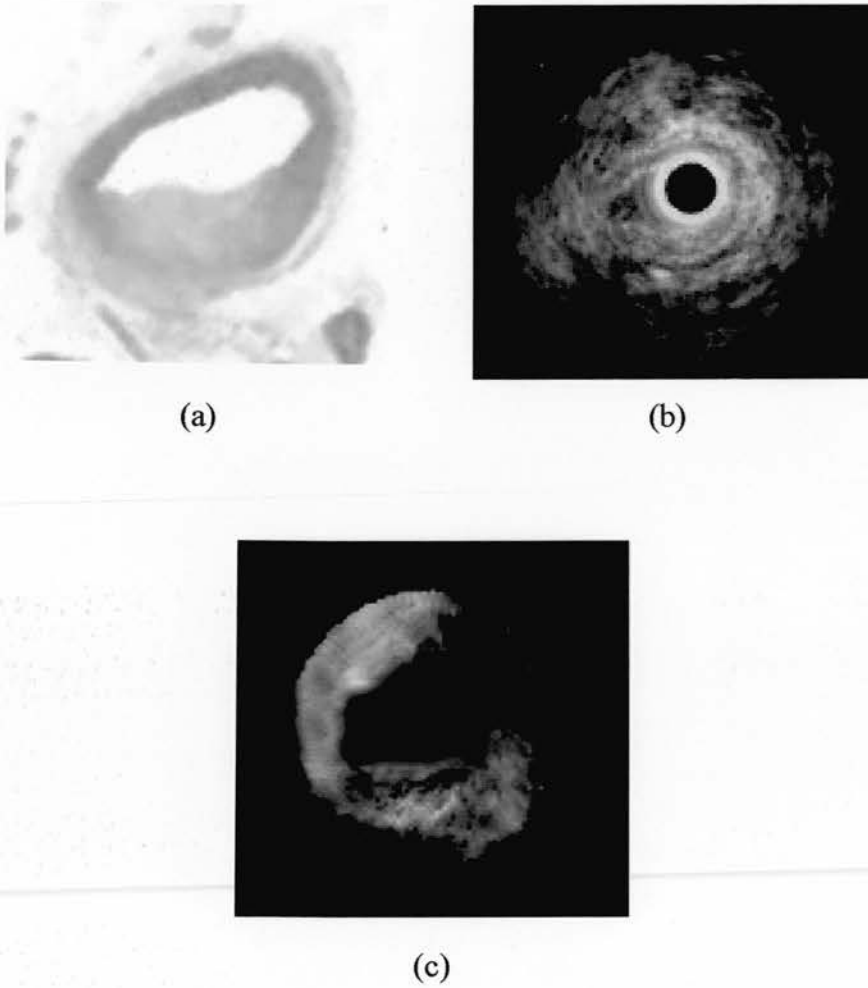


*Figure 7.8 : Histological (a), side-viewing IVUS (b) and forward-viewing IVUS (c) cross-sections of a carotid artery with an eccentric fibrofatty plaque extending from 2 to 9 o'clock. The side-viewing catheter just manages to fit in the residual lumen leaving only a small area free (in the left side of the image). The small size of the lumen and the ring-down around the side-viewing catheter make it difficult to accurately depict the lumen boundary. The forward-viewing IVUS catheter is at an angulated orientation with respect to the vessel axis, therefore part of the lumen and the vessel wall are not included in the field of view. The part of the lumen, though, which is displayed in the forward-viewing image is in good morphological agreement with histology.*

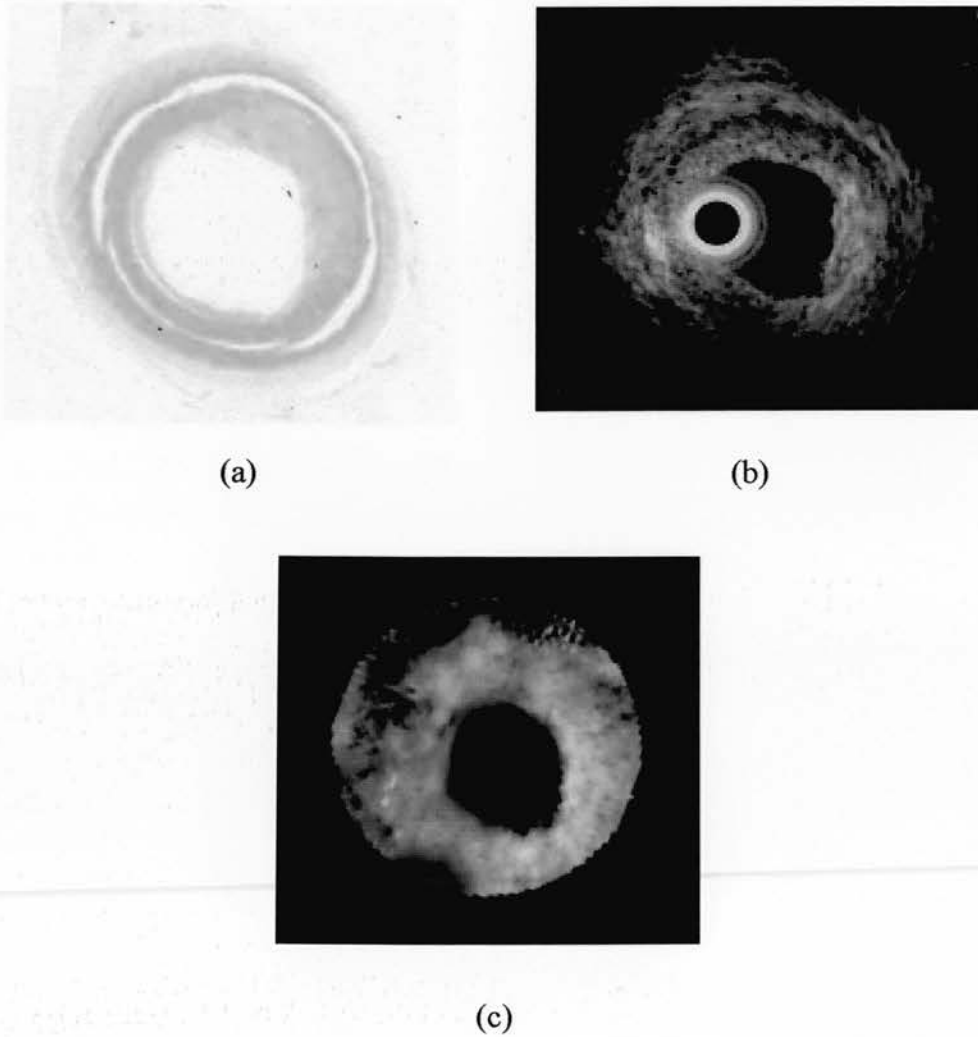


*Figure 7.9 : Histological (a), side-viewing IVUS (b) and forward-viewing IVUS (c) cross-sections of a carotid artery with an eccentric fibrotic plaque extending from 11 to 5 o'clock. The lumen shape is accurately depicted in both IVUS images. A split in the vessel wall, indicated by a white ring in the histological section, is partly displayed in the side-viewing image as a dark ring from 10 to 4 o'clock. A segment of the split is seen also in the forward-viewing image, between 9 and 12 o'clock. The rest of this split lies outside the field of view of the forward-viewing catheter.*



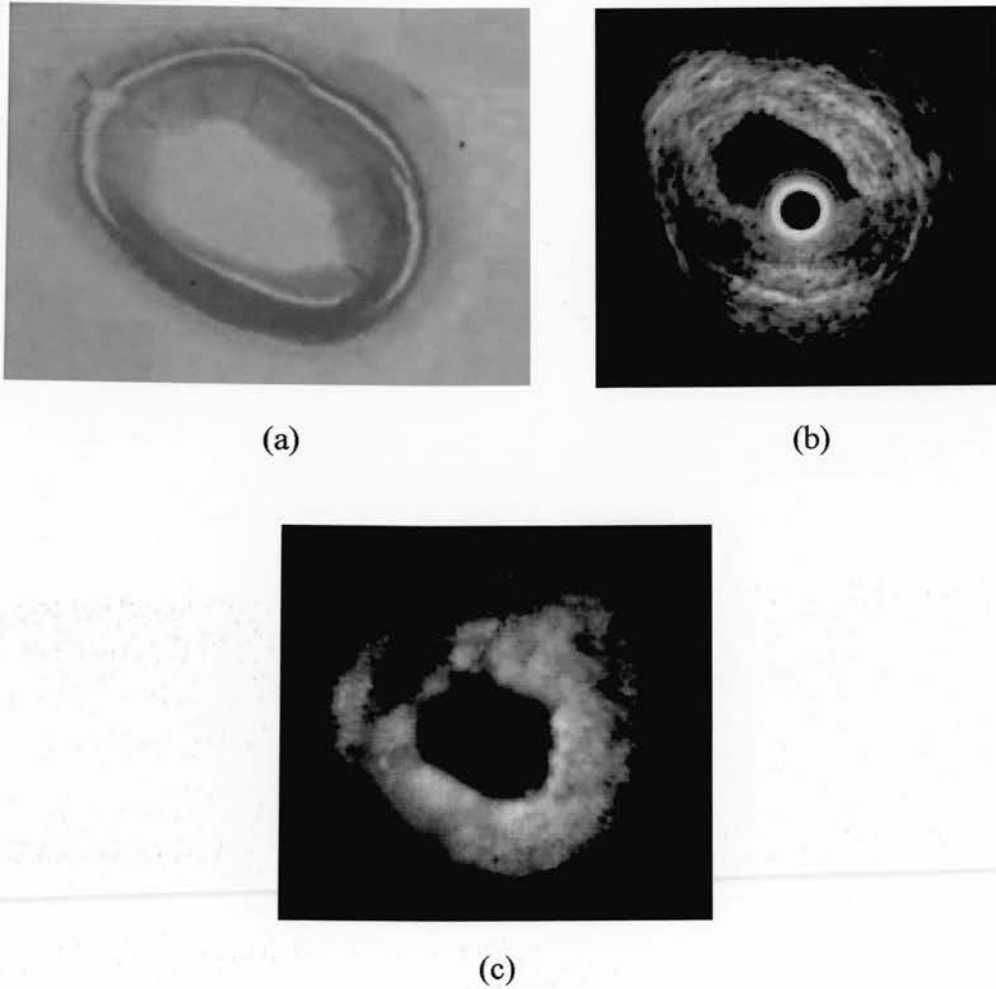


*Figure 7.10 : Histological (a), side-viewing IVUS (b) and forward-viewing IVUS (c) cross-sections at a more distal part of the carotid artery shown in Figure 7.9. An eccentric dense fibrotic plaque is seen between 9 and 5 o'clock in the histological section. The lumen shape is accurately depicted in the side-viewing image. It is also well preserved in the forward-viewing image, although not as accurately as in the side-viewing one. The vessel wall split shown in Figure 7.9, obscures the transmission of the ultrasound beam in the axial direction, causing the 'shadow' between 9 and 1 o'clock in the forward-viewing image.*

The femoral artery shown earlier in Figures 7.5b to 7.5d was heavily diseased and served as a perfect example for displaying the imaging potential of forward-viewing IVUS, since it was not possible to insert the side-viewing catheter at all. Reconstructed cross-sectional forward-viewing IVUS images provided visualisation of the severe or total occlusions (Figure 7.11).

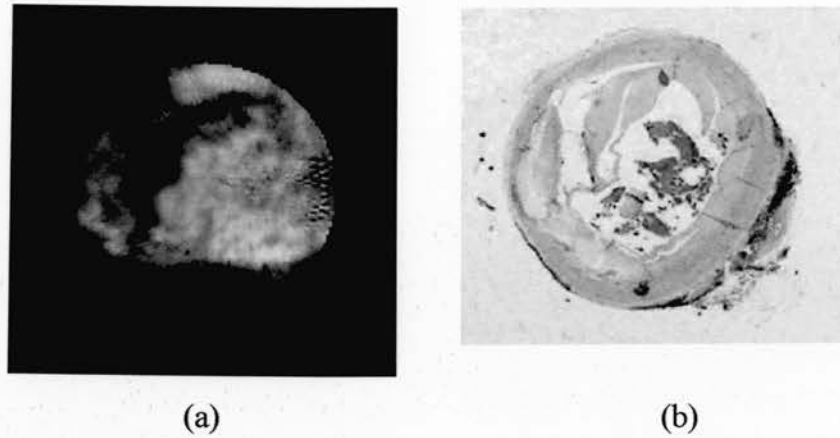


*Figure 7.11 : Reconstructed cross-sectional forward-viewing IVUS images of a heavily diseased femoral artery. The image in (a) corresponds to a vessel segment with an almost complete (98%) occlusion caused by large amount of thrombus. A crescent-shaped split in the vessel wall is also seen between 8 and 1 o'clock. The corresponding histological cross-section is shown in (b). During the process of paraffin embedding, thrombus shrunk and was partly removed, hence the lumen area in the histological section is larger than originally and does not agree with the ultrasound image.*

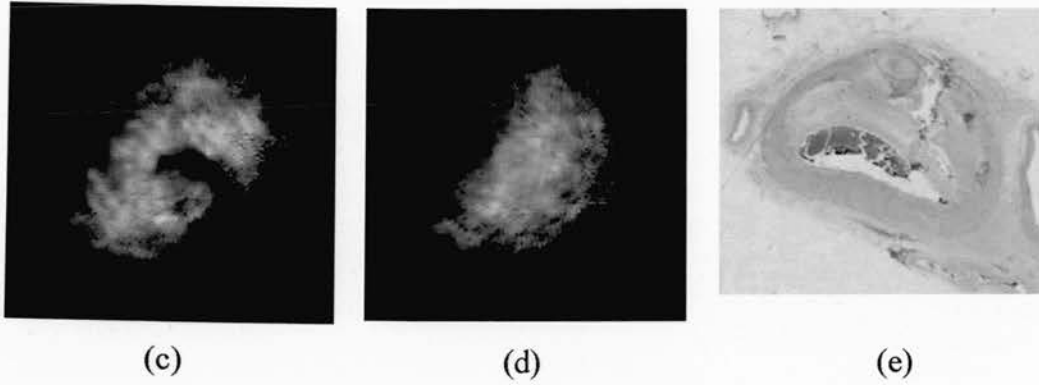


*Figure 7.11 (continued) : Images (c) and (d) are from another segment of the same vessel. An almost complete occlusion is seen in image (c); the corresponding histological cross-section is shown in (e). A total occlusion is seen in (d); no histological cross-section is available. The 'shadows' seen between 4 and 8 o'clock in (a), 3 and 7 o'clock in (c) and (d), as well as 8 and 12 o'clock in (d), are caused by calcium deposits in regions between the catheter and the displayed vessel cross-sections.*

The forward-viewing IVUS catheter also proved particularly useful in visualising bifurcations both in two and three dimensions. An example of carotid bifurcation imaging is shown in Figure 7.12.

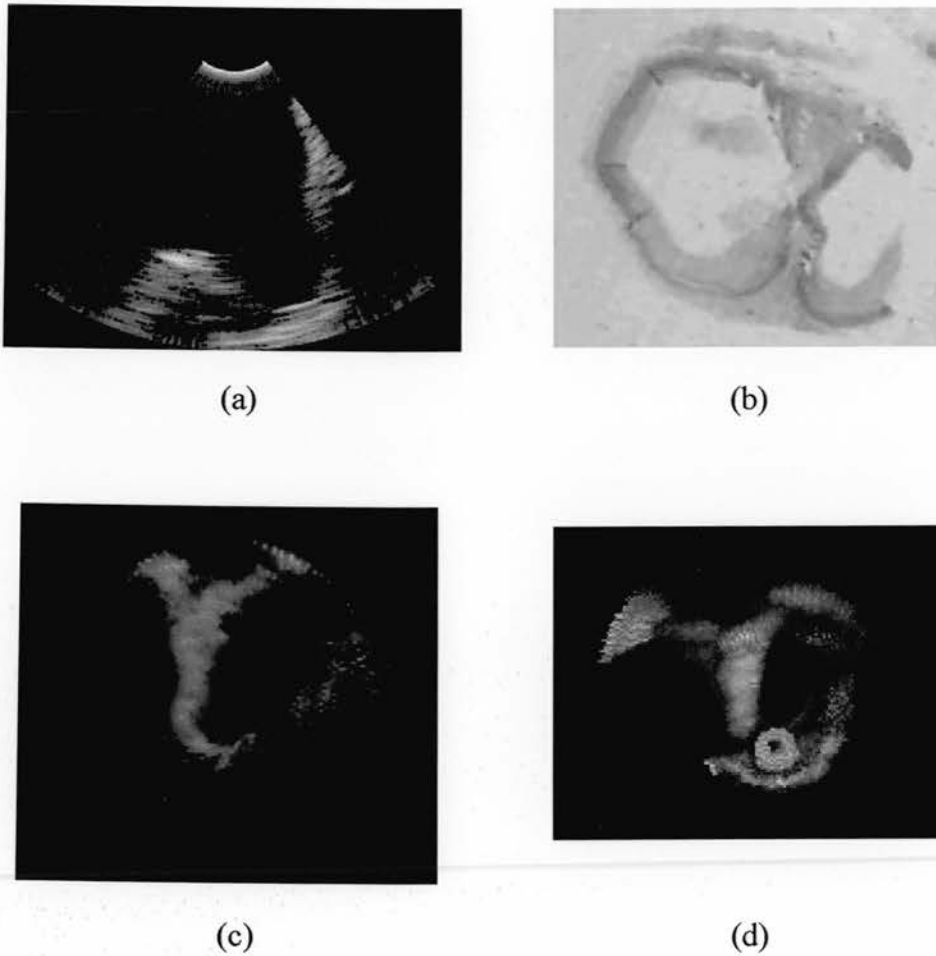


*Figure 7.12 : (a) Forward-viewing IVUS longitudinal image (acquired frame) from a carotid artery bifurcation. One side of the arterial wall is seen before the bifurcation at the top right part of the sector image. The flow divider and the distal branch lumens are seen in the bottom part of the sector image. Note the stenosis in the right branch. A histological cross-section of the bifurcation is shown in (b) and a corresponding reconstructed cross-sectional forward-viewing IVUS image is shown in (c). The flow divider and one distal lumen are seen in this IVUS image, while the other distal lumen is outside the catheter's field of view. The image in (d) displays a rendered volume of the bifurcation as seen from the catheter tip. An echogenic 'structure' seen before the bifurcation in (d), is the transducer 'ring-down' immediately in front of the catheter tip.*

## 7.4 Dimensional quantification

Eleven measurements of lumen area were made on histological slices, with the aid of a Zeiss microscope (Zeiss Axioskop, Carl Zeiss, Göttingen, Germany), and on the corresponding cross-sectional forward-viewing IVUS images, with the segmentation and measurement scheme described earlier in sections 5.3.2 and 5.4.1. There was a systematic tendency for the lumen areas derived from the forward-viewing IVUS images to underestimate those derived from the histological sections. This finding is in agreement with the work of Liang and Hu (1997a) and is attributed to the sub-optimal lateral resolution of the transducer, which causes broadening of the vessel wall and plaque echoes along with apparent luminal narrowing. Errors in lumen area size varied from 11 to 34% and a paired t-test between areas derived from histology and forward-viewing IVUS, revealed *significant* difference at 5% level. There was a good correlation ( $R=0.95$ ) and a good linear fit between the measurement sets (Figure 7.13), nevertheless there was no agreement between the two methods as demonstrated by a Bland-Altman plot (Figure 7.14).

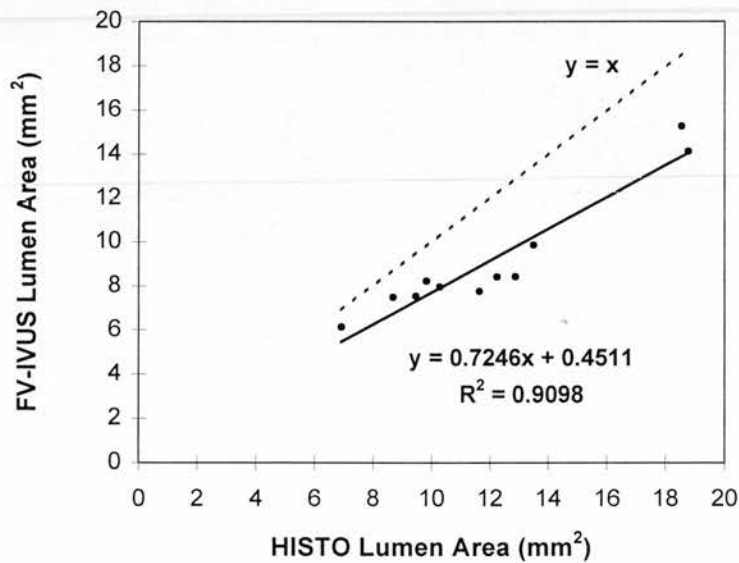


*Figure 7.13 : Correlation of lumen area measurements derived from forward-viewing IVUS images and histological sections. The ultrasonic method underestimated the luminal dimensions, however, a good linear fit was seen.*

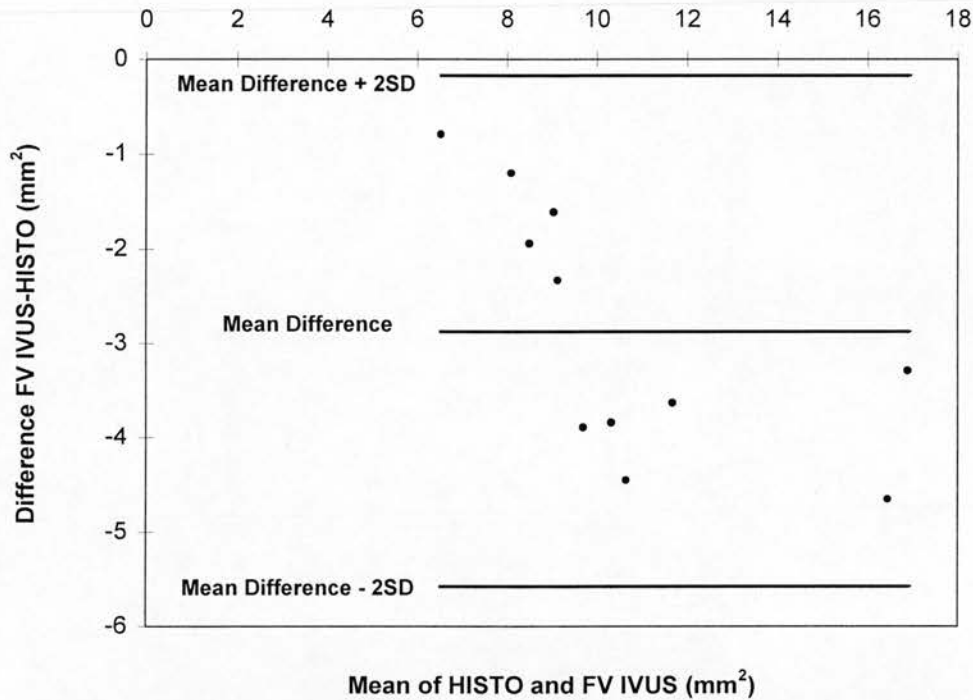


*Figure 7.14 : Bland-Altman plot of the difference versus mean of the two techniques for measuring lumen area (forward-viewing IVUS and histology). There is no agreement between the two methods. Instead there is a bias of the lumen areas measured by the ultrasonic method to underestimate the ones measured by histology.*

## 7.5 Discussion

The results of this forward-viewing IVUS study of human vessels *in vitro* have been promising. Both the acquired longitudinal and the reconstructed cross-sectional images demonstrated the ability of the forward-viewing system, based on the rotational scan, to visualise relatively healthy lumens, bifurcations, thickened atherosclerotic walls and, most importantly, very severe and complete vessel occlusions. There is no distortion of features on the acquired images such as caused in the system of Liang and Hu (1997a) by the shape of the acquisition frame. The reconstructed images appear to be of higher resolution compared to those produced

by the spiral scanning system of Back et al. (1994). The complete grey-scale range of the images is displayed and in this respect, this is an extension and improvement of the work of Ng et al. (1994) which was restricted to a binary display only.

A number of images confirmed the potential of forward-viewing IVUS in imaging totally occluded vessels, where side-viewing IVUS is not applicable. Moreover, in the case of less severely stenosed vessels, the cross-sectional images produced with the forward-viewing catheter, were in good agreement with histology and side-viewing IVUS images as regards the location of the plaque and the shape of the residual lumen. This feature, as well as the information on the axial extent of the disease provided by the longitudinal images, are strong indicators of the potential of forward-viewing IVUS in guiding interventional treatments. During such a procedure, forward-viewing IVUS would initially enable introduction of the guidewire and interventional device through the correct path and branch points, reducing the risk of vessel wall perforation. In the case of severe stenoses, forward-viewing IVUS could provide accurate imaging of the state and morphology of the disease without the need to cross the site of interest, thereby minimising vascular trauma. Forward-viewing IVUS would be particularly suited to interventional therapies performed by devices which remove atherosclerotic tissue in front of them, e.g. laser ablation or rotational atherectomy. Simultaneous on-line imaging of the location of both the interventional device and the occlusion would allow precise targeting of the diseased site by the device. Visual assessment of the recanalisation procedure would provide valuable feedback in the attempt to maximise lumen gain, while minimising vessel injury (Figure 7.15).

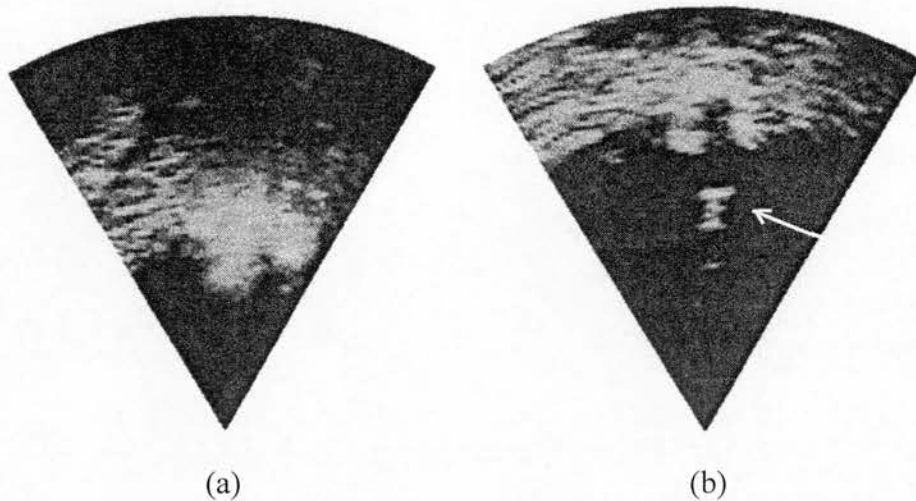


*Figure 7.15 : Laser ablation guided by the forward-viewing IVUS catheter described in Liang and Hu (1997a). Panel (a) shows the lumen occlusion and the formation of gas bubbles during ablation. In panel (b) the tip of the laser catheter, indicated by an arrow, is seen before the occlusion. A crater in the plaque can be observed, just in front of the laser catheter (from Liang and Hu 1997b).*

The axial resolution of IVUS transducers lies in the range between 80 and 200  $\mu\text{m}$ , and is significantly better than the lateral resolution which is depth-dependent and varies from 225 to 1000  $\mu\text{m}$  (Foster et al. 1997; Hoskins and McDicken 1994; Li et al. 1994; Roelandt et al. 1993b). The majority of the variation in vessel wall and plaque features is arranged along the vessel's radial direction. Side-viewing systems take advantage of the axial resolution along the radial direction to distinguish vessel wall layers and plaque components to a certain extent.

In the case of forward-viewing IVUS, the axial resolution could help the discrimination of plaque components lying along or near the catheter axis. The discrimination of the remaining vessel wall and plaque features is dependent on the lateral resolution. Since this resolution is much poorer than the axial, it is not



surprising that the typical 3-layered vessel wall appearance was seen only in a few cases of acquired frames (e.g. Figure 7.5c). Overall, there was a lack of wall layer discrimination in the reconstructed cross-sectional forward-viewing images. It needs to be said though, that the majority of the scanned vessels were carotid arteries, which are elastic type of arteries with the media as echogenic as the other wall layers. However, even for the scanned segments of the femoral artery, which is a muscular type with an echolucent media, the vessel wall layers could not be distinguished on the grey-scale cross-sectional forward-viewing images.

Another reason, apart from the lateral resolution, for this lack of wall layer differentiation might be the fact that the backscatter from the intima, the elastic laminae and the adventitia is dependent on the angle of the beam incidence with the vessel wall. The backscatter of these layers, in the axial direction of the vessel, reduces with angular deviation from normal incidence. On the other hand, the backscatter of the muscular media in the axial direction, is fairly constant and independent of the angle of the beam incidence with the vessel. Hence, for the range of angles of beam incidence with the vessel wall encountered in a forward-viewing acquisition frame, the difference between the backscatter of the media and the rest of the wall layers can be very small (de Kroon et al. 1991a and 1991b). As a consequence it is difficult to differentiate these layers on the grey-scale images.

The presence of calcium in the atherosclerotic plaque was relatively easy to identify on the forward-viewing images. Calcific deposits caused strong levels of echo, followed by acoustic shadowing observed either on the same longitudinal image or on reconstructed cross-sectional images corresponding to regions beyond the calcium location. Other tissue types were not directly identified on the grey-scale images. One reason for this is the magnitude of the transducer's beam width. When several tissue types are sampled by the same beam, the returned echo does not purely reflect any particular type of tissue. In addition, the backscatter from atherosclerotic plaque exhibits an angular dependence. In the study of Picano et al. (1985), it was shown that with the exception of calcium, it is difficult to discriminate the other atherosclerotic tissue types (namely fibrous, fatty and fibrofatty) under conditions of

angular scattering. It seems that, based on the information provided from the forward-viewing echo images alone, some degree of decision making on the selection of recanalisation strategy is feasible. This would apply to cases where the presence of calcium in the plaque is confirmed; rotational atherectomy is a suitable tool for removing calcium. More advanced tissue classification methods, such as those based on spectral and textural analysis of the RF signal (Linker et al. 1991; Nailon 1997; Spencer et al. 1997; Watson et al. 2000; Wilson et al. 1994), will probably need to be applied on forward-viewing IVUS data, taking into account the angular dependence of backscatter, in order to aid the decision making on therapeutic strategies for stenosed vessels.

The least encouraging aspect of the forward-viewing IVUS system was its tendency to underestimate luminal dimensions, caused by the imperfect lateral resolution of the current IVUS transducers. As regards clinical application, a more accurate system would be extremely useful in determining the appropriate size of the interventional device to be used for recanalisation. This would help maximise lumen gain while avoiding unnecessary catheter exchanges and saving time during treatment. Underestimating lumen area measurements would lead to selection of a smaller diameter interventional tool which would not achieve maximum recanalisation. Nevertheless, this type of choice would not impose any risk of vascular trauma, as opposed to the choice of a larger diameter tool derived from overestimating lumen area measurements. Improving the lateral resolution of IVUS transducers, by some means of beam focusing, will undoubtedly enhance the dimensional accuracy of a forward-viewing IVUS system. In addition, it might also aid the tissue characterisation effort, as well as the discrimination of vessel wall layers.

In this *in vitro* work with human vessels, the useful length of the field of view varied from 3.1 to 6.8 mm distal to the tip of the 30 MHz catheter, depending on the amount of atherosclerotic tissue present in front of the catheter. The extent of the plaque can be sometimes longer than the above distances. In such cases more ultrasound penetration would be required and, in that respect, a 20 MHz transducer

would be more suitable for depicting the extent of the disease. This was confirmed in experiments carried out with a block of the TMM described in section 2.6.1. When the TMM block was placed right in front of the 30 MHz catheter, the maximum penetration depth was limited to approximately 6-7 mm. When a 20 MHz catheter was used instead, the penetration depth was increased to approximately 11-12 mm. This 5 mm gain in the imaging field size is considerable, nevertheless the magnitude of the lateral resolution of a 20 MHz transducer would not help in correctly quantifying luminal dimensions and identifying vessel wall layers and plaque components. It seems that efficient beam focusing would be essential for a 20 MHz forward-viewing catheter and, in this respect, the phased array technology with its potential for dynamic focusing would be a very attractive way of implementing such a catheter. In the alternative case of employing a single element device for scanning a sector ahead of the catheter, a small lens would be required to provide the necessary focusing.

For accurate 3D acquisition and reconstruction, it is essential to maintain a uniform sector rotation and a fixed axis of rotation. Taking the current technology into account, any of the two previously mentioned catheter designs would rely on a flexible drive shaft to achieve uniform sector rotation. However, such a shaft is prone to non-uniform rotational artifacts in tortuous vessels (ten Hoff 1989), where it may not be able to provide one-to-one rotation transmission from its distal part to the catheter tip. A rotational encoder may need to be incorporated in the design of the catheter to overcome this problem. Vessel movement with cardiac cycle, means that volume acquisition needs to be completed within a short part of the cardiac cycle in order to ensure a fixed axis of rotation. Diastole would probably be the most suitable cycle phase for volume acquisition, since motion during this phase is relatively reduced. ECG triggering would, therefore, be required to synchronise the volume acquisition with this phase of the cardiac cycle.

Both the mechanical single element and the phased array catheter designs would provide focusing in the direction of the scan plane only. To achieve focusing in the out-of-plane direction annular or 2D arrays may be used. A miniature annular

array would be combined with a mechanical sweeping mechanism to provide a sector frame of reduced slice thickness. The difficulty and complexity in miniaturising this design may delay its implementation for some time.

A 2D array at the catheter tip would be capable of providing focusing and steering in both lateral and elevational planes. This design would have the potential of generating 2D sector images of reduced slice thickness at any angular orientation. In addition, it could acquire the complete volume data in real-time, with a fully electronically controlled scanning action (Whittingham 1997). This would eliminate the need for the drive shaft and the rotational encoder mentioned previously. Two dimensional array probes have only recently been manufactured for non-invasive use. Miniaturisation of 2D arrays is an extremely challenging task and its achievement may not be expected in the near future. Nevertheless, this design promises to be the ultimate solution for high quality forward-viewing IVUS imaging.

## **7.6 Conclusion**

This chapter has described the application of a forward-viewing IVUS catheter based on the rotational scan, in imaging human vessels. Three dimensional data sets were successfully acquired and assessed for a number of carotid and femoral arteries *in vitro*. The reconstructed images demonstrated the ability of the forward-viewing IVUS catheter to visualise severely stenosed and totally occluded vessels, where the current side-viewing IVUS systems cannot be used. The results from this *in vitro* study provide promise that forward-viewing IVUS could also become a useful tool for 3D evaluation and characterisation of severely diseased vessels, aiding the selection of appropriate therapeutic modalities. The angular dependence of backscatter along the layered structures in the vessel wall appears to cause some difficulties in imaging them. Further research into the use of RF processing techniques on the scattered signals, is required in order to overcome these difficulties. Improvements regarding the lateral resolution of IVUS transducers are

also required, so that forward-viewing IVUS systems can provide accurate lumen quantification, necessary for defining the appropriate size of interventional tools.

In conclusion, the rotational scan is a very promising technique for implementing a forward-viewing IVUS imaging system suitable for anatomical assessment of stenosed vessels and for guidance of recanalisation procedures. In addition, Doppler processing of the returned echoes could provide colour flow images, illustrating the spatial distribution of blood flow and enabling study of vascular haemodynamics. This potential application is explored in the following chapter.

## **CHAPTER 8**

# **DOPPLER COLOUR FLOW IMAGING AND FLOW QUANTIFICATION WITH FORWARD-VIEWING IVUS**

### **8.1 Introduction**

Apart from the morphological and anatomical assessment, another method used for estimating the severity of a stenotic lesion is the functional assessment. This involves measurement of blood velocity and flow in the stenosed artery before and after an interventional procedure. Intravascular ultrasound methods have been developed for these purposes and are currently used in clinical practice, nevertheless there are certain limitations governing their use.

The purpose of this chapter was to investigate the potential use of a forward-viewing IVUS system in estimating blood velocity and flow in stenosed vessels. At first, the currently used IVUS techniques are presented along with their limitations. Following that, a new technique is described for blood flow estimation and colour flow imaging with the use of forward-viewing IVUS. Preliminary results are presented for flow through normal and stenosed vessel phantoms. Finally, the merits and limitations of this new method are discussed with reference to potential application in clinical practice.

## **8.2 IVUS techniques for functional assessment of stenosed vessels**

There are currently two techniques which employ IVUS for functional assessment of stenotic lesions. The first one makes use of Doppler wires either alone or in conjunction with IVUS imaging catheters, while the second method employs only imaging catheters and provides an estimate of blood velocity and flow based on the decorrelation properties of the ultrasound signals. The principles of operation of these techniques are detailed below.

### **8.2.1 Estimation of blood velocity and flow using Doppler wires**

The Doppler wire (FloWire, Cardiometrics Inc, Mountain View, California, USA) is a very thin flexible wire of either 0.018" (0.45 mm) or 0.014" (0.35 mm) diameter. A single element transducer of 12 or 15 MHz frequency is located at the tip of the wire. This transducer emits a 28° broad beam in forward direction (Figure 8.1).

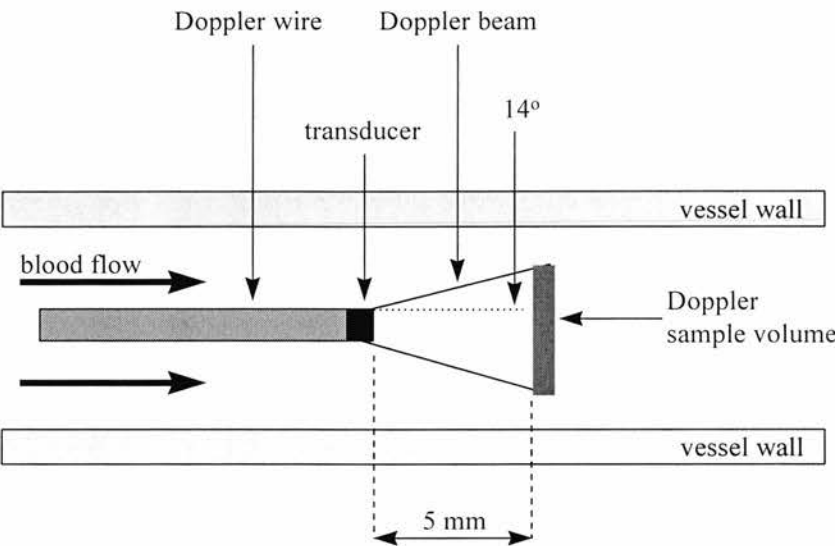


*Figure 8.1 : Schematic diagram of a Doppler wire and its operation in a vessel.*

Insertion of a catheter or wire in a blood vessel disturbs the flow pattern. Experimental work has shown that in the case of flow coming from behind the catheter/wire (as happens in coronary arteries), a distance approximately 10 times the



catheter/wire diameter is required for recovery of the flow pattern (Tadaoka et al. 1990). Therefore, in the case of Doppler wires, the sample volume is located 5 mm from the wire tip. The Doppler wire is connected to a dedicated system which performs spectral analysis (FFT) on the Doppler signals (FloMap, Cardiometrics Inc, Mountain View, California, USA). The system provides display of the Doppler spectrum on a screen along with spectral envelope tracing and an estimate of the time average of the spectral peak velocity (average peak velocity - APV).

Estimation of the APV at locations proximal to the stenosis and within the stenosis itself allows calculation of the stenotic velocity ratio which can be used for a haemodynamic estimation of the percent stenosis pre and post intervention (Johnson et al. 1989). Moreover, the APV is used for quantitative measurements of flow when the Doppler wire is used in conjunction with an IVUS imaging catheter. In that case, the Doppler wire acts also as a guidewire over which the IVUS catheter is advanced (Figure 8.2).

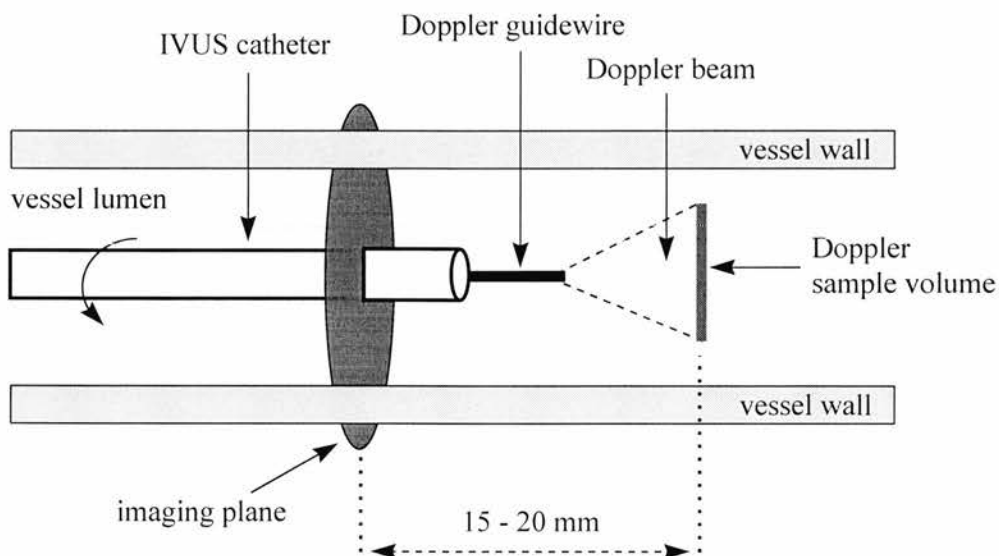


*Figure 8.2 : Arrangement of IVUS imaging catheter and Doppler wire for measuring blood flow.*



The IVUS images allow measurement of lumen cross-sectional area (CSA). Blood flow  $Q$  is generally measured as

$$Q = V_{mean} \cdot CSA \quad (8.1)$$

where  $V_{mean}$  is the mean velocity across the lumen cross-section. In the case of IVUS imaging/Doppler wire combination, blood flow is estimated as

$$Q = 0.5 \cdot APV \cdot CSA \quad (8.2)$$

where 0.5 is a factor which has been validated empirically with model tubes *in vitro* and canine models *in vivo* (Doucette et al. 1992). It corrects for assumed parabolic flow, where the mean velocity is half the peak velocity provided by the Doppler wire. The velocity profile in pulsatile arterial flow is not parabolic, nevertheless, Doucette et al. (1992) have shown that changes of pulsatility had small effect on the APV in model tubes of diameter similar to that of coronary arteries, and that the measured APV values were very close to the expected ones when parabolic flow was assumed.

The Doppler wire is also used to assess the flow response to substances infused in the blood circulation. Comparison of the 'baseline' APV with the one achieved following the infusion of agents such as adenosine, substance P (a hormone found in human body) and nitric oxides, enables the study of the mechanism and site of action of vasoactive agents affecting the coronary circulation (Sudhir et al. 1993), and permits assessment of coronary flow reserve and the state of endothelium (Rieber et al. 1998; Newby and Fox *in press*).

### **8.2.2 Limitations of measuring blood velocity and flow with Doppler wires**

The Doppler wires are designed to detect the peak velocity of the arterial flow. For achieving this they employ a single broad beam in order to insonate as much of the lumen area as possible. At the location of the sample volume (5 mm from the wire tip), the beam is approximately 2.5 mm broad. This is a considerable proportion of the lumen diameter in coronary arteries and in theory increases the possibility of sampling the peak velocity. However, this is not completely successful in practice. Computational work has revealed that the velocity estimate provided by a

Doppler wire is dependent on the wire's position within the artery (Moraes and Evans 1995). This situation is frequently encountered in clinical practice, where the wire tip can be pointing away from the central flow streamline, e.g. towards the vessel wall. The operators then need to manipulate the wire in order to achieve a position that provides improved Doppler signal and velocity estimate. In some cases this procedure proves to be time consuming (Figure 8.3), while there is still some uncertainty about whether or not the correct signal has been obtained.

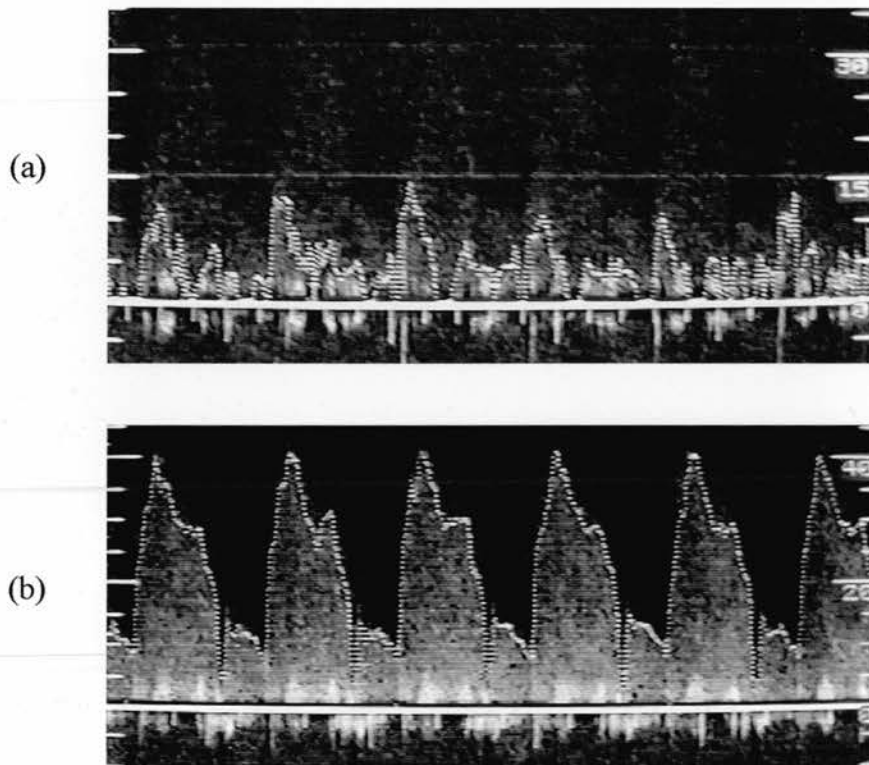


*Figure 8.3 : Evidence of the position dependence of a Doppler wire output in vivo. (a) Only the edge of the beam sampled the flow correctly, and as a result a weak spectral signal appeared which could not be tracked by the envelope detector correctly. The resulting envelope is shown by a bright line. (b) Correct flow sampling required up to 15 minutes manipulation and repositioning of the Doppler wire.*

The simultaneous use of an IVUS catheter and a Doppler wire is not always possible due to radiofrequency interference between the two systems. When the Doppler device is on, a radial artifact appears on the IVUS image as a result of cross-talk (Isner et al. 1993). This artifact is not present when the Doppler device is off. As a result, these two systems may need to be operated in a sequential mode. Moreover, velocity and CSA measurements are taken at different sites which can be 15 to 20 mm apart (Figure 8.2). This is because the IVUS transducer is located a few mm proximal to the tip of the IVUS catheter, and the Doppler sample volume needs to be at certain distance distal to the catheter tip in order to obtain measurements from an area free of the flow disturbance caused by the insertion of the catheter (Sudhir et al. 1993, Tadaoka et al. 1990). The inability to assess the haemodynamic parameters simultaneously in space and time may limit the applicability and accuracy of the method in severely diseased vessels.

### **8.2.3 Decorrelation based estimation of blood velocity and flow**

Recently, a new method for flow quantification has been developed (Crowe et al. 1996; Li et al. 1998). It employs use of an IVUS catheter only, for providing cross-sectional images along with velocity information. Velocity estimates across the vessel lumen are derived from the decorrelation rate of the RF ultrasound signals.

When a cluster of blood particles (scatterers) moves across the imaging plane, the RF signals decorrelate monotonically and approximately linearly with displacement of the scatterers (Figure 8.4). Based on this principle, measured decorrelation values of RF signals from blood can be converted to displacements. By measuring the decorrelation at controlled time intervals, blood velocity estimates are derived from the ratio of displacement and time. Spatial integration of these velocity estimates over the lumen CSA enables volumetric flow quantification with quoted errors in the range of 4-10% (Li et al. 1998; Carlier et al. 1998).

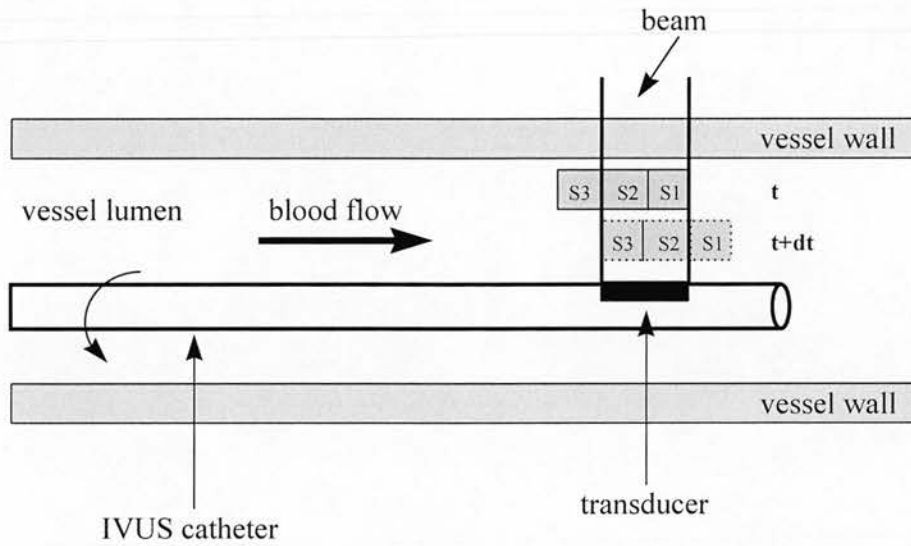


*Figure 8.4 : Decorrelation of RF signals due to movement of blood scatterers through the ultrasound beam. During the time interval  $dt$  the group of scatterers S1 leaves the beam space, while the group S3 enters the beam. At time  $t$  the RF signal is generated by the scattering groups S1 and S2; at time  $t+dt$  the RF signal is generated by the groups S2 and S3. Decorrelation between the RF signals at times  $t$  and  $t+dt$  is due to the scatterers leaving and entering the beam (S1 and S3 respectively) as well as to the scatterers moving within the beam (S2). The scatterers are at the same radial distance from the transducer at both times  $t$  and  $t+dt$ ; for simplicity of illustration they have been drawn at different radial distances.*

The main limitation of this method is that the velocity and blood flow information can only be provided at the transducer site which lies in a region of disturbed flow pattern caused by the presence of the catheter itself. In other words the device cannot be used for study of flow patterns in stenotic lesions. Furthermore, the decorrelation method cannot determine flow direction, hence it is not suited for regions of flow reversal. Finally, such a device is of limited use in severely diseased vessels (with more than 70% luminal stenosis), where the catheter size ( $0.9 \text{ mm}^2$  cross-sectional area) causes further blood flow obstruction.

### **8.3 A forward-viewing IVUS system for flow imaging and quantification**

The previously discussed limitations of the Doppler wire and decorrelation method in measuring the haemodynamic parameters of stenosed vessels could be overcome by a system which would permit both the imaging and velocity measurement functions to be performed

- at the same site distal to the catheter tip,
- in a region where the flow is not disturbed by the presence of the catheter and
- inside the stenosed area.

The above requirements could, in principle, be met by forward-viewing IVUS systems employing one transducer only and using the same RF signals for the purposes of image production and velocity estimation. At least, it was thought that a duplex Doppler mode could be operated with which velocity signals could be obtained from an appropriate site in the vessel and hence, avoid the errors encountered with Doppler wires. In order to test this hypothesis, a flow phantom was developed for use in conjunction with the forward-viewing imaging system described in chapter 6. Appropriate software was also written for deriving velocity information from the RF signals. The complete set up is described in the following sections.

#### **8.3.1 Blood mimicking fluid**

The blood mimicking fluid (BMF) described by Ramnarine et al. (1998 and 1999) was used for the purposes of this study. It consisted of 5  $\mu\text{m}$  Orgasol™ particles (2001UDNAT1 Orgasol, ELF Atochem, Paris, France) mixed in a fluid base of pure water, pure glycerol, Sigma D4876 dextran 185000D and ICI synperonic N surfactant.

The Orgasol™ particles mimicked the scattering properties of the red blood cells. The proportion of water/glycerol in the fluid base determined the speed of sound ( $1548 \pm 5 \text{ m s}^{-1}$ ) and the density ( $1.037 \pm 2 \text{ gr cm}^{-3}$ ) of the BMF. The dextran increased the viscosity ( $4.1 \pm 0.1 \text{ mPa s}$ ) to levels similar to those of human blood at high shear rates, while the surfactant ensured that the Orgasol™ particles were

sufficiently dispersed. The relative proportion of the ingredients by weight is shown in Table 8.1.

*Table 8.1 : Composition of the blood mimicking fluid (from Ramnarine et al. 1999).*

BMF Ingredients	Weight proportion (%)
Orgasol™ 5 µm	1.82
Water	83.86
Glycerol	10.06
Sigma D4876 dextran 185000D	3.36
ICI synperonic N surfactant	0.9

8.3.2 Flow phantom

A gear pump (model 185-000, Micropump Inc, Vancouver, Washington, USA), was used to pump the BMF from an open reservoir through a flow circuit as shown in Figure 8.5. The pump was driven by a dc motor, the rotation speed of which was controlled by a power supply.

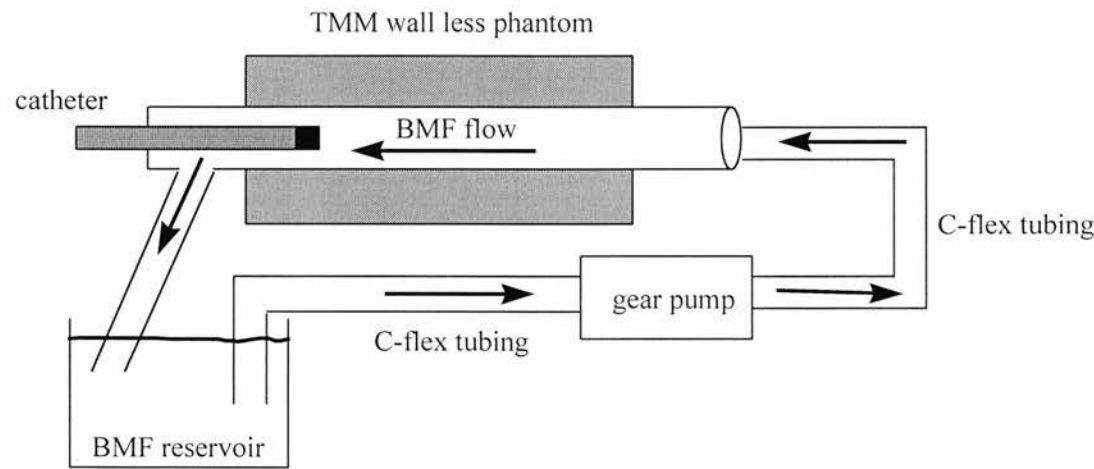


*Figure 8.5 : Schematic diagram of the flow phantom used for Doppler studies with forward-viewing IVUS.*

The BMF was directed via C-flex tubing (Cole-Parmer, Vernon Hills, Illinois, USA) into straight wall-less TMM vessel phantoms which simulated healthy vessels as well as vessels with symmetrical and eccentric stenoses (Figure 8.6). The lumen diameter was 8 mm for the healthy parts of the vessel phantoms, while the symmetrical stenosis had 5.6 mm minimum lumen diameter and the eccentric stenosis 5 mm minimum lumen diameter (30% and 37% diameter stenosis respectively).

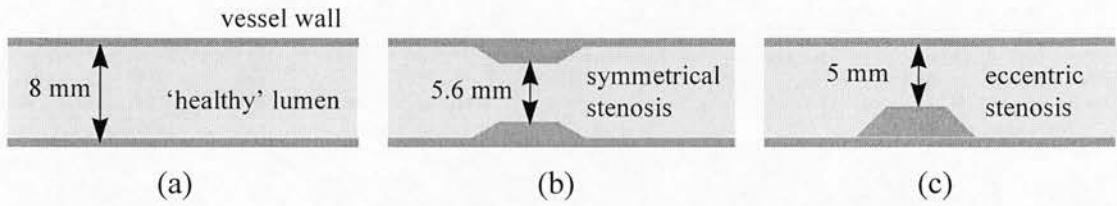


*Figure 8.6 : Schematic diagrams of the TMM vessel phantoms used for Doppler studies with forward-viewing IVUS. Simulations of healthy vessel, 30% symmetrical diameter stenosis and 37% eccentric diameter stenosis are shown in (a), (b) and (c) respectively.*

The vessel phantoms were manufactured by casting TMM round a perspex mould in a tank. The TMM described in section 2.6.1 was used for this purpose. Layers of foam were used at the joints of the TMM structure with the inlet and outlet of the flow phantom, in order to avoid any BMF leakage (Figure 8.7). When the TMM was cast the foam layers were soaked by it, sealing the inlet and outlet efficiently (Figure 8.8).



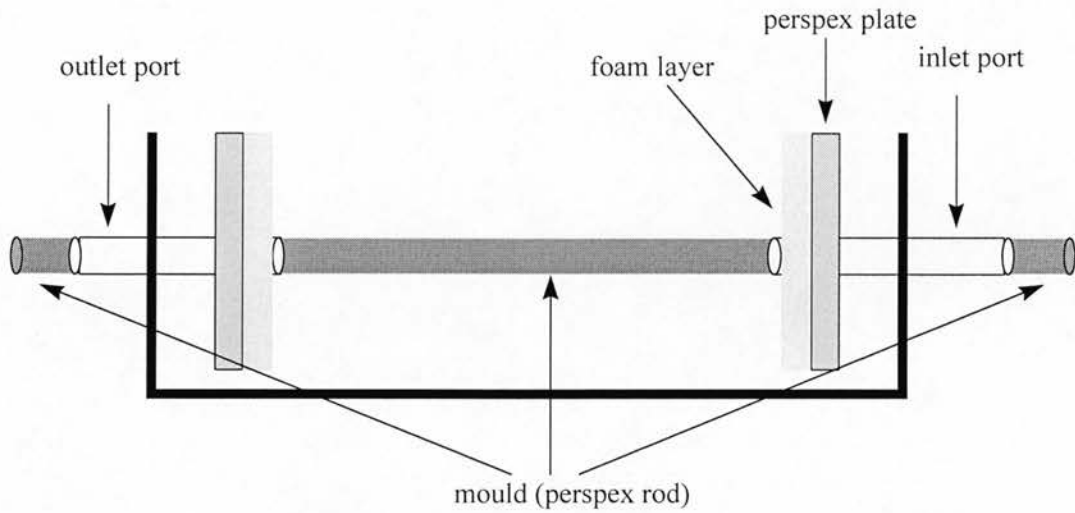


*Figure 8.7 : Arrangement of mould and foam layers for casting a wall-less TMM vessel phantom and avoiding any BMF leakage.*

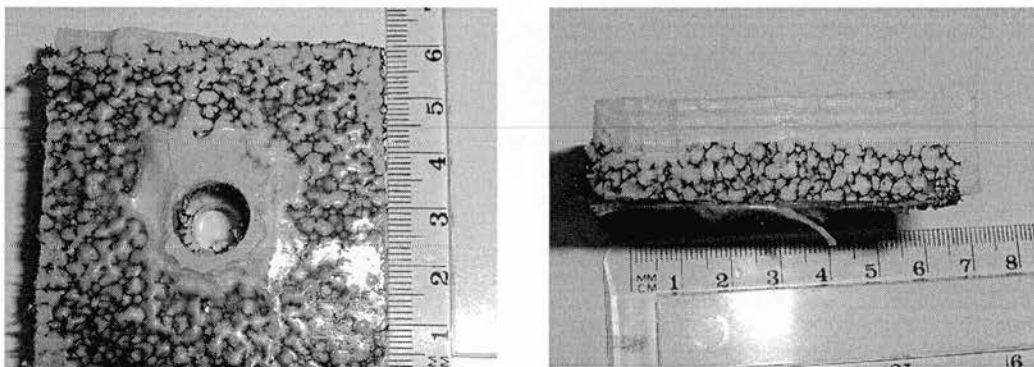


*Figure 8.8 : Photographs of foam layers (black colour) soaked with TMM (grey colour) after the TMM had been cast to form the vessel phantom. The soaked foam provides a very good seal preventing BMF leakage at the inlet and outlet of the flow phantom.*



The forward-viewing catheter was inserted into the vessel phantom from the end opposite to the BMF inlet. In this way, the BMF flow was towards the catheter (Figure 8.5). This is contrary to the situation encountered in coronary arteries, where the blood flow is away from the catheter. However, simulation of flow away from the catheter would not have been practically applicable in this study, due to the fact that the 3.8 mm forward-viewing catheter would have caused flow disturbance extending to nearly 3-4 cm distal to its tip (Tadaoka et al. 1990). This kind of distance is well beyond the field of view of IVUS transducers, and consequently the device could not provide meaningful results. On the other hand, when flow is directed towards the catheter, the region of flow disturbance is shorter (as shown later in section 8.4.2.1) and undisturbed flow lay within part of the field of view of the 30 MHz transducer. If accurate and reliable system performance was shown for undisturbed flow in one direction, it would be reasonable to expect similar performance for the opposite direction, too.

The catheter was aligned parallel to the centreline of the TMM vessel phantom and the whole assembly was horizontally orientated. All experiments were carried out at room temperature (22° C), under steady flow conditions.

### **8.3.3 Data acquisition system**

The data acquisition system employed in this Doppler study was the one developed for forward-viewing IVUS imaging (section 6.5.3). The same intravascular ultrasound scanner and forward-viewing catheter with the 30 MHz transducer were used. Once again, the motor rotation in the patient interface unit of the scanner was disabled and A-mode RF lines were acquired from the scanner's output port and digitised by the 12-bit 100 MHz A/D card.

This time though, the study was restricted to two dimensions only. Sector frames were acquired, consisting of 120 lines-of-sight arranged across a 72° sector. Sixteen pulses were transmitted along each line of sight to enable velocity estimation along that direction, according to a procedure described in the following section. The

same RF data was also used for image production. The RF signals received from the 16 transmitted pulses along each direction, were averaged in order to reduce the effects of the random backscatter from the BMF particles and enhance the image quality (Li et al. 1994). Following that, 2D grey scale sector images were produced according to the software scheme described earlier in sections 2.5.4 and 6.5.3.

#### **8.3.4 Blood velocity estimation and display**

From all the techniques developed for velocity estimation and colour flow imaging, the two dimensional autocorrelation method (Loupas et al. 1995a and 1995b) is regarded as the most accurate. Based on this fact, it was decided to adopt this technique for the purposes of the forward-viewing IVUS/Doppler study.

Initially, Hilbert transform was performed on all the 16 RF signals received for each direction within the sector frame. Let  $rf(m,n)$  be the original RF signal from a sample volume and  $h(m,n)$  its Hilbert transform, with  $m$  being the sample index within the sample volume and  $n$  the transmission pulse index along a line of sight. The analytical complex signal  $z(m,n)$  is then expressed as

$$z(m,n) = rf(m,n) - jh(m,n) \quad (8.3)$$

The two dimensional autocorrelation method estimates both the mean Doppler and the mean RF frequency in each sample volume. Estimation of the mean RF frequency is important since the mean frequency of the transmitted pulse spectrum changes with propagation. As the ultrasonic pulse propagates in tissue, its higher frequency components are attenuated stronger than its lower frequency components, therefore the mean frequency of the pulse spectrum reduces. On the other hand, non-linear propagation in tissue gives rise to harmonic frequencies which can increase the mean frequency of the pulse spectrum. The combined result of these two mechanisms is random fluctuations of the mean RF frequency of the transmitted pulse throughout the region of measurements.

The mean Doppler and the mean RF frequency in the sample volume are calculated from the autocorrelation function  $\gamma$  of the complex signal  $z(m,n)$

$$\gamma(a,b) = \sum_{m=0}^{M-a-1} \sum_{n=0}^{N-b-1} z(m,n)z^*(m+a,n+b) \quad (8.4)$$

where  $a$  and  $b$  define the lag,  $M$  is the length of the sample volume and  $N$  the number of transmissions per line of sight. For this study,  $M$  is equal to the pulse length of the 30 MHz transducer (11 samples - Figure 6.6) and  $N$  is equal to 16. The mean Doppler frequency in the sample volume is estimated as

$$f_{Doppler} = \frac{1}{2\pi} \tan^{-1} \left\{ \frac{\text{Im}[\gamma(0,1)]}{\text{Re}[\gamma(0,1)]} \right\} \quad (8.5)$$

and the mean RF frequency as

$$f_{RF} = \frac{1}{2\pi} \tan^{-1} \left\{ \frac{\text{Im}[\gamma(1,0)]}{\text{Re}[\gamma(1,0)]} \right\} \quad (8.6)$$

The ratio of the mean Doppler and RF frequencies is proportional to the mean axial velocity. The velocity in the sample volume is finally estimated as

$$v = \frac{ct_s f_{Doppler}}{2T_p f_{RF} \cos \theta} \quad (8.7)$$

where  $c$  is the speed of sound in the BMF,  $t_s$  is the digitisation rate of the RF signal (10 nsec when using the PDA12 digitiser),  $T_p$  is the pulse repetition period (138.9  $\mu$ sec for the HP Sonos Intravascular scanner) and  $\theta$  is the angle between the ultrasound scan line and the axis of the vessel phantom.

By performing the above calculations for every sample volume along a line of sight, a set of velocity values are derived for a particular direction of the ultrasound beam within the sector frame. When this is repeated for all the lines of sight in a sector frame, then velocity estimations are derived for the whole 2D frame. This data can then be scan converted and presented as a colour display with shades of red indicating flow towards the catheter and shades of blue indicating flow away from the catheter. The colour flow image can be overlaid on the grey scale 'anatomical' image to create a composite display of the vessel morphology and the flow in its lumen. In addition, the velocity profile across the lumen diameter can be displayed for any part of the lumen lying within the sector image.

The whole procedure of processing the RF signals off-line in order to derive velocity information for every frame and subsequently display colour flow images and velocity profiles, has been implemented in software using IDL programming (Research Systems, Boulder, Colorado, USA).

### **8.3.5 Flow quantification**

The forward-viewing IVUS system can also be used for flow quantification purposes. On the grey scale image, the lumen diameter can be measured at a region of interest. Subsequently, the diameter size can be converted to lumen CSA, assuming that the lumen has circular shape. Velocity profile information is also available for the same region of interest. The mean or peak velocity across the lumen diameter can then be used for flow quantification according to equations 8.1 or 8.2 respectively.

## **8.4 Results**

### **8.4.1 Measurement range**

Steady flow rates from 45.3 up to 172.8 ml min<sup>-1</sup> could be achieved in the flow phantom, by varying the voltage supplied to the dc motor from 1.5 to 6 V. Smooth motor operation was not possible for supply voltages less than 1.5 V, while for voltages above 6 V air bubbles were generated by the pump and spread around the flow circuit. The relationship between the motor speed (supplied voltage) and the flow rate was established by timed collection of BMF in a reservoir (Table 8.2). A very good linear fit was found:

$$Q \text{ (ml min}^{-1}\text{)} = 28.229 \text{ Motor Voltage (V)} + 4.194, \quad r = 0.999.$$

*Table 8.2 : Steady flow and velocity data in relation to the voltage supplied to the motor driving the pump. The velocity data was derived for conditions of parabolic flow in a tubular structure of 8 mm lumen diameter.*

<b>Motor voltage (V)</b>	<b>BMF weight (gr/min)</b>	<b>Flow rate (ml/min)</b>	<b>Parabolic flow mean velocity (cm/s)</b>	<b>Parabolic flow peak velocity (cm/s)</b>
1.5	47.0	45.3	1.50	3.00
2.5	78.5	75.7	2.51	5.02
3	92.6	89.3	2.96	5.92
4	121.8	117.5	3.90	7.80
5	151.0	145.6	4.83	9.66
6	179.2	172.8	5.73	11.46

The intravascular ultrasound scanner used in this study, had been designed for imaging purposes only. As a consequence, the scanner's PRF of 7200 Hz, although adequate for imaging, was low when Doppler applications were concerned. This low PRF limited the range of velocities which could be detected free of aliasing phenomena, according to the following equation

$$v_{\max} = \frac{PRFc}{4f_t \cos\theta} \quad (8.8)$$

where  $c$  is the speed of sound in the BMF,  $f_t$  is the transmitted frequency and  $\theta$  is the angle between the ultrasound beam and the flow. For PRF=7200 Hz,  $c=1548 \text{ m s}^{-1}$ ,  $f_t=28 \text{ MHz}$  (according to Figure 6.7) and  $\theta=0^\circ$ , the maximum unambiguously detected velocity was approximately  $9.95 \text{ cm s}^{-1}$ . This velocity value was much lower than the ones encountered in healthy and diseased coronary vessels under baseline or hyperaemic conditions, ranging from 20 to over  $100 \text{ cm s}^{-1}$ . The velocity limit of  $9.95 \text{ cm s}^{-1}$  corresponded to  $150 \text{ ml min}^{-1}$  parabolic flow, which was just below the maximum flow rate achieved in the flow phantom.

### 8.4.2 Parabolic flow

The fidelity of the new Doppler/IVUS system was tested under parabolic flow conditions in the ‘healthy’ vessel phantom. The inlet length ( $L$ ) for development of parabolic flow in a tube is given by the empirically derived equation

$$L = 0.03d \text{ Re} \quad (8.9)$$

where  $d$  is the lumen diameter and  $\text{Re}$  is the Reynolds number defined as

$$\text{Re} = \frac{v_{\text{mean}} d}{\nu} = \frac{v_{\text{mean}} d \rho}{\eta} \quad (8.10)$$

(Evans et al. 1989), with  $v_{\text{mean}}$  being the mean velocity of the parabolic flow,  $\nu$  the kinematic viscosity of the fluid,  $\eta$  its dynamic viscosity and  $\rho$  its density. By combining equations 8.9 and 8.10 it becomes

$$L = \frac{0.03 v_{\text{mean}} d^2 \rho}{\eta} = \frac{0.03 v_{\text{max}} d^2 \rho}{2\eta} \quad (8.11)$$

For the case of BMF (with  $\rho=1.037 \text{ gr cm}^{-3}$  and  $\eta=4.1 \text{ mPa s}$  or  $0.041 \text{ gr cm}^{-1} \text{ s}^{-1}$ ), flowing in a lumen of 8 mm diameter, the required inlet length for development of parabolic flow with  $v_{\text{max}}=9.95 \text{ cm s}^{-1}$  (so that no aliasing occurs), is approximately 2.4 cm. Hence, it was decided to place the catheter at a 10 cm distance from the inlet point to ensure that parabolic flow would have developed near the catheter tip.

#### 8.4.2.1 Flow disturbance caused by the catheter

An ATL HDI5000 ultrasound scanner (ATL, Bothell, Washington, USA) was used to assess the extent of flow disturbance caused by the presence of the catheter in the lumen of the phantom. A 12 MHz linear array probe operating in colour Doppler mode was placed on the outer surface of the ‘healthy’ vessel phantom, right above the lumen. For the range of flow rates achieved in the flow phantom, colour Doppler images were recorded and subsequently processed with the HDILab package (ATL, Bothell, Washington, USA) to derive velocity profiles across the vessel at several locations distal to the catheter tip (Figure 8.9).



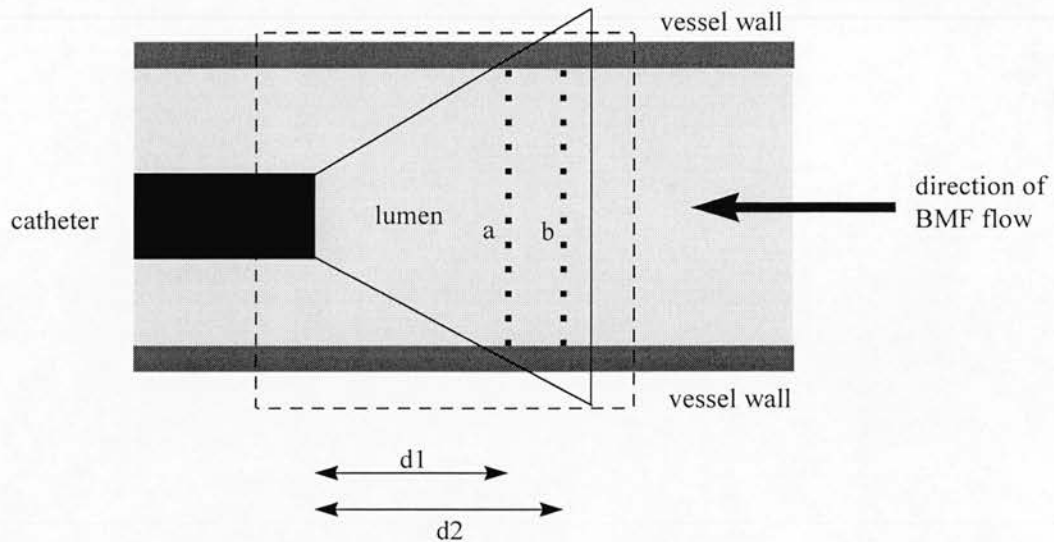


*Figure 8.9 : Schematic diagram illustrating generation of velocity profile data across the lumen of a vessel phantom. The same principle is applied on colour flow images produced either by the ATL HDI5000 scanner or the forward-viewing IVUS system. In the former case, the region of the colour flow data is indicated by the dashed rectangle, while in the latter case colour flow data is obtained within the solid triangular area. Velocity profile at distance **d1** from the catheter tip is generated by collecting the velocity data of all the 'lumen' pixels lying along the dotted line **a**, which is vertical to the vessel walls. Similarly, velocity profile at distance **d2** from the catheter tip is generated from the velocity data of all the 'lumen' pixels lying along the dotted line **b**.*

As shown in Figure 8.10, the catheter caused suppression of the parabolic velocity profiles for a range of distances extending approximately 5 mm distal to its tip. At that distance and beyond, there was a good parabolic fit on the derived velocity profiles ( $R > 0.95$  - Figure 8.10b). The size of this disturbed region provided an indication that meaningful velocity information could be derived in part of the far field of the 30 MHz IVUS transducer. It should be noted that the size of this disturbed region refers to flow towards the catheter and is smaller than that expected for flow away from the catheter.

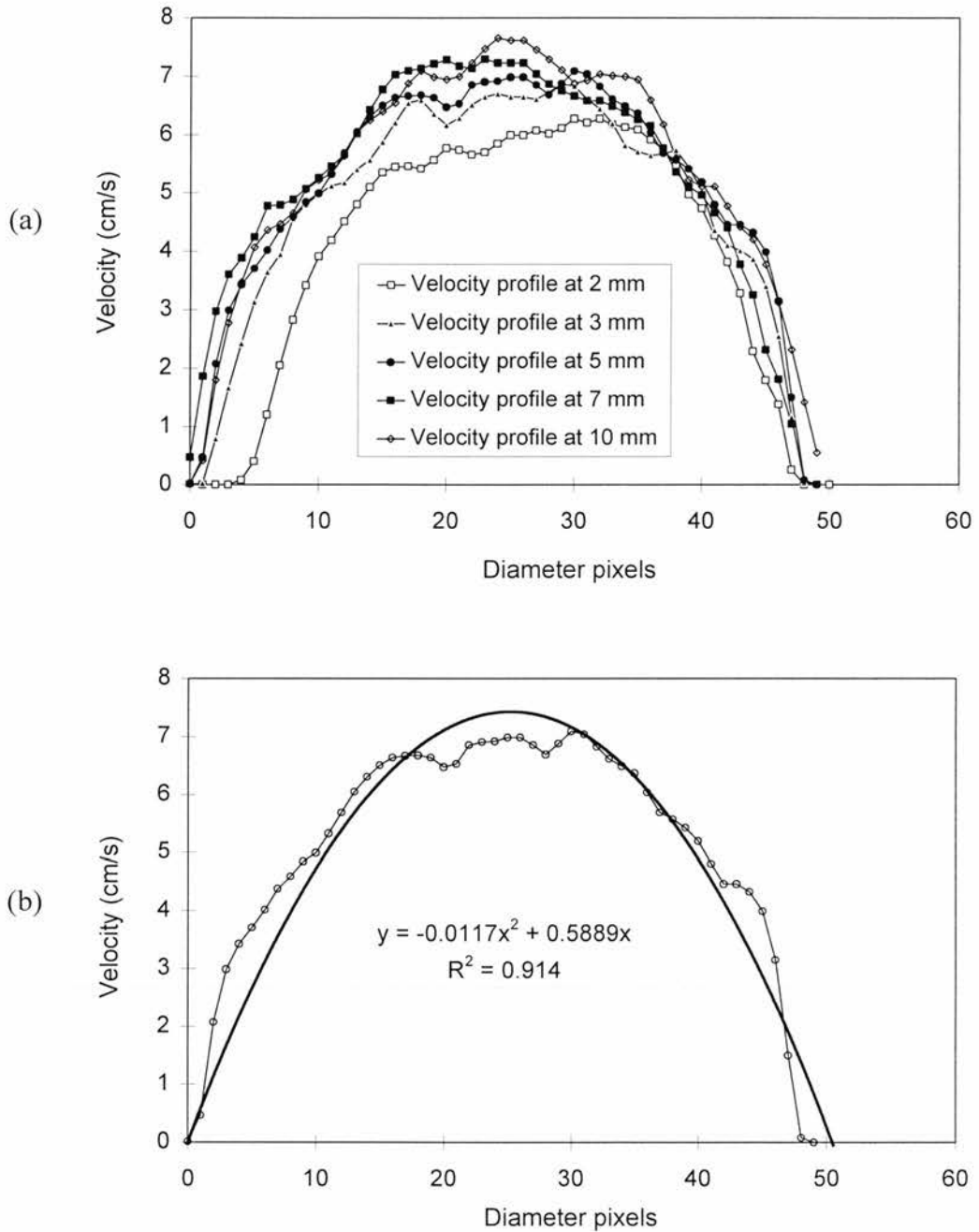


*Figure 8.10 : (a) Velocity profiles obtained with an ATL HDI5000 scanner at several locations distal to the catheter tip under parabolic flow conditions. Disturbed profiles are observed at distances less than 5 mm distal to the catheter tip. (b) Parabolic fit (shown with solid line) on the measured velocity profile at 5 mm distal to the catheter tip.*



#### **8.4.2.2 Detection of parabolic flow with the forward-viewing IVUS system**

Having approximated the extent of flow disturbance caused by the presence of the catheter, the ability of the forward-viewing IVUS system to detect undisturbed parabolic flow was examined. The obtained experimental results were consistent with the theoretical predictions for all for the flow rates shown in Table 8.2. As a general observation, the forward-viewing IVUS system provided velocity profiles in good agreement with the expected parabolic profiles for a range of distances between 5 and 7 mm from the catheter tip. The agreement was improved when a number of velocity estimation frames were averaged, typically 8. This averaging improved the SNR and smoothed the noise spikes seen in stand alone frames (Figure 8.11).

At distances longer than 7 mm distal to the catheter tip, the derived velocity values were significantly lower than the expected ones (Figure 8.12). This underestimation was due to spatial averaging caused by the lateral dimension of the ultrasound beam. As shown in Figure 6.8, the beam width increased significantly at distances longer than 7 mm from the transducer face. For example, at about 8 and 9 mm from the transducer face, the beam was nearly 2 mm wide. In a case like this, the velocity value allocated to a sample volume by the autocorrelation algorithm, was a blend of the velocities sampled by the wide beam. The relatively lower velocities sampled by the side parts of the wide beam, effectively contributed to a calculated value lower than the real one sampled by the middle part of the beam.

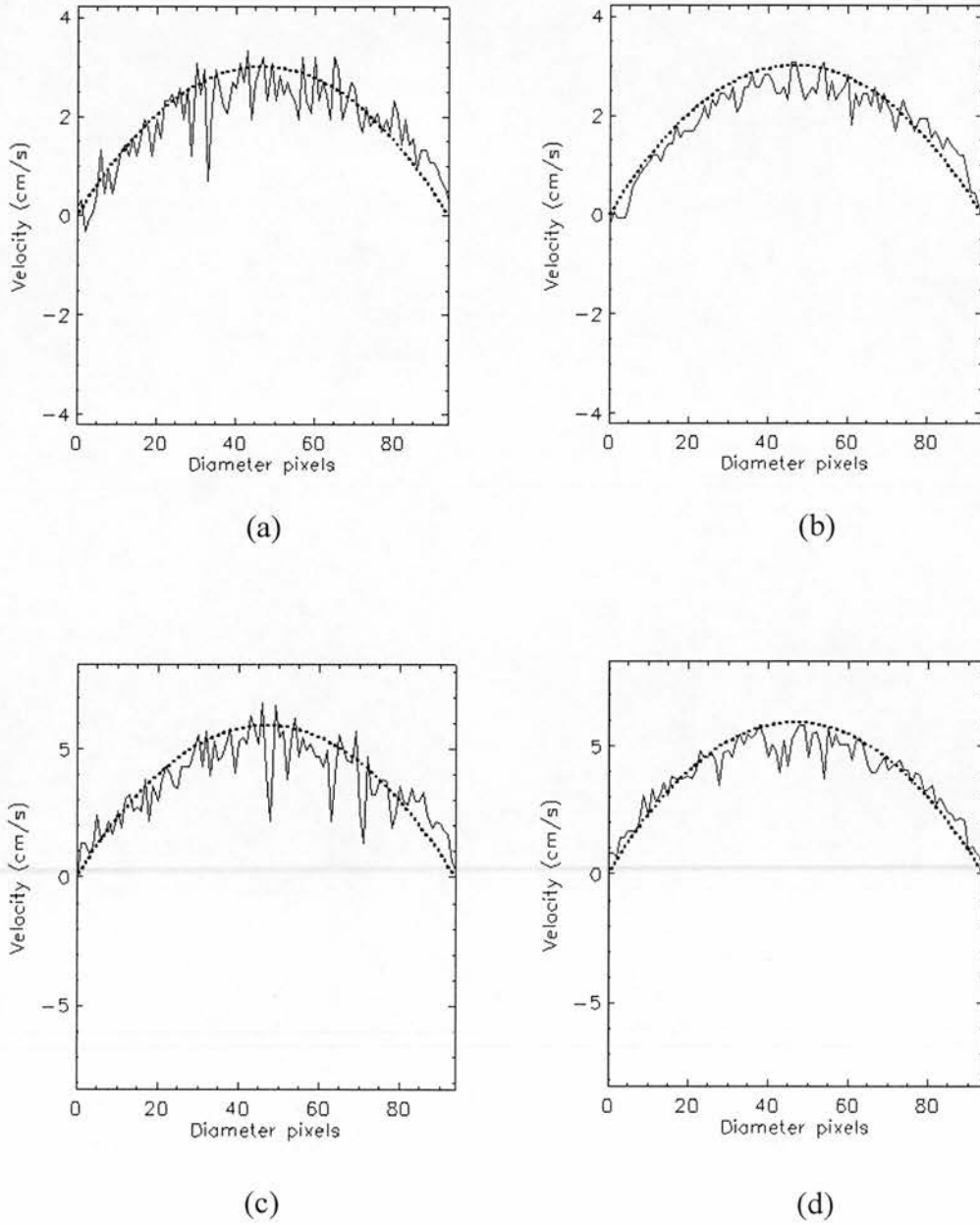


**Figure 8.11** : Estimated velocity profiles (solid lines) plotted against the expected ones (dashed lines) for parabolic flow. Plots (a) and (b) refer to velocities derived from a single frame and 8 averaged frames respectively, at 5.46 mm distal to the catheter tip, for 45.3 ml min<sup>-1</sup> flow rate. Plots (c) and (d) are similar to (a) and (b) respectively, but at 6.13 mm distal to the catheter tip and for a 89.3 ml min<sup>-1</sup> flow rate.

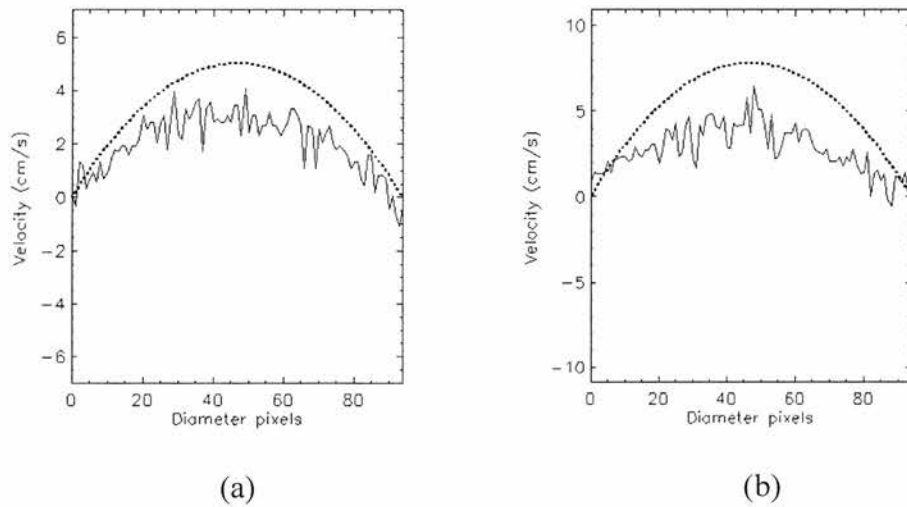


*Figure 8.12 : Estimated velocity profiles (solid lines) plotted against the expected ones (dashed lines) for parabolic flow. Plot (a) refers to velocities derived from a single frame at 8.35 mm distal to the catheter tip, for 75.5 ml min<sup>-1</sup> flow rate. Plot (b) is similar to (a) but at 8.70 mm distal to the catheter tip and for a 117.5 ml min<sup>-1</sup> flow rate. Both plots illustrate the significant underestimation of velocities at those distances from the catheter tip where the beam is very wide.*

Another observation consistent for all the flow rates, was the overestimation of the velocities very close to the vessel walls. This was caused by the finite size of the beam. The estimated velocity profile was in fact the result of a convolution between the real velocity profile and the shape of the sample volume (Hughes and How 1993). This effectively increased the level of estimated velocities near the vessel walls. A direct consequence was the overestimation of the mean velocity across the lumen diameter, too (Table 8.3).

*Table 8.3 : Overestimation of mean velocity by the forward-viewing IVUS system, under parabolic flow conditions.*

<b>Flow rate (ml/min)</b>	<b><i>Expected</i> mean velocity (cm/s)</b>	<b><i>Measured</i> mean velocity (cm/s)</b>	<b>Mean velocity discrepancy (%)</b>
45.3	1.50	1.84	+22.7
75.7	2.51	3.18	+26.7
89.3	2.96	3.71	+25.3
117.5	3.90	4.55	+16.7
145.6	4.83	5.43	+12.4

Hence, from the experiments with parabolic flow, it was evident that the forward-viewing IVUS device could be used confidently for Doppler studies at regions between 5 to 7 mm distal to the catheter tip. The system provided good estimation of the peak velocity, but overestimated the mean velocity across the lumen. Therefore, it was decided to use the peak velocity estimate for flow quantification according to equation 8.2.

#### 8.4.3 Symmetrical stenosis

For the case of the vessel phantom with the symmetrical stenosis, sector frames were acquired with the Doppler sample volumes located *proximal* to the stenosis as well as *inside* the stenosis. Here the term *proximal* is used with respect to the reference system of the catheter and the stenosis (as illustrated later in Figure 8.14a) and not with respect to the direction of flow. If the latter was used as reference, the term *distal* would be most appropriate as the sample volume would be downstream the stenosis.

Despite the fact that the forward-viewing catheter was stiff, two cases of catheter orientation were simulated:

- a) catheter *coaxial* to the long axis of the lumen, by sweeping the transducer from  $-36^\circ$  to  $36^\circ$  and
- b) catheter *deflected* at  $16^\circ$  angle to the long axis of the lumen, by sweeping the transducer from  $-20^\circ$  to  $52^\circ$ .

The 30% diameter stenosis is equivalent to 51% area stenosis ( $CSA_{sten}=0.49CSA_{prox}$ ). According to the continuity equation

$$v_{prox} CSA_{prox} = v_{sten} CSA_{sten} \quad (8.12)$$

the velocity inside the stenosis would be

$$v_{sten} = \frac{v_{prox} CSA_{prox}}{0.49 CSA_{prox}} = 2.04 v_{prox} \quad (8.13)$$

In order to detect all the velocities at any part of the vessel phantom without suffering from aliasing, it was essential to limit the flow rate so that the peak velocity in the stenosis was no higher than  $9.95 \text{ cm s}^{-1}$ . Consequently, assuming parabolic flow, the velocity in the normal part of the phantom should be no higher than  $4.87 \text{ cm s}^{-1}$ . This limitation corresponded to a maximum flow rate of  $73.4 \text{ ml min}^{-1}$ .

Velocity estimates were derived from sample volumes in the region 5 to 7 mm distal to the catheter tip, located proximal to and inside the stenosis. For flow rates lower than the above limit, the estimated velocity profiles seemed to be affected by the electronic noise of the system. The most likely reason was that the flow was so weak that the level of velocity variability introduced by noise was comparable to the actual velocity level. Frame averaging was necessary to enable velocity estimation (Figure 8.13).

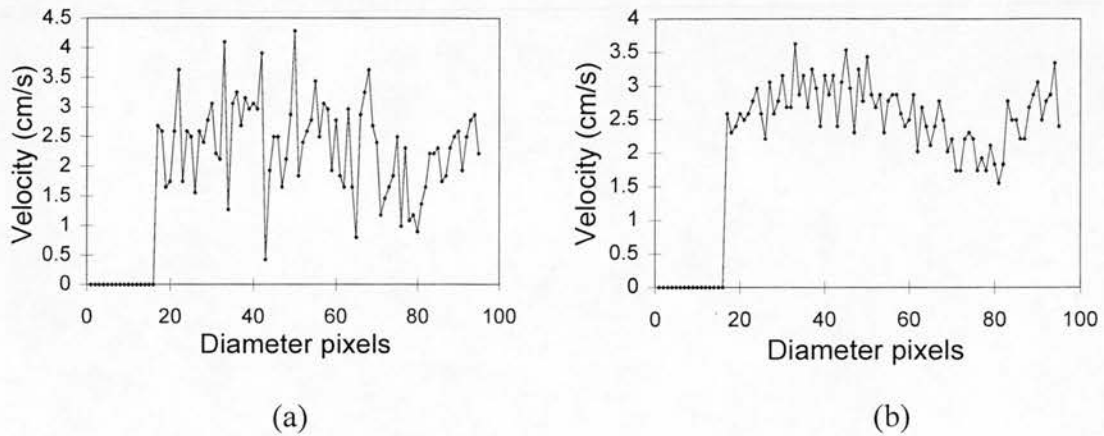


*Figure 8.13 : Velocity profile plots proximal to a symmetrical stenosis. The profile in (a) is derived using data from a single frame only and is severely distorted by noise. The profile in (b) is derived from averaging 8 frames and is significantly smoother than that in (a).*

Figure 8.14 shows typical velocity profiles for sample volumes at 6 mm distal to the catheter tip, for a flow rate of  $45.3 \text{ ml min}^{-1}$ . Moving average curves were fit on the derived experimental profiles to further smooth the effect of noise and allow more reliable estimation of peak velocity. Peak velocity was measured as the average of 10 experimental points in the area which corresponded to the peak of the moving average curve. Under the assumption of parabolic flow and in accordance with the continuity theory, the peak velocity would be  $3 \text{ cm s}^{-1}$  proximal to and  $6.12 \text{ cm s}^{-1}$  inside the stenosis. For the coaxial and deflected catheter orientations the peak velocity *proximal* to the stenosis was measured to be  $2.95$  and  $2.99 \text{ cm s}^{-1}$  respectively. Similarly, it was measured to be  $5.7$  and  $5.8 \text{ cm s}^{-1}$  *inside* the stenosis for coaxial and deflected catheter orientation respectively. Hence, the orientation of the catheter did not seem to affect the peak velocity measurements. The above estimates also showed that, as far as the peak velocity was concerned, the system performance was in good agreement with the continuity theory, if parabolic flow was assumed. This was valid for both catheter orientations.

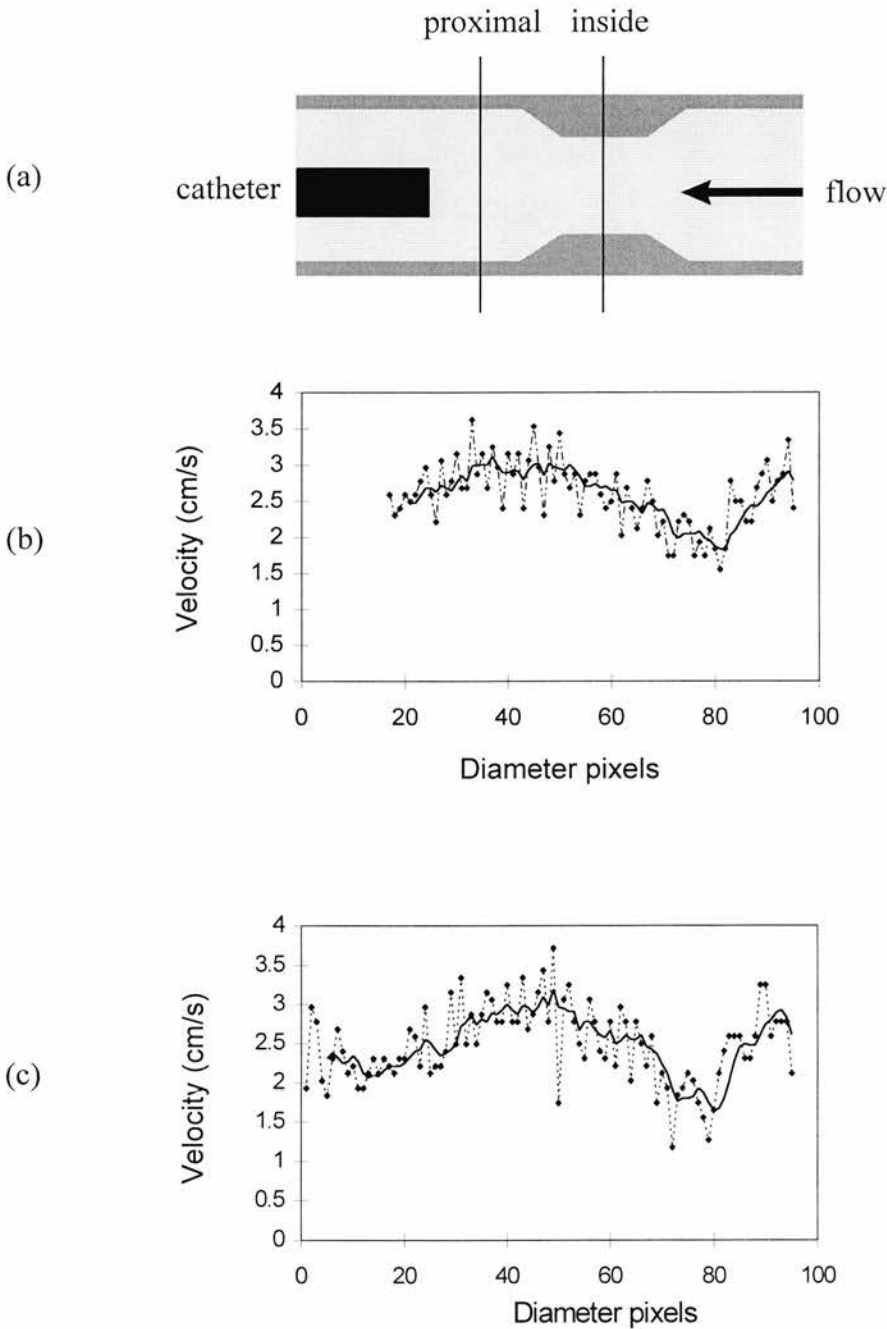


*Figure 8.14 : Velocity profiles at 6 mm distal to the catheter tip, for  $45.3 \text{ ml min}^{-1}$  flow rate through a vessel phantom with a symmetrical stenosis. (a) Schematic diagram showing the direction of flow and the location of measurements, (b) velocity profile obtained proximal to the stenosis with deflected catheter orientation and (c) velocity profile obtained proximal to the stenosis with coaxial catheter orientation.*

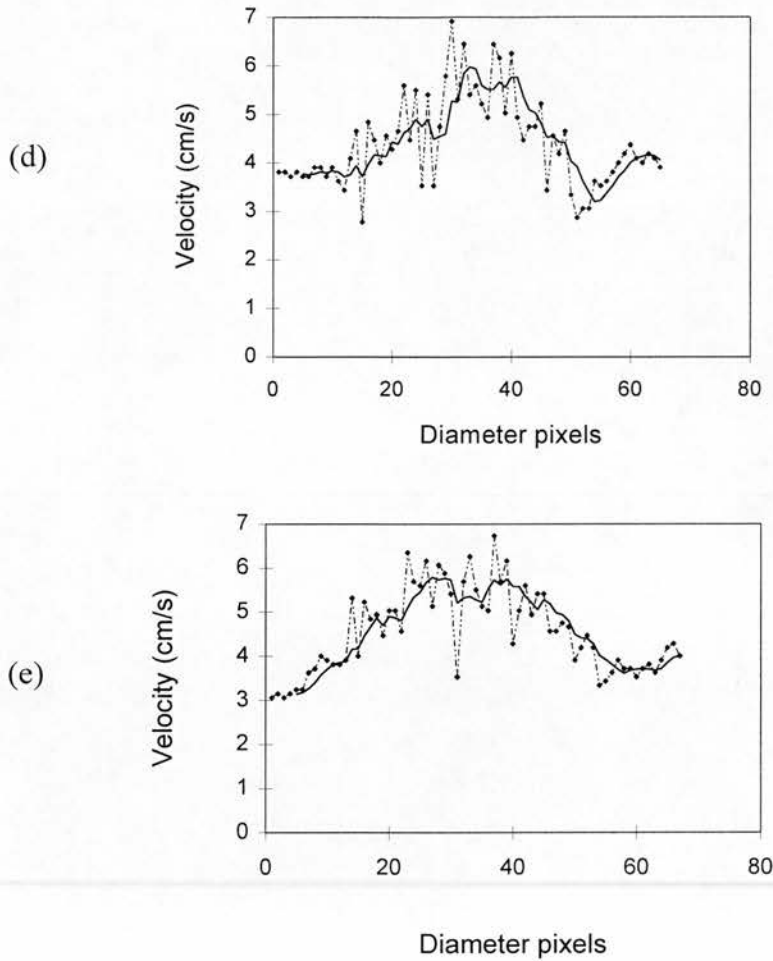


*Figure 8.14 (continued) : (d) Velocity profile obtained inside the stenosis with deflected catheter orientation and (e) velocity profile obtained inside the stenosis with coaxial catheter orientation. The dotted lines represent the experimental profiles which resulted from averaging of 8 acquired frames. The solid lines represent moving average fits on the experimental profiles. Note the 'side lobes' in the profiles shown in (b) and (c). They correspond to a region next to the vessel wall. This is no clear explanation for their existence; computation modelling of fluid dynamics could possibly provide some insight to this.*



Diameter measurements were also taken on the grey scale images, at 6 mm distal to the catheter tip, and converted to CSA assuming circular lumen shapes. These, combined with the estimated peak velocities at the same locations, provided flow estimation inside the stenosis and proximal to it. Table 8.4 lists the derived flow values and the measurement discrepancy in relation to the expected flow rate.

*Table 8.4 : Estimations of lumen CSA, peak velocity and flow rate at sample volumes located proximal to and inside a symmetrical cylindrical stenosis.*

	Diameter (mm)	CSA (cm <sup>2</sup> )	Peak velocity (cm/s)	Flow rate (ml/min)	Real flow rate (ml/min)	Flow discrepancy (%)
Proximal	7.33	0.422	2.95	37.4	45.3	-17.4
Inside	5.14	0.207	5.70	35.4	45.3	-21.8

Measured flow rates were approximately 17 to 22% lower than expected. This was caused to a small extent by slight underestimation of peak velocity (1.7-6.8%), but was mostly due to underestimation of lumen diameter attributed to the beam width in the far field of the transducer. At 6 mm distal to the catheter tip, the walls of the vessel phantom appeared quite thick on the grey scale image, with their echoes occupying part of the lumen space (Figure 8.15). As a result, the measured diameters were smaller than the manufacturing dimensions and, consequently, led to CSA and flow rate underestimation.

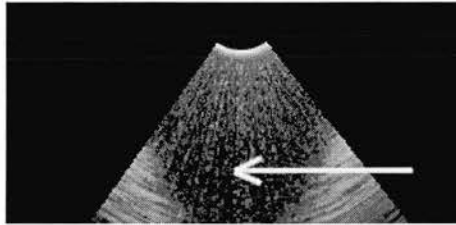


*Figure 8.15 : Image of the vessel phantom proximal to the stenosis. The arrow indicates the Doppler sample volume and the region of lumen CSA measurement, 6 mm distal to the transducer face. Due to the increased beam width at that point, the apparent diameter is smaller than it is at distances closer to the transducer.*

Colour flow images were produced and overlaid by software onto the grey scale images. For simplicity, the software scheme utilised a constant lumen diameter equal to the one measured on the grey scale image at 5 mm distal to the catheter tip. On the composite images, the region of meaningful sample volumes (5 to 7 mm distal to the catheter tip) was indicated with white lines (Figure 8.16).

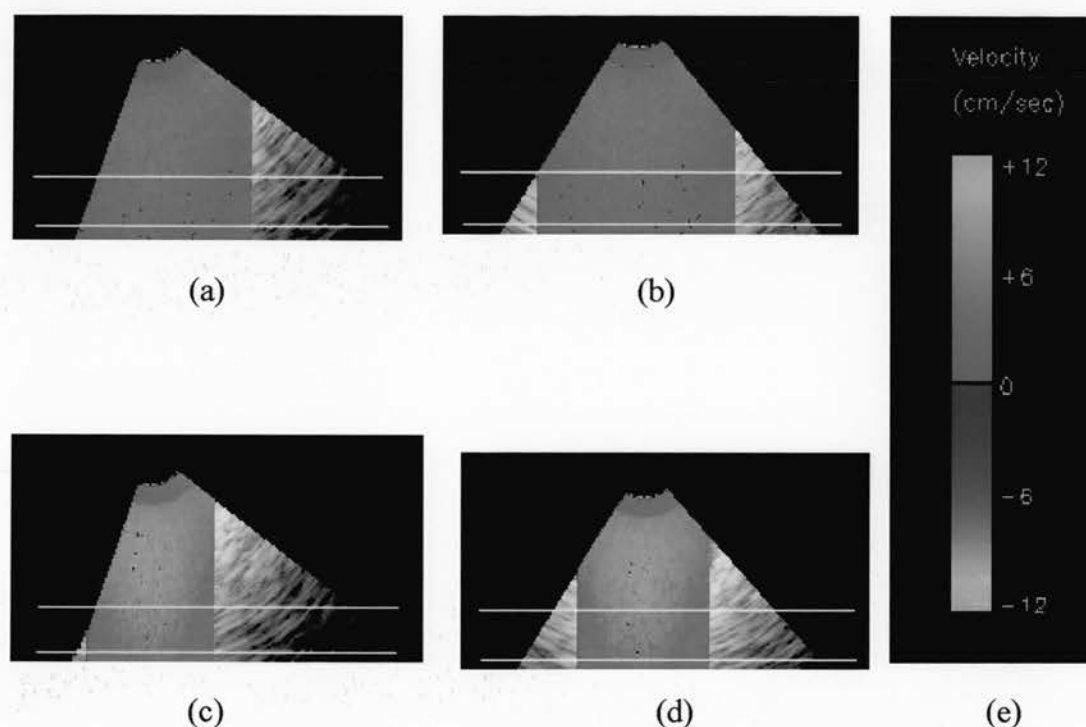


*Figure 8.16 : Composite grey scale/colour flow images for the vessel phantom with a symmetrical 30% diameter stenosis. The white lines indicate the meaningful region for Doppler measurements, i.e. 5 to 7 mm distal to the catheter tip. (a) Deflected catheter orientation proximal to the stenosis, (b) coaxial catheter orientation proximal to the stenosis, (c) deflected catheter orientation inside the stenosis, (d) coaxial catheter orientation inside the stenosis and (e) colour bar used for the production of the colour flow images. For each scan line of the colour flow images, correction for the angle  $\theta$  between the ultrasound line and the axis of the vessel phantom has been applied.*

In Figure 8.17, composite images are shown for a flow rate which caused aliasing in the stenosis. This is reflected by the blue colour in the image.

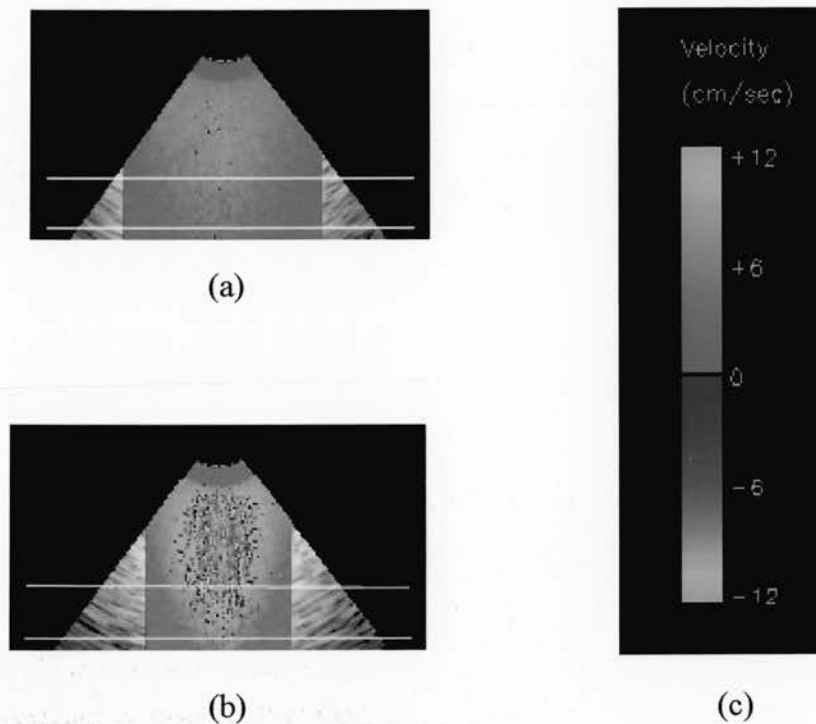


*Figure 8.17 : Composite images for the same vessel phantom as in Figure 8.16, at higher flow rate which caused aliasing. (a) Coaxial catheter orientation proximal to the stenosis, (b) coaxial catheter orientation inside the stenosis and (c) colour bar used for the production of the colour flow images. Aliasing is indicated in (b) by the presence of blue colour.*

#### 8.4.4 Eccentric stenosis

When the vessel phantom with the eccentric stenosis was used, sector frames were acquired at a ‘normal’ part proximal to the stenosis, at the transition region from ‘normal’ to stenosed lumen, as well as inside the stenosis. Two cases of catheter orientation were simulated, *coaxial* and *deflected* at an angle to the long axis of the vessel phantom, as for the vessel phantom with the symmetrical stenosis.

The 37% diameter stenosis is equivalent to 61% area stenosis and according to the continuity theory (equation 8.12) the velocity inside the stenosis would be

$$v_{sten} = \frac{v_{prox} CSA_{prox}}{0.39 CSA_{prox}} = 2.56 v_{prox} \quad (8.14)$$

For the reason mentioned earlier in section 8.4.3, the maximum flow rate at which aliasing does not occur in this particular vessel phantom is restricted to 58.6 ml min<sup>-1</sup>.

Similar comments apply for the eccentric stenosis, as in the case of the symmetrical one. More specifically, frame averaging was required to improve the SNR at the low flow rates used and provide more reliable velocity estimates. The peak velocity estimates did not seem to be affected by the catheter orientation. For a flow rate of 45.3 ml min<sup>-1</sup>, the peak velocity *proximal* to the stenosis was measured to be 2.96 and 3.00 cm s<sup>-1</sup> for coaxial and deflected catheter orientations respectively. As regards *inside* the stenosis, the peak velocity was measured to be 7.21 and 6.55 cm s<sup>-1</sup> for coaxial and deflected catheter orientations respectively. If parabolic flow was assumed, the peak velocity would be 3.00 and 7.68 cm s<sup>-1</sup> *proximal* and *inside* the stenosis respectively, according to the continuity theory. The derived velocity estimates showed that, under the assumption of parabolic flow, the system performance was in good agreement with the continuity theory, as far as the peak velocity was concerned. Figure 8.18 shows velocity profiles obtained proximal and inside the eccentric stenosis at 6 mm distal to the catheter tip.

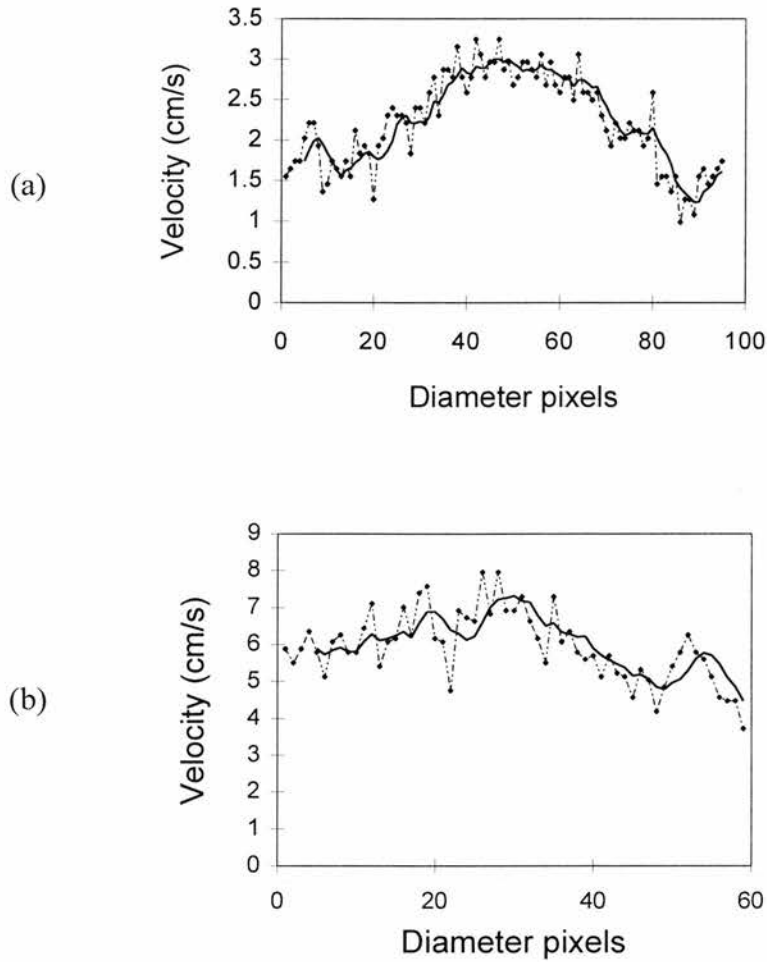


*Figure 8.18 : Velocity profiles at 6 mm distal to the catheter tip, for  $45.3 \text{ ml min}^{-1}$  flow rate through a vessel phantom with an eccentric stenosis: (a) profile obtained proximal to the stenosis with coaxial catheter orientation, (b) profile obtained inside the stenosis with coaxial catheter orientation. The dotted lines represent the experimental profiles which resulted from averaging of 8 acquired frames. The solid lines represent moving average fits on the experimental profiles.*

At 6 mm distal to the catheter tip, measured flow rates were approximately 14 to 16% lower than expected (Table 8.5). One reason for this was the underestimation of peak velocity (1.3-6.1%). An additional reason was the underestimation of lumen diameter caused by the beam width in the far field of the transducer, as explained in section 8.4.3. Another source of error was the estimation of lumen CSA from a single lumen diameter measurement, based on the assumption of circular lumen shape. This assumption is not valid for eccentric stenoses and, inherently, contributes to errors in flow rate measurements.

*Table 8.5 : Estimations of lumen CSA, peak velocity and flow rate at sample volumes located proximal to and inside an eccentric stenosis.*

	<b>Diameter (mm)</b>	<b>CSA (cm<sup>2</sup>)</b>	<b>Peak velocity (cm/s)</b>	<b>Flow rate (ml/min)</b>	<b>Real flow rate (ml/min)</b>	<b>Flow error (%)</b>
<b>Proximal</b>	7.4	0.430	2.96	38.2	45.3	-15.7
<b>Inside</b>	4.8	0.181	7.21	39.1	45.3	-13.7

In Figure 8.19 composite grey scale/colour flow images are shown for parts of the vessel phantom proximal to the stenosis, inside the stenosis as well as at the transition from 'normal' to stenosed lumen. The region of meaningful sample volumes, 5 to 7 mm distal to the catheter tip, is indicated with white lines.

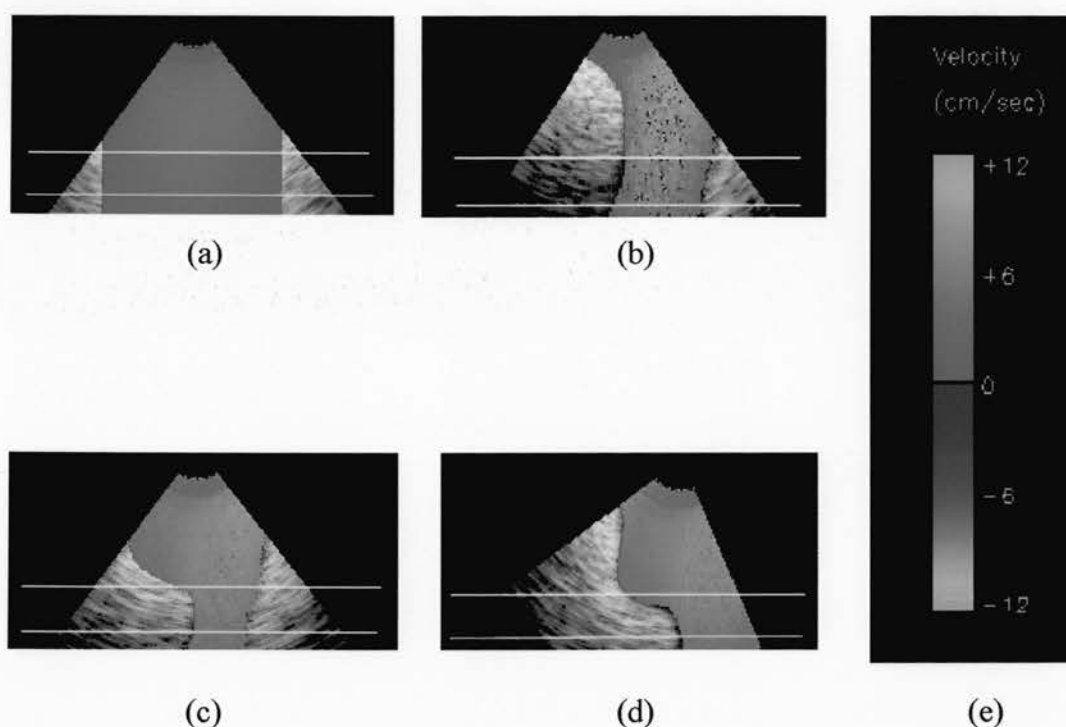


*Figure 8.19 : Composite grey scale/colour flow images for the vessel phantom with an eccentric 37% diameter stenosis. The white lines indicate the meaningful region for Doppler measurements, i.e. 5 to 7 mm distal to the catheter tip. (a) Coaxial catheter orientation proximal to the stenosis, (b) coaxial catheter orientation inside the stenosis, (c) coaxial catheter orientation at the transition from 'normal' to stenosed lumen, (d) deflected catheter orientation at the transition from 'normal' to stenosed lumen and (e) colour bar used for the production of the colour flow images.*



## **8.5 Discussion and Conclusion**

This preliminary Doppler study with forward-viewing IVUS has provided encouraging results. With the aid of a forward-viewing IVUS system which utilised one transducer only, it was possible to perform both imaging and velocity measurement functions in a stenosed lesion, distal to the catheter tip, where the flow was not disturbed by the presence of the catheter. Thus, this new system was proven capable of overcoming the spatial restrictions regarding flow quantification, encountered in both the side-viewing decorrelation systems and the systems combining Doppler wires with side-viewing IVUS catheters.

The multiple-beam approach examined in this study for the purposes of velocity and flow estimation, has enabled production of colour flow images and velocity profiles across the lumen diameter. Under parabolic flow conditions, the derived velocity profiles were very close to the expected ones. In the case of symmetrical and eccentric stenoses, the new technique provided good estimation of the peak velocity across the lumen, irrespective of the catheter orientation. This is clearly a great advantage over the single-beam Doppler wires where clinical practice is concerned, since it eliminates the time consuming need for repositioning the wire within the lumen until the Doppler signal is optimised.

There were several limitations in this study. The main one was the sole use of steady flow at low flow rates. The restriction to steady flow was imposed by the non-real-time operation of the system (section 6.8.1). The restriction to low flow rates was due to aliasing problems arising from the low PRF of the ultrasound scanner. As a direct result of the use of low flow rates, the electronic noise of the system had a strong influence on the derived velocity profiles, introducing velocity variability of similar order to the actual velocity values. Averaging of velocity frames was thus essential in order to derive more reliable velocity estimates.

Another limitation of this particular study involved the use of flow towards the catheter, as opposed to the flow away from the catheter encountered in human coronary arteries. The reasons for this were the size of the forward-viewing catheter

used in this work, along with the requirement of locating the sample volume in a region of undisturbed flow inside the field of view of the transducer (section 8.3.2). Further work is, therefore, required to validate the system performance under high rate pulsatile flow away from the catheter.

The system consistently overestimated the velocities at the vessel wall and the mean velocity across the lumen diameter. This was caused by the finite size of the ultrasound beam, however, it could be partly eliminated by deconvolution of the measured velocity profile and the sample volume shape (Dellabianca et al. 1997; Hughes and How 1993).

Flow measurements were taken at regions lying in the far field of the transducer, where the lateral resolution was imperfect and caused underestimation of luminal dimensions, which in turn contributed to underestimation of flow rates. The assumption of circular lumen shape adopted in order to derive CSA estimation from lumen diameter measurements can lead to further flow quantification errors in the case of non-symmetrical stenoses. It is necessary to extend the 2D approach for CSA measurement to three dimensions by acquiring a conical volume with the rotational scanning pattern. The 3D approach would permit segmentation of reconstructed cross-sectional images (section 5.3), thus enabling more direct and accurate CSA measurements. In addition to that, it would be possible to produce 3D flow profiles and colour flow images. ECG gating would be required to enable volume acquisition at diastole during which vascular motion is reduced, thus minimising measurement errors arising from systolic-diastolic changes in vessel dimensions during cardiac cycle.

The new system makes use of the same RF signals, from one transducer only, for both anatomical image production and velocity estimation. Hence, it would be possible to perform both functions in parallel with the aid of dedicated hardware (DSPs) and thus develop a real-time system free of cross-talk problems. This would also enable the frame averaging necessary for reliable velocity estimation at low flow rates.

If a forward-viewing IVUS catheter of 1 mm diameter was manufactured and used for combined imaging/Doppler purposes in arteries where the flow was away from the catheter (e.g. coronary arteries), then the sample volume would have to be located at 10 mm distal to the catheter tip (Tadaoka et al. 1990). The field of view of a 30 MHz transducer does not reach that far, however this kind of distance is within the capabilities of a 20 MHz transducer. At that distance in the far field though, the beam of a single element transducer would be considerably wide, leading to spatial averaging of velocities and distortion in measured velocity profiles. It seems that, even though such a multiple-beam system could estimate the peak velocity more accurately than the single-beam Doppler wires, the deconvolution process may need to be integrated within the system operations in order to partly avoid the above problems. Alternatively, the use of 20 MHz phased array catheters could be considered, because of their potential to dynamically focus the beam in both the transmission and reception zones (Eberle 1997; O'Donnell et al. 1997a).

## CHAPTER 9

### CONCLUSIONS AND FURTHER DEVELOPMENT

#### 9.1 Introduction

Forward-viewing IVUS imaging is a promising technique to overcome the inability of the conventional side-viewing IVUS systems to image severely stenosed or totally occluded vessels. Previous efforts towards forward-viewing IVUS have demonstrated the potential of this technique, nevertheless such systems have not seen wide acceptability so far. The main reasons are:

- a) the difficulty of manufacturing a small flexible catheter of similar dimensions to the side-viewing ones and
- b) the image quality has not yet matched that of the side-viewing IVUS.

Imaging tubular structures from the inside, along the forward direction, is a new and largely unexplored field in ultrasound technology when referring to arterial dimensions. If forward-viewing IVUS were to become routinely used in clinical practice, requirements would exist for cost-effective systems providing good image quality and quantitative accuracy, enabling reliable morphological and dimensional assessment of diseased vessels, aiding decision making on therapeutic strategies and interventional tool size, and guiding recanalisation procedures. System cost and performance are directly related to the scanning and acquisition technique. There are many ways to scan ahead of the catheter tip, and indeed, the previous efforts towards forward-viewing IVUS have employed different scanning techniques. There has been no clear justification for the choice of the acquisition formats, other than perhaps the relative design and manufacturing ability of the different groups.

The aim of this research was to investigate appropriate scanning patterns to assist the development of a future three dimensional forward-viewing IVUS imaging system. In the first part of the research, a number of different scanning patterns were examined with the aid of a scaled-up scanning system and scaled-up vessel phantoms, so that the effort was concentrated on the development and assessment of the scanning patterns without being constrained by the small size of real life systems. The data sets acquired with the different scanning patterns under investigation, were assessed with respect to their image quality and quantitative accuracy of luminal dimensions. The clinical utility and the manufacturing feasibility of a practical forward-viewing IVUS instrument were also taken into account in order to complete the framework of comparison among these scanning patterns.

In the second part of the research, the most promising scanning pattern according to all the above criteria was implemented in a small catheter for imaging human arteries *in vitro*. This allowed assessment of the feasibility and suitability of the preferred technique in imaging real arterial structures. At a further stage, the suitability of this technique for Doppler studies was also assessed. It is hoped that this thesis will provide the basis for future manufacturing research and development in the field of forward-viewing intravascular ultrasound.

## **9.2 Conclusions from the study with the scaled-up system**

In chapters 2 and 3, the development and evaluation of a versatile scaled-up system was described, capable of implementing a number of scanning patterns for 3D forward-viewing IVUS imaging. Five scanning patterns were implemented and examined: conical, spiral, rotational, fan and compound scan. A large number of images from scaled-up vessel phantoms were acquired to allow an extensive assessment of the image quality provided by the scanning patterns in two and three dimensions and the factors which affect it (chapter 4). The same data permitted

assessment of the accuracy of the scanning patterns in measuring luminal dimensions (chapter 5).

It was seen that compounding had a great impact in improving the image quality. Nevertheless, the compound scan is not clinically practical due to the difficulties in manipulating the catheter inside the vessels and to the increased acquisition and processing time which would exceed the allowance of real-time interventional procedures.

The conical scan is the easiest to manufacture, since its manufacturing requirements are no different from those of the side-viewing systems. The current technology of flexible drive shafts could be used directly, with no modifications, resulting in a relatively inexpensive disposable device. However, this pattern suffered from poor image quality at the vessel wall and a reduced field of view. Due to the latter, it also proved unsuitable for quantitative applications. The above disadvantages limit the clinical use of a system based on the conical scan, and perhaps this is the reason why no consideration and interest has been shown all these years for such a cost effective forward-viewing device.

The image quality of the fan scan seemed to be strongly affected by the frame density of the scanned volume. Subsequently, the fan scan is not very promising for real-time application. In addition to that, this specific pattern is probably the most difficult and most expensive to miniaturise at the catheter scale, due to its requirement for two miniature sweeping mechanisms at the catheter tip.

Overall, the spiral and the rotational scans appeared to provide the best image quality, after the compound scan, and have the potential for real-time operation. The spiral scan in particular, proved the most suitable pattern for imaging structures of circular symmetry. Both these patterns require one sweeping and one rotational mechanism for their operation. The existing rotational mechanism technology used in the side-viewing devices could be of use for the spiral and rotational scans, leaving only the requirement of miniaturising a single sweeping mechanism.

On the other hand, the spiral scan was the least accurate in measuring luminal dimensions. This pattern suffered from severe underestimation of luminal dimensions



at distances away from the transducer focus, especially in the regions where the lumen was at its narrowest. In these cases, the measured lumen CSA was 40 or even 60% lower than the 'design' area. The rotational and fan scans performed better than the spiral scan in this aspect. The rotational scan, in particular, proved the most accurate pattern quantitatively. In the majority of the examined data sets, it came up with the smallest measurement errors. This is a very important advantage of the rotational scan when clinical applications are concerned, since accurate measurement of the minimum lumen size in a vessel segment forms the basis for selecting the size of the treatment device.

An additional advantage of the rotational scan is its ability to provide readily available, clinically useful information, in the form of real-time 2D longitudinal images of the vessel at any transducer orientation, something unobtainable with the other scanning patterns.

The conclusion arising from the work with the scaled-up system and vessel phantoms, is that the most promising technique for 3D forward-viewing IVUS is the rotational scan. This scanning pattern provided good image quality, was shown to be the most accurate in quantitative measurements, and is capable of displaying real-time 2D clinically useful information.

### **9.3 Conclusions from the study with the small catheter**

Based on the outcome of the study with the vessel phantoms, a small scale mechanical catheter was designed and constructed (chapter 6), implementing the rotational scan for 3D forward-viewing IVUS imaging of human arteries *in vitro*. Operating at 30 MHz, the catheter was integrated with an intravascular ultrasound scanner and an RF data acquisition system. Use of test phantoms showed that the new scanning system was accurate, preserving the geometry of scanned objects.

Three dimensional data sets were successfully acquired from a number of carotid and femoral arteries (chapter 7). The reconstructed images demonstrated the

ability of the forward-viewing system based on the rotational scan, to visualise relatively healthy lumens, bifurcations, thickened atherosclerotic walls and, most importantly, very severe and complete vessel occlusions, where the side-viewing IVUS systems cannot be used. There was a good agreement with histology regarding the location of the plaque and the shape of the residual lumen in stenosed vessels, indicating that forward-viewing IVUS can be used as a guiding tool for recanalisation procedures. The results also provided some hope that forward-viewing IVUS could become a useful tool for evaluation and characterisation of severely diseased vessels, aiding the selection of appropriate therapeutic modalities. Improvements regarding the lateral resolution of IVUS transducers are required though, so that forward-viewing IVUS can provide accurate lumen quantification, necessary for defining the appropriate size of interventional tools.

At a further stage, the catheter was used for Doppler studies in tissue mimicking flow phantoms simulating cases of healthy and stenosed vessels (chapter 8), in an attempt to overcome sample volume location uncertainties associated with current Doppler wire techniques. These preliminary studies provided encouraging results. It was possible, with the forward-viewing IVUS/Doppler system, to perform both imaging and velocity measurement functions in a stenosed lesion, distal to the catheter tip, where the flow was not disturbed by the presence of the catheter. This new system was proven capable of providing colour flow images, velocity profiles and good estimation of peak velocity, irrespective of the catheter orientation inside the lumen.

The results of this research show that the rotational scan is a very promising technique for implementing a forward-viewing IVUS system suitable for anatomical and functional assessment of stenosed vessels, and for guidance of recanalisation procedures.



## **9.4 Future developments**

The manufacturing of a small flexible forward-viewing IVUS catheter based on the rotational scan is still a challenging task. However, the latest technology developments in catheter arrays, micro-motors and micro-gears, provide hope that the production of such a system may be possible in the near future.

The imaging studies with the human vessels were performed *in vitro* only, with the use of a stiff catheter. When the manufacturing of a small flexible forward-viewing catheter based on the rotational scan becomes feasible, *in vivo* work would be required to validate the device and assess the influence of factors like cardiac cycle motion on the quality of the images.

The Doppler studies were carried out in straight vessel phantoms, under steady flow conditions only, at low flow rates, with the flow towards the catheter. Further work is required to verify the system performance in tortuous flow phantoms at high rate pulsatile flow away from the catheter.

The use of 20 MHz rather than 30 MHz transducers seems to be more preferable for reasons of ultrasound penetration through the stenoses and for measuring blood velocity at regions of undisturbed flow distal to the catheter tip. For IVUS transducers operating at 20 MHz, improvements in lateral resolution are essential in order to enhance the dimensional accuracy of a forward-viewing system and aid the characterisation of plaque components and discrimination of vessel wall layers. The phased array technology with its potential to dynamically focus the beam in both the transmission and reception zones, could be a particularly attractive way of implementing such a system. Deconvolution of the measured velocity profiles with the shape of the sample volume should be integrated in the Doppler system in order to avoid, to a certain extent, spatial averaging of velocities and distortion in velocity profiles.

This study has proven the utility of forward-viewing IVUS in visualising severe arterial stenoses in three dimensions. It would be worth exploring to see if this tool can also be used for confident characterisation of the bulky masses of plaque

which block the arteries. Knowledge of plaque composition and morphology obtained with IVUS can aid decision making on therapeutic strategies for atherosclerosis and potentially reduce the cost of treatment. Methods employing spectral and textural analysis of IVUS RF data have been developed, for characterising the basic plaque components (Linker et al. 1991; Nailon 1997; Spencer et al. 1997; Watson et al. 2000; Wilson et al. 1994). It would be worth investigating the application of such methods with RF data acquired with forward-viewing IVUS systems.

## REFERENCES

- Al-Mejrad A S K H (1996).  
Medical ultrasound: a study of real-time three dimensional ultrasound imaging.  
PhD Thesis, University of Edinburgh, Edinburgh, UK.
- Aretz H T, Martinelli M A & LeDet E G (1989).  
Intraluminal ultrasound guidance of transverse laser coronary atherectomy.  
International Journal of Cardiac Imaging 4: 153-157.
- Aretz H T, Gregory K W, Martinelli M A, Gregg R E, LeDet E G, Hatch G F, Sedlacek T & Haase W C (1991).  
Ultrasound guidance of laser atherectomy.  
International Journal of Cardiac Imaging 6: 231-237.
- Ascer E, Veith F J, Gupta S K, Krasowski G, Samson R H, Scher L A, White-Flores S A & Sprayregen S (1985).  
Six year experience with expanded polytetrafluoroethylene arterial grafts for limb salvage.  
Journal of Cardiovascular Surgery 26(5): 468-472.
- Back M R, Kopchok G E, White R A, Scoccianti M, Donayre C E, Maeuser H & Brener B (1994).  
Forward-looking intravascular ultrasonography: *in vitro* imaging of normal and atherosclerotic human arteries.  
American Surgeon 60: 738-743.
- Baim D S, Simonton C A, Popma J J, Hinohara T, Bersin R M, DeFeo T, Kent K M, Yock P G & Kuntz R E (1996).  
Mechanism of luminal enlargement by optimal atherectomy - IVUS insights from the OARS study.  
Journal of the American College of Cardiology 27 (Suppl): 291A.
- Barillot C (1993).  
Surface and volume rendering techniques to display 3-D data.  
IEEE Engineering in Medicine and Biology 12(1): 111-119.
- Barry C D, Allott C P, John N W, Mellor P M, Arundel P A, Thomson D S & Waterton J C (1997).  
Three-dimensional freehand ultrasound: image reconstruction and volume analysis.  
Ultrasound in Medicine and Biology 23(8): 1209-1224.

- Barzilai B, Saffitz J E, Miller J G & Sobel B E (1987).  
Quantitative ultrasonic characterisation of the nature of atherosclerotic plaques in human aorta.  
*Circulation Research* 60(3): 459-463.
- Bijnens B, Herregods M-C, Nuyts J, Vandeweghe G, Suetens P & van der Werf F (1994).  
Acquisition and processing of the radio-frequency signal in echocardiography: a new global approach.  
*Ultrasound in Medicine and Biology* 20(2): 167-176.
- Bom N, Lancée C T & van Egmond F C (1972).  
An ultrasonic intracardiac scanner.  
*Ultrasonics* 10: 72-76.
- Bom N, Slager C J, van Egmond F C, Lancée C T & Serruys P W (1988).  
Intra-arterial ultrasonic imaging for recanalization of by spark erosion.  
*Ultrasound in Medicine and Biology* 14(4): 257-261.
- Bom N, ten Hoff H, Lancée C T, Gussenhoven W J & Bosch J G (1989).  
Early and recent intraluminal ultrasound devices.  
*International Journal of Cardiac Imaging* 4: 79-88.
- Bonnefous O & Pesque P (1986).  
Time domain formulation of pulse-Doppler ultrasound and blood velocity estimation by cross correlation.  
*Ultrasonic Imaging* 8: 73-85.
- Bonnefous O, Pesque P & Bernard X (1986).  
A new velocity estimator for color flow mapping.  
*Proceedings of IEEE Ultrasonics Symposium*: 855-860.
- Bouma C J, Niessen W J, Zuiderveld K J, Gussenhoven E J & Viergever M A (1996).  
Evaluation of segmentation algorithms for intravascular ultrasound images.  
*Lecture Notes in Computer Science* 1131: 203-212.
- Bovik A C (1988).  
On detecting edges in speckle imagery.  
*IEEE Transactions on Acoustics, Speech and Signal Processing* 36 : 1618-1627.
- Brathwaite P A, Chandran K B, McPherson D D & Dove E L (1996).  
Lumen detection in human IVUS images using region-growing.  
*Computers in Cardiology*: 37-40.

Brown G, Albers J J, Fisher L D, Schaefer S M, Lin J-T, Kaplan C, Zhao X-Q, Bisson B D, Fitzpatrick V F & Dodge H T (1990).

Regression of coronary artery disease as a result of intensive lipid-lowering therapy in men with high levels of apolipoprotein B.

The New England Journal of Medicine 323: 1289-1298.

Bruining N, von Birgelen C, Mallus M T, de Feyter P J, de Vrey E, Li W, Prati F, Serruys P W & Roelandt J R T C (1996).

ECG-gated ICUS image acquisition combined with a semi-automated contour detection provides accurate analysis of vessel dimensions.

Computers in Cardiology: 53-56.

Carlier S G, Céspedes E I, Li W, Mastik F, van der Steen A F W, Bom K & Serruys P W (1998).

Coronary blood flow imaging and volume flow quantification with an intravascular ultrasound imaging catheter: initial clinical experience.

Circulation 98(17) Supplement: I-507.

Castaneda-Zuniga W R, Formanek A, Tadavarthy M, Vlodaver Z, Edwards J E, Zollikofer C & Amplatz K (1980).

The mechanism of balloon angioplasty.

Radiology 135(3): 565-571.

Cavaye D M, Tabbara M R, Kopchok G E, Laas T E & White R A (1991).

Three dimensional vascular ultrasound imaging.

American Surgeon 57 (12): 751-755.

Cavaye D M & White R A (1993).

Intravascular ultrasound imaging. Raven Press, New York, USA.

Céspedes E I, de Korte C L, van der Steen A F W, von Birgelen C & Lancée C T (1997).

Intravascular elastography: principles and potentials.

Seminars in Interventional Cardiology 2:55-62.

Chae J S, Briskin A F, Maurer G & Siegel R J (1992).

Geometric accuracy of intravascular ultrasound imaging.

Journal of the American Society of Echocardiography 5: 577-587.

Coy K M, Park J C, Fishbein M C, Laas T, Diamond G A, Adler L, Maurer G & Siegel R J (1992).

*In vitro* validation of three-dimensional intravascular ultrasound for the evaluation of arterial injury after balloon angioplasty.

Journal of the American College of Cardiology 20: 692-700.

Craig J J (1989).

Intoduction to robotics mechanics and control, Second Edition, Addison-Wesley Publishing Company, Wokingham, UK.

Crowe J R, Shapo B M, Stephens D N, Bleam D, Eberle M J, Wu C C, Muller D W M, Kovatch J A, Lederman R J & O'Donnell M (1996).

Coronary artery flow imaging with an intraluminal array.

Proceedings of the IEEE Ultrasonics Symposium : 1481-1484.

Davies M J (1990).

A macro and micro view of coronary vascular insult in ischemic heart disease.

Circulation 82(Supplement II): II38-II46.

de Korte C L, Céspedes I, van der Steen A F W & Lancée C T (1997).

Intravascular elasticity imaging using ultrasound: Feasibility studies in phantoms.

Ultrasound in Medicine and Biology 23(5): 735-746.

de Korte C L, van der Steen A F W, Céspedes E I, Pasterkamp G (1998).

Intravascular ultrasound elastography in human arteries: initial experience *in vitro*.

Ultrasound in Medicine and Biology 24(3): 401-408.

de Kroon M G M, van der Wal L F, Gussenhoven W J & Bom N (1991a).

Angle-dependent backscatter from the arterial wall.

Ultrasound in Medicine and Biology 17(2): 121-126.

de Kroon M G M, van der Wal L F, Gussenhoven W J, Rijsterborgh H & Bom N (1991b).

Backscatter directivity and integrated backscatter power of arterial tissue.

International Journal of Cardiac Imaging 6: 265-275.

Delabays A, Pandian N G, Cao Q-L, Suseng L, Marx G, Ludomirski A & Schwartz S L (1995).

Transthoracic real-time three-dimensional echocardiography using a fan-like scanning approach for data acquisition: methods, strengths, problems and initial clinical experience.

Echocardiography 12(1): 49-59.

De Lezo S J, Romero M, Medina A, Pan M, Pavlovic D, Vaamonde R, Hernández E, Melián F, Rubio F L, Marrero J, Segura J, Irurita M & Cabrera J A (1993).

Intracoronary ultrasound assessment of directional coronary atherectomy: immediate and follow-up findings.

Journal of the American College of Cardiology 21: 298-307.

- Dellabianca C, Dotti D, Lombardi R & Magistrali S (1997).  
Improved shear-stress evaluation from velocity profiles.  
IEEE Ultrasonics Symposium : 1281-1284.
- Di Mario C, The S H K , Madretsma S, van Suylen R J, Wilson R A, Bom N, Serruys P W, Gussenhoven E J & Roelandt J R T C (1992).  
Detection and characterization of vascular lesions by intravascular ultrasound: an *in vitro* study correlated with histology  
Journal of the American Society of Echocardiography 5:135-146.
- Di Mario C, Madretsma S, Linker D, The S H K, Bom N, Serruys P, Gussenhoven E & Roelandt J R T C (1993).  
The angle of incidence of ultrasonic beam: A critical factor for the image quality in intravascular ultrasonography.  
American Heart Journal 125: 442-448.
- Di Mario C, von Birgelen C, Prati F, Soni B, Li W, Bruining N, de Jaegere P P T, de Feyter P J, Serruys P W & Roelandt J R T C (1995a).  
Three dimensional reconstruction of cross sectional intracoronary ultrasound: clinical or research tool?  
British Heart Journal 73 (Suppl 2): 26-32.
- Di Mario C, Gil R, Camenzind E, Ozaki Y, von Birgelen C, Umans V, de Jaegere P, de Feyter P J, Roelandt J R & Serruys P W (1995b).  
Quantitative assessment with intracoronary ultrasound of the mechanisms of restenosis after percutaneous transluminal coronary angioplasty and directional coronary atherectomy.  
American Journal of Cardiology 75(12): 772-777.
- Di Mario C, Akiyama T, Moussa I, Reimers B, Jang Y T, Tobis J & Colombo A (1997).  
First experience with imaging core wires.  
Seminars in Interventional Cardiology 2: 69-73.
- Donald I, MacVicar J & Brown T G (1958).  
Investigation of abdominal masses by pulsed ultrasound.  
Lancet 1: 1188-1194.
- Donald I & Brown T G (1961).  
Demonstration of tissue interfaces within the body by ultrasonic echo sounding.  
British Journal of Radiology 34: 539-546.
- Doucette J W, Corl P D, Payne H M, Flynn A E, Goto M, Nasi M & Segal J (1992).



- Validation of Doppler guide wire for intravascular measurement of coronary artery flow velocity.  
*Circulation* 85: 1899-1911.
- Eberle M J (1997).  
The latest in electronic imaging.  
*Seminars in Interventional Cardiology* 2: 19-23.
- Edler I, Gustafson I, Karlefors T & Christensson B (1961).  
Ultrasoundcardiography.  
*Acta Medica Scandinavica*: Supplement 370.
- Erbel R, Roth T, Koch L, Ge J, Gorge G, Serruys P W, Bom N, Lancée C T & Roelandt J (1997).  
IVUS of micromotors for cardiovascular imaging.  
*Minimally Invasive Therapy & Allied Technology* 6: 195-198.
- Evans D H, McDicken W N, Skidmore R & Woodcock J P (1989).  
Doppler Ultrasound. Physics, Instrumentation and Clinical Applications.  
John Wiley & Sons Ltd, Chichester, UK.
- Evans J L, Ng K-H, Vonesh M J, Kramer B L, Meyers S N, Mills T A, Kane B J, Aldrich W N, Jang Y-T, Yock P G, Rold M D, Roth S I & McPherson D D (1994).  
Arterial imaging with a new forward-viewing intravascular ultrasound catheter, I. Initial studies.  
*Circulation* 89: 712-717.
- Fenster A & Downey D B (1996).  
3-D ultrasound imaging: A review.  
*IEEE Engineering in Medicine and Biology Magazine* 15(6): 41-51.
- Fitzgerald P J, Belef M, Connolly A J, Sudhir K & Yock P G (1995).  
Design and initial testing of an ultrasound-guided directional atherectomy device.  
*American Heart Journal* 129(3): 593-598.
- Fine D, Perring S, Herbetko J, Hacking C N, Flemming J S & Dewbury K C (1991).  
Three-dimensional (3D) ultrasound imaging of the gallbladder and dilated biliary tree: reconstruction from real-time B-scans.  
*The British Journal of Radiology* 64: 1056-1057.
- Finet G, Maurincomme E, Tabib A, Crowley R J, Magnin I, Roriz R, Beaune J, Amiel M (1993).  
Artifacts in intravascular ultrasound imaging: analyses and implications.  
*Ultrasound in Medicine and Biology* 19: 533-537.



- Foster F S, Knapik D A, Machado J C, Ryan L K & Nissen S E (1997).  
High-frequency intracoronary ultrasound imaging.  
Seminars in Interventional Cardiology 2: 33-41.
- Fourrier J L, Bertrand M E, Auth D C, Lablanche J M, Gommeaux A & Brunetaud J M (1989).  
Percutaneous coronary rotational angioplasty in humans: Preliminary report.  
Journal of the American College of Cardiology 14(5): 1278-1282.
- Gardineer B & Vilkomerson D (1994).  
Apparatus and method for forward looking volume imaging.  
US Patent No. 5373845.
- Ge J, Erbel R, Gerber T, Gorge G, Koch L, Haude M & Meyer J (1994).  
Intravascular ultrasound imaging of angiographically normal coronary arteries: a prospective study *in vivo*.  
British Heart Journal 71: 572-578.
- Geschwind H J, Blair J D, Mongkolsmai D, Kern M J, Stern J, Deligonul U, Kennedy H L & Smith S (1987).  
Development and experimental application of contact probe catheter for laser angioplasty.  
Journal of the American College of Cardiology 9(1), 101-107.
- Geselschap J H, Heilbron M J, Hussain F M, Daskalakis T M, Wilson E P, Kopchok G E & White R A (1998).  
The effect of angulation on intravascular ultrasound imaging observed in vascular phantoms.  
Journal of Endovascular Surgery 5: 126-133.
- Ghosh A, Nanda N C & Maurer G (1982).  
Three-dimensional reconstruction of echocardiographic images using the rotation method.  
Ultrasound in Medicine and Biology 8(6): 655-661.
- Gil R, von Birgelen C, Prati F, Di Mario C, Ligthart J & Serruys P W (1996).  
Usefulness of three-dimensional reconstruction for interpretation and quantitative analysis of intracoronary ultrasound during stent deployment.  
The American Journal of Cardiology 77: 761-764.
- Gilja O H, Thune N, Matre K, Hausken T, Odegaard S & Berstad A (1994).  
*In vitro* evaluation of three-dimensional ultrasonography in volume estimation of abdominal organs.

Ultrasound in Medicine and Biology 20(2): 157-165.

Glagov S, Weisenberg E, Zarins C K, Stankunavicius R & Kolettis G J (1987).  
Compensatory enlargement of human atherosclerotic coronary arteries.  
New England Journal of Medicine 316(22): 1371-1375.

Glagov S, Zarins C K, Giddens D P & Ku D N (1988).  
Hemodynamics and atherosclerosis. Insights and perspectives gained from studies of  
human arteries.  
Archives of Pathology and Laboratory Medicine 112(10): 1018-1031.

Gonzalez E R (1997).  
Thrombolytic therapy for acute myocardial infarction.  
Hospital Pharmacy 32(11): 1498-1509.

Gown A M, Tsukada T & Ross R (1986).  
Human atherosclerosis. II. Immunocytochemical analysis of the cellular composition  
of human atherosclerotic lesions.  
American Journal of Pathology 125(1): 191-207.

Grüntzig A R, Senning A & Siegenthaler W E (1979).  
“Nonoperative dilation of coronary-artery stenosis. Percutaneous transluminal  
coronary angioplasty”.  
The New England Journal of Medicine, 301: 61-68.

Guiteras V P, Bourassa M G, David P R, Bonan R, Crepeau J, Dyrda I & Lesperance  
J (1987).  
Restenosis after successful percutaneous transluminal coronary angioplasty: the  
Montreal Heart Institute experience.  
American Journal of Cardiology 60(3): 50B-55B.

Gussenhoven E J, Essed C E, Lancée C T, Mastik F, Frietman P, van Egmond F C,  
Reiber J, Bosch H, van Urk H, Roelandt J & Bom N (1989a).  
Arterial wall characteristics determined by intravascular ultrasound imaging: an *in  
vitro* study.  
Journal of the American College of Cardiology 14: 947-952.

Gussenhoven E J, Essed C E, Frietman P, Mastik F, Lancée C T, Slager C, Serruys P,  
Gerritsen P, Pieterman H & Bom N (1989b).  
Intravascular echographic assessment of vessel wall characteristics: a correlation  
with histology.  
International Journal of Cardiac Imaging 4: 105-116.

Gussenhoven E J, van der Lugt A, The S H K, de Feyter P, Serruys P W, van Suylen R J, Lancée C T, van Urk H & Pieterman H (1993a).

Similarities and differences between coronary and iliofemoral arteries related to intravascular ultrasound.

In Roelandt J R T C, Gussenhoven E J & Bom N (editors) *Intravascular ultrasound*. Kluwer Academic Publishers, Dordrecht, The Netherlands, pp. 45-62.

Gussenhoven E J, van der Lugt A, van Strijen M, Li W, Kroeze H, The S H K, van Egmond F C, Honkoop J, Peters R J G, de Feyter P, van Urk H & Pieterman H (1993b).

Displacement sensing device enabling accurate documentation of catheter tip position.

In Roelandt J R T C, Gussenhoven E J & Bom N (editors) *Intravascular ultrasound*. Kluwer Academic Publishers, Dordrecht, The Netherlands, pp. 157-166.

Hangartner J R W, Charleston A J, Davies M J & Thomas A C (1986).

Morphological characteristics of clinically significant coronary artery stenosis in stable angina.

*British Heart Journal* 56(6): 501-508.

Hausmann D, Friedrich G, Sudhir K, Mullen W L, Soni B, Fitzgerald P J & Yock P G (1994).

3D intravascular ultrasound imaging with automated border detection using 2.9F catheters.

*Journal of the American College of Cardiology* 23 (Supplement): p.174A.

Herd J A, Ballantyne C M, Farmer J A, Ferguson J J, Jones P H, West M S, Gould K L & Gotto Jr A M (1997).

Effects of fluvastatin on coronary atherosclerosis in patients with mild to moderate cholesterol elevations (Lipoprotein and Coronary Atherosclerosis Study [LCAS]).

*The American Journal of Cardiology* 80: 278-286.

Hiro T, Hall P, Maiello L, Itoh A, Colombo A., Jang Y T, Salmon S M & Tobis J M (1998).

Clinical feasibility of 0.018-inch intravascular ultrasound imaging device.

*American Heart Journal* 136: 1017-1020.

Hodgson J McB, Graham S P, Savakus A D, Dame S G, Stephens D N, Dhillon P S, Brands D, Sheehan H, Eberle M J (1989).

Clinical percutaneous imaging of coronary anatomy using an over-the-wire ultrasound catheter system.

*International Journal of Cardiac Imaging* 4: 187-193.

Hodgson J Mc B, Frey A W, Mueller C & Roskamm H (1996).

Comparison of acute procedure cost and equipment utilization with strategies of ICUS guided vs angiographic guided PTCA and stenting: Preliminary results of Strategy of ICUS-guided PTCA and Stenting (SIPS) Study.  
Circulation 94(8) (Suppl I), I-325.

Hoskins P R & McDicken W N (1994).  
Techniques for the assessment of the imaging characteristics of intravascular ultrasound scanners.  
The British Journal of Radiology 67: 695-700.

Hu J & Hu X (1995).  
An approach to automatic segmentation of 3D intravascular ultrasound images.  
IEEE Nuclear Science Symposium and Medical Imaging Conference 3: 1461-1464.

Huertas A & Medioni G (1986).  
Detection of intensity changes with subpixel accuracy using Laplacian-Gaussian masks.  
IEEE Transactions on Pattern Analysis and Machine Intelligence PAMI-8 (5) : 651-664.

Hughes P E & How T V (1993).  
Quantitative measurement of wall shear rate by pulsed Doppler ultrasound.  
Journal of Medical Engineering & Technology 17(2): 58-64.

Imran MA (1995).  
Flexible elongate device having forward looking ultrasonic imaging.  
US Patent No. 5379772.

Isner J M, Kishel J, Kent K M, Ronan J A Jr, Ross A M & Roberts W C (1981).  
Accuracy of angiographic determination of left main coronary arterial narrowing. Angiographic-histologic correlative analysis in 28 patients.  
Circulation 63(5): 1056-1064.

Isner J M, Kaufman J, Rosenfeld K, Pieczek A, Schainfeld R, Ramaswamy K & Kosowsky B D (1993).  
Combined physiologic and anatomic assessment of percutaneous revascularization using Doppler guidewire and ultrasound catheter.  
American Journal of Cardiology 71: 70D-86D.

Johnson E L, Yock P G, Hargrave V K, Srebro J P, Manubens S M, Seitz W & Ports T A (1989).  
Assessment of severity of coronary stenoses using a Doppler catheter. Validation of a method based on the continuity equation.  
Circulation 80: 625-635.

- Joyner C R, Reid J M & Bond J P (1963).  
Reflected ultrasound in the assessment of mitral valve disease.  
*Circulation* 27: 503-511.
- Jukema J W, Bruschke A V G, van Boven A J, Reiber J H C, Bal E T, Zwinderman A H, Jansen H, Boerma G J M, van Rappard F M & Lie K I (1995).  
Effects of lipid lowering by pravastatin on progression and regression of coronary artery disease in symptomatic men with normal to moderately elevated serum cholesterol levels. The Regression Growth Evaluation Statin Study (REGRESS).  
*Circulation* 91: 2528-2540.
- Kasai C, Namekawa K, Koyano A & Omoto R (1985).  
Real-time two-dimensional blood flow imaging using an autocorrelation technique.  
*IEEE Transactions on Sonics and Ultrasonics* 32 (3): 458-464.
- Kass M, Witkin A & Terzopoulos D (1988).  
Snakes: Active contour models.  
*International Journal of Computer Vision* 1 (4): 321-331.
- Kawata M, Okada T, Igarashi N, Okajima K & Domoto Y (1997).  
Assessment of intravascular ultrasound-bearing balloon catheter-guided percutaneous transluminal coronary angioplasty and stenting.  
*Heart and Vessels* 12 Suppl.:185-187.
- Kazi A, Rouget J, Li L L & DuFour L D (1995).  
Ultrasound catheter with mechanically steerable beam.  
US Patent No. 5377685.
- Kensey K, Nash J E, Abrahams C & Zarins C K (1987).  
Recanalization of obstructed arteries with a flexible, rotating tip catheter.  
*Radiology* 165: 387-389.
- Kimura B J, Bhargava V, Palinski W, Russo R J & DeMaria AN (1996).  
Distortion of intravascular images because of nonuniform angular velocity of mechanical-type transducers.  
*American heart Journal* 132: 328-336.
- Kimura T & Nobuyoshi M (1997).  
Remodelling and restenosis: intravascular ultrasound studies.  
*Seminars in Interventional Cardiology* 2: 159-166.
- Klein H M, Günther R W, Verlande M, Schneider W, Vorwerk D, Kelch J & Hamm M (1992).

3D-Surface reconstruction of intravascular ultrasound images using personal computer hardware and a motorised catheter control.  
Cardiovascular and Interventional Radiology 15: 97-101.

Kovach J A, Mintz G S, Pichard A D, Kent K M, Popma J J, Satler L F & Leon M B (1993).

Sequential intravascular ultrasound characterization of the mechanisms of rotational atherectomy and adjunct balloon angioplasty.

Journal of the American College of Cardiology 22(4): 1024-1032.

Lammer J & Karmel F (1988).

Percutaneous transluminal laser angioplasty with contact probes.

Radiology 168(3): 733-737.

Lancée C T, Bom N & Roelandt J (1995).

Future Directions in Intravascular Ultrasound: From micro-motors to imaging guidewire systems.

Echocardiography 12: 275-281.

Lansky A J, Popma J J, Mintz G S, Laird J R, Saucedo & Leon M B (1998).

Lipid-lowering therapy after coronary revascularization: the interventional cardiologist's perspective.

The American Journal of Cardiology 81(7A): 55E-62E.

Laskey W K, Brady S T, Kussmaul W G, Waxler A R, Krol J, Herrmann H C, Hirshfield J W Jr & Sehgal C (1993).

Intravascular ultrasonographic assessment of the results of coronary artery stenting.

American Heart Journal 125(6): 1576-1583.

Lee C K & Benkeser P J (1991).

Investigation of a forward-looking IVUS imaging transducer.

Proceedings of the IEEE Ultrasonics Symposium, 691-694.

Lee D-Y, Eigler N, Luo H, Nishioka T, Tabak S W, Forrester J S & Siegel R J (1995).

Effect of intracoronary ultrasound imaging on clinical decision making.

American Heart Journal 129: 1084-1093.

Leon M B, Mintz G S & Keren G (1993).

The use of intracoronary ultrasound to assess post-intervention vessel wall response.

In Hanrath P, Uebis R & Krebs W (editors). Cardiovascular Imaging by Ultrasound. Kluwer Academic Publishers, Dordrecht, The Netherlands, pp. 375-387.

Li W, Bosch J G, Zhong Y, van Urk H, Gussenhoven E J, Mastik F, van Egmond F, Rijsterborgh H, Reiber J H C & Bom N (1993).  
Image segmentation and 3D reconstruction of intravascular ultrasound images.  
Acoustical Imaging 20: 489-496.

Li W, Gussenhoven E J, Zhong Y, The S H K, Pieterman H, van Urk H & Bom K (1994).  
Temporal averaging for quantification of lumen dimensions in intravascular ultrasound images.  
Ultrasound in Medicine and Biology 20: 117-122.

Li W (1997).  
Image and signal processing in intravascular ultrasound.  
PhD Thesis, Erasmus University, Rotterdam, The Netherlands.

Li W, van der Steen A F W, Lancée C T, Céspedes I & Bom N (1998).  
Blood flow imaging and volume flow quantitation with intravascular ultrasound.  
Ultrasound in Medicine and Biology 24 (2) : 203-214.

Liang D H & Hu B S (1997a).  
A forward-viewing intravascular ultrasound catheter for intracoronary use.  
Biomedical Instrumentation & Technology 31: 45-53.

Liang D H & Hu B S (1997b).  
Forward-looking catheters.  
Seminars in Interventional Cardiology 2: 75-81.

Linker D T, Kleven A, Grønningsæther Å, Yock P G & Angelsen B A J (1991).  
Tissue characterisation with inter-arterial ultrasound: special promise and problems.  
International Journal of Cardiac Imaging 6: 225-263.

Lockwood G R, Ryan L K, Gotlieb A I, Lonn E, Hunt J W, Liu P & Foster F S (1992).  
*In vitro* high resolution intravascular imaging in muscular and elastic arteries.  
Journal of the American College of Cardiology 20(1): 153-160.

Losordo D W, Rosenfield K, Pieczek A, Baker K, Harding M & Isner J M (1992).  
How does angioplasty work? Serial analysis of human iliac arteries using intravascular ultrasound.  
Circulation 86(6): 1845-1858.

Loupas T, Powers J T & Gill R W (1995a).



An axial velocity estimator for ultrasound blood flow imaging, based on a full evaluation of the Doppler equation by means of a two dimensional autocorrelation approach.

IEEE Transactions on Ultrasonics, Ferroelectrics and Frequency Control 42(4) : 672-688.

Loupas T, Peterson R B & Gill R W (1995b).

Experimental evaluation of velocity and power estimation for ultrasound blood flow imaging, by means of a two-dimensional autocorrelation approach.

IEEE Transactions on Ultrasonics, Ferroelectrics and Frequency Control 42(4) : 689-699.

Ludomirsky A, Siberbach M, Kenny A, Shiota T, Rice M J, Klas B, Krauzowicz B, Klein P, Derman R & Sahn D J (1994).

Superiority of rotational scan reconstruction strategies for transthoracic 3-dimensional real-time echocardiographic studies in pediatric patients with CHD.

Journal of the American College of Cardiology Supplement: 196A.

Maroney J F, Aldrich W N, Belef W M (1994).

Forward viewing imaging catheter.

US Patent No. 5373849.

Marr D & Hildreth E (1980).

Theory of edge detection.

Proceedings of the Royal Society of London B207: 187-217.

Martin R W, Bashein G, Detmer P R & Moritz W E (1990).

Ventricular volume measurement from a multiplanar transesophageal ultrasonic imaging system: an *in vitro* study.

IEEE Transactions on Biomedical Engineering 37(5): 442-449.

Matar FA, Mintz G S, Douek P, Farb A., Virmani R, Javier S P, Popma J J, Pichard A D, Kent K M, Salter L F, Keller M & Leon M B (1994).

Coronary artery lumen volume measurement using three-dimensional intravascular ultrasound : validation of a new technique.

Catheterization and Cardiovascular Diagnosis 33: 214-220.

McCann H A, Sharp J C, Kinter T M, McEwan C N, Barillot C & Greenleaf JF (1988).

Multidimensional ultrasonic imaging for cardiology.

Proceedings of the IEEE 76(9): 1063-1073.

McDicken W N (1991).



Diagnostic Ultrasonics. Principles and use of instruments, Third Edition, Churchill Livingstone, Edinburgh, UK.

McPherson D D & Kane B J (1997).

Intravascular ultrasound. Three-Dimensional Applications and Forward Viewing. Cardiology Clinics 15: 63-76.

Mintz G S, Potkin B N, Keren G, Salter L F, Pichard A D, Kent K M, Popma J J & Leon M B (1992).

Intravascular ultrasound evaluation of the effect of rotational atherectomy in obstructive atherosclerotic coronary artery disease.

Circulation 86: 1383-1393.

Mintz G S, Pichard A D, Kovach J A, Kent K M, Satler L F, Javier S P, Popma J J & Leon M B (1994a).

Impact of preintervention intravascular ultrasound imaging on transcatheter treatment strategies in coronary artery disease.

American Journal of Cardiology 73: 423-430.

Mintz G S, Pichard A D, Satler L F, Chuang Y C, Ditrano C J & Popma J J (1994b).

Intravascular ultrasound predictors of angiographic restenosis.

Circulation 90 (Suppl) : I-163.

Mintz G S, Kovach J A, Javier S P, Pichard A D, Kent K M, Popma J J, Salter L F & Leon M B (1995).

Mechanisms of lumen enlargement after excimer laser coronary angioplasty: An intravascular study.

Circulation 92(12): 3408-3414.

Moraes R & Evans D H (1995).

Effects of nonuniform insonation by catheter-tipped Doppler transducers on velocity estimation.

Ultrasound in Medicine and Biology 21(6): 779-791.

Moriuchi M, Tobis J M, Mahon D, Gessert J, Griffith J, McRae M, Moussabek O & Henry W L (1990)

The reproducibility of intravascular ultrasound imaging *in vitro*.

Journal of the American Society of Echocardiography 3: 444-450.

Mudra H, Klauss V, Blasini R, Kroetz M, Rieber J, Regar E & Theisen K (1994).

Ultrasound guidance of Palmaz-Schatz intracoronary stenting with a combined intravascular ultrasound balloon catheter.

Circulation 90: 1252-1261.

- Nailon W H (1997).  
Tissue characterisation from intravascular ultrasound using texture analysis.  
PhD Thesis, University of Edinburgh, Edinburgh, UK.
- Nakamura S, Mahon D J, Leung C Y, Maheswaran B, Gutfinger D E, Yang J, Zelman R & Tobis J M (1995).  
Intracoronary ultrasound imaging before and after directional coronary atherectomy: *in vitro* and clinical observations.  
American Heart Journal 129: 841-851.
- Nelson T R & Elvins T T (1993).  
Visualization of 3D ultrasound data.  
IEEE Computer Graphics & Applications 13: 50-57.
- Nelson T R & Pretorius D H (1997).  
Interactive acquisition, analysis, and visualisation of sonographic volume data.  
International Journal of Imaging Systems and Technology 8: 26-37.
- Nelson T R & Pretorius D H (1998).  
Three-dimensional ultrasound imaging.  
Ultrasound in Medicine and Biology 24(9): 1243-1270.
- Newby D E & Fox K A A.  
Intravascular assessment and drug administration in the coronary circulation.  
The British Journal of Clinical Pharmacology (in press).
- Ng K-H, Evans J L, Vonesh M J, Meyers S N, Mills T A, Kane B J, Aldrich W N, Jang Y-T, Yock P G, Rold M D, Roth S I & McPherson, D D (1994).  
Arterial imaging with a new forward-viewing intravascular ultrasound catheter, II. Three-dimensional reconstruction and display of data.  
Circulation 89: 718-723.
- Nishimura R A, Edwards W D, Warnes C A, Reeder G S, Holmes D R, Tajik A J, Yock P G (1990).  
Intravascular ultrasound imaging: *in vitro* validation and pathologic correlation.  
Journal of the American College of Cardiology 16: 145-154.
- Nissen S E, Grines C L, Gurley J C, Sublett K, Haynie D, Diaz C, Booth D C & DeMaria A N (1990).  
Application of a new phased-array ultrasound imaging catheter in the assessment of vascular dimensions. *In vivo* comparison to cineangiography.  
Circulation 81: 660-666.
- Nissen S E, Gurley J C, Booth D C & Demaria A N (1993).

Coronary intravascular ultrasound: rationale, technology and initial clinical applications.

In Hanrath P, Uebis R & Krebs W (editors). Cardiovascular Imaging by Ultrasound. Kluwer Academic Publishers, Dordrecht, The Netherlands, pp. 355-374.

O'Donnell M, Eberle M J, Stephens D N, Litzza J L, San Vicente K, Shapo B M (1997a).

Synthetic phased arrays for intraluminal imaging of coronary arteries.

IEEE Transactions on Ultrasonics, Ferroelectrics and Frequency Control 44:714-721.

O'Donnell M, Eberle M J, Stephens D N, Litzza J L, Shapo B M, Crowe J R, Choi C D, Chen J J, Muller D M W, Kovach J A, Lederman R L, Ziegenbein R C, Wu C C, San Vicente K & Bleam D (1997b).

Catheter arrays: Can intravascular ultrasound make a difference in imaging coronary artery disease.

Proceedings of the IEEE Ultrasonics Symposium, vol 2, 1447-1456.

Ofili E O & Nanda N C (1994).

Three-dimensional and four-dimensional echocardiography.

Ultrasound in Medicine and Biology 20(8): 669-675.

Painter J A, Mintz G S, Wong S C, Popma J J, Pichard A D, Kent K M, Satler L F & Leon M B (1995).

Serial intravascular ultrasound studies fail to show evidence of chronic Palmaz-Schatz stent recoil.

American Journal of Cardiology 75: 398-400.

Pérez J E, Waggoner A D, Barzilai B, Melton H E, Miller J G & Sobel B E (1992).

On-line assessment of ventricular function by automatic boundary detection and ultrasonic backscatter imaging.

Journal of the American College of Cardiology 19: 313-320.

Picano E, Landini L, Distanto A, Salvadori M, Lattanzi F, Masini M & L'Abbate A (1985).

Angle dependence of ultrasonic backscatter in arterial tissues: a study in vitro. Circulation 72(3): 572-576.

Post M J, de Smet B J, van der Helm Y, Borst C & Kuntz R E (1997).

Arterial remodelling after balloon angioplasty or stenting in an atherosclerotic experimental model.

Circulation 96(3): 996-1003.

Potkin B N, Bartorelli A L, Gessert J M, Neville R F, Almagor Y, Roberts W C & Leon M B (1990).

Coronary artery imaging with intravascular high-frequency ultrasound.  
*Circulation* 81: 1575-1585.

Prati F, Di Mario C, Gil R, von Birgelen C, Camenzind E, van Swijndregt W J M, de Feyter P J, Serruys P W & Roelandt J R T C (1996).  
Usefulness of on-line three-dimensional reconstruction of intracoronary ultrasound for guidance of stent deployment.  
*The American Journal of Cardiology* 77: 455-461.

Prati F, Di Mario C, Moussa I, Reimers B, Mallus M T, Parma A, Lioy E & Colombo A (1999).  
In-stent neointimal proliferation correlates with the amount of residual plaque burden outside the stent - An intravascular ultrasound study.  
*Circulation* 99(8): 1011-1014.

Prause G P M, DeJong S C, McKay C R & Sonka M (1996).  
Semi-automated segmentation and 3-D reconstruction of coronary trees: biplane angiography and intravascular ultrasound data fusion.  
*Proceedings of the Society of Photo-optical Instrumentation Engineers* 2709: 82-92.

Ramnarine K V, Nassiri D K, Hoskins P R & Lubbers J (1998).  
Validation of a new blood-mimicking fluid for use in Doppler flow test objects.  
*Ultrasound in Medicine and Biology* 24(3): 451-459.

Ramnarine K V, Hoskins P R, Routh H F & Davidson F (1999).  
Doppler backscatter properties of a blood-mimicking fluid for Doppler performance assessment.  
*Ultrasound in Medicine and Biology* 25(1): 105-110.

Rieber J, Klauss V, König A, Henneke K H, Spes C, Regar E, Werner F, Meiser B, Reichart B, Theisen K & Mudra H (1998).  
Assessment of intraindividual variability of coronary flow reserve in angiographically normal coronary arteries in transplant recipients: a study with intracoronary Doppler and intravascular ultrasound.  
*Transplantation Proceedings* 30: 1926-1927.

Roelandt J R T C, Sutherland G R, Iliceto S & Linker D T, editors (1993a).  
*Cardiac Ultrasound*. Churchill Livingstone, Edinburgh, UK.

Roelandt J R T C, Di Mario C, de Feyter P J, van den Brand M, Serruys P W & Bom N (1993b).  
Intravascular Ultrasound: instrumentation, image interpretation, promises and pitfalls.

In Hanrath P, Uebis R, Krebs W (editors). Cardiovascular Imaging by Ultrasound. Kluwer Academic Publishers, Dordrecht, The Netherlands, pp 325-341.

Roelandt J R T C, Di Mario C, Pandian N G, Wenguan L, Keane D, Slager C J, de Feyter P J & Serruys P W (1994a)

Three-dimensional reconstruction of intracoronary ultrasound images. Rationale, approaches, problems and directions.

Circulation 90: 1044-1055.

Roelandt J R T C, ten Cate F J, Vletter W B & Taams M A (1994b).

Ultrasonic dynamic three-dimensional visualisation of the heart with a multiplane transesophageal imaging transducer.

Journal of the American Society of Echocardiography 7: 217-229.

Rohling R N (1998).

3D Freehand ultrasound: Reconstruction and spatial computing.

PhD Thesis, University of Cambridge, Cambridge, UK.

Rosenfield K, Losordo D W, Ramaswamy K, Pastore J O, Langevin R E, Razvi S, Kosowsky B D & Isner J M (1991).

Three-dimensional reconstruction of human coronary and peripheral arteries from images recorded during two-dimensional intravascular ultrasound examination.

Circulation 84: 1938-1956.

Rosenfield K, Kaufman J, Pieczek A M, Langevin R E, Palefski P E, Razvi S A & Isner J M (1992).

Human coronary and peripheral arteries: On-line three-dimensional reconstruction from two-dimensional intravascular US scans.

Radiology 184: 823-832.

Russo P, Orszulak T A, Schaff H V & Holmes D R (1986).

Use of internal mammary artery grafts for multiple coronary artery bypasses.

Circulation 74 (Suppl III), III48-52.

Ryan L K & Foster F S (1997).

Tissue equivalent Vessel Phantoms for Intravascular Ultrasound.

Ultrasound in Medicine and Biology, 23 (2): 261-273.

Salustri A & Roelandt J R T C (1995).

Ultrasonic three-dimensional reconstruction of the heart.

Ultrasound in Medicine and Biology 21(3): 281-293.

Sanborn T A, Cumberland D C, Greenfield A J & Welch C L (1988).

Percutaneous laser thermal angioplasty: Initial results and 1-year follow-up in 129 femoropopliteal lesions.  
*Radiology* 168(1): 121-125.

Schwarten D E, Katzen B T, Simpson J B & Cutcliff W B (1988)  
Simpson catheter for percutaneous transluminal removal of atheroma.  
*American Journal of Roentgentology* 150(4): 799-801.

Schwarzacher S P, Fitzgerald P J & Yock P G (1997).  
Clinical use of intravascular ultrasound.  
*Seminars in Interventional Cardiology* 2: 1-9.

Sherman C T, Litvack F, Grundfest W, Lee M, Hickey A, Chaux A, Kass R, Blanche C, Matloff J, Morgenstern L, Ganz W, Swan H J C & Forrester J (1986).  
Coronary angioscopy in patients with unstable angina pectoris.  
*New England Journal of Medicine* 315(15): 913-919.

Siegel R J, Chae J-S, Forrester J S & Ruiz C E (1990).  
Angiography, angioscopy, and ultrasound imaging before and after percutaneous balloon angioplasty.  
*American Heart Journal* 120(5): 1086-1090.

Siegel R J, Ariani M, Fishbein M C, Chae J-S, Park J C, Maurer G & Forrester J S (1991).  
Histopathologic validation of angioscopy and intravascular ultrasound.  
*Circulation* 84: 109-117.

Sigwart U, Puel J, Mirkovitch V, Joffre F & Kappenberger L (1987).  
“Intravascular stents to prevent occlusion and restenosis after transluminal angioplasty”.  
*New England Journal of Medicine* 316(12): 701-706.

Simpson J B, Selmon M R, Robertson G C, Cipriano P R, Hayden W G, Johnson D E & Fogarty T J (1988).  
Transluminal atherectomy for occlusive peripheral vascular disease.  
*American Journal of Cardiology* 61(14): 96G-101G.

Singh R N, Sosa J A & Green G E (1983).  
“Long-term fate of the internal mammary artery and saphenous vein grafts”.  
*Journal of Thoracic and Cardiovascular Surgery* 86(3): 359-363.

Slager C J, Essed C E, Schuurbiers J C H, Bom N, Serruys P W & Meester G T (1985).  
Vaporization of atherosclerotic plaques by spark erosion.

Journal of the American College of Cardiology 5(6), 1382-1386.

Slager C J, Wentzel J J, Oomen J A F, Schuurbiens J C H, Krams R, von Birgelen C, Tjon A, Serruys P W & de Feyter P J (1997).

True reconstruction of vessel geometry from combined X-ray angiographic and intracoronary ultrasound data.

Seminars in Interventional Cardiology 2: 43-47.

Sonka M, Zhang X, Siebes M, Bissing M S, DeJong S C, Collins S M & McKay C R (1995a).

Segmentation of intravascular ultrasound images : a knowledge-based approach.

IEEE Transactions on Medical Imaging 14 : 719-732.

Sonka M, Liang W, Zhang S, DeJong S, Collins S M & McKay C R (1995b).

Three-dimensional automated segmentation of coronary wall and plaque from intravascular ultrasound pullback sequences.

Computers in Cardiology 203: 637-640.

Spencer T, Ramo M P, Salter D M, Anderson T, Kearney P P, Sutherland G R, Fox K A A & McDicken W N (1997).

Characterisation of atherosclerotic plaque by spectral analysis of intravascular ultrasound: an *in vitro* methodology.

Ultrasound in Medicine and Biology 23(2): 191-203.

Spencer T, Pye S, Ramo M P, Sutherland G R & McDicken W N.

The spectral characteristics of 30 MHz intravascular ultrasound transducers.

Submitted for publication in Ultrasonics.

Stack R S, Perez J A, Newman G F, McCann R L, Wholey M H, Cummins F E, Galichia J T, Hoffmann P U, Tchong J E, Sketch Jr M H, Lee M M & Phillips H R (1989).

Treatment of peripheral vascular disease with the transluminal extraction catheter: results of a multicenter study.

Journal of the American College of Cardiology 13, 227A.

Stary H C, Chandler A B, Dinsmore R E, Fuster V, Glagov S, Insull Jr W, Rosenfield M E, Schwartz C J, Wagner W D, Wissler R W (1995).

A definition of advanced types of atherosclerotic lesions and a histological classification of atherosclerosis.

Circulation 92: 1355-1374.

St Goar F G, Pinto F J, Alderman E L, Valentine H A, Schroeder J S, Gao S Z, Stinson E B & Popp R L (1992).



Intracoronary ultrasound in cardiac transplant recipients. *In vivo* evidence of “angiographically silent” intimal thickening.  
Circulation 85: 979-987.

Stone G W, St Goar F G & Linnemeier T J (1996).  
Initial clinical experience with a novel low-profile integrated ultrasound-angioplasty catheter.  
Catheterization and Cardiovascular Diagnosis 38(3): 303-307.

Stone G W, Hodgson J M, St Goar F G, Frey A, Mudra H, Sheehan H & Linnermeier T J (1997).  
Improved procedural results of coronary angioplasty with intravascular ultrasound-guided balloon sizing. The CLOUT Pilot Trial.  
Circulation 95: 2044-2052.

Sudhir K, MacGregor J S, Barbant S D, Foster E, Fitzgerald P J, Chatterjee K & Yock P G (1993).  
Assessment of coronary conductance and resistance vessel reactivity in response to nitroglycerin, ergonovine and adenosine: *in vivo* studies with simultaneous intravascular two-dimensional and Doppler ultrasound.  
Journal of the American College of Cardiology 21: 1261-1268.

Tadaoka S, Kagiya M, Hiramatsu O, Ogasawara Y, Tsujioka K, Wada Y, Sawayama T & Kajiya F (1990).  
Accuracy of 20-MHz Doppler catheter coronary artery velocimetry for measurement of coronary blood flow velocity.  
Catheterization and Cardiovascular Diagnosis 19: 205-213.

Tanaka M, Neyazaki T, Kosaka S, Sugi H, Oka S, Ebina T, Terasawa Y, Unno K & Nitta K (1971).  
Ultrasonic evaluation of anatomical abnormalities of heart in congenital and acquired heart diseases.  
British Heart Journal 33: 686-698.

Tenaglia A N, Buller C E, Kisslo K B, Stack R S & Davidson C J (1992).  
Mechanisms of balloon angioplasty and directional atherectomy as assessed by intracoronary ultrasound.  
Journal of the American College of Cardiology 20(3): 685-691.

ten Hoff H, Korbijn A, Smit T H, Klinkhammer J F F & Bom N (1989).  
Imaging artifacts in mechanically driven ultrasound catheters.  
International Journal of Cardiac Imaging 4: 195-199.

ten Hoff H (1993).



Scanning mechanisms for intravascular ultrasound imaging. A flexible approach.  
PhD Thesis, Erasmus University Rotterdam, The Netherlands.

ten Hoff H, Hamm M A, Lowe G E & Koger J D (1997).  
Technical aspects of ultrasound imaging guidewires.  
Seminars in Interventional Cardiology 2: 63-68.

The S H K, Gussenhoven E J, Zhong Y, Li W, van Egmond F, Pieterman H, van Urk  
H, Gerritsen G P, Borst C, Wilson R A & Bom N (1992).  
Effect of balloon angioplasty on femoral artery evaluated with intravascular  
ultrasound imaging.  
Circulation 86(2): 483-493.

Thrush A J, Bonnett D E, Elliott M R, Mutob S S & Evans D H (1997).  
An evaluation of the potential and limitations of three-dimensional reconstructions  
from intravascular ultrasound images.  
Ultrasound in Medicine and Biology 23(3): 437-445.

Tierlinck C J P M, Fish P, Hoskins P R, Lubbers J, Fredfeldt K E, Kollmann C,  
Schaarschmidt U G, Zeqiri B, Nassiri D (1997).  
Validation of a flow Doppler test object for diagnostic ultrasound scanners.  
EC TNO Report contract MAT-CT 940091, TNO Prevention and Health, Leiden.

Tierlinck C J P M, Bezemer R A, Kollmann C, Lubbers J, Hoskins P R, Fish P,  
Fredfeldt K, Schaarschmidt U G & Ramnarine K V (1998).  
Development of an example flow test object and comparison of five of these objects,  
constructed in various laboratories.  
Ultrasonics 36 : 653-660.

Tobis J M, Mallery J, Mahon D, Lehmann K, Zalesky P, Griffith J, Gessert J,  
Moriuchi M, McRae M, Dwyer M-L, Greep N & Henry W (1991).  
Intravascular ultrasound imaging of human coronary arteries *in vivo*. Analysis of  
tissue characterizations with comparison to *in vitro* histological specimens.  
Circulation 83: 913-926.

Torre V & Poggio T A (1986).  
On edge detection.  
IEEE Transactions on Pattern Analysis and Machine Intelligence PAMI-8(2): 147-  
163.

Tyras D H, Barner H B, Kaiser G C, Codd J E, Pennington D G & Willman V L  
(1980).  
"Bypass grafts to the left anterior descending coronary artery. Saphenous vein versus  
internal mammary artery".

Journal of Thoracic and Cardiovascular Surgery 80(3): 327-333.

Udupa J K & Herman G T (1989).  
Volume rendering versus surface rendering.  
Communications of the ACM 32:1364-1366.

van der Lugt A, Hartlooper A, van Essen J A, Li W, von Birgelen C, Reiber J H C & Gussenhoven E J (1998).  
Reliability and reproducibility of automated contour analysis in intravascular ultrasound images of femoropopliteal arteries.  
Ultrasound in Medicine and Biology 24(1) : 43-50.

Veith F J, Gupta S K, Ascer E, White-Flores S, Samson R H, Scher L A, Towne J B, Bernhard V M, Bonier P, Flinn W R, Astelford P, Yao J S T & Bergan J J (1986).  
"Six-year prospective multicenter randomized comparison of autologous saphenous vein and expanded polytetrafluoroethylene grafts in infrainguinal arterial reconstructions".  
Journal of Vascular Surgery 3(1): 104-114.

von Birgelen C, Erbel R, Di Mario C, Li W, Prati F, Ge J, Bruining N, Gorge G, Slager C J, Serruys P W & Roelandt J R T C (1995).  
Three-dimensional reconstruction of coronary arteries with intravascular ultrasound.  
Herz 20: 277-289.

von Birgelen C, Gil R, Ruygrok P, Prati F, Di Mario C, van der Giessen W J, de Feyter P J & Serruys P W (1996a).  
Optimized expansion of the Wallstent compared with the Palmaz-Schatz stent: On-line observations with two- and three-dimensional intracoronary ultrasound after angiographic guidance.  
American Heart Journal 131: 1067-1075.

von Birgelen C, Kutryk M J B, Gil R, Ozaki Y, Di Mario C, Roelandt J R T C, de Feyter P J & Serruys P W (1996b).  
Quantification of the minimal luminal cross-sectional area after coronary stenting by two- and three-dimensional intravascular ultrasound versus edge detection and videodensitometry.  
American Journal of Cardiology 78: 520-525.

von Birgelen C, van der Lugt A, Nicosia A, Mintz G S, Gussenhoven E J, de Vrey E, Mallus M T, Roelandt J R T C, Serruys P W & de Feyter P J (1996c).  
Computerised assessment of coronary lumen and atherosclerotic plaque dimensions in three-dimensional intravascular ultrasound correlated with histomorphometry.  
American Journal of Cardiology 78: 1202-1209.

von Birgelen C, Di Mario C, Reimers B, Prati F, Bruining N, Gil R, Serruys P W & Roelandt J R T C (1996d).

Three-dimensional intracoronary ultrasound imaging. Methodology and clinical relevance for the assessment of coronary arteries and bypass grafts.

Journal of Cardiovascular Surgery 37: 129-139.

von Birgelen C, Mintz G S, de Feyter P J, Bruining N, Nicosia A, Di Mario C, Serruys P W & Roelandt J R T C (1997).

Reconstruction and quantification with three-dimensional intracoronary ultrasound. An update on techniques, challenges, and future directions.

European Heart Journal 18: 1056-1067.

Waller B F (1989a).

Anatomy, histology and pathology of the major epicardial coronary arteries relevant to echocardiographic imaging techniques.

Journal of the American Society of Echocardiography 2: 232-252.

Waller B F (1989b).

The eccentric coronary atherosclerotic plaque: morphologic observations and clinical relevance.

Clinical Cardiology 12: 14-20.

Watson R J, McLean C C, Moore M P, Spencer T, Salter D M, Anderson T, Fox K A A & McDicken W N (2000).

Classification of arterial plaque by spectral analysis of *in vitro* RF IVUS data.

Ultrasound in Medicine and Biology 26(1): 73-80.

Wells P N T (1977).

Biomedical Ultrasonics, Academic Press, London, UK.

Werner G S, Gastmann O, Ferrari M, Scholz K H, Schunemann S & Figulla H R (1999).

Determinants of stent restenosis in chronic coronary occlusions assessed by intracoronary ultrasound.

American Journal of Cardiology 83(8): 1164-1169.

White R A, Kopchok G E, Tabbara M R, Cavaye D M & Cormier F (1992).

Intravascular ultrasound guided holmium:YAG laser recanalization of occluded arteries.

Lasers Surgery Medicine 12: 239-245.

Whittingham T A (1991).

Resolution and information limitations from transducer arrays.

Physics in Medicine and Biology 36(11): 1503-1514.

- Whittingham T A (1997).  
New and future developments in ultrasonic imaging.  
The British Journal of Radiology 70: S119-S132.
- Whittingham T A (1999).  
Transducers and beam forming in medical ultrasonic imaging.  
Insight 41(1): 8-12.
- Wiet S P, Ng K-H, Vonesh M J, Aldrich W N, Jang Y T, Yock P G, Kane B J, Greene R, Meyers S N, Roth S I & McPherson D D (1994).  
Initial *in vivo* studies using a new forward-viewing intravascular ultrasound catheter.  
Journal of the American College of Cardiology Suppl: 291A.
- Williams D J & Shah M (1992).  
A fast algorithm for active contours and curvature estimation.  
CVGIP - Image Understanding 55(1): 14-26.
- Wilson L S, Neale M L, Talhami H E & Appleberg M (1994).  
Preliminary results from attenuation-slope mapping of plaque using intravascular ultrasound.  
Ultrasound in Medicine and Biology 20: 529-542.
- Yock P G, Fitzgerald P J, Linker D T & Angelsen B A J (1991).  
Intravascular ultrasound guidance for catheter-based coronary interventions.  
Journal of the American college of Cardiology 17(6): 39B-45B.
- Zarins C K, Giddens D P, Bharadvaj B K, Sottiurai V S, Mabon R F & Glagov S (1983).  
Carotid bifurcation atherosclerosis. Quantitative correlation of plaque localization with flow velocity profiles and wall shear stress.  
Circulation Research 53(4): 502-514.

## LIST OF PUBLICATIONS

### Abstracts

L Gatzoulis, T Anderson, SD Pye, CC McLean, KV Ramnarine, D Northridge, KAA Fox, WN McDicken.

*"Development of a simulation forward-viewing intravascular ultrasound imaging system using the radiofrequency signal".*

Echocardiography : A Journal of Cardiovascular Ultrasound and Allied Techniques, Volume 15, Number 6, Part 2, S96, 1998.

L Gatzoulis, T Anderson, SD Pye, R O'Donnell, CC McLean, KV Ramnarine, N Uren, WN McDicken.

*"Comparison of scanning techniques for three-dimensional forward-viewing intravascular ultrasound imaging".*

European Journal of Echocardiography, Abstracts Supplement: S88, 1999.

### Papers in preparation

L Gatzoulis, T Anderson, SD Pye, R O'Donnell, CC McLean, WN McDicken.

*"Scanning techniques for three dimensional forward-viewing intravascular ultrasound imaging".*

L Gatzoulis, RJ Watson, LB Jordan, SD Pye, T Anderson, N Uren, DM Salter, KAA Fox, WN McDicken.

*"Three dimensional forward-viewing intravascular ultrasound imaging of human arteries in vitro".*

L Gatzoulis, KV Ramnarine, SD Pye, T Anderson, DE Newby, PR Hoskins, WN McDicken.

*"Doppler colour flow imaging and flow quantification with forward-viewing intravascular ultrasound".*

## Conference presentations

L Gatzoulis, T Anderson, SD Pye, CC McLean, KV Ramnarine, D Northridge, KAA Fox, WN McDicken.

*"Development of a simulation forward-viewing intravascular ultrasound imaging system using the radiofrequency signal"*.

Euroecho 2, The second annual and plenary meeting of the Working Group on Echocardiography, Trieste, Italy, 9-12 December 1998 (oral presentation).

L Gatzoulis, T Anderson, SD Pye, R O'Donnell, CC McLean, RJ Watson, KV Ramnarine, N Uren, D Northridge, KAA Fox, WN McDicken.

*"Simulation of a forward-viewing intravascular ultrasound imaging system using a scaled up model"*.

The Physics and Technology of Medical Ultrasound, Meeting of The Institute of Physics and Engineering in Medicine, York, UK, 30-31 March 1999 (oral presentation).

L Gatzoulis, T Anderson, SD Pye, R O'Donnell, CC McLean, KV Ramnarine, N Uren, WN McDicken.

*"Comparison of scanning techniques for three-dimensional forward-viewing intravascular ultrasound imaging"*.

Euroecho 3, The third annual and plenary meeting of the Working Group on Echocardiography, Vienna, Austria, 8-11 December 1999 (poster presentation).

L Gatzoulis, RJ Watson, LB Jordan, SD Pye, T Anderson, N Uren, WN McDicken.

*"Three dimensional forward-viewing intravascular ultrasound imaging of human arteries in vitro"*.

WFUMB 2000, The 9<sup>th</sup> Congress of the World Federation for Ultrasound in Medicine and Biology, Florence, Italy, 6-10 May 2000 (oral presentation).

L Gatzoulis, KV Ramnarine, SD Pye, T Anderson, DE Newby, WN McDicken.

*"Doppler colour flow imaging and flow quantification with forward-viewing intravascular ultrasound"*.

WFUMB 2000, The 9<sup>th</sup> Congress of the World Federation for Ultrasound in Medicine and Biology, Florence, Italy, 6-10 May 2000 (poster presentation).